

Gravitational-wave detection beyond the quantum shot-noise limit

The integration of squeezed
light in GEO 600

Von der QUEST-Leibniz-Forschungsschule der
Gottfried Wilhelm Leibniz Universität Hannover
zur Erlangung des Grades

Doktor der Naturwissenschaften

Dr. rer. nat.

genemigte Dissertation von

Dipl.-Phys.

Emil Schreiber

2018

Referent: Prof. Dr. Karsten Danzmann
Korreferentin: Prof. Dr. Katherine L. Dooley
Korreferent: Prof. Dr. Roman Schnabel
Tag der Promotion: 15. Januar 2018



The work presented in this thesis was carried out at the
Max Planck Institute for Gravitational Physics (Albert Einstein Institute)
and Institute for Gravitational Physics, Leibniz Universität Hannover,
Callinstraße 38, 30167 Hannover, Germany

This thesis was assigned LIGO document number LIGO-P1800001-v2.
A digital version is available at: dcc.ligo.org/LIGO-P1800001/public



Abstract

The first detections of gravitational waves have opened an exciting new field of astronomy. One of the most fundamental limitations for the sensitivity of current and future interferometric gravitational-wave detectors is imposed by the quantum nature of light: Quantum vacuum fluctuations entering the interferometer through the readout port will contribute to the detection noise, at high frequencies in the form of shot noise and at low frequencies by radiation pressure noise. A promising way to reduce this quantum noise is the injection of squeezed states of light that have a lower uncertainty in one quadrature than the vacuum state. The GEO 600 gravitational-wave detector demonstrated the use of squeezed light in 2010 and it is now the first detector to routinely apply squeezing to improve its sensitivity beyond the limits set by classical quantum shot noise.

This thesis details the practical aspects of long-term stable and efficient squeezed-light integration in a large-scale gravitational-wave detector. Imperfections that can limit the amount of observable non-classical noise improvement, such as optical losses and phase fluctuations, were studied in detail and methods for their mitigation were developed. Novel control schemes for the active stabilisation of the squeezed light field's phase and alignment were one main focus of the investigations. At the same time, important experience was gathered in the operation of the squeezed light source over long timescales.

Over the course of the thesis work, improvements were implemented that significantly increased the performance of the squeezed-light application. Squeezing was injected with an overall duty cycle of 88 %, reaching a noise reduction of up to 4.4 dB, corresponding to a 40 % lowered shot-noise level.

This work has firmly established the practical application of squeezing as a mature technology. The gained knowledge will directly inform the implementation of squeezed light for all future gravitational-wave detectors.

Keywords: *Gravitational-wave detection, squeezed light, shot noise*

Kurzzusammenfassung

Mit der Detektion der ersten Gravitationswellen eröffnet sich ein spannendes neues Feld der Astronomie. Für die aktuellen wie auch zukünftigen Gravitationswellendetektoren ergibt sich eine wichtige fundamentale Begrenzung der erreichbaren Empfindlichkeit aus der Quantennatur des Lichtes. Vakuumfluktuationen, die durch den Interferometerausgang einkoppeln, führen zu Rauschen im Interferometersignal, bei hohen Frequenzen in der Form von Schrotrauschen und bei niedrigen Frequenzen als Strahlungsdruckrauschen. Eine vielversprechende Methode zur Unterdrückung dieses Quantenrauschens ist die Nutzung von gequetschtem Licht. Gequetschte Zustände des Lichtfeldes zeigen eine verringerte Unschärfe gegenüber dem Vakuumzustand in einer ihrer Quadraturen. Der Gravitationswellendetektor GEO 600 hat 2010 die erfolgreiche Verwendung von gequetschtem Licht demonstriert und ist seitdem der erste Detektor, der diese Technologie permanent einsetzt und damit kontinuierlich Empfindlichkeiten jenseits des klassischen Schrotrauschens erzielt.

Diese Arbeit befasst sich mit den praktischen Aspekten einer langzeitstabilen und effizienten Integration von gequetschtem Licht in Gravitationswellendetektoren. Realistische Beschränkungen der erreichbaren quantenmechanischen Rauschunterdrückung, wie etwa optische Verluste und Phasenrauschen, wurden ausführlich untersucht und es wurden Methoden entwickelt diese zu verbessern. Ein Schwerpunkt war dabei die Erforschung neuartiger Kontrolltechniken zur aktiven Stabilisierung von Phasenlage und Ausrichtung des gequetschten Lichtstrahls. Darüber hinaus wurden wichtige Erfahrungen mit dem kontinuierlichen Betrieb der Quetschlichtquelle über lange Zeiträume gesammelt.

Im Laufe dieser Arbeit konnten deutliche Verbesserungen der Leistungsfähigkeit des Quetschlichtsystems erreicht werden. Gequetschtes Licht kam mit einem Anteil von 88 % an der Gesamtlaufzeit des Detektors zum Einsatz und verbesserte dabei das Schrotrauschen um bis zu 4.4 dB, was einer Reduktion des Rauschpegels um 40 % entspricht.

Die erreichten Erfolge konnten zeigen, dass die Verwendung von gequetschtem Licht eine ausgereifte Technologie darstellt. Das neu erlangte Wissen wird direkt dazu beitragen, Quetschlicht zu einem festen Bestandteil aller zukünftigen Gravitationswellendetektoren zu machen.

Schlagwörter: *Gravitationswellendetektion, gequetschtes Licht, Schrotrauschen*

Contents

Abstract	v
Figures and tables	xi
List of figures	xi
List of tables	xiii
Glossary	xv
Abbreviations	xv
Reoccurring mathematical symbols	xvi
Pictograms	xviii
1 Introduction	1
1.1 Gravitational waves	2
1.2 Laser interferometers for gravitational-wave detection	5
1.3 Noise sources in interferometric gravitational-wave detectors	9
1.4 Quantum enhancement	12
1.5 About this thesis	13
2 Theoretical background	15
2.1 Quantum states of light	16
2.1.1 Quantization of the electromagnetic field	16
2.1.2 Coherent states	17
2.1.3 Quadrature operators	18
2.1.4 Squeezed states	19
2.1.5 Phase space representation	22
2.1.6 Generation of squeezed light	25
2.1.7 Detection of squeezed light	26
2.1.7.1 Direct measurement with a photodiode	27
2.1.7.2 Balanced homodyne detection	28
2.1.8 Quantum noise in interferometers	29
2.1.8.1 Shot noise	31
2.1.8.2 Radiation-pressure noise	33
2.1.8.3 Noise spectral densities	34
2.1.8.4 The standard quantum limit	36

Contents

2.2	Influence of imperfections	39
2.2.1	Losses	39
2.2.2	Contributions from classical noise	40
2.2.3	Phase noise	41
2.2.4	Backscattering	43
2.2.5	Combination of imperfections	47
3	Long-term operation of the GEO 600 squeezed-light source	53
3.1	The GEO 600 squeezer	54
3.2	Auxiliary laser systems and PLLs	55
3.3	Green pump light	60
3.3.1	SHG	60
3.3.2	Modecleaner for the green pump light	66
3.3.3	Power control with a Mach–Zehnder interferometer	69
3.4	Optical parametric amplifier	69
3.4.1	Bright alignment beam	70
3.4.2	Coherent-control field	72
3.4.3	Phase matching	73
3.4.4	Measuring the parametric gain	74
3.4.5	OPA cavity degradation	76
3.5	On-board balanced homodyne detector	77
3.6	Automated operation	78
3.6.1	Locking of the squeezer subsystems	78
3.6.2	Shutter control	80
3.6.3	Duty cycle	81
4	Squeezed light injection	83
4.1	The GEO 600 gravitational wave detector	85
4.2	Phase control	86
4.2.1	Three ways to generate the coherent-control signal	86
4.2.2	Performance of the different phase-control signals	89
4.2.3	Noise locking	92
4.2.4	Overview of the complete phase control scheme	94
4.2.5	Residual phase noise	96
4.3	Alignment control	99
4.3.1	The effect of misalignment	100
4.3.2	Alignment actuators	102
4.3.3	Alignment signals from differential wavefront sensing	104
4.3.4	Beam centring	107
4.3.5	Gouy-phase telescope design	108
4.3.6	Diagonalization of the alignment controls	110

4.3.7	Performance of the automatic squeezing alignment	112
4.4	Mode matching	116
4.5	Optical losses	119
4.5.1	Measuring optical losses	120
4.5.2	Polarization effects	121
4.5.3	Reflection off the interferometer	125
4.5.4	Transmission through the OMC	126
4.5.5	Quantum efficiency of the detection PD	126
4.5.6	Loss budget of the injection path	126
4.5.7	A new design for the Faraday isolator assembly	128
4.6	Backscattering	131
4.6.1	Coupling of stray-light phase fluctuations	131
4.6.2	Linear coupling of squeezing-angle fluctuations	133
4.6.3	Optimizing the backscatter isolation	134
4.7	Electronic dark noise	136
5	Characterization and long-term performance	139
5.1	Detection-noise improvement by squeezing	140
5.2	Measuring squeezing levels	140
5.2.1	Calculating squeezing level from two reference times	142
5.2.2	Online estimation	143
5.3	Estimating parameters of the squeezing injection	144
5.4	Squeezing performance over the years at GEO 600	146
6	Summary and outlook	149
	Appendices	153
A	Detailed optical layout of GEO 600	155
B	Manuals	157
B.1	Overview of MEDM screens and monitors	157
B.2	List of possible problems	160
	Bibliography	163
	Publications	177
	Acknowledgements	187

Figures and tables

List of figures

1.1	The gravitational-wave signal GW150914	2
1.2	Effect of a gravitational wave	4
1.3	Simple Michelson interferometer	6
1.4	Simplified layout of Advanced LIGO	6
1.5	Map of the second-generation detector network	8
1.6	Noise budget of Advanced LIGO	10
2.1	Variance of a squeezed state	21
2.2	Wigner function and representation as uncertainty ellipse	23
2.3	Examples of quantum states in the phasor representation	24
2.4	Detecting squeezed states	28
2.5	Quantum noise propagation in a Michelson interferometer	30
2.6	Shot noise in a Michelson interferometer	33
2.7	Quantum noise for different circulating powers	37
2.8	Quantum noise with squeezing	38
2.9	Squeezing ratio as a function of losses	40
2.10	Squeezing ratio as a function of phase noise	42
2.11	Backscattering at the squeezed-light source	44
2.12	Squeezing ratio as a function of backscatter noise	47
2.13	Influence of different imperfections	48
2.14	Combined influence of imperfections	49
2.15	Influence of losses and phase noise	51
3.1	Layout of the GEO 600 squeezed-light source	56
3.2	Photo of the squeezed-light source	57
3.3	Squeezer auxiliary lasers and PLL setup	58
3.4	Green pump generation and stabilization	60
3.5	Schematic cross section of the SHG cavity	61
3.6	Photo of the degraded SHG coupling mirror	62
3.7	SHG power over the years	63
3.8	Green pump power over the years	64
3.9	Mode scan of the green modecleaner cavity	67

Figures and tables

3.10	Finesse and transmissivity of the green modecleaner	68
3.11	Diagram of the OPA	70
3.12	Optimal p-pol. offset as a function of OPA temperature	74
3.13	Parametric amplification and deamplification	75
3.14	Output mode of damaged OPA	76
3.15	Balanced homodyne measurement	78
3.16	Overview of the squeezer's digital control	79
3.17	Overview of the shutter control	80
3.18	Duty cycle of the GEO 600 squeezed-light source	82
4.1	Schematic overview of the GEO 600 gravitational-wave detector	84
4.2	Inside of the detector's main building	85
4.3	Three possible locations to generate the squeezer phase-control signal	87
4.4	Spectra of squeezer phase error signals	90
4.5	Squeezing-level fluctuations with different phase-control signals	91
4.6	Influence of OPA temperature on optimal squeezing phase	92
4.7	Two-week trend of the noise-lock feedback	94
4.8	Overview of the complete squeezer-phase control scheme	95
4.9	Phase noise caused by the optical fibre	98
4.10	Relative alignment of two Gaussian beams	100
4.11	Degradation of squeezing due to misalignment	101
4.12	Model of the in-air injection beam path	103
4.13	Calibration of the alignment actuators	105
4.14	Alignment sensors and actuators	106
4.15	Galvanometer scanners for beam centring	108
4.16	Optical layout of the OMC reflection path	109
4.17	Model of the OMC-reflection Gouy-phase telescope	109
4.18	Switching the alignment control on	111
4.19	Alignment-error spectra	113
4.20	Squeezing-level fluctuations with different alignment-control signals	114
4.21	Suppressing an artificial alignment excitation	115
4.22	Mode scans of the OMC	117
4.23	Influence of mode-matching lenses	118
4.24	Overview of the complete injection path	119
4.25	Two possible setups for accurately measuring optical losses	121
4.26	Angle-of-incidence dependence of PBS transmission and extinction	122
4.27	Squeezing transmission while turning waveplates	123
4.28	Influence of waveplate settings	124
4.29	Reflectivity of the signal-recycling cavity	125
4.30	Drawing of the new Faraday assembly	129

4.31	Photo of the completed Faraday assembly	129
4.32	Backscatter noise with large-amplitude path-length excitation	132
4.33	Observed effect of reduced backscatter isolation	134
4.34	Backscattering with squeezer frequency offset	135
4.35	Detection schemes for photocurrent to voltage conversion	137
4.36	Improved dark noise with the new readout electronics	138
5.1	Spectrum of h with and without squeezing	141
5.2	Determining the squeezing level with noise floor estimation	142
5.3	Interface of the online squeezing-level monitor	144
5.4	Apparent RMS phase noise as a function of backscattering	146
5.5	Estimating losses and phase noise	147
5.6	Histogram of the squeezing level over the last six years	148
A.1	Optical layout of the output path with squeezing injection	155
A.2	Complete optical layout of GEO 600	155

List of tables

4.1	Known sources of residual phase noise	97
4.2	Loss budget of the squeezing injection	127
6.1	Imperfections and reachable squeezing levels now and in the future	151

Glossary

Abbreviations

a.u.	arbitrary units
ADC	analogue-to-digital converter
AEI	Albert Einstein Institute
AOM	acousto-optic modulator
AR	anti-reflective
BDO	beam directing optic
BLRMS	band-limited root-mean-square fluctuations
CC	coherent control
CCD	charge-coupled device
CCSB	coherent-control sideband
CDS	LIGO Control and Data Acquisition System
cts.	counts
DAC	digital-to-analogue converter
DC	direct current (used to describe the 0 Hz part of a general signal)
DWS	differential wavefront sensing
EOM	electro-optic modulator
EP	error point
EPICS	Experimental Physics and Industrial Control System
FB	feedback
FSR	free spectral range
GUI	graphical user interface
GW	gravitational wave
HOM	higher-order mode
HR	highly reflective
IFO	interferometer
IR	infrared
LED	light-emitting diode
LIGO	Laser Interferometer Gravitational-Wave Observatory
LSC	LIGO Scientific Collaboration

Reoccurring mathematical symbols

MDWS	modulated differential wavefront sensing
MEDM	Motif Editor and Display Manager (graphical user interface for CDS)
MISB	Michelson sideband (used for angular control of the interferometer)
Nd:YAG	neodymium-doped yttrium aluminium garnet ($\text{Nd:Y}_3\text{Al}_5\text{O}_{12}$)
NPRO	non-planar ring oscillator
OPA	optical parametric amplifier
OPO	optical parametric oscillator
p-pol.	p-polarization (here linearly polarized in horizontal direction)
PBS	polarizing beamsplitter
PD	photodiode, photodetector
PLL	phase-locked loop
PPKTP	periodically poled potassium titanyl phosphate (KTiOPO_4)
PZT	piezoelectric transducer
QPD	quadrant photodetector
QUEST	Centre for Quantum Engineering and Space-Time Research
RF	radio frequency
RIN	relative intensity noise
RMS	root mean square (square root of the mean square of a time series)
s-pol.	s-polarization (here linearly polarized in vertical direction)
SHG	second-harmonic generator
SNR	signal-to-noise ratio
SQL	standard quantum limit
TEM	transverse electromagnetic mode

Reoccurring mathematical symbols



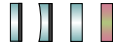
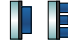





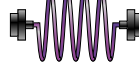









\hat{a}^\dagger, \hat{a}	creation and annihilation operator
c	speed of light, $c = 2.998 \times 10^8$ m/s
$\hat{D}(\alpha)$	displacement operator
E	electric field
\mathcal{F}	finesse of a cavity
f	frequency
g	classical parametric gain
\hat{H}	Hamiltonian
$h(t)$	gravitational-wave strain
$\tilde{h}(f)$	amplitude spectral density of gravitational-wave strain
\hbar	reduced Planck constant, $\hbar = 1.055 \times 10^{-34}$ J s
$i(t)$	photo current

Reoccurring mathematical symbols

L	interferometer arm length
l	optical loss
m	mass
\hat{n}	photon-number operator
P	light power
r	squeezing parameter
\mathbf{r}	location, $\mathbf{r} = (x, y, z)$
R_-, R_+	squeezing ratio and antisqueezing ratio
$R_{-,dB}$	squeezing ratio in decibel
$\hat{S}(\xi)$	squeezing operator
t	time
V_-, V_+	variance of the squeezed and antisqueezed quadrature
$W(x_+, x_-)$	Wigner function
$\hat{X}_+, \hat{X}_-, \hat{X}_\phi$	quadrature operators (amplitude, phase, arbitrary angle)
α, β	field amplitude
$ \alpha\rangle$	coherent state
$ \alpha, \xi\rangle$	bright squeezed state
ε	complex misalignment parameter
η	optical efficiency
θ	squeezing phase
λ	wavelength
ξ	complex squeezing parameter
$ \xi\rangle$	squeezed vacuum state
τ	measurement interval
ϕ	phase (of a bright light field)
ω, ω_0	angular frequency (of carrier field)
Ω	angular frequency offset
$\langle \hat{X} \rangle$	expectation value of operator \hat{X}
$\text{Var}(\hat{X})$	variance of operator \hat{X}
\bar{x}	mean of $x(t)$
\tilde{x}_{RMS}	root mean square value of $x(t)$
$S_x(f)$	single-sided power-spectral density of $x(t)$
$\tilde{x}(f)$	single-sided amplitude-spectral density of $x(t)$

Pictograms

The graphical symbols are based on Alexander Franzen's ComponentLibrary [Fra06].

	laser beams (1064 nm, 532 nm)
	laser
	mirrors (flat, curved, partially transmissive, dichroic)
	piezo-actuated mirrors (1-axis, 3-axis)
	lenses (convex, concave)
	nonlinear crystal
	polarizing beamsplitters (different orientations)
	Faraday isolator
	waveplates ($\lambda/2$, $\lambda/4$)
	optical fibre with fibre couplers
	electro-optic modulator
	acousto-optic modulator
	iris aperture, shutter
	beam dump, neutral-density filter
	photodetectors (single-element, quadrant)
	control signal
	sum, difference
	local oscillator, demodulator, phase shifter
	generic controller

Introduction

Roughly 1.3 billion years ago two black holes, one with 36 solar masses, the other with 29 solar masses, collided after a long inspiral. The collision emitted a huge amount of energy, for a brief moment outshining the entire visible universe, in the form of gravitational waves. These gravitational waves travelled outwards at the speed of light, ever so slightly stretching and compressing the spacetime they crossed. On the 14th of September 2015 they passed earth, producing the tiny yet detectable signal shown in figure 1.1 in the two LIGO gravitational-wave detectors [LVC16a]. For the first time in history, after decades of developing the necessary techniques, and almost 100 years after their prediction by Albert Einstein, gravitational waves had been detected. We are now at the beginning of an era of gravitational-wave astronomy.

This thesis is about one of the experimental aspects of gravitational wave detection. In the ever-ongoing effort of increasing the sensitivity of current and future detectors an important limitation is the presence of quantum measurement noise. I report on the reduction of quantum noise by the application of non-classical states of light at the German–British gravitational-wave detector GEO 600. In this introductory chapter I will briefly outline the general background before going into more theoretical detail in chapter 2. Much more detailed introductions to gravitational waves, their detection, and the role of quantum noise can, for example, be found in [SS09], [DK12] and [BHS18].

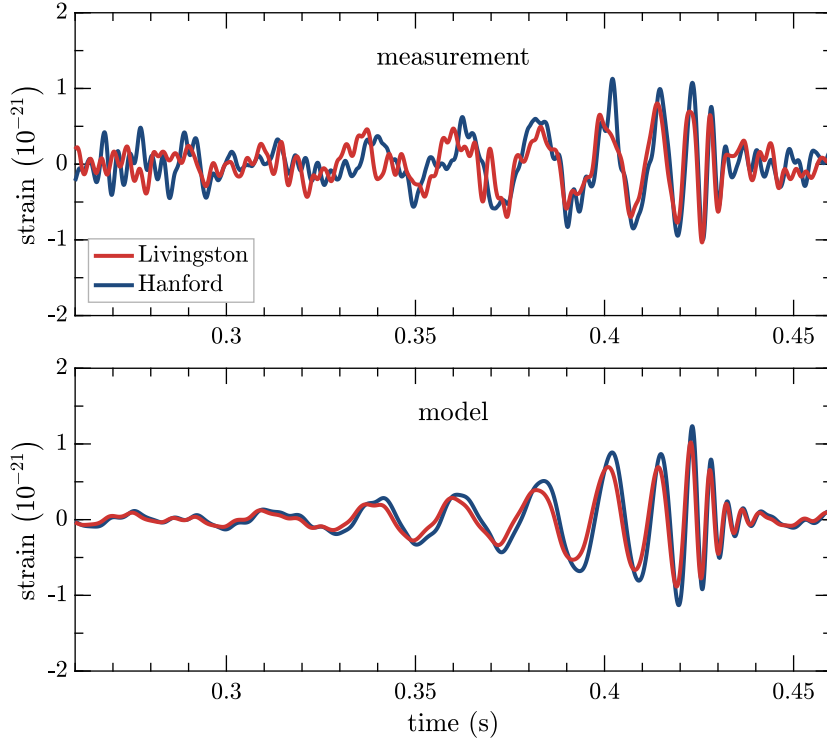


Figure 1.1: The gravitational-wave signal GW150914. The upper plot shows the output signal of the two LIGO gravitational-wave detectors, calibrated to units of strain and band-pass filtered to remove low- and high-frequency background noise. The time trace of the Hanford detector was sign flipped and shifted by 7 ms to better show the similarity of the two signals. The lower plot shows the simulated signals from a numerical relativity model with the model parameters adjusted to match the observation. This figure is a reproduction of a similar figure in [LVC16a] using data from [LSC16].

1.1 Gravitational waves

Gravitational waves are a direct consequence of Einstein’s general theory of relativity [Ein16; Ein18]. They are wave-like solutions to the Einstein field equations described as small perturbations of a nearly flat spacetime metric $g_{\mu\nu}$ in empty space [Sau17]:

$$g_{\mu\nu} = \eta_{\mu\nu} + h_{\mu\nu} \quad (1.1)$$

with the flat Minkowski metric

$$\eta = \begin{pmatrix} -1 & 0 & 0 & 0 \\ 0 & 1 & 0 & 0 \\ 0 & 0 & 1 & 0 \\ 0 & 0 & 0 & 1 \end{pmatrix} \quad (1.2)$$

and a small perturbation term with $|h_{\mu\nu}| \ll 1$.

Solving the Einstein field equations in appropriate coordinates (the so-called *transverse traceless gauge*) leads to

$$h = \begin{pmatrix} 0 & 0 & 0 & 0 \\ 0 & h_+ & h_\times & 0 \\ 0 & h_\times & -h_+ & 0 \\ 0 & 0 & 0 & 0 \end{pmatrix}, \quad (1.3)$$

where the two independent components h_+ and h_\times are the amplitudes of the two polarizations of a wave travelling along the z -axis at the speed of light c . They are called the $+$ -polarization and \times -polarization (pronounced ‘plus’ and ‘cross’) of the gravitational wave.

The effect of such a metric can be described as a periodic stretching and compressing of space perpendicular to the direction of travel of the gravitational wave. This is depicted in figure 1.2. The proper distance L of two free test masses is changed by a small amount δL . This distance change along a given direction is called *strain* and it is described by the dimensionless quantity¹ [AD05]

$$h(t) = \frac{2\delta L(t)}{L}. \quad (1.4)$$

Sources of gravitational waves are time-variable mass distributions with a changing quadrupole moment. A good example for this are two massive objects orbiting each other. Spherically symmetric mass distributions do not produce any gravitational waves.

¹ The factor of two in this definition of strain comes directly from integrating the metric along the geodesic line connecting the two test masses. It also leads to the convenient relation $h = \Delta L/L$ for the arm-length difference ΔL of a Michelson interferometer when both arms experience the effect of the gravitational wave in opposite directions.

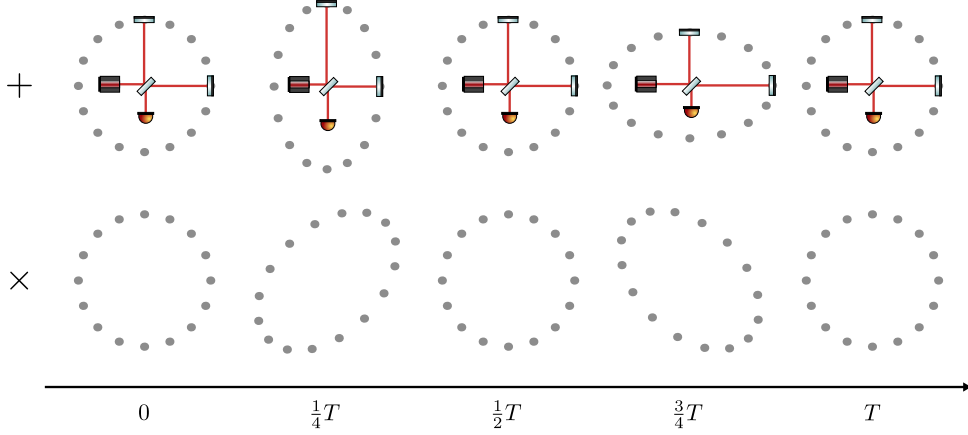


Figure 1.2: Effect of a passing gravitational wave on a ring of free-falling test masses over one full period. The wave is travelling perpendicular to the image plane and shown here are the two possible polarizations. Also depicted is a Michelson interferometer to show how its two interferometer arms are affected by the passing wave.

The amplitude of a gravitational wave depends on the source’s mass and the speed with which its quadrupole moment changes. An approximation is given in [SS09]:

$$h \lesssim \frac{2GMv^2}{c^4 r}, \quad (1.5)$$

where G is the gravitational constant, Mv^2 describes the internal kinetic energy of the changing mass distribution, and r is the observers distance to the source. The bound is approached for highly non-spherical systems and it is obtained for the extreme case of two compact, equal-mass objects orbiting around their common centre of mass.

Gravitational-wave amplitudes are generally tiny. Extreme masses and extreme velocities are needed to generate an appreciable effect. The strongest signals reaching earth are expected to come from the most violent astrophysical events such as supernovae or coalescing neutron stars and black holes. And even these signals will be small. More local events like planetary movements generate gravitational-wave amplitudes that are many orders of magnitude lower.

The ability to detect gravitational-waves promises to be a completely new way of observing astrophysical events, complementary to observations in the electromagnetic spectrum. The first detections of coalescing black-hole binaries [LVC16a; LVC16b; LVC17a; LVC17b] have revealed events to us that might have been completely dark,

1.2 Laser interferometers for gravitational-wave detection

hidden to conventional telescopes. The joint observation of a binary neutron star merger in the gravitational-wave and electromagnetic spectrum [LVC17c; LVC17d] has allowed various new possibilities of exploring these astrophysical objects. There is great hope that future multi-messenger astronomy will lead to even more surprising new discoveries in physics, astrophysics and cosmology [SS09].

To appreciate the challenge of detecting gravitational waves, we can take as an example two solar-mass black holes orbiting each other with an orbital velocity of half the speed of light at a distance of 100 million light-years from us. Plugging this into equation (1.5) we get a relative length change in the order of $h \approx 10^{-21}$. That means that a kilometre-long measurement apparatus is only stretched and compressed by 10^{-18} m. This is less than a thousandth of a proton diameter. Detecting such tiny length changes is in many ways an enormous experimental challenge.

1.2 Laser interferometers for gravitational-wave detection

A direct way to observe gravitational waves is to measure the distance of two (ideally) force-free test masses. This can be done by determining the time it takes light to pass back and forth between them. Instead of an absolute measurement, the best approach is to measure the relative change between two paths that are affected differently by the passing gravitational wave.

A *Michelson interferometer* is a device to observe the relative phase shift of two light beams caused by different travel times along orthogonal measurement paths. It was developed by Albert Abraham Michelson and originally used in the famous Michelson–Morley experiment [MM87]. While the goal was to observe the effect of an assumed luminiferous ether, the experiment ultimately demonstrated the constancy of the speed of light. Today, the same instrument is the basis of interferometric gravitational-wave detectors.

In the simple Michelson setup (see figure 1.3) the interferometer output power depends on the arm length difference $\Delta L = L_x - L_y$ as follows [Sau17]:

$$P_{\text{out}} = P_{\text{in}} \cos^2\left(2\pi \frac{\Delta L}{\lambda}\right), \quad (1.6)$$

where λ is the light wavelength, or

$$P_{\text{out}} = P_{\text{in}} \cos^2\left(\frac{1}{2}\phi\right), \quad (1.7)$$

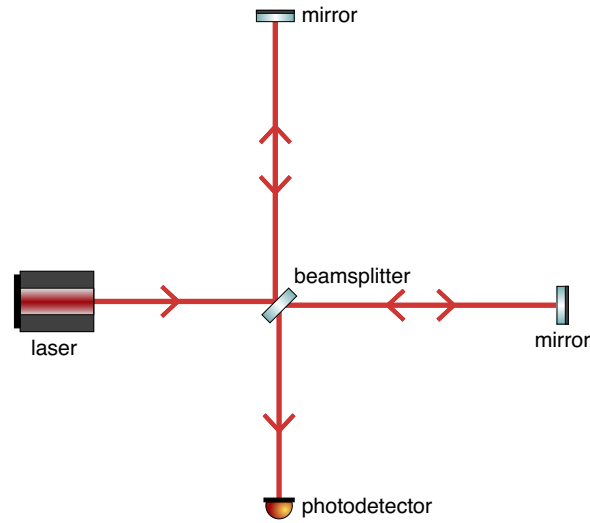


Figure 1.3: A simple Michelson interferometer. The beam of a coherent light source is split at a 50:50 beamsplitter, the two beams travel along the so-called interferometer arms, are reflected, and recombined at the beamsplitter. The two beams interfere constructively or destructively based on their phase relation. A photodetector is placed at the open port of the beamsplitter to record the resulting power at the interferometer output.

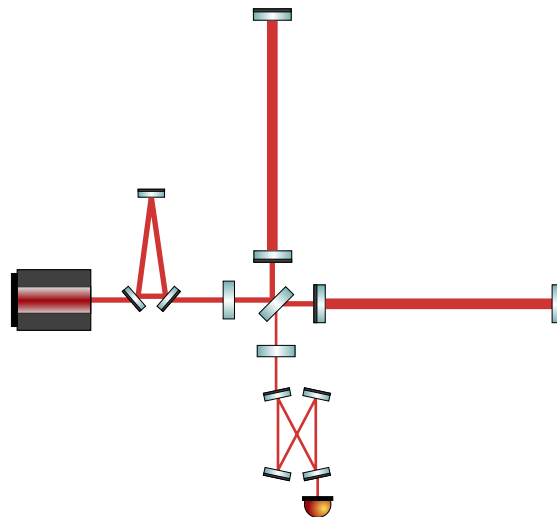


Figure 1.4: Simplified layout of Advanced LIGO. Compared to the simple Michelson interferometer a modern interferometric gravitational-wave detector includes additional optics for input and output modecleaners, arm cavities, as well as power and signal recycling.

1.2 Laser interferometers for gravitational-wave detection

where ϕ is the phase difference of the two beams after one round-trip. The interferometer therefore serves to translate phase fluctuations in the arms into measurable intensity changes at its output which can be observed with a photodetector.

While still following the same principle, modern interferometric gravitational-wave detectors have been developed far beyond a simple Michelson interferometer. Among the many technical improvements are some important additions to the optical layout (see figure 1.4):

- A partially transmissive **power-recycling mirror** at the input port serves to form a resonant cavity together with the interferometer, thereby increasing the circulating power.
- A **signal-recycling mirror** at the output port can resonantly enhance the signal, either broadband or for a specific signal frequency.
- Resonant **Fabry–Pérot cavities** in the arms can store the light for longer than the simple round-trip time which increases the effective arm length significantly.
- **Modecleaner cavities** at the input and output serve to reduce unwanted phase and amplitude fluctuations as well as spatial imperfections of the laser beam.

Other interferometer topologies that deviate more strongly from the simple Michelson setup but still follow many of the same principles are also being considered for future applications [e.g. Mia⁺14; Dan⁺17].

At the time of writing in 2017 four large-scale interferometric gravitational-wave detectors are operational and others are being built or planned (see figure 1.5). *GEO 600* in Hannover, Germany – the main setting of this thesis – is the smallest one of them at 600 m arm length. It has been operational quasi-continuously since its initial data-taking run in 2002 [Wil⁺04]. Over the years, it has received many incremental upgrades and serves as a testbed for advanced technologies, many of which have already found use also in the other detectors [Aff⁺14]. The two *Advanced LIGO* detectors, located in the USA in Livingston, Louisiana and Hanford, Washington, are 4 km long. They have recently finished their second observation run after a major upgrade phase that ended in 2015 [LSC15]. *Advanced Virgo* with 3-km long arms is located near Pisa, Italy. It is back in operation after its own upgrade programme [Virgo15] and successfully joined the LIGO detectors for the last weeks of the latest observation run, in time to contribute to the first joined detections



Figure 1.5: A map of the second-generation gravitational-wave detector network. GEO 600, Virgo and the two LIGO detectors are currently operational, KAGRA is under construction, and LIGO India is planned. Combined detections by as many detectors as possible distributed around the globe help with localizing the source of the signal in the sky.

together with LIGO [LVC17b; LVC17c]. At the end of 2017, both LIGO and Virgo are now in a commissioning phase again, planned to be a bit longer than a year, to further improve their respective sensitivity. In addition, the Japanese detector *KAGRA* is currently under construction [Som12] and a third LIGO facility is planned to be built in India.

For the future, plans for the so-called third generation of detectors are being made: In Europe there is a collaborative effort towards the so-called *Einstein Telescope* [Pun⁺10] and the LIGO Scientific Collaboration is working on a project titled *Cosmic Explorer* [Abb⁺17]. Furthermore, the ESA mission *LISA* [Ama⁺17] is a project to bring an interferometric gravitational-wave detector into space. Scheduled for launch in 2034, it will complement the ground-based detector network in a new frequency band.

1.3 Noise sources in interferometric gravitational-wave detectors

The main factor that determines the sensitivity of a gravitational-wave detector is the presence of noise. Various mechanisms lead to fluctuations that mask a gravitational-wave signal, either by physically changing the arm length difference that is being measured, or by introducing noise in the detection of the resulting light signal.² Some of the contributing noise mechanisms are of a technical nature, others are quite fundamental. Building a sensitive detector means reducing these unwanted fluctuations as far as possible. As an example, figure 1.6 shows a simulated noise budget of the Advanced LIGO detectors at their target sensitivity [LSC15]. The most important noise sources are:

- **Seismic noise:** Seismic motion of the ground will cause the mirrors to move, creating a false signal. Much development work has gone into active and passive isolation of the mirrors. They are hung from multi-stage pendulums which provide very good suppression of the seismic motion above the resonance frequency of the suspension. Additional active controls improve the performance at low frequencies. However, the influence of seismic noise still rises steeply towards lower frequencies.
- **Gravity-gradient noise (also known as Newtonian noise):** Even for a theoretically perfect suspension the test masses are still influenced by their surroundings through gravitational attraction. Density variations in the ground with frequencies at the low end of the measurement band can change the local gravitational field enough that this will be a consideration for future gravitational-wave detectors. The gravitational influence cannot be shielded, but one option for reducing the noise is to determine the gravitational field changes with independent sensors to then remove their contribution from the detector signal.
- **Control noises (not depicted):** Active control systems are essential for keeping the interferometer in stable operation. Nevertheless, these systems can also contribute technical noise to the output signal. This can happen, for example, through out-of-loop feedback noise, unintended cross-couplings between control loops, or nonlinearities. Although purely technical, these

² Although the output signal of a gravitational-wave detector will at almost any time be dominated by noise, it is still conventional to always call this signal the measured gravitational-wave strain h .

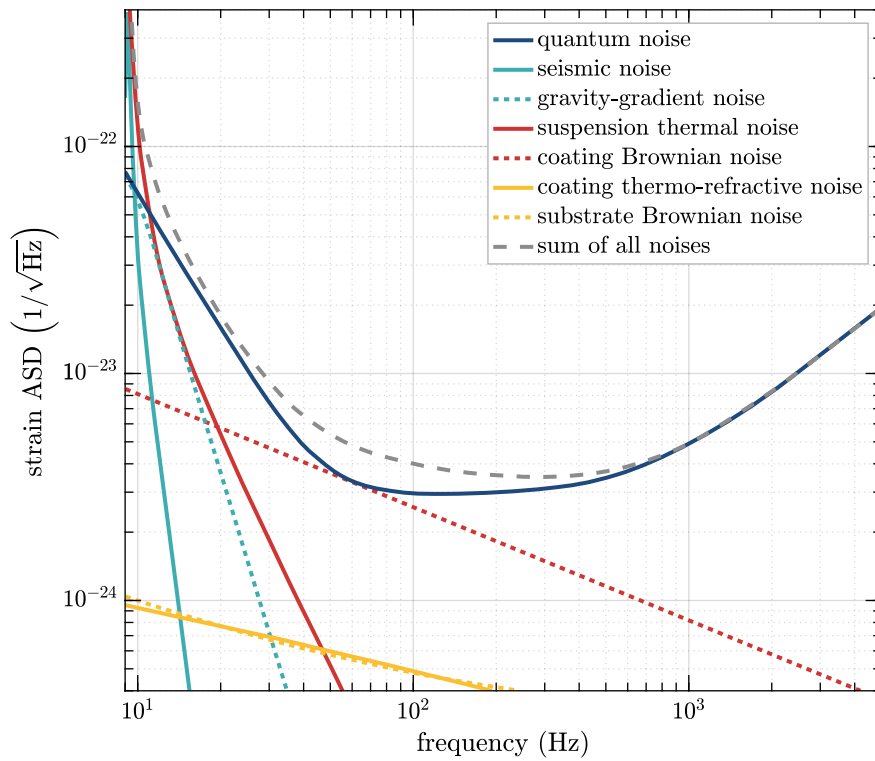


Figure 1.6: Noise budget of Advanced LIGO at target sensitivity. The simulated effect of different noise sources is shown here as an amplitude spectral density scaled to units of strain. The figure is adapted from [LSC15].

1.3 Noise sources in interferometric gravitational-wave detectors

noises are still quite important for practical operation of the detectors and a lot of commissioning work goes into mitigating them by optimizing the control systems.

- **Thermal noise:** Today’s gravitational-wave detectors operate at room temperature. The Brownian motion of the molecules that make up the test masses leads to thermal noise. This occurs in the suspension, in the mirror substrate, or in the coating. Thermal noise in the coating can couple either through the distortion of the coating surface (coating Brownian noise) or through variations of the coating’s refractive index (coating thermo-refractive noise). Coating Brownian noise is currently the most limiting one of these. Work is ongoing in order to try new substrate materials and develop low-noise coatings, as well as going towards cryogenic operation for future detectors [Hir⁺14].
- **Dark noise (not depicted):** The readout electronics and signal-processing chain also contribute noise to the detector’s output signal. This is called dark noise because it is the noise that remains without any light impinging on the photodetector. Making sure that dark noise is low enough to not be a contributing factor requires a careful design of the readout electronics.
- **Quantum noise:** Finally, there is the quantum noise that is quite fundamentally linked to the detection process. Two factors play a role here: The first is *quantum shot noise* (also known as photon-counting noise) that arises from the quantized detection of the interferometer’s output light field on the photodetector. For a classical laser beam the photons hitting the photodetector are uncorrelated and will arrive randomly. So the number of photons detected per unit of time follows a Poisson distribution and will fluctuate around its mean \bar{n} with standard deviation $\sqrt{\bar{n}}$. The second manifestation of quantum noise is the so-called *radiation-pressure noise* (sometimes also called quantum back-action noise). This is caused by the optomechanical interaction of the interferometer light field with the mirrors through radiation pressure. Radiation-pressure noise is primarily a concern at low detection frequencies close to the suspension resonances. Towards higher frequencies it drops with $1/f^2$ and the shot noise becomes dominant. Increasing the light power inside the interferometer will reduce the relative shot noise, but it increases the radiation-pressure noise. I will describe the two forms of quantum noise in an interferometric gravitational-wave detector in detail in section 2.1.8 of the next chapter.

Current gravitational-wave detectors are primarily limited by seismic and technical

noises at low frequencies and quantum shot noise at high frequencies. Ultimately, the goal is to reduce all other noises far enough that quantum noise will be dominant over almost the entire detection band. This makes quantum noise an important focus of future detector designs.

1.4 Quantum enhancement

As long as radiation-pressure noise is not yet dominating at low frequencies, the primary way to reduce shot noise is increasing the circulating light power inside the interferometer. However, this is technically challenging. Achieving high optical power in the first place requires suitable high-power lasers and high resonant enhancement factors. Furthermore, problems with thermal lensing and optomechanical instabilities (Sidle-Sigg instabilities and parametric instabilities) become increasingly more relevant with higher powers [Bla⁺12]. Specific technical challenges with high-power operation for the case of GEO 600 are discussed by Affeldt [Aff14] and Wittel [Wit⁺14; Wit15]. With these limitations in mind, other ways of mitigating the effects of quantum noise are very relevant.

In 1980, after some controversy about the exact quantum-mechanical description of the interferometer detection process, Caves [Cav80] showed that both forms of quantum noise can be attributed to the presence of vacuum fluctuations of the electromagnetic field entering the interferometer through the dark output port. One year later, he went on to propose a way to improve quantum-noise limited interferometers by injecting a squeezed vacuum state [Cav81].

Squeezed states of light are non-classical quantum states that have a reduced quantum-mechanical uncertainty in one measurement quadrature when compared to a classical coherent state. Still being limited by the Heisenberg uncertainty principle, this means that the uncertainty in the orthogonal quadrature is increased. As Caves could show, injecting a squeezed vacuum state at the dark port of the interferometer can either decrease the shot noise at the cost of more radiation-pressure noise, or vice versa. While the effect is generally the same as varying the circulating light power, this gives a new way of controlling the quantum noise where a power increase is technically infeasible. Also, since radiation-pressure noise and shot noise dominate in different frequency bands, it is possible to apply so-called frequency-dependent squeezing to reduce both at the same time [Kim⁺01; Che⁺05; Eva⁺13].

When the use of squeezed light for interferometry was first proposed, squeezing had not yet been experimentally demonstrated. It was four years later in 1985 that

Slusher et al. [Slu⁺85] succeeded in generating squeezed light for the first time by the process of four-wave mixing. The observed reduction of quantum noise in this experiment was 0.3 dB. Since then, over the following three decades, significant advances have been made in the generation and detection of squeezed light [And⁺16], driven not least by the outlook of applications in gravitational-wave detection [Sch17]. The latest record level of observed squeezing is 15.3 dB [Vah⁺16].

In 2010, a squeezed-light source specifically designed for this purpose was installed at GEO 600 [Vah⁺10] and not long after quantum enhancement of a large-scale gravitational-wave detector was demonstrated there for the first time [LSC11]. In another experiment the same was achieved at the LIGO Hanford observatory [LSC13]. At GEO 600 the application was made a permanent feature of the detector which is now operating successfully for many years [Gro⁺13].

1.5 About this thesis

My thesis focuses on the operation and characterization of the GEO 600 squeezed-light application. **Chapter 2** starts with a short theoretical introduction to the quantum nature of light and the generation and detection of squeezed states are discussed. The second half of the chapter describes limiting factors for the practical observation of squeezing. The squeezed-light source itself is introduced in **chapter 3** which also presents the experience gathered with the long-term operation. **Chapter 4** forms the centre of this thesis and will discuss the many different aspects of the integration of squeezed light into the interferometer, such as the investigation of active control schemes for the stabilization of phase and alignment, the mitigation of optical losses and electronic dark noise, and the prevention of backscattering. Different ways to characterize the squeezing performance are then presented in **chapter 5** together with the main results of achieved squeezing levels. Finally, **chapter 6** gives a short summary and outlook.

The thesis makes references to measurements and data collected over a time span of several years (from the end of 2012 to the end of 2017). During this time there have been many small- and large-scale changes to the experiment. The measurements therefore do not all show the instrument in the same state. I provide further details for context where necessary.

The work on squeezing at GEO 600 has been a collaborative effort and as such many people have contributed to the results presented here. I will give specific credit to main contributors at the beginning of each chapter, respectively, and it should

Chapter 1 Introduction

be understood that almost no project was conducted by one person alone. During my PhD time the GEO 600 squeezing team consisted mainly of (in alphabetical order) Hartmut Grote, Henning Vahlbruch, James Lough, Katherine Dooley, Matteo Leonardi, and myself.

Theoretical background

This chapter will lay out the theoretical background of squeezed light and its application to gravitational-wave detectors.

In the first part, the necessary mathematical framework will be introduced to discuss quantum states of light. I will cover squeezed states and how they are generated and detected. Also, the role of quantum noise in a Michelson-like interferometer will be described and how this can be changed by injecting squeezed light. This introductory part follows the comprehensive text of Walls and Milburn [WM08] while borrowing notational conventions from Gerry and Knight [GK05].

Then, in the second part of the chapter, I will present some analytical calculations to describe the influence of imperfections in a realistic squeezed light application and how they limit the amount of achievable non-classical noise reduction.

2.1 Quantum states of light

The limitation of a gravitational-wave detector's sensitivity by shot noise and radiation-pressure noise and their improvement through the application of squeezed states of light are inherently non-classical phenomena. While often helpful, neither the classical wave picture of light fields nor the photon picture will provide a complete explanation of the observed effects. Rather, the full quantum nature of light needs to be taken into account.

2.1.1 Quantization of the electromagnetic field

The electric field of an electromagnetic wave in free space at location $\mathbf{r} = (x, y, z)$ and time t can be written in the form [WMO8]

$$\hat{\mathbf{E}}(\mathbf{r}, t) = i \sum_k \sqrt{\frac{\hbar\omega_k}{2\varepsilon_0}} \left[\hat{a}_k \mathbf{u}_k(\mathbf{r}) e^{-i\omega_k t} + \hat{a}_k^\dagger \mathbf{u}_k^*(\mathbf{r}) e^{i\omega_k t} \right]. \quad (2.1)$$

Here, \hbar is the reduced Planck constant and ε_0 is the vacuum permittivity. The index k enumerates different modes of the electric field with angular frequencies ω_k and spatial distribution functions $\mathbf{u}_k(\mathbf{r})$. The distribution functions form an orthonormal set and they describe the modes' spatial properties like propagation direction, mode shape, and polarization. \hat{a}_k and \hat{a}_k^\dagger are dimensionless field amplitudes. In a classical description these would be complex numbers, whereas for the quantization of the electromagnetic field they are replaced by operators, following the commutation relations

$$\begin{aligned} [\hat{a}_k, \hat{a}_{k'}] &= 0, \\ [\hat{a}_k, \hat{a}_{k'}^\dagger] &= \delta_{kk'}. \end{aligned} \quad (2.2)$$

The Hamiltonian for the total energy of this field is

$$\hat{H} = \sum_k \hbar\omega_k \left(\hat{a}_k^\dagger \hat{a}_k + \frac{1}{2} \right). \quad (2.3)$$

This corresponds to the sum of the number of photons in each mode multiplied by the energy per photon, plus an additional contribution of $\frac{1}{2}\hbar\omega_k$ which is the ground state energy of each mode. The operator product $\hat{a}_k^\dagger \hat{a}_k$ is called the *photon number*

2.1 Quantum states of light

operator of mode k :

$$\hat{n}_k := \hat{a}_k^\dagger \hat{a}_k . \quad (2.4)$$

The eigenstates of the number operator are written as $|n_k\rangle$ and are called the *number states* or *Fock states*. It can be shown that the operators \hat{a}_k and \hat{a}_k^\dagger act on a number state $|n_k\rangle$ by removing or adding a photon of mode k [GK05]:

$$\begin{aligned} \hat{a}_k |n_k\rangle &= \sqrt{n_k} |n_k - 1\rangle , \\ \hat{a}_k^\dagger |n_k\rangle &= \sqrt{n_k + 1} |n_k + 1\rangle . \end{aligned} \quad (2.5)$$

We therefore call \hat{a}_k and \hat{a}_k^\dagger the annihilation and creation operator, respectively. The state with no photons in any mode is termed the *vacuum state* which is defined by

$$\hat{n}_k |0\rangle = 0 . \quad (2.6)$$

In the following we will drop the index k and only consider a single optical mode (one frequency, one polarization, one spatial mode), such as it would exist inside a non-degenerate high-finesse cavity [Sch17].¹

2.1.2 Coherent states

Photon number states are a useful representation of optical fields with very low photon numbers. However, experimentally realizable bright states of many photons are mostly either superpositions or mixtures of number states. A different set of states that is particularly well suited for the quantum-mechanical description of continuous-wave laser beams are the so-called *coherent states* [Gla63]. These states are generated by applying the *displacement operator*

$$\hat{D}(\alpha) := \exp(\alpha \hat{a} - \alpha^* \hat{a}^\dagger) , \quad \alpha \in \mathbb{C} \quad (2.7)$$

to the vacuum state to get a coherent state labelled $|\alpha\rangle$:

$$|\alpha\rangle := \hat{D}(\alpha) |0\rangle . \quad (2.8)$$

¹ A more rigorous description of light fields with sidebands is given by the *two-photon formalism* as introduced by Caves and Schumaker [CS85; SC85]. I use the simpler one-frequency approach here, which is sufficient to describe most important effects and frequency-dependent aspects will be introduced as necessary.

Chapter 2 Theoretical background

The coherent states are the eigenstates of the annihilation operator \hat{a} with eigenvalue α :

$$\hat{a} |\alpha\rangle = \alpha |\alpha\rangle . \quad (2.9)$$

Their average photon number is given by

$$\bar{n} = \langle \alpha | \hat{n} | \alpha \rangle = |\alpha|^2 . \quad (2.10)$$

Since \hat{a} is a non-Hermitian operator, it does not directly correspond to a physically measurable observable. Rather, the eigenvalue α describes a non-observable complex field amplitude.

2.1.3 Quadrature operators

Based on the creation and annihilation operator we can introduce the two Hermitian *quadrature operators*

$$\begin{aligned} \hat{X}_+ &:= \frac{1}{2} (\hat{a}^\dagger + \hat{a}) , \\ \hat{X}_- &:= \frac{i}{2} (\hat{a}^\dagger - \hat{a}) . \end{aligned} \quad (2.11)$$

Using equation 2.2 we derive the commutation relation

$$[\hat{X}_+, \hat{X}_-] = \frac{i}{2} . \quad (2.12)$$

Considering one scalar component of the electrical field for the simple case of a single-mode plane wave along the z -axis, we can write [GK05]

$$\hat{E}_x(z, t) = \mathcal{E}_0 \sin(\omega z/c) (\hat{a} e^{-i\omega t} + \hat{a}^\dagger e^{i\omega t}) , \quad (2.13)$$

where we have absorbed all constant factors from equation 2.1 into the prefactor \mathcal{E}_0 . Rewriting this in terms of \hat{X}_+ and \hat{X}_- gives

$$\hat{E}_x(z, t) = 2\mathcal{E}_0 \sin(\omega z/c) (\hat{X}_+ \cos(\omega t) + \hat{X}_- \sin(\omega t)) . \quad (2.14)$$

This makes it evident that \hat{X}_+ and \hat{X}_- correspond to field amplitudes of oscillations with a phase offset of 90° . For a coherent state $|\alpha\rangle$ the expectation values of the two quadrature operators are the real and imaginary part of the complex field

amplitude α :

$$\begin{aligned}\langle \alpha | \hat{X}_+ | \alpha \rangle &= \text{Re}(\alpha), \\ \langle \alpha | \hat{X}_- | \alpha \rangle &= \text{Im}(\alpha).\end{aligned}\tag{2.15}$$

The \hat{X}_+ quadrature is conventionally called the *amplitude quadrature* and \hat{X}_- the *phase quadrature*. The choice of a coordinate system is, however, mostly free and usually depends on the presence of a bright reference field. We can define the quadrature operator along an arbitrary angle ϕ as

$$\hat{X}_\phi := \hat{X}_+ \cos \phi + \hat{X}_- \sin \phi = \frac{1}{2}(\hat{a}^\dagger e^{i\phi} + \hat{a} e^{-i\phi}).\tag{2.16}$$

The previously defined operators \hat{X}_+ and \hat{X}_- are then the special cases for $\phi = 0$ and $\phi = \pi/2$, respectively.

The variance of the quadrature operators for a coherent state $|\alpha\rangle$ is

$$\text{Var}(\hat{X}_\phi) = \langle \alpha | \hat{X}_\phi^2 | \alpha \rangle - \langle \alpha | \hat{X}_\phi | \alpha \rangle^2 = \frac{1}{4}\tag{2.17}$$

for all quadrature angles ϕ and independent of α . In particular, the variance of all coherent states is the same as it is for the vacuum state. Following the Heisenberg uncertainty principle and using equation 2.12 we get the uncertainty relation

$$\text{Var}(\hat{X}_+) \text{Var}(\hat{X}_-) \geq \frac{1}{16}.\tag{2.18}$$

For coherent states equality is achieved. They thus belong to the class of minimum-uncertainty states.

2.1.4 Squeezed states

The Heisenberg relation 2.18 allows for states where one quadrature uncertainty is lower than that of the vacuum state, at the cost of an increased uncertainty in the orthogonal quadrature. Such states with $\text{Var}(\hat{X}_\phi) < \frac{1}{4}$ for some quadrature angle ϕ are called *squeezed states*.

Mathematically, squeezed states can be generated by application of the *squeeze operator*

$$\hat{S}(\xi) := \exp\left(\frac{1}{2}\xi^* \hat{a}^2 - \frac{1}{2}\xi \hat{a}^{\dagger 2}\right), \quad \xi = r e^{2i\theta}.\tag{2.19}$$

Chapter 2 Theoretical background

It is a unitary operator with

$$\hat{S}^\dagger(\xi) = \hat{S}^{-1}(\xi) = \hat{S}(-\xi). \quad (2.20)$$

To understand the effect of the squeeze operator we can observe its effect on the two quadrature operators \hat{X}_θ and $\hat{X}_{\theta+\frac{\pi}{2}}$ rotated to match the squeezing angle θ [WM08]:

$$\hat{S}^\dagger(\xi) \left(\hat{X}_\theta + i\hat{X}_{\theta+\frac{\pi}{2}} \right) \hat{S}(\xi) = \hat{X}_\theta e^{-r} + i\hat{X}_{\theta+\frac{\pi}{2}} e^r. \quad (2.21)$$

This means that the squeeze operator attenuates one component of the complex field amplitude, while amplifying the orthogonal component. The degree of amplification and deamplification is determined by the squeezing parameter $r = |\xi|$.

Applying the squeeze operator to the vacuum state results in a squeezed vacuum state

$$|\xi\rangle := \hat{S}(\xi) |0\rangle \quad (2.22)$$

and further application of the displacement operator gives a bright squeezed state

$$|\alpha, \xi\rangle := \hat{D}(\alpha) \hat{S}(\xi) |0\rangle. \quad (2.23)$$

The quadrature variance of these squeezed states is decreased along the direction given by θ and increased in the orthogonal direction (for $r > 0$):

$$\begin{aligned} \text{Var}(\hat{X}_\theta) &= \frac{1}{4} e^{-2r}, \\ \text{Var}(\hat{X}_{\theta+\frac{\pi}{2}}) &= \frac{1}{4} e^{2r}. \end{aligned} \quad (2.24)$$

We call these quadratures the *squeezed* and *antisqueezed* quadratures. For a general quadrature angle ϕ that is not aligned with the squeezing angle θ the variance becomes [BR04]

$$\text{Var}(\hat{X}_\phi) = \frac{1}{4} \left(\cos^2(\phi - \theta) e^{-2r} + \sin^2(\phi - \theta) e^{2r} \right). \quad (2.25)$$

This relation is illustrated in figure 2.1.

The expected photon number of a bright squeezed state is

$$\langle \alpha, \xi | \hat{n} | \alpha, \xi \rangle = |\alpha|^2 + \sinh^2 r. \quad (2.26)$$

To save some notational burden in the later parts of this chapter, we make the

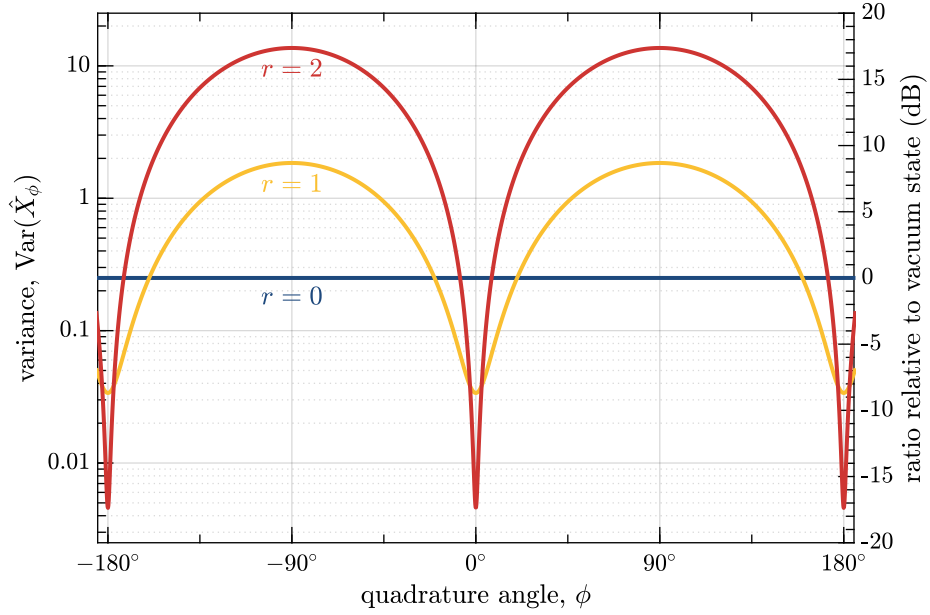


Figure 2.1: Variance of a squeezed state as a function of the quadrature angle for three different values of the squeezing parameter r . The horizontal axis indicates the angle of the readout quadrature ϕ relative to the squeezing angle $\theta = 0$. The two vertical axes mark the measured variance in that quadrature, once in linear units and once in the conventional units of decibel relative to the variance of the vacuum state (or any other unsqueezed state). Potential imperfections in the detection are not considered here.

following definitions for a general squeezed state:

$$V_+ := \max_{\phi} \text{Var}(\hat{X}_{\phi}), \quad (2.27)$$

$$V_- := \min_{\phi} \text{Var}(\hat{X}_{\phi}).$$

These are the variances of the antisqueezed and squeezed quadrature, respectively. Additionally, with the variance of the vacuum state V_{vac} , we define the (amplitude) *squeezing ratio* as

$$R_+ := \sqrt{\frac{V_+}{V_{\text{vac}}}} = e^r, \quad (2.28)$$

$$R_- := \sqrt{\frac{V_-}{V_{\text{vac}}}} = e^{-r},$$

which is often given in units of decibel:²

$$\begin{aligned} R_{\pm,\text{dB}} &= 20 \log_{10}(R_{\pm}) \text{ dB} \\ &= 10 \log_{10}(V_{\pm}/V_{\text{vac}}) \text{ dB}. \end{aligned} \quad (2.29)$$

2.1.5 Phase space representation

To visualize coherent and squeezed states of light we can consider them in a phase-space picture. There are several possible phase-space representations of quantum states. A description that proved particularly useful is the *Wigner function*. For the simple case of an arbitrary pure state $|\psi\rangle$ the Wigner function can be written in the form [BR04]

$$W(x_+, x_-) = \frac{2}{\pi} \langle \psi | \hat{D}(x_+ + ix_-) \hat{\Pi} \hat{D}^\dagger(x_+ + ix_-) | \psi \rangle, \quad (2.30)$$

where $\hat{\Pi}$ is the parity operator that acts on coherent states as $\hat{\Pi} |\alpha\rangle = |-\alpha\rangle$.

The Wigner function is a quasi-probability distribution over the 2-dimensional quadrature space ('quasi' because, unlike a classical probability distribution, it can take negative values for certain quantum states). Its marginal projections onto the quadrature axes give the probability distribution $P(x_{\pm})$ of measuring amplitude x_{\pm} in a measurement of quadrature \hat{X}_{\pm} :

$$P(x_{\pm}) = \int_{-\infty}^{\infty} dx_{\mp} W(x_+, x_-) \quad (2.31)$$

and equivalently for quadrature \hat{X}_{ϕ} with arbitrary quadrature angle.

The Wigner function for a coherent state $|\alpha\rangle$ is [WM08]

$$\begin{aligned} W(x_+, x_-) &= \frac{2}{\pi} \exp[-2|x_+ + ix_- - \alpha|^2] \\ &= \frac{2}{\pi} \exp[-2(x_+ - \text{Re}(\alpha))^2 - 2(x_- - \text{Im}(\alpha))^2]. \end{aligned} \quad (2.32)$$

² Note that the sign of the squeezing ratio in dB is often omitted and only included explicitly where it helps to distinguish between squeezing (variance is reduced, negative sign) and antisqueezing (variance is increased, positive sign). For example, if the noise level changed by $R_{-, \text{dB}} = -3 \text{ dB}$ it is said that 3 dB of squeezing were achieved.

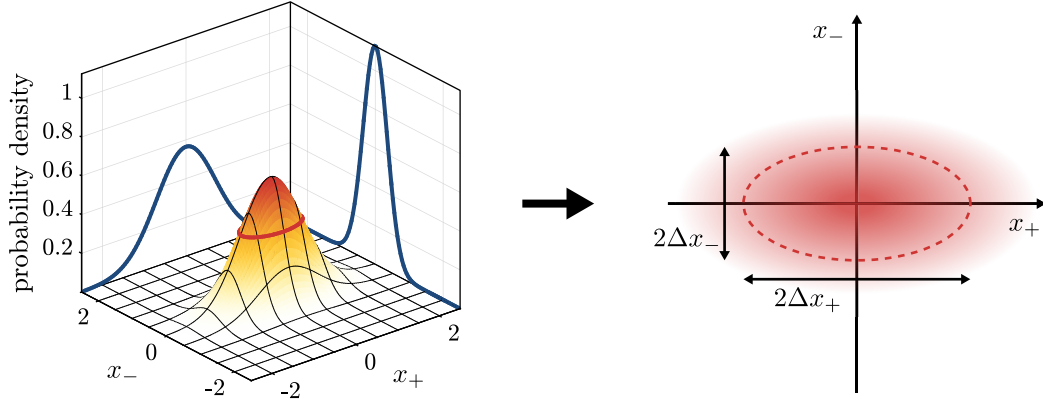


Figure 2.2: Wigner function and representation as uncertainty ellipse. The left panel shows the Wigner function of a phase squeezed vacuum state, as well as its projections onto the two quadrature axes. The right panel shows the simplified representation of the same state as an ellipse with major and minor axes of length $2\Delta x_+ = e^r$ and $2\Delta x_- = e^{-r}$, respectively.

This is a symmetric Gaussian distribution centred around α . The contour lines $W(x_+, x_-) = \text{const.}$ are circles. The Wigner functions of squeezed states are also Gaussian distributions, but with elliptical contour lines. For example, the Wigner function of a squeezed vacuum state squeezed along the \hat{X}_+ quadrature is given by

$$W(x_+, x_-) = \frac{2}{\pi} \exp\left[-2x_+^2 e^{2r} - 2x_-^2 e^{-2r}\right]. \quad (2.33)$$

We can understand the Wigner function as an extension of the classical phasor picture that is often used to represent electro-magnetic modulations in the phase space. Where a classical wave is described by a single vector in phase space, a quantum state has an additional uncertain region. In a simplified picture we can draw the Wigner function of a squeezed state as an uncertainty ellipse centred around the coherent excitation α , with the length of the major or minor axis along quadrature \hat{X}_θ proportional to the uncertainty

$$\Delta x_\theta = \sqrt{\text{Var}(\hat{X}_\theta)}. \quad (2.34)$$

Figure 2.2 illustrates the correspondence between the Wigner function and the representation as an uncertainty ellipse, and figure 2.3 shows additional examples for various states. This quantum phasor picture is sometimes called a *ball-on-a-stick diagram*.

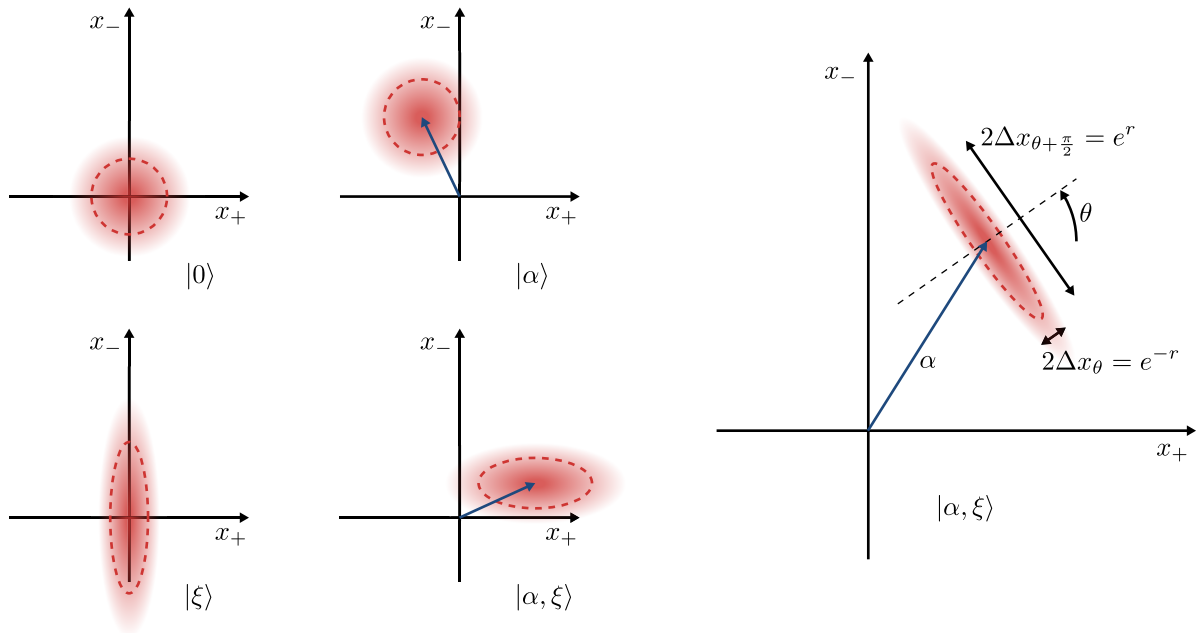


Figure 2.3: Examples of different quantum states in the phasor representation. The left side shows the noise ellipses of the vacuum state, a coherent state, a vacuum state squeezed along the amplitude quadrature \hat{X}_+ , and a bright state squeezed along the phase quadrature \hat{X}_- . The right side depicts a bright squeezed state with arbitrary squeezing angle θ and its uncertainties along the rotated quadratures \hat{X}_{θ} and $\hat{X}_{\theta+\frac{\pi}{2}}$.

A strength of the classical phasor picture is that superpositions of fields can be easily illustrated as vector addition of their phasors. The same is still true for the coherent part of the quantum phasor representation, but some care must be taken when combining the uncertainty regions of two superimposed states: The Wigner function is not additive and there are interference effects that can, for example, lead to partial cancellation of uncertainties in the case of entangled input states.

The coherent and squeezed states discussed so far are all minimum-uncertainty states. Their uncertainty ellipses therefore all have the same area proportional to

$$\Delta x_\theta \Delta x_{\theta+\frac{\pi}{2}} = \sqrt{\text{Var}(\hat{X}_\theta) \text{Var}(\hat{X}_{\theta+\frac{\pi}{2}})} = \frac{1}{4}, \quad (2.35)$$

with θ being the direction of the major or minor axis. Section 2.2 will show how realistic imperfections in the propagation of squeezed states lead to increased uncertainties and thus larger uncertainty regions in the phasor diagram.

2.1.6 Generation of squeezed light

The practical production of squeezed states requires some nonlinear interaction process. One such process is the *parametric down-conversion* in an actively pumped nonlinear medium. This effect is present in a medium where the dielectric polarization

$$\mathcal{P}(E) = \varepsilon_0 \left(\chi^{(1)} E + \chi^{(2)} E^2 + \chi^{(3)} E^3 + \dots \right) \quad (2.36)$$

has a non-zero second order term with coefficient $\chi^{(2)}$. In a $\chi^{(2)}$ interaction the energy of an incident pump photon can be re-emitted in the form of two new photons at lower frequencies. We consider the degenerate case where a pump photon of frequency $\omega_p = 2\omega$ gives rise to two equal photons at the fundamental frequency ω . The Hamiltonian that describes this interaction is [WM08]

$$\hat{H} = \hbar\omega \hat{a}^\dagger \hat{a} + \hbar\omega_p \hat{b}^\dagger \hat{b} + i\hbar\chi \left(\hat{a}^2 \hat{b}^\dagger - \hat{a}^\dagger \hat{b} \right), \quad (2.37)$$

where \hat{a} and \hat{b} are the annihilation operators of the fundamental and pump field, respectively. The coefficient χ signifies the interaction strength, which is proportional to $\chi^{(2)}$, but also depends on the specific experimental parameters. The pump field in mode \hat{b} is a strong coherent state and, with the assumption that it is not significantly depleted by the interaction process, we can rewrite the Hamiltonian in terms of a classical field $\beta e^{-i\omega_p t}$:

$$\hat{H} = \hbar\omega \hat{a}^\dagger \hat{a} + \hbar\omega_p |\beta|^2 + i\hbar\chi \left(\beta^* \hat{a}^2 e^{i\omega_p t} - \beta \hat{a}^\dagger \hat{b} e^{-i\omega_p t} \right). \quad (2.38)$$

Transforming from the Schrödinger picture to the interaction picture, explicitly including the free time evolution, we can write the interaction part of the Hamiltonian as [GK05]

$$\hat{H}_I(t) = i\hbar\chi\left(\beta^*\hat{a}^2e^{-2i\omega t}e^{i\omega_p t} - \beta\hat{a}^{\dagger 2}e^{2i\omega t}e^{-i\omega_p t}\right), \quad (2.39)$$

which simplifies to the time-independent

$$\hat{H}_I = i\hbar\chi\left(\beta^*\hat{a}^2 - \beta\hat{a}^{\dagger 2}\right) \quad (2.40)$$

when considering $\omega_p = 2\omega$. The corresponding time evolution operator then is

$$\begin{aligned} \hat{U}_I(t) &= \exp\left(-i\hat{H}_I t/\hbar\right) \\ &= \exp\left(\chi\beta^*t\hat{a}^2 - \chi\beta t\hat{a}^{\dagger 2}\right). \end{aligned} \quad (2.41)$$

This clearly has the same form as the squeeze operator $\hat{S}(\xi)$ defined in equation 2.19 with squeezing parameter $\xi = 2\chi\beta t$. The meaning of t here is the interaction time of the input field with the nonlinear process [DK12]. This time is typically given by the effective light travel time through the nonlinear medium, which is increased by placing the medium inside a resonant cavity.

The effect of the parametric down-conversion can be understood as a phase-sensitive amplification process that amplifies all occurring fluctuations in one quadrature and deamplifies them in the orthogonal quadrature. A very illustrative explanation of this parametric amplification process in a semiclassical picture is given by Bauchrowitz et al. [BWS13]. The technical details of achieving high parametric amplifications with a realistic nonlinear medium are quite intricate. Some aspects of this will be discussed in chapter 3. Much more in-depth information on the efficient generation of squeezed states in the context of gravitational-wave detection can, for example, be found in [McK08].

2.1.7 Detection of squeezed light

Measuring coherent and squeezed states of light is done with semiconductor photodiodes that convert the impinging photons into an electric current. The detected photocurrent is proportional to the photon number of the measured light field:

$$\hat{i} \propto \hat{n} = \hat{a}^\dagger \hat{a}. \quad (2.42)$$

To facilitate the following calculations, the photon number operator can be rewritten by decomposing \hat{a} into a steady-state term and a fluctuation term:

$$\hat{a} = \langle \hat{a} \rangle + \delta \hat{a} \quad (2.43)$$

and therefore

$$\begin{aligned} \hat{n} &= (\langle \hat{a} \rangle^* + \delta \hat{a}^\dagger)(\langle \hat{a} \rangle + \delta \hat{a}) \\ &= |\langle \hat{a} \rangle|^2 + \langle \hat{a} \rangle \delta \hat{a}^\dagger + \langle \hat{a} \rangle^* \delta \hat{a} + \delta \hat{a}^\dagger \delta \hat{a}. \end{aligned} \quad (2.44)$$

For a coherent state $|\alpha\rangle$ or squeezed state $|\alpha, \xi\rangle$ we know the expectation value is $\langle \hat{a} \rangle = \alpha = |\alpha|e^{i\phi}$ with $\phi = \arg(\alpha)$ and we can further write

$$\begin{aligned} \hat{n} &= |\alpha|^2 + |\alpha| \left(e^{i\phi} \delta \hat{a}^\dagger + e^{-i\phi} \delta \hat{a} \right) + \delta \hat{a}^\dagger \delta \hat{a} \\ &= |\alpha|^2 + 2|\alpha| \delta \hat{X}_\phi + \delta \hat{a}^\dagger \delta \hat{a}, \end{aligned} \quad (2.45)$$

where $\delta \hat{X}_\phi$ is the fluctuation term of the quadrature operator \hat{X}_ϕ along the direction given by α . Finally, for strong coherent excitations with $|\alpha| \gg |\delta \hat{a}|$ the last term becomes negligible and we get

$$\hat{n} \approx |\alpha|^2 + 2|\alpha| \delta \hat{X}_\phi. \quad (2.46)$$

2.1.7.1 Direct measurement with a photodiode

In the simplest case we have one light field detected by a single photodiode. We assume a bright squeezed state $|\alpha, \xi\rangle$ with $\alpha = |\alpha|e^{i\phi}$ and $\xi = r e^{i\theta}$. With the approximation 2.46 we get

$$\bar{n} = \langle \alpha, \xi | \hat{n} | \alpha, \xi \rangle \approx |\alpha|^2 \quad (2.47)$$

and

$$\begin{aligned} \text{Var}(\hat{n}) &= 4|\alpha|^2 \text{Var}(\hat{X}_\phi) \\ &= |\alpha|^2 \left(\cos^2(\phi - \theta) e^{-2r} + \sin^2(\phi - \theta) e^{2r} \right). \end{aligned} \quad (2.48)$$

This means that the variance of the detected signal depends on the applied squeezing and scales with the coherent amplitude $|\alpha|$ of the light field. The minimum fluctuations of the detected signal are achieved for $\phi = \theta$, when the squeezing is applied in phase with the coherent excitation.

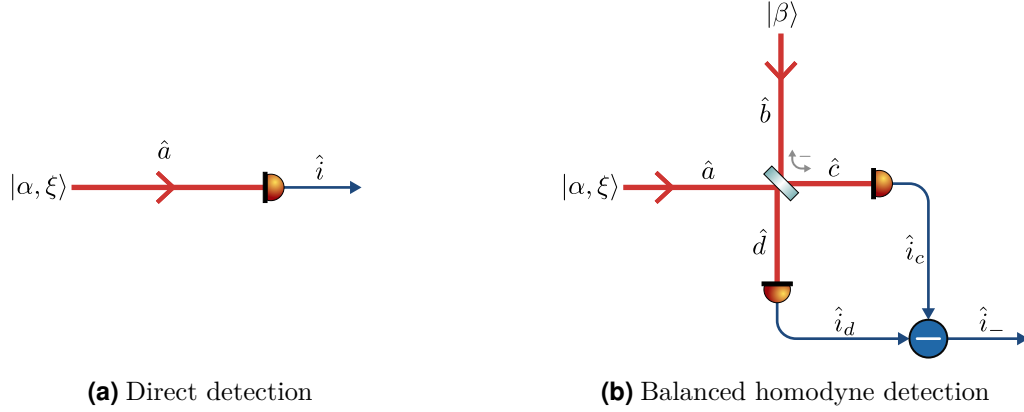


Figure 2.4: Detecting squeezed states either directly on a single photodiode or combined with a strong local oscillator field in a balanced homodyne detector.

For an unsqueezed coherent state the variance is equal to the mean photon number \bar{n} . This is the same result that we would expect when we consider independent photons hitting the photodetector, so that the number of photons detected in a specific time interval follows a Poisson distribution. When squeezing reduces the variance of the photocurrent, the photon number follows a sub-Poissonian distribution and the photons can no longer be regarded as independent.

Any measurement where the signal of interest is encoded in the intensity of a coherent light field will have an intrinsic uncertainty due to these photon-number fluctuations. This effect is called *photon-counting error* or more commonly *shot noise*. The signal-to-noise ratio of a shot-noise-limited measurement scales with the square root of the photon number:

$$SNR^{\text{sn}} \propto \frac{\bar{n}}{\Delta n} = \frac{\langle \hat{n} \rangle}{\sqrt{\text{Var}(\hat{n})}} = \frac{|\alpha|^2}{\sqrt{|\alpha|^2}} = |\alpha| = \sqrt{\bar{n}}. \quad (2.49)$$

If instead of a coherent state, a squeezed state with optimally oriented squeezing angle is hitting the photodetector, the signal-to-noise ratio can be improved by the factor e^r .

2.1.7.2 Balanced homodyne detection

A single photodiode can only detect the quadrature fluctuations in the amplitude quadrature of a bright state. If we want to characterize a quantum state in more than one quadrature and also for detecting squeezed vacuum states, we can apply

a technique called *balanced homodyne detection*. For this, the field of interest is combined with a strong coherent field, called a *local oscillator*, on a 50/50 beamsplitter (other splitting ratios would give *unbalanced* homodyne detection). The two output ports of the beamsplitter are sensed with two photodiodes and the difference of the resulting photocurrents is recorded. Figure 2.4b illustrates the setup.

To describe this scheme we need to consider four fields: the input field \hat{a} , the local oscillator field \hat{b} , and the two beamsplitter output fields \hat{c} and \hat{d} . We assume that all fields have the same frequency ω . They are connected via a beamsplitter matrix as follows:

$$\begin{pmatrix} \hat{c} \\ \hat{d} \end{pmatrix} = \frac{1}{\sqrt{2}} \begin{pmatrix} 1 & -1 \\ 1 & 1 \end{pmatrix} \begin{pmatrix} \hat{a} \\ \hat{b} \end{pmatrix} = \begin{pmatrix} \frac{1}{\sqrt{2}}(\hat{a} - \hat{b}) \\ \frac{1}{\sqrt{2}}(\hat{a} + \hat{b}) \end{pmatrix}. \quad (2.50)$$

The difference of the measured photocurrents then is

$$\langle \hat{i}_c \rangle - \langle \hat{i}_d \rangle \propto \langle \hat{n}_c \rangle - \langle \hat{n}_d \rangle = \langle \hat{c}^\dagger \hat{c} - \hat{d}^\dagger \hat{d} \rangle = \langle \hat{a}^\dagger \hat{b} + \hat{b}^\dagger \hat{a} \rangle. \quad (2.51)$$

For a strong local oscillator with $|\langle \hat{b} \rangle| = |\beta| \gg |\langle \hat{a} \rangle|$ we can split $\hat{b} = \beta + \delta\hat{b}$ and neglect terms of order $\hat{a}^\dagger \delta\hat{b}$ to arrive at

$$\begin{aligned} \langle \hat{n}_c \rangle - \langle \hat{n}_d \rangle &= |\beta| \langle \hat{a}^\dagger e^{i\phi} + \hat{a} e^{-i\phi} \rangle \\ &= 2|\beta| \langle \hat{X}_{a,\phi} \rangle, \end{aligned} \quad (2.52)$$

where $\hat{X}_{a,\phi}$ is the quadrature operator of mode \hat{a} along the direction given by the local-oscillator phase ϕ . In the same way, we can derive that the variance of the signal is proportional to

$$\text{Var}(\hat{n}_c - \hat{n}_d) = 4|\beta|^2 \text{Var}(\hat{X}_{a,\phi}). \quad (2.53)$$

This means that the balanced homodyne signal can be used to directly measure an arbitrary quadrature of the input field.

2.1.8 Quantum noise in interferometers

With the concepts introduced so far we can now look at a quantum-mechanical description of the light fields inside an interferometric detector. We assume a simple Michelson interferometer as depicted in figure 2.5 and consider the light fields at six different locations, represented by the annihilation operator of the respective mode [Cav81]: Modes \hat{a}_1 and \hat{a}_2 are the input fields of the interferometer. Field \hat{a}_1 is the main input, where usually a strong coherent state with optical power $P = \hbar\omega\bar{n}_{a_1}/\tau$

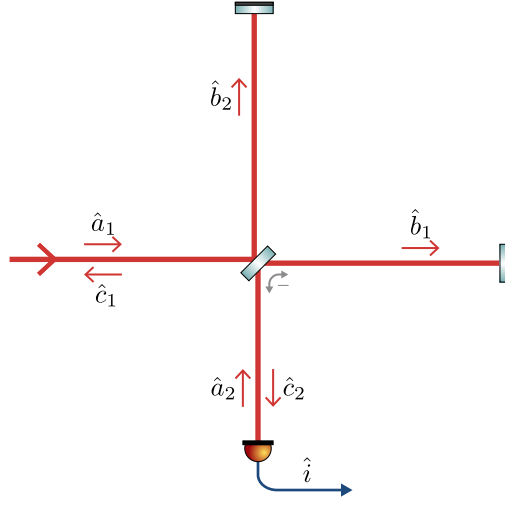


Figure 2.5: Quantum noise propagation in a Michelson interferometer. This diagram illustrates the different fields used for the quantum noise calculations for an ideal interferometer. In a real experiment, the counter-propagating fields $\hat{a}_{1/2}$ and $\hat{c}_{1/2}$ can be separated by means of a Faraday isolator.

is injected, where τ is the measurement interval. Field \hat{a}_2 is the mode entering through the detection port which also needs to be considered. For a classical interferometer no light is injected here which means that this mode is in the vacuum state. The fields \hat{b}_1 and \hat{b}_2 represent the modes after the beamsplitter, inside the interferometer arms. Finally, \hat{c}_1 and \hat{c}_2 are the two output modes travelling in the opposite direction as \hat{a}_1 and \hat{a}_2 . The main output signal is generated with a photodetector measuring the power in mode \hat{c}_2 , resulting in a photocurrent $\hat{i} \propto \hat{n}_{c_2} =: \hat{n}_{\text{out}}$.

The different light fields can be related to each other via the beamsplitter matrix. Neglecting all non-essential phase factors we can write

$$\begin{pmatrix} \hat{b}_1 \\ \hat{b}_2 \end{pmatrix} = \frac{1}{\sqrt{2}} \begin{pmatrix} 1 & -1 \\ 1 & 1 \end{pmatrix} \begin{pmatrix} \hat{a}_1 \\ \hat{a}_2 \end{pmatrix} = \begin{pmatrix} \frac{1}{\sqrt{2}}(\hat{a}_1 - \hat{a}_2) \\ \frac{1}{\sqrt{2}}(\hat{a}_1 + \hat{a}_2) \end{pmatrix} \quad (2.54)$$

and

$$\begin{pmatrix} \hat{c}_1 \\ \hat{c}_2 \end{pmatrix} = \frac{1}{\sqrt{2}} \begin{pmatrix} 1 & -1 \\ 1 & 1 \end{pmatrix} \begin{pmatrix} e^{i\phi/2}\hat{b}_1 \\ e^{-i\phi/2}\hat{b}_2 \end{pmatrix} = \begin{pmatrix} \frac{1}{\sqrt{2}}(e^{i\phi/2}\hat{b}_1 - e^{-i\phi/2}\hat{b}_2) \\ \frac{1}{\sqrt{2}}(e^{i\phi/2}\hat{b}_1 + e^{-i\phi/2}\hat{b}_2) \end{pmatrix}, \quad (2.55)$$

where an additional phase shift $\phi = 4\pi\Delta L/\lambda$ introduced by an arm-length difference

ΔL is included. Combining the equations 2.54 and 2.55 yields

$$\begin{aligned} \begin{pmatrix} \hat{c}_1 \\ \hat{c}_2 \end{pmatrix} &= \begin{pmatrix} \frac{1}{2} \left(e^{i\phi/2} (\hat{a}_1 - \hat{a}_2) - e^{-i\phi/2} (\hat{a}_1 + \hat{a}_2) \right) \\ \frac{1}{2} \left(e^{i\phi/2} (\hat{a}_1 - \hat{a}_2) + e^{-i\phi/2} (\hat{a}_1 + \hat{a}_2) \right) \end{pmatrix} \\ &= \begin{pmatrix} i \sin(\phi/2) \hat{a}_1 - \cos(\phi/2) \hat{a}_2 \\ \cos(\phi/2) \hat{a}_1 - i \sin(\phi/2) \hat{a}_2 \end{pmatrix}. \end{aligned} \quad (2.56)$$

We can thus analyse the fields at the output as well as inside the interferometer arms as a function of the injected states.

2.1.8.1 Shot noise

The shot noise of the interferometric detection is determined by the properties of the photon-number operator for the output mode \hat{c}_2 which can be written as

$$\hat{c}_2^\dagger \hat{c}_2 = \cos^2\left(\frac{\phi}{2}\right) \hat{a}_1^\dagger \hat{a}_1 + \sin^2\left(\frac{\phi}{2}\right) \hat{a}_2^\dagger \hat{a}_2 + i \sin\left(\frac{\phi}{2}\right) \cos\left(\frac{\phi}{2}\right) \left(\hat{a}_2^\dagger \hat{a}_1 - \hat{a}_1^\dagger \hat{a}_2 \right). \quad (2.57)$$

We assume a strong coherent state is injected in mode \hat{a}_1 and choose the quadrature coordinates such that its amplitude α is real. For $\langle \hat{a}_1 \rangle \gg \langle \hat{a}_2 \rangle$ the second term in equation 2.57 can then be neglected and the third term can be approximated using $\hat{a}_1^\dagger \hat{a}_2 \approx \alpha \hat{a}_2$ to get

$$\begin{aligned} \hat{c}_2^\dagger \hat{c}_2 &= \cos^2\left(\frac{\phi}{2}\right) \hat{a}_1^\dagger \hat{a}_1 + i \alpha \sin\left(\frac{\phi}{2}\right) \cos\left(\frac{\phi}{2}\right) \left(\hat{a}_2^\dagger - \hat{a}_2 \right) \\ &= \cos^2\left(\frac{\phi}{2}\right) \hat{a}_1^\dagger \hat{a}_1 + \alpha \sin(\phi) \hat{X}_{a_2-} \end{aligned} \quad (2.58)$$

with the phase quadrature operator \hat{X}_{a_2-} of mode \hat{a}_2 .

The detected photon number depends on the phase difference ϕ as

$$\bar{n}_{\text{out}} = \langle \hat{c}_2^\dagger \hat{c}_2 \rangle = \alpha^2 \cos^2\left(\frac{\phi}{2}\right). \quad (2.59)$$

It can therefore be used as a measure for small phase fluctuations $d\phi$ with

$$\frac{d\bar{n}_{\text{out}}}{d\phi} = -\frac{1}{2} \alpha^2 \sin(\phi), \quad (2.60)$$

or in terms of changes of the differential arm length

$$\frac{d\bar{n}_{\text{out}}}{d\Delta L} = -\frac{2\pi}{\lambda} \alpha^2 \sin(\phi). \quad (2.61)$$

Chapter 2 Theoretical background

The variance of the measured photon number is

$$\text{Var}(\hat{n}_{\text{out}}) = \text{Var}(\hat{c}_2^\dagger \hat{c}_2) = \alpha^2 \cos^4\left(\frac{\phi}{2}\right) + \alpha^2 \sin^2(\phi) \text{Var}(\hat{X}_{a_2-}). \quad (2.62)$$

These inherent fluctuations of the interferometer's output signal can be translated to apparent fluctuations of the differential arm length by combining the last two equations to get

$$\text{Var}(\Delta L) = \frac{\lambda^2}{4\pi^2\alpha^2 \sin^2(\phi)} \left(\cos^4\left(\frac{\phi}{2}\right) + \sin^2(\phi) \text{Var}(\hat{X}_{a_2-}) \right). \quad (2.63)$$

This expression diverges for $\phi = k\pi$, $k \in \mathbb{N}$ and it has removable singularities for $\phi = (k + \frac{1}{2})\pi$, $k \in \mathbb{N}$. These singular operating points correspond to the *bright* and *dark fringe*, respectively, where the output signal reaches its maximum or minimum and the derivative $\frac{d\bar{n}_{\text{out}}}{d\phi}$ vanishes (see figure 2.6). Outside the singularities equation 2.63 can be simplified to

$$\text{Var}(\Delta L) = \frac{\lambda^2}{16\pi^2\alpha^2} \left(\cot^2\left(\frac{\phi}{2}\right) + 4\text{Var}(\hat{X}_{a_2-}) \right). \quad (2.64)$$

We see that the apparent length fluctuations are caused by a combination of the quantum noise of the coherent input field dependent on the operating point and a constant contribution from the phase fluctuations of the field entering at the output port. The first term approaches zero for operating points near the dark fringe, which is therefore the preferred mode of operation.³ There we can write

$$\text{Var}(\Delta L) \approx \frac{\lambda^2}{4\pi^2\alpha^2} \text{Var}(\hat{X}_{a_2-}). \quad (2.65)$$

For the classical case of a vacuum state incident at the output port the effective arm-length fluctuations become

$$\text{Var}(\Delta L) \approx \frac{1}{4} \cdot \frac{\lambda^2}{4\pi^2\alpha^2} = \frac{\hbar c \lambda}{8\pi P \tau}. \quad (2.66)$$

Replacing the vacuum state with a squeezed vacuum state will reduce the length noise in the case of phase squeezing, or increase it for amplitude squeezing.

³ The technique of operating the interferometer at a small offset from the dark fringe is called *DC readout* or *self-homodyne detection* [Hil⁺09]. It is the preferred readout scheme of the current generation of gravitational-wave detectors. Other readout techniques are *homodyne readout* with a separately supplied local oscillator or *heterodyne readout* using modulation sidebands.

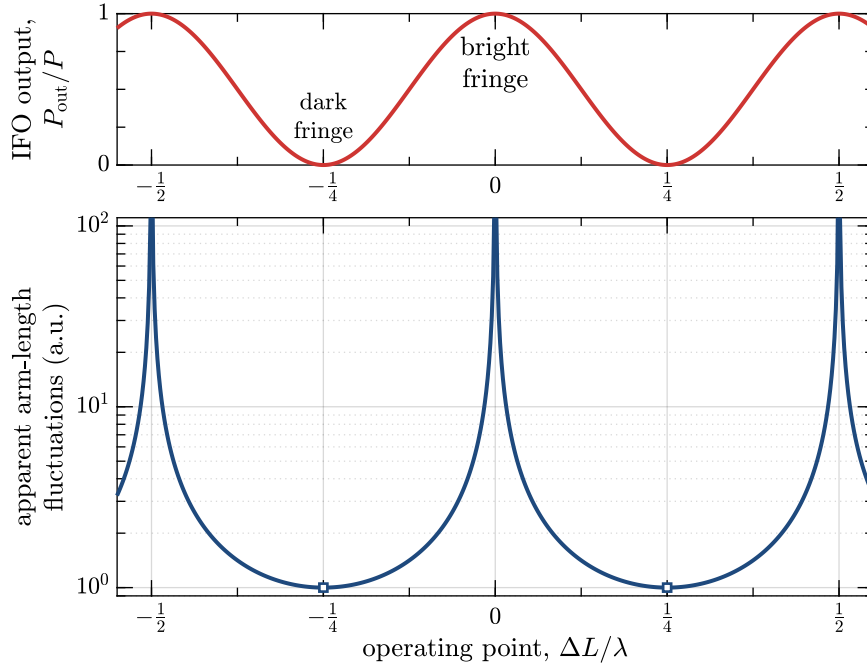


Figure 2.6: Shot noise in a Michelson interferometer as a function of the operating point. The upper plot shows the normalized interferometer output power. Small fluctuations of the arm-length difference will lead to a signal in the output power, with the signal strength proportional to the slope of the graph. The lower plot depicts the inherent shot noise of the measured output power scaled to equivalent arm length fluctuations. This noise level diverges at the bright fringe and approaches its minimum for operating points close to the dark fringe. Directly at the dark fringe there is a singularity (square markers) where the signal vanishes. Other readout schemes can operate directly at the dark fringe and lead to the same theoretical shot-noise limit [Sau17]. For this plot an ideal Michelson interferometer is assumed without any imperfections.

2.1.8.2 Radiation-pressure noise

The mirrors of a gravitational wave detector are suspended and act like free masses well above the suspension resonance frequency. This makes them susceptible to the optomechanical influence of the reflected light fields. Radiation pressure exerts a force on the mirrors proportional to the number of incident photons. Fluctuations of the radiation pressure thus lead to fluctuations of the mirror positions, physically changing the arm-length difference that is being measured.

The differential force that is being applied to the two end mirrors is proportional to

the difference between the rate of photons in modes \hat{b}_1 and \hat{b}_2 [Cav81]:

$$\begin{aligned}\Delta\hat{F} &= \frac{2\hbar\omega}{c\tau}(\hat{b}_2^\dagger\hat{b}_2 - \hat{b}_1^\dagger\hat{b}_1) \\ &= -\frac{2\hbar\omega}{c\tau}(\hat{a}_1^\dagger\hat{a}_2 + \hat{a}_2^\dagger\hat{a}_1).\end{aligned}\tag{2.67}$$

Again assuming a strong coherent state with real amplitude α in the input mode, we can derive (in the same way as for the homodyne detector in section 2.1.7.2)

$$\text{Var}(\Delta\hat{F}) \approx \left(\frac{4\hbar\omega}{c\tau}\right)^2 \alpha^2 \text{Var}(\hat{X}_{a_2+}),\tag{2.68}$$

where \hat{X}_{a_2+} is the amplitude quadrature of mode \hat{a}_2 . This means that the fluctuations of the radiation pressure are due to the amplitude-quadrature fluctuations in mode \hat{a}_2 . The quantum (and classical) fluctuations of the bright input state, to first order, do not contribute to noise in the detection. For a vacuum state incident at the output port the variance of the radiation-pressure force is

$$\text{Var}(\Delta\hat{F}) \approx \frac{1}{4} \left(\frac{4\hbar\omega}{c\tau}\right)^2 \alpha^2 = \frac{8\pi\hbar}{c\lambda\tau} P.\tag{2.69}$$

Radiation-pressure noise and shot noise are due to the two conjugate quadratures of the same field that enters the interferometer through the output port. So, reducing the phase fluctuations to improve the shot noise will increase the radiation-pressure noise and vice versa.

2.1.8.3 Noise spectral densities

So far, the quantum fluctuations of the observables of interest have been expressed as variances. The more commonly used way to describe a noisy signal is in terms of noise spectral densities. The *single-sided power spectral density* (PSD) $S_x(f)$ is defined for positive signal frequencies f as twice the Fourier transform of the autocorrelation function [BP10]. The PSD is a measure for the noise power of a signal contained in a certain frequency band. Integrating the PSD over all frequencies gives the variance:

$$\text{Var}(x(t)) = \int_0^\infty df S_x(f).\tag{2.70}$$

2.1 Quantum states of light

For a frequency-independent white-noise signal, detected with finite measurement bandwidth $B = \frac{1}{2\tau}$, the above equation can be simplified to [Che07]

$$\text{Var}(x(t)) = S_x \cdot B = \frac{S_x}{2\tau}. \quad (2.71)$$

We can apply this to convert the apparent arm-length fluctuations due to unsqueezed shot noise (equation 2.66) into the frequency-independent PSD

$$S_{\Delta L}^{\text{sn}}(f) = \frac{\hbar c \lambda}{4\pi P}. \quad (2.72)$$

This PSD can be expressed in units of equivalent gravitational-wave strain $h = \Delta L/L$ for a detector of length L (see section 1.1) as

$$S_h^{\text{sn}}(f) = \frac{\hbar c \lambda}{4\pi P L^2}. \quad (2.73)$$

Often an *amplitude spectral density* (ASD) is used, which is just the square root of the PSD and has the advantage of scaling linearly with the signal amplitude. The ASD of the apparent strain fluctuations caused by shot noise is

$$\tilde{h}^{\text{sn}}(f) := \sqrt{S_h^{\text{sn}}(f)} = \frac{1}{2L} \sqrt{\frac{\hbar c \lambda}{\pi P}}. \quad (2.74)$$

Similarly, the white PSD of the force noise caused by radiation pressure fluctuations (equation 2.69) is given by

$$S_{\Delta F}^{\text{rp}}(f) = \frac{16\pi\hbar}{c\lambda} P. \quad (2.75)$$

To convert this to displacement noise we multiply with the transfer function of a free mass [Sau17]:

$$S_{\Delta L}^{\text{rp}}(f) = \left(\frac{1}{4\pi^2 f^2 m} \right)^2 S_{\Delta F}^{\text{rp}}(f) = \frac{\hbar P}{\pi^3 c \lambda m^2 f^4}. \quad (2.76)$$

Here m is the mass of each end mirror. Written as a strain ASD this is

$$\tilde{h}^{\text{rp}}(f) = \frac{1}{m f^2 L} \sqrt{\frac{\hbar P}{\pi^3 c \lambda}}. \quad (2.77)$$

The calculations so far assumed a simple Michelson interferometer. A full description of a realistic gravitational-wave detector is more complicated and requires the consideration of the recycling techniques, the dynamic response of the interferometer, and

many other effects [LRR00; BCM03; Har⁺03; Mia⁺14]. The essential limitations of the achievable sensitivity through radiation-pressure noise and shot noise, however, remain the same.

2.1.8.4 The standard quantum limit

The interferometer output will see a combination of the two forms of quantum noise. With the spectral densities calculated above and assuming that radiation-pressure noise and shot noise are uncorrelated, the total *optical-readout noise* is

$$\tilde{h}^{\text{qn}}(f) = \sqrt{\left(\tilde{h}^{\text{rp}}(f)\right)^2 + \left(\tilde{h}^{\text{sn}}(f)\right)^2}. \quad (2.78)$$

Because of the $1/f^2$ dependence of the radiation-pressure noise this contribution will dominate at low frequencies, while the shot noise dominates at the high-frequency end, with the cross-over point determined by the light power inside the interferometer (see figure 2.7). For any given frequency there is an optimal power $P_{\text{opt}}(f) = \pi c \lambda m f^2$ that minimizes the total quantum noise at that frequency [Sau17]. The minimum achievable noise spectral density at every frequency is called the *standard quantum limit* (SQL):

$$\tilde{h}^{\text{SQL}}(f) := \min_P(\tilde{h}^{\text{qn}}(f)) = \frac{1}{\pi f L} \sqrt{\frac{\hbar}{m}}. \quad (2.79)$$

The application of squeezing in either the amplitude quadrature or phase quadrature also cannot reduce the quantum noise past the SQL. Instead it acts like a change of light power by a factor of $e^{\pm 2r}$ where r is the squeezing parameter. However, introducing a squeezed vacuum state with a squeezing angle in-between 0° and 90° will introduce correlations of the \hat{X}_{a_2+} and \hat{X}_{a_2-} quadratures. This leads to partial cancellation of the two noise mechanisms in the frequency regime where they are of similar magnitude, making it possible to surpass the SQL by up to a factor of $R_- = e^{-r}$. The optimum squeezing angle is dependent on the measurement frequency. By applying a frequency-dependent rotation of the squeezing ellipse it is possible to apply optimally oriented squeezing at all frequencies at the same time (see figure 2.8) [Har⁺03]. One way to generate such *frequency-dependent squeezing* is to reflect the generated squeezed light field off a detuned cavity [Che⁺05; Oel⁺16], but there are also other approaches [e.g. Mik⁺06; Ma⁺17].

The previous analysis only considered squeezed and coherent states. One might ask the question whether injecting a squeezed vacuum state into the output port is

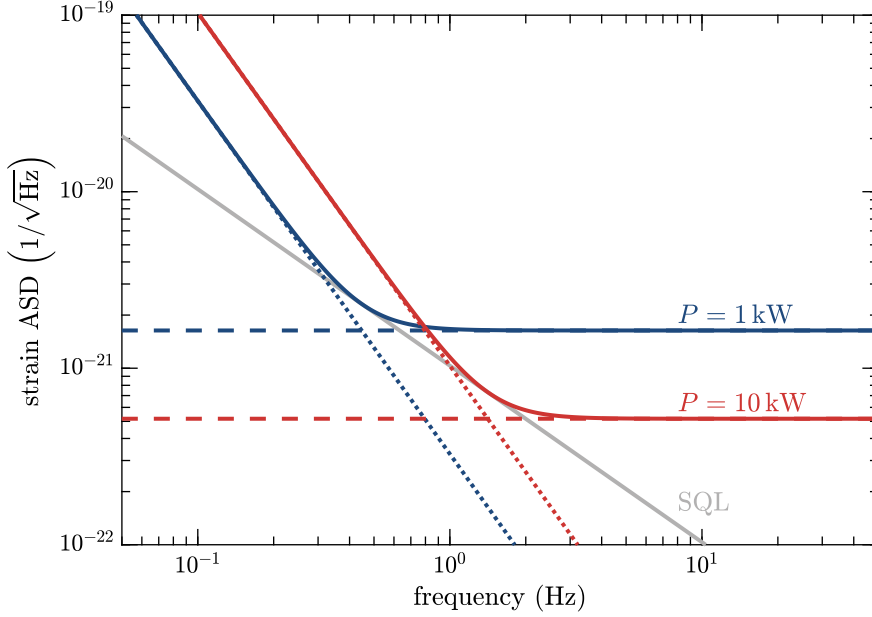


Figure 2.7: Quantum noise for two different powers. Depicted is the shot noise (dashed lines) and radiation pressure noise (dotted lines) of a generic Michelson interferometer ($L = 1$ km, $m = 1$ kg, $\lambda = 1064$ nm). Different circulating powers lead to different trade-offs between low- and high-frequency noise with an optimal power for each given frequency. The lowest reachable points together form the standard quantum limit.

actually the optimal strategy, or whether there might be other quantum states that yield even higher improvements. Theoretical analysis by Lang and Caves [LC13] showed that indeed squeezed vacuum states are optimal, at least for a simplified interferometer model and without considering losses. Analysis by Demkowicz-Dobrzański et al. [DBS13] suggests that the same holds true even in a more realistic scenario including losses. We can extend this question further by allowing arbitrary quantum states at both interferometer inputs (instead of a coherent state at the main input port) and fix the mean photon number as the limiting resource. For an idealized interferometer Lang and Caves [LC14] determine that the optimal solution in this case is to inject equally squeezed vacuum states at both ports. However, this would require extremely high squeezing factors in order to compete with the high photon numbers typically used in gravitational-wave interferometry (up to several megawatts of circulating power). Practically it seems almost impossible to generate strongly squeezed vacuum states with high mean photon number that are still close to minimum uncertainty.

Already the current generation of advanced gravitational-wave detectors is foreseen

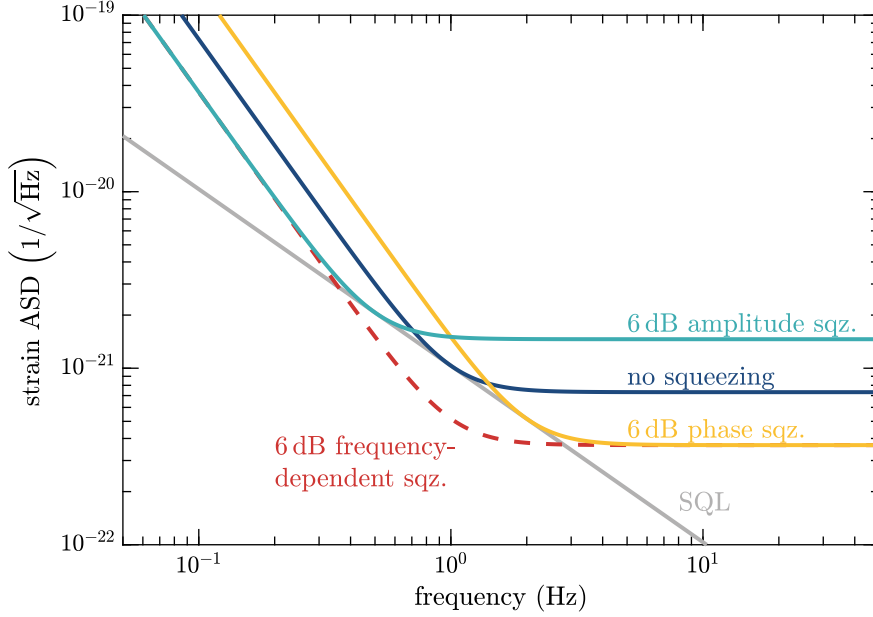


Figure 2.8: Quantum noise with squeezing. Pure phase or amplitude squeezing has an effect that is equivalent to changing the circulating power in the interferometer. Phase squeezing reduces the shot noise and increases the radiation-pressure noise, and vice versa for amplitude squeezing. However, if the squeezing angle can be made frequency dependent it is possible to improve the noise at all frequencies and thereby beat the SQL. This plot assumes the same interferometer parameters as figure 2.7 with a light power of 5 kW.

to be limited by both radiation-pressure noise and shot noise over a significant part of their frequency range once they approach their design sensitivity [LSC15; Virgo15]. This makes frequency-dependent solutions an important feature of future squeezing applications. So far, however, radiation-pressure noise has not yet been observed in any interferometer with kilogram-scale mirrors. At the current operating powers, radiation-pressure fluctuations are still masked by other technical low-frequency noise sources [Mar⁺16]. For GEO 600 the SQL is far below its achieved sensitivity. Therefore this thesis is focused on the mitigation of shot noise with frequency-independent squeezing.

2.2 Influence of imperfections

In an experimental application of squeezed states of light the inevitable imperfections of any real-world optical setup will be an important factor. Squeezed states are, in a sense, fragile and disturbances will easily increase the carefully squeezed quadrature fluctuations. The following sections will highlight the most important mechanisms that can deteriorate the performance of a squeezed-light measurement.

2.2.1 Losses

Optical losses in the propagation of a quantum state can most easily be modelled as a beamsplitter that reflects part of the signal out of the main mode. Consequently, it must also couple in vacuum fluctuations from the open port of the beamsplitter. For a power loss l the relation of input mode \hat{a}_0 and output mode \hat{a}_l can be written as

$$\hat{a}_l = \sqrt{1-l}\hat{a}_0 - \sqrt{l}\hat{b}, \quad (2.80)$$

where \hat{b} is the mode of the unused input port of the beamsplitter. The quadrature variance of the resulting output state then is

$$\text{Var}(\hat{X}_{a,\phi}^l) = (1-l)\text{Var}(\hat{X}_{a,\phi}^0) + l\text{Var}(\hat{X}_{b,\phi}), \quad (2.81)$$

which uses the fact that the vacuum fluctuations entering at \hat{b} are uncorrelated to those of the input state. For a squeezed state with initial variances V_{\pm} in the antisqueezed and squeezed quadratures we get

$$V_{\pm}^l = (1-l)V_{\pm} + lV_{\text{vac}}, \quad (2.82)$$

or expressed in terms of squeezing ratios:

$$R_{\pm}^l = (1-l)R_{\pm} + l. \quad (2.83)$$

This relation is illustrated in figure 2.9. Another convenient measure to characterize a loss mechanism is the efficiency $\eta = 1-l$. The combination of several losses is then simply described by the product of the individual efficiencies $\eta_{\text{tot}} = \prod \eta_i$.

Apart from direct optical losses there are a number of other mechanisms that also lead to a reduction of the observed squeezing level by introducing effective losses: Imperfections in the optical resonator where the squeezing is produced (the optical parametric amplifier, see section 3.4) lead to a limited escape efficiency. Also, any real

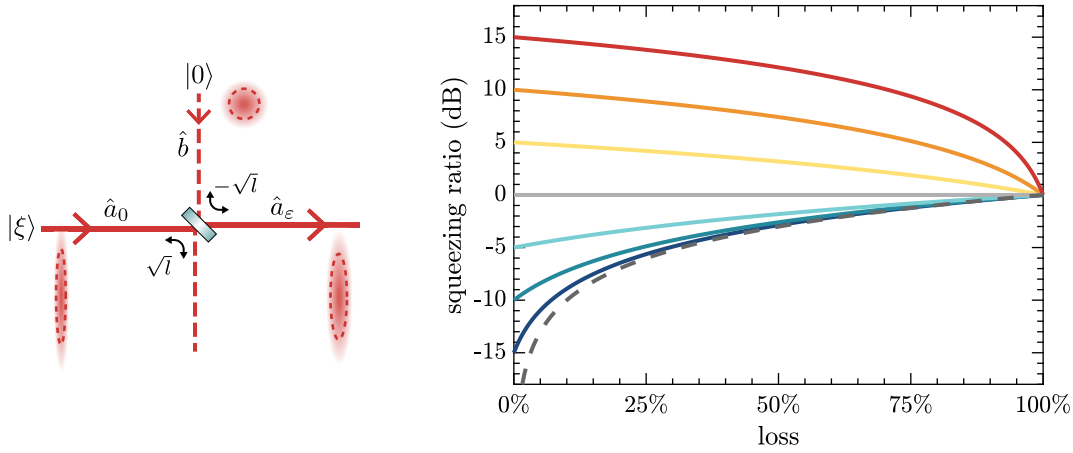


Figure 2.9: Squeezing ratio as a function of losses. The solid lines show the resulting (anti-)squeezing ratio for different levels of input squeezing under the influence of optical losses. The dashed line shows the limit for infinite input squeezing. The squeezed quadrature is degraded more quickly by losses than the antisqueezed quadrature. For 100 % loss no squeezing is left, as expected, because the input state is completely replaced by the vacuum state.

photodiode used for the detection will have a non-perfect quantum efficiency where not every impinging photon leads to a corresponding electron in the photocurrent, effectively losing those photons. Finally, only the overlapping parts of the mode of a squeezed vacuum field and the bright coherent field needed for the detection (the local oscillator in a homodyne measurement or the coherent field component in a direct detection, see section 2.1.7) will contribute and any mismatch, again, causes an effective loss. Such a reduced mode overlap results from angular or lateral misalignment between the contributing beams, a mismatch of the waist size or position, any other beam imperfections in the form of higher-order modes, or a difference in polarization. The practical aspects of these effects and their control are discussed in detail in chapter 4.

2.2.2 Contributions from classical noise

The observation of the reduced noise level due to squeezing depends sensitively on other classical noises being present in the detected signal. An important contributor of classical noise are the detection electronics that convert the photocurrent to a detectable voltage signal, and potentially the subsequent analogue and digital signal-processing stages. These random signal fluctuations are often called *dark noise* because they are still present even without any photons on the photodiode.

Further noise can originate from technical noise in the amplitude of the coherent light field, or also from excess shot noise if additional unsqueezed light fields reach the photodetector.

If we assume that classical noise with variance V_{class} is present in a specific frequency band of the detected signal and we want to measure a squeezed state with reduced quantum noise $V_- = R_- V_{\text{vac}} = e^{-2r}$, then the total observed fluctuations are

$$V_-^{\text{obs}} = V_- + V_{\text{class}}. \quad (2.84)$$

Therefore the observable noise level is directly limited by the classical noise contribution. If we consider the fact that the measured noise level without any squeezing applied $V_{\text{vac}}^{\text{obs}}$ will also be affected by the classical noise, we can calculate the effectively observed squeezing ratio:

$$\begin{aligned} R_-^{\text{obs}} &= \frac{V_-^{\text{obs}}}{V_{\text{vac}}^{\text{obs}}} \\ &= \frac{V_- + V_{\text{class}}}{V_{\text{vac}} + V_{\text{class}}} \\ &= \left(1 - \frac{V_{\text{class}}}{V_{\text{vac}} + V_{\text{class}}}\right) \frac{V_-}{V_{\text{vac}}} + \frac{V_{\text{class}}}{V_{\text{vac}} + V_{\text{class}}} \\ &= \left(1 - \frac{V_{\text{class}}}{V_{\text{vac}}^{\text{obs}}}\right) R_- + \frac{V_{\text{class}}}{V_{\text{vac}}^{\text{obs}}}. \end{aligned} \quad (2.85)$$

This has the same form as equation 2.83. The effect of classical noise is therefore observationally equivalent to an additional (potentially frequency-dependent) loss $l = V_{\text{class}}/V_{\text{vac}}^{\text{obs}}$ [App⁺07].⁴ For example, a dark-noise level with an ASD that is a factor of ten below the measured unsqueezed noise level can be compared to a $(\frac{1}{10})^2 = 1\%$ optical loss.

2.2.3 Phase noise

Relative fluctuations of the angle between the squeezed and the measured quadrature degrade the squeezing performance by coupling some of the increased noise from the antisqueezed quadrature into the measurement quadrature. A time-varying phase

⁴ Note that classical noise contributions are not exactly equivalent to optical losses in that they degrade both the unsqueezed as well as the squeezed noise level, whereas losses in the squeezing injection only affect the squeezed noise level. However, without further information, both effects are not distinguishable from observations of the squeezing performance alone.

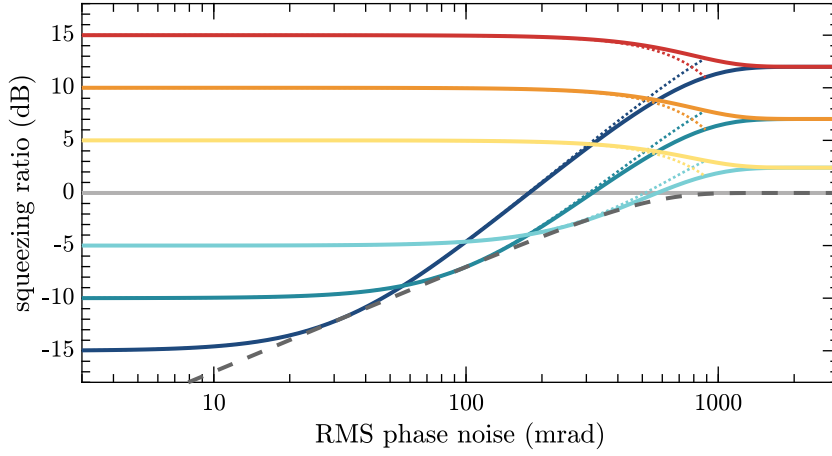


Figure 2.10: Squeezing ratio as a function of RMS phase noise. Phase fluctuations cause the quadrature variances to get increasingly mixed, leading to a clear degradation of the squeezing level. This effect is more pronounced the higher the initial squeezing and antisqueezing values are. The dotted lines in the plot show the small-angle approximation given in equation 2.87. The grey dashed line indicates the maximum achievable squeezing level for a given phase noise level. This plot shows the idealized case assuming no optical loss.

offset $\theta(t)$ leads to a mixing of the variances according to

$$V_{\pm}^{\theta}(t) = V_{\pm} \cos^2 \theta(t) + V_{\mp} \sin^2 \theta(t). \quad (2.86)$$

Since the squeezing phase is typically actively controlled (see section 4.2) it is relatively easy to avoid a constant offset. However, even with the best control there will remain some random fluctuations. Fluctuations with frequencies higher than the measurement rate $1/\tau$ will not be resolved and instead an averaged squeezing level will be measured [Oel16]. If we model the fluctuations as normally distributed around $\bar{\theta} = 0$ with a small root-mean-square (RMS) deviation $\tilde{\theta}_{\text{RMS}}$ we can write the averaged variance of the resulting measurement as [ATF06]

$$\begin{aligned} V_{\pm}^{\tilde{\theta}_{\text{RMS}}} &= \int_{-\infty}^{\infty} dx \frac{e^{-x^2/2\tilde{\theta}_{\text{RMS}}^2}}{\sqrt{2\pi}\tilde{\theta}_{\text{RMS}}} (V_{\pm} \cos^2 x + V_{\mp} \sin^2 x) \\ &\approx V_{\pm} \cos^2 \tilde{\theta}_{\text{RMS}} + V_{\mp} \sin^2 \tilde{\theta}_{\text{RMS}}. \end{aligned} \quad (2.87)$$

For relatively small fluctuations ($\tilde{\theta}_{\text{RMS}} \lesssim 100$ mrad) an RMS phase error thus acts equivalently to a constant offset of the same magnitude. Different mechanisms that will contribute to the squeezing-angle fluctuations are discussed in detail in [Dwy+13].

The negative effect of RMS phase noise is more pronounced for strongly squeezed states where the antisqueezed quadrature has a highly increased variance (see figure 2.10). For a given amount of phase error, there is a point where further increasing the input squeezing parameter r will lead to a decreasing performance in the measurement. There is thus a maximum amount of squeezing that can usefully be applied in the presence of phase noise.

2.2.4 Backscattering

Quantum-noise-limited interferometric measurements are very sensitive to the influence of scattered light [Hil07; OFW12; Ste⁺12]. Stray light that reaches the photodetectors by something other than the intended path will generally have a randomly fluctuating phase and will add a noisy contribution to the measured signal. Typical scattering sources are, for example, small imperfections of optical surfaces. In the special case of a squeezed-light enhanced measurement, the squeezing source itself can become an important scatterer [Chu⁺14]. Stray light⁵ hitting the parametric amplifier can be scattered back along with the squeezed light field, creating unwanted additional fluctuations. To describe this process, special care must be taken to consider the nonlinear interaction of the stray-light field with the parametric amplifier.

In a squeezing-enhanced interferometer the squeezed vacuum field is typically injected at the output port with the help of a Faraday rotator (see figure 2.11). Polarization imperfections can lead to some light from the interferometer output being sent backwards along the squeezing-injection path. Additional Faraday isolators are used to suppress this back-propagating light, but some small amount will reach the squeezed-light source. We care specifically for back-propagating light in the same polarization and spatial mode as the squeezed field because when scattered back towards the interferometer, light in this mode will reach the main photodetector with high efficiency. In the case of GEO 600 the squeezed-light source is an optical parametric amplifier (OPA) formed by a pumped nonlinear crystal inside a linear cavity (see section 3.4 of the next chapter). For the back-propagating stray-light field, the OPA is a highly over-coupled resonant cavity, which means that most of the field enters the cavity where it experiences the parametric gain before being reflected back towards the interferometer. This can also be understood as seeding the OPA

⁵ Here and in the following I use the terms ‘stray light’ and ‘scattering’ in the sense that this is light on an unintended path. It should be noted that this does not necessarily involve diffuse scattering.

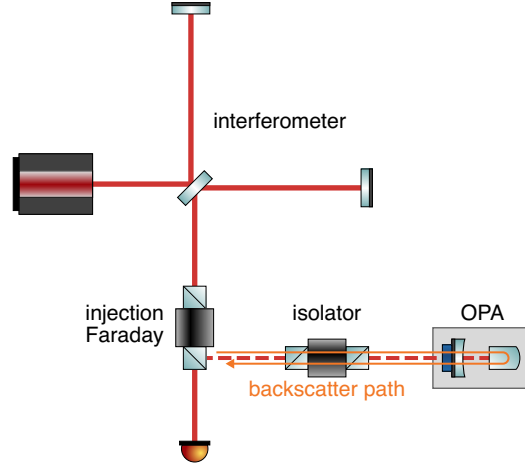


Figure 2.11: Backscattering at the squeezed-light source in a squeezing-enhanced interferometer. A small amount of interferometer-output light will reach the squeezed-light source, where it experiences the nonlinear interaction and is sent back into the interferometer together with the squeezed-vacuum field.

with the bright stray-light field instead of a vacuum field, thus creating a displaced squeezed state.

Treating the stray-light field impinging upon the squeezed-light source as a purely classical field, we can write it as

$$\beta(t) = b(t)e^{i\phi(t)}e^{i\omega t} \quad (2.88)$$

with a randomly fluctuating phase $\phi(t)$. This can be rewritten in the basis of an arbitrary, potentially varying squeezing angle $\theta(t)$ as

$$\beta = b \left[\cos(\phi - \theta)e^{i\theta} + \sin(\phi - \theta)e^{i(\theta + \frac{\pi}{2})} \right], \quad (2.89)$$

where we have dropped the explicit time dependence to simplify the notation. In the OPA the stray-light field is parametrically amplified and deamplified along the quadrature given by θ with squeezing parameter r :

$$\beta_{\text{bsc}} = b \left[e^{-r} \cos(\phi - \theta)e^{i\theta} + e^r \sin(\phi - \theta)e^{i(\theta + \frac{\pi}{2})} \right]. \quad (2.90)$$

This light field will travel with the squeezed vacuum field and eventually interfere with the interferometer-output field on the detection photodiode. Assuming that the backscatter amplitude β_{bsc} is small compared to the interferometer-output field α and choosing the coordinate system such that α is real, the noise signal caused by

backscattering can be written as

$$\begin{aligned} i_{\text{bsc}}(t) &\propto \alpha \text{Re}(\beta_{\text{bsc}}) \\ &= \alpha b [e^{-r} \cos(\phi - \theta) \cos(\theta) + e^r \sin(\phi - \theta) \sin(\theta)]. \end{aligned} \quad (2.91)$$

To analyse this expression, we split the phases into two parts:

$$\begin{aligned} \phi(t) &= \Phi(t) + \delta\phi(t), \\ \theta(t) &= \Theta(t) + \delta\theta(t), \end{aligned} \quad (2.92)$$

with slowly changing contributions $\Phi(t)$ and $\Theta(t)$ (at frequencies below the detection band) and fast but small fluctuations $\delta\phi(t), \delta\theta(t) \ll 1$. In normal squeezing operation, the squeezing angle is actively controlled to $\Theta(t) = 0$ to match the squeezed quadrature with the readout quadrature. The phase of the stray light field, on the other hand, is completely uncontrolled and $\Phi(t)$ will in general drift over many fringes. Equation 2.91 can now be expressed as

$$\begin{aligned} i_{\text{bsc}}(t) &\propto \alpha b [e^{-r} \cos(\Phi + \delta\phi - \delta\theta) \cos(\delta\theta) + e^r \sin(\Phi + \delta\phi - \delta\theta) \sin(\delta\theta)] \\ &= \alpha b [e^{-r} \cos(\Phi) \cos(\delta\phi - \delta\theta) \cos(\delta\theta) - e^{-r} \sin(\Phi) \sin(\delta\phi - \delta\theta) \cos(\delta\theta) \\ &\quad - e^r \sin(\Phi) \cos(\delta\phi - \delta\theta) \sin(\delta\theta) - e^r \cos(\Phi) \sin(\delta\phi - \delta\theta) \sin(\delta\theta)] \\ &\approx \alpha b [e^{-r} \cos(\Phi) - e^{-r} \sin(\Phi) \delta\phi - 2 \sinh(r) \sin(\Phi) \delta\theta]. \end{aligned} \quad (2.93)$$

This shows that the noise signal due to backscattered light is made up of three contributions: The first term describes a nonlinear coupling of the slow phase changes $\Phi(t)$ of the stray light field. This can be neglected as long as the absolute magnitude of these low-frequency fluctuations is not large enough to up-convert them into the detection band. The second term describes a linear coupling of the small-amplitude phase fluctuations $\delta\phi(t)$ of the stray light field. The third term, finally, shows a linear coupling of residual squeezing-angle fluctuations $\delta\theta(t)$ in the presence of a stray light field. It is interesting to note that due to the e^{-r} -dependence the first two coupling mechanisms actually get better when applying more squeezing: The parametric gain in the squeezed-light source deamplifies the scattered light field (along with the vacuum fluctuations) in the correct quadrature to reduce its influence on the detected signal [Dwy13]. The coupling of squeezing-angle fluctuations, however, increases with the squeezing parameter r .

Earlier theoretical and experimental investigation of backscatter noise from a squeezed-light source have described the coupling of the stray light's phase fluctuations, but

have generally assumed the squeezing angle to be constant [Dwy13; Chu+14; Oel+14]. To the best of my knowledge, linear coupling of squeezing-angle fluctuations has not previously been identified as an important mechanism.⁶ Our experimental results show, however, that this coupling can be a limiting factor (see section 4.6).

Following equation 2.93, the effect of backscatter noise can be expressed as a power spectral density in units of relative intensity noise on the photodetector [Chu+14]:

$$S_{\text{RIN}}^{\text{bsc}}(f) \approx \frac{\eta_{\text{inj}} P_{\text{stray}}}{P_{\text{out}}} \left[\frac{1}{2} e^{-2r} S_{\delta\phi}(f) + 2 \sinh^2(r) S_{\delta\theta}(f) \right], \quad (2.94)$$

where P_{out} is the carrier-light power at the interferometer output, P_{stray} is the amount of stray light in the fundamental mode impinging upon the OPA, and η_{inj} is the efficiency of the squeezed-light injection. Here we have dropped the nonlinear coupling term and have averaged over all possible values of Φ .⁷ The phase noises $S_{\delta\phi}(f)$ and $S_{\delta\theta}(f)$ will be of similar magnitude outside of the control bandwidth of the squeezing-angle control loop. In this case the coupling of squeezing-angle fluctuations $\delta\theta$ will be the dominant effect for meaningful squeezing levels ($r \gtrsim 0.7$ corresponding to 3 dB). The fact that the coupling increases with increasing parametric gain leads to a situation where there is a maximum amount of squeezing that can be applied before the added backscatter noise outweighs the reduction of quantum noise (see figure 2.12).

To mitigate the effect of backscatter noise there are several general approaches: On the one hand, the amount of stray light reaching the squeezer P_{stray} needs to be limited as far as possible. This depends mainly on the imperfections of the injection Faraday rotator and on the number and quality of additional Faraday isolators in the injection path. On the other hand, fluctuations of the squeezing phase can be reduced. This is anyway the goal, but in contrast to the effect of RMS phase fluctuations discussed in the previous section, we now need to specifically consider the noise spectrum in the detection band. The amount of residual phase noise will depend on the active control and on the intrinsic phase stability of the overall optical setup.

⁶ [God+05] and [McK08] describe a very detailed model of noise couplings in parametric down-conversion for the case of a bright seed beam. The full model allows for the consideration of phase fluctuations, but the analysis is performed under the simplifying assumption of perfect phase matching or constant offsets.

⁷ The formula also assumes that $\delta\phi(t)$ and $\delta\theta(t)$ are uncorrelated. This is not strictly true since both phases depend on the propagation phase of the injection path (which is travelled once by the squeezed light field and twice by the backscattered light). Equation 2.94 might therefore underestimate the combined noise slightly.

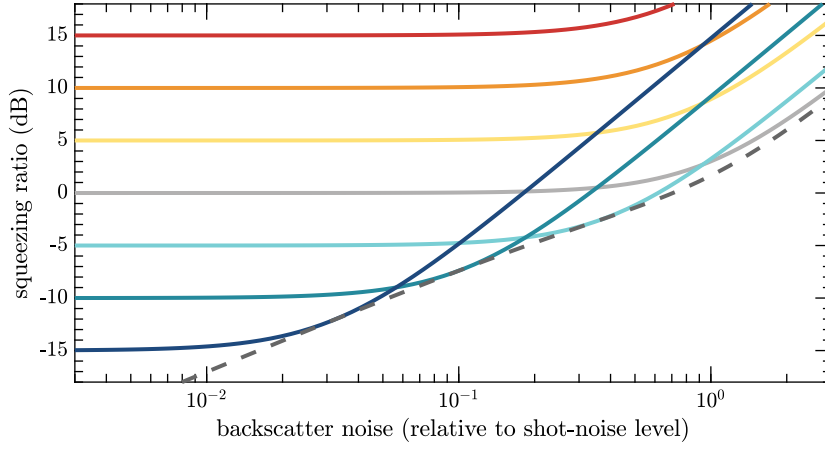


Figure 2.12: Squeezing ratio as a function of backscatter noise. Stray light impinging upon the squeezed-light source leads to a linear coupling of phase noise into the output signal, thus degrading the observable squeezing enhancement. This plot assumes equal noise levels for the stray light phase and squeezing phase at the detection frequency ($S_{\delta\phi}(f) \approx S_{\delta\theta}(f)$ in equation 2.94). The x-axis is scaled such that a noise level of 1 means that the backscatter noise is as high as the shot noise when no squeezing is applied.

If the squeezing source is built as a ring cavity instead of the linear cavity used at GEO 600, the stray light field is intrinsically decoupled from the squeezed vacuum field which propagates in the opposite direction. Optical imperfections still lead to coupling of the stray light, but suppressed by over 40 dB [Chu⁺11], which is roughly equivalent to one additional Faraday isolator.

Wade et al. [Wad⁺13] have suggested a technique for backscatter evasion by a combined modulation of the injection phase and pump phase to frequency shift the backscatter noise out of the detection band. The technique was demonstrated in a proof-of-principle experiment, but effective suppression without increasing the RMS phase noise of the squeezing injection appears challenging.

2.2.5 Combination of imperfections

In a real squeezing application, the amount of observable squeezing (and antisqueezing) will be determined by the combination of optical losses, classical noise contributions, RMS phase noise, and backscatter noise. Turning this around, we can characterize the imperfections by measuring the squeezing performance. A typical way to do this is to vary the parametric gain and determine the observed squeezing and antisqueezing

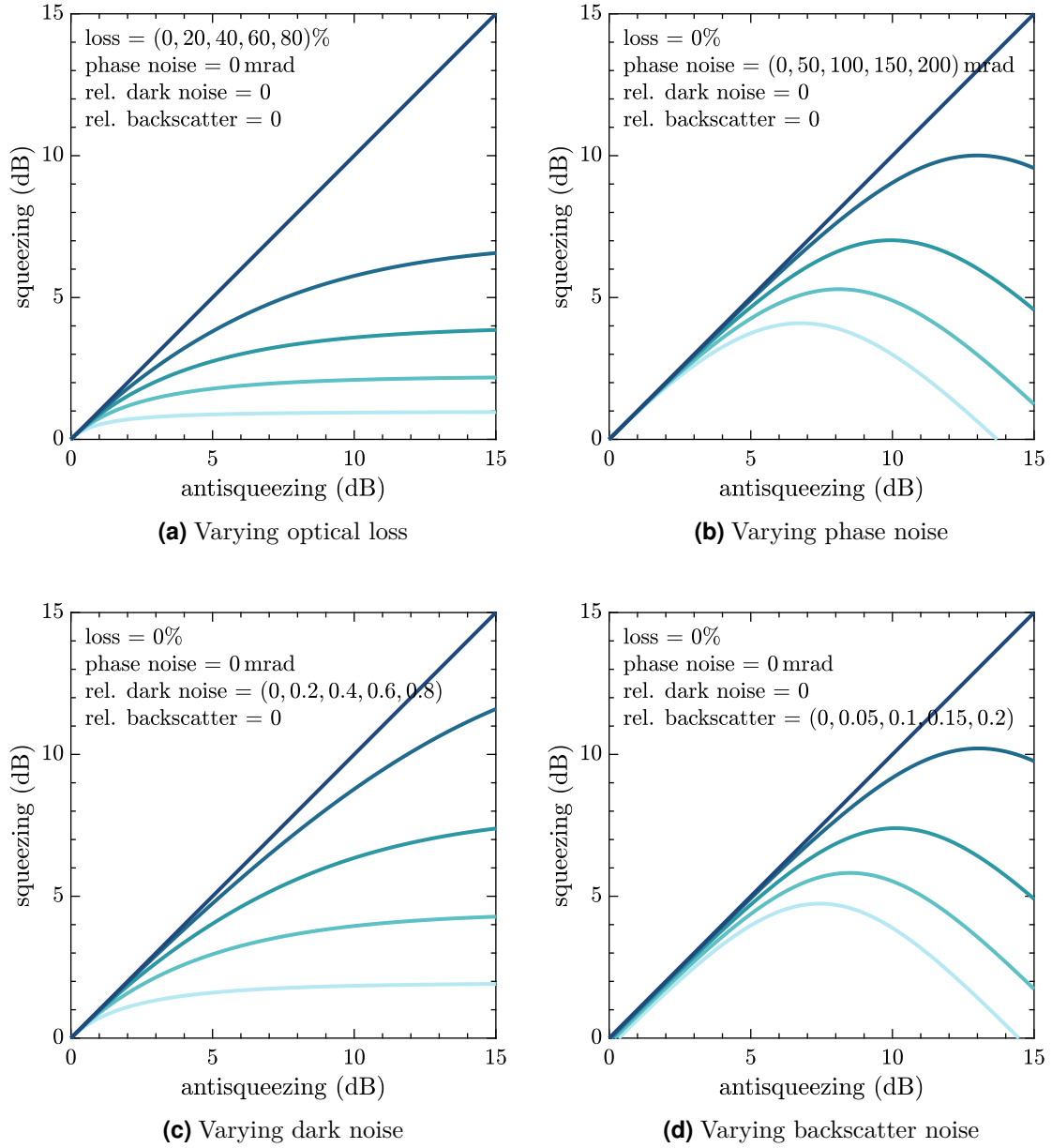


Figure 2.13: Influence of different imperfections on the observed squeezing and antisqueezing level, starting from a perfect squeezed state. The model parameters are listed in the respective plot.

2.2 Influence of imperfections

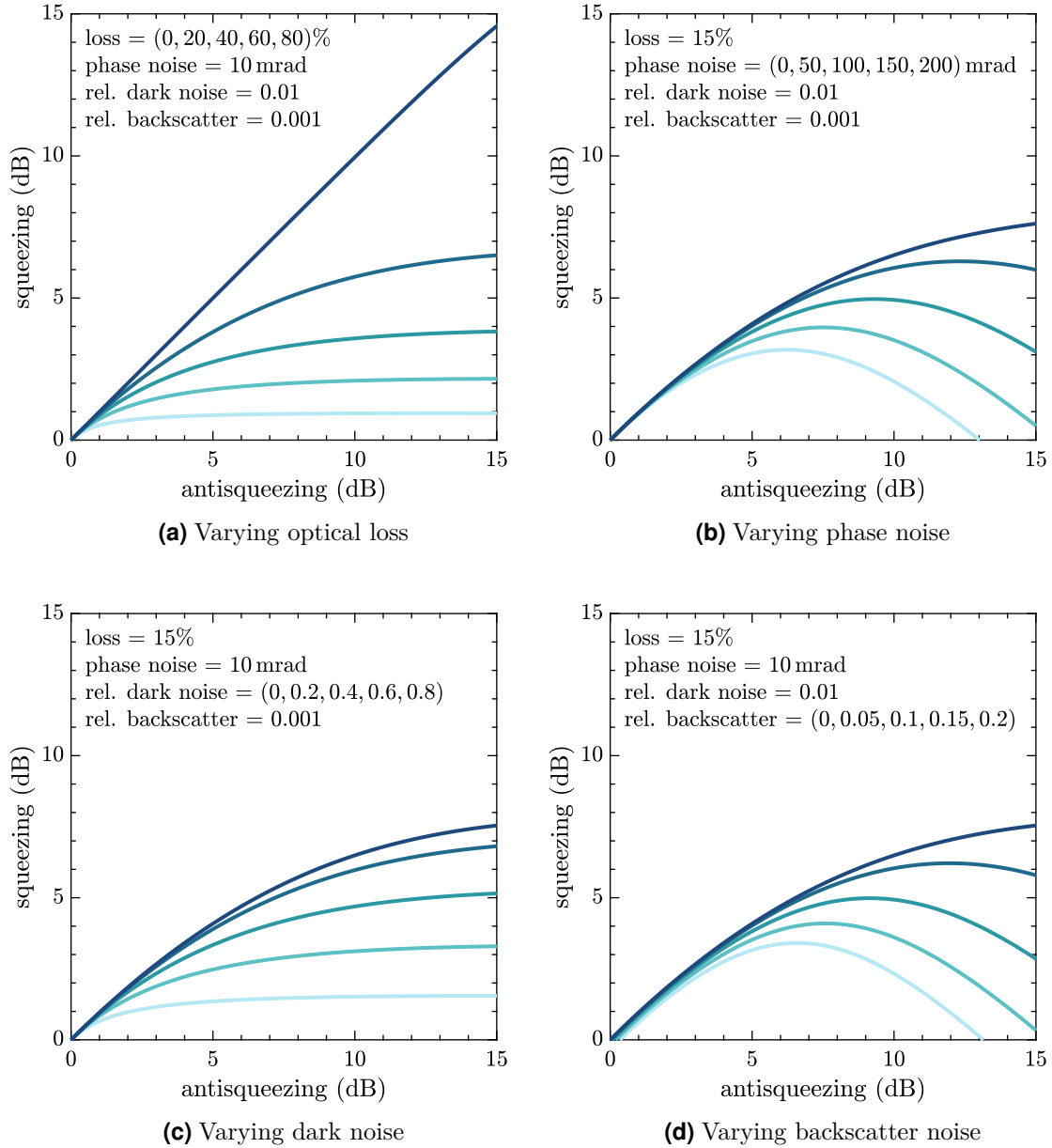


Figure 2.14: Combined influence of imperfections on the observed squeezing and antisqueezing level. In each panel one of the parameters is varied while the others are kept constant.

levels. Figures 2.13 and 2.14 show models of observed squeezing plotted against observed antisqueezing for different combinations of imperfections. At low parametric gains the effects of losses and dark noise dominate the performance. Towards higher gains RMS phase noise and backscatter noise become increasingly important. As can be seen, there are no observable differences between the influence of optical losses and dark noise and only minor deviations between the influence of RMS phase noise and backscatter noise. This means that they cannot be distinguished in this kind of measurement and other independent experiments need to be performed for further characterization (as will be described in chapter 4).

It is expected that, ultimately, optical losses and RMS phase noise will be the two dominant factors that will dictate the achievable squeezed-light improvement.⁸ Combining equations 2.83 and 2.87 we can write the observed squeezing ratio in the presence of phase noise $\tilde{\theta}_{\text{RMS}}$ and total losses l as⁹

$$R_{\pm}^{l, \tilde{\theta}_{\text{RMS}}} = (1 - l) \left(R_{\pm} \cos^2 \tilde{\theta}_{\text{RMS}} + R_{\mp} \sin^2 \tilde{\theta}_{\text{RMS}} \right) + l. \quad (2.95)$$

Figure 2.15 illustrates the combined effect on the maximum observable squeezing level. It can be seen that for optical losses of several tens of percent the phase noise level has only a slight influence, but it becomes increasingly important as the efficiency improves. For reaching 10 dB effective squeezing (the declared goal for future gravitational-wave detectors) losses need to be lower than 10% and only a few milliradians of RMS phase noise can be tolerated. Reaching even higher effective squeezing levels seems exceedingly difficult as of today, but not impossible in principle.

⁸ For example, reducing the dark noise ASD to less than one tenth of the shot-noise level is possible (though not trivial, as will be discussed in section 4.7). This would be equivalent to an optical loss of less than 1% and it appears almost impossible to ever reach such low total losses in a squeezed-light enhanced interferometer.

⁹ The question arose whether the order of application matters when modelling the effects of phase noise and losses. Explicitly calculating both options easily shows that there is no difference.

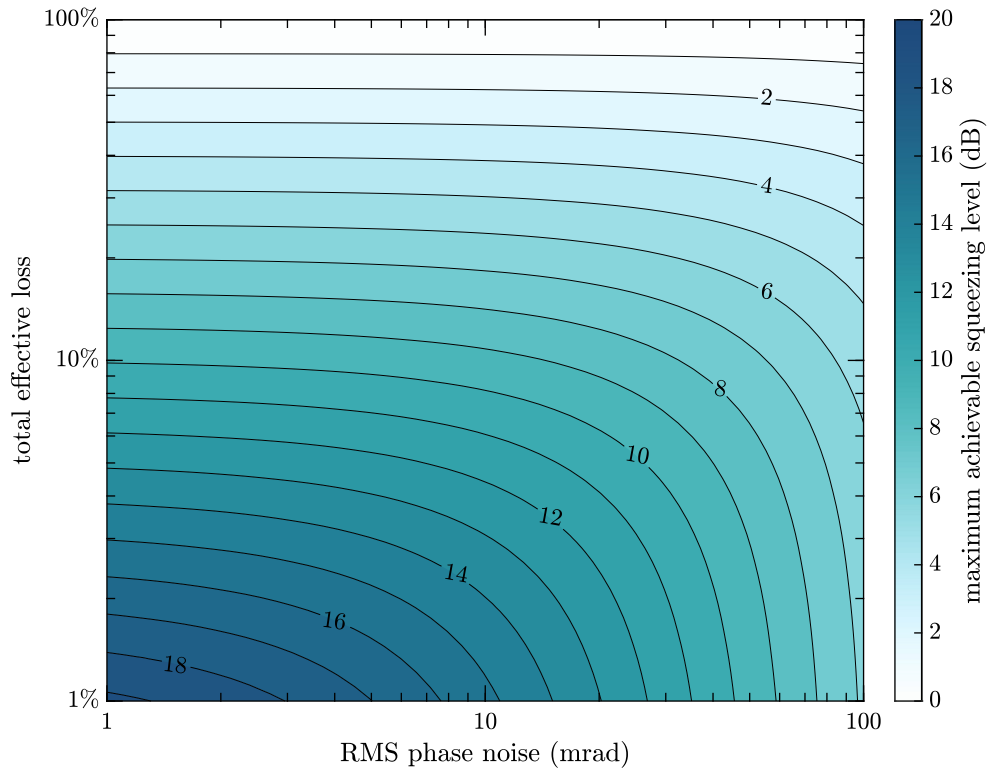


Figure 2.15: Influence of losses and phase noise. This plot shows the maximum achievable noise reduction through squeezing in the presence of both phase noise and losses. For each level of phase noise the applied squeezing strength is optimized to yield the best observed squeezing. The optimum squeezing strength does not depend on the optical losses.

Long-term operation of the GEO 600 squeezed-light source

A cornerstone of the continuous application of squeezing in a gravitational-wave observatory is the operation and maintenance of the squeezed-light source. Around-the-clock operation over many years poses challenges typically not found in table-top experiments.

This chapter introduces GEO 600's squeezed-light source and its subsystems and describes the experiences gathered over the last years. This includes regular and one-off maintenance tasks, observations of degrading components, and the automated control of the device. The integration with the rest of the detector will then be described in the [next chapter](#).

Much more detailed information on the original design and construction of the squeezing source can be found in the theses of Henning Vahlbruch [[Vah08](#)] and Alexander Khalaidovski [[Kha11](#)]. Previous work on the automated control is presented in chapter 5 of Nico Lastzka's thesis [[Las10](#)] and chapter 7 of Christian Gräf's thesis [[Grä13](#)]. Summarized results are published in [[Vah⁺10](#)], [[Kha⁺12a](#)] and [[Kha⁺12b](#)].

The experimental work and technical maintenance described in this chapter was a collaborative effort of several people from the GEO 600 squeezer team, but special credit must be given to Henning Vahlbruch who built replacement components and was the leading hand in many of the major hardware interventions.

3.1 The GEO 600 squeezer

Many years of development work were necessary to develop sources of squeezed states of light suitable for application in gravitational-wave detectors. About two decades after the first demonstration of squeezing [Slu⁺85], state-of-the-art squeezing experiments were approaching the benchmark level of 10 dB quantum-noise reduction, which was reached in 2007 [Vah⁺08]. At the same time significant progress was made with detecting squeezed light at the low audio-band frequencies targeted for earth-bound gravitational-wave detection (roughly 10 Hz to 10 kHz) [McK⁺04; Vah⁺06; Vah⁺07]. A first demonstration of squeezed-light injection in a large Michelson interferometer with suspended optics, although still outside the gravitational-wave frequency band, was performed at the Caltech 40 m prototype facility [God⁺08].

At the GEO 600 detector, application of squeezed states of light was declared one of the major goals of the *GEO-HF* upgrade programme [Wil⁺06; Doo⁺16]. For this purpose, a squeezed-light source was conceptually designed specifically for use in GEO 600 [Vah08]. The design goals included a compact and transportable setup to fit the limited existing space at the detector facility, high robustness and controllability to enable stable operation over long time scales, and fully automated operation. The squeezed-light source was assembled and characterized by Vahlbruch et al. [Vah⁺10] in a cleanroom lab at the AEI Hannover. It was finished in 2009 [Vah⁺10] and then transported to the GEO 600 site at the beginning of 2010.

The GEO 600 squeezer operates on the principle of optical parametric down-conversion as described in section 2.1.6, where a nonlinear crystal is pumped with light at twice the carrier frequency and placed inside an optical cavity to form the so-called *optical parametric amplifier* (OPA).¹ Figure 3.1 shows the complete layout of the squeezed light source with all its optical subsystems:

- Three **lasers** that are frequency-locked to the main laser of GEO 600 provide the necessary light fields for producing and controlling the squeezed vacuum state.
- **Green pump light** is produced in a second-harmonic generator and then

¹ Often the term optical parametric *oscillator* (OPO) is used instead in cases where no bright carrier field is present to be amplified. For simplicity and consistency with earlier works in our group I will use ‘OPA’ throughout this thesis. Calling it an ‘amplifier’ can be justified by arguing that even without a carrier input field the OPA does still amplify and deamplify the quadrature fluctuations of the vacuum field.

subsequently spatially cleaned and intensity-stabilized.

- The pump field is then sent into the **OPA** to produce the squeezed vacuum field.
- For the control of the squeezing angle **coherent-control** sidebands are generated to travel alongside the squeezed vacuum field.
- An additional **bright alignment beam** can be sent into the OPA to serve as a marker of the OPA output mode for alignment purposes.
- There is also an **on-board balanced homodyne detector** that can be used for the direct characterization of the achievable squeezing performance.

These systems will be discussed in turn in the following sections.

3.2 Auxiliary laser systems and PLLs

The squeezed-light source uses a 2 W master laser and two 200 mW auxiliary lasers. All three are 1064 nm *Mephisto* laser systems [Inn04] made by InnoLight GmbH. The *Mephisto* lasers are Nd:YAG solid-state lasers in an NPRO configuration. They include temperature and pump-current control and an active amplitude-noise suppression (called a *noise eater*). The squeezer's master laser is phase locked to a pick-off of GEO 600's main laser using a commercial PLL system [Inn08] also made by InnoLight (see section 4.2 for an overview of the complete phase control system). Two further PLLs then lock the auxiliary lasers to fixed frequency offsets from the master laser. The common frequency of all four lasers is a free parameter. Additionally, the lasers typically have at least two possible temperature operating points for every given frequency [Inn04]. This gives the freedom to choose the operating points such that multimode operation can be avoided for all four lasers.

The maximum frequency offset that the InnoLight PLLs can reliably lock to is about 120 MHz (specified only up to 50 MHz). For the auxiliary laser that provides the p-polarized (p-pol.) beam for locking the OPA, a larger frequency offset became necessary (see section 3.4). To achieve this, the beat signal of the p-pol. laser with the master laser is additionally demodulated with an externally provided local-oscillator signal before being sent to the PLL. This shifts the beat frequency down and enables locking with a total offset of up to 1.5 GHz.

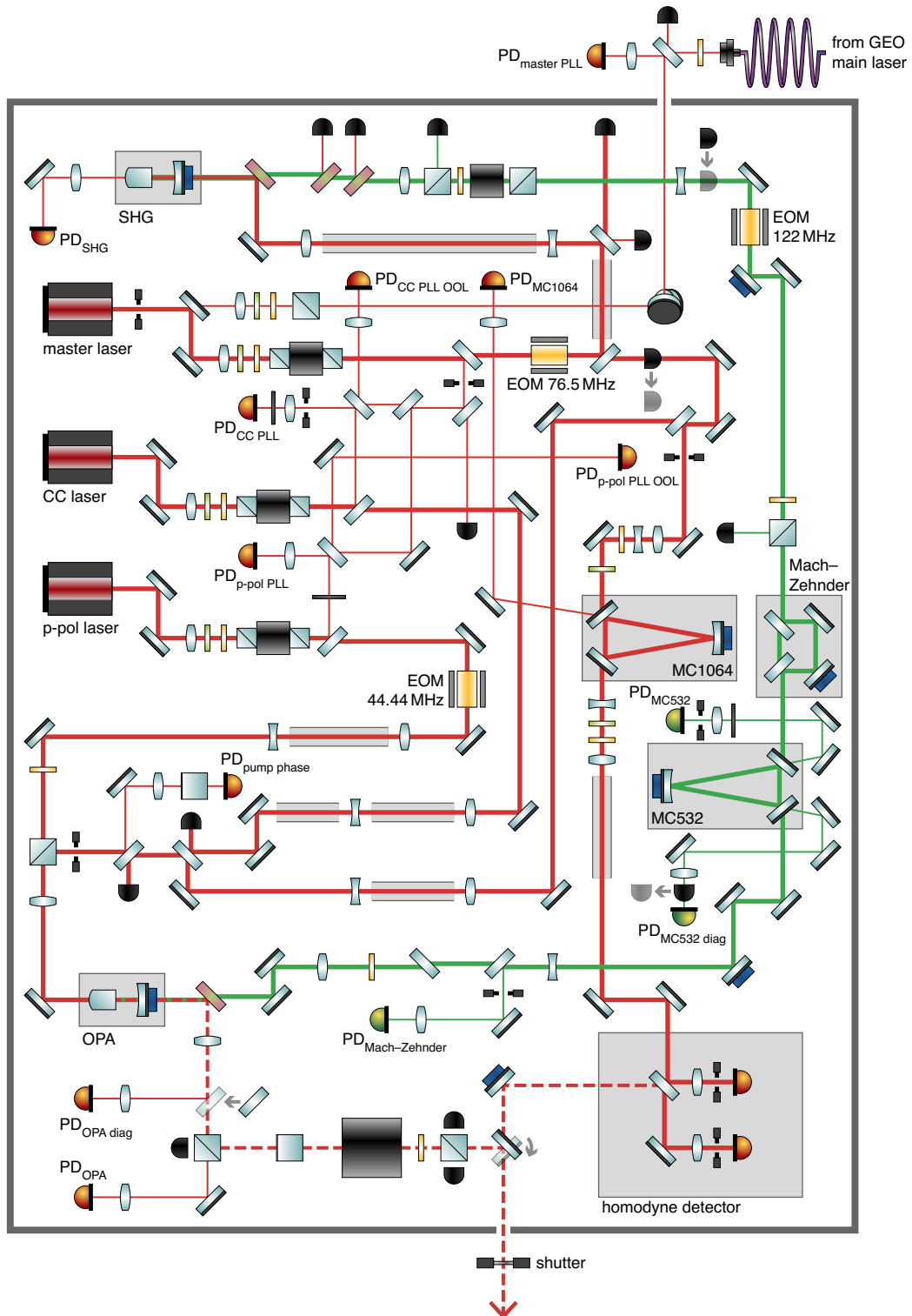


Figure 3.1: Layout of the GEO 600 squeezed-light source. This diagram shows all optics installed on the squeezer breadboard. Since its installation at GEO 600 some minor alterations have been made and shown here is the state as of 2017. The drawing is not exactly to scale, but it shows the correct topology.

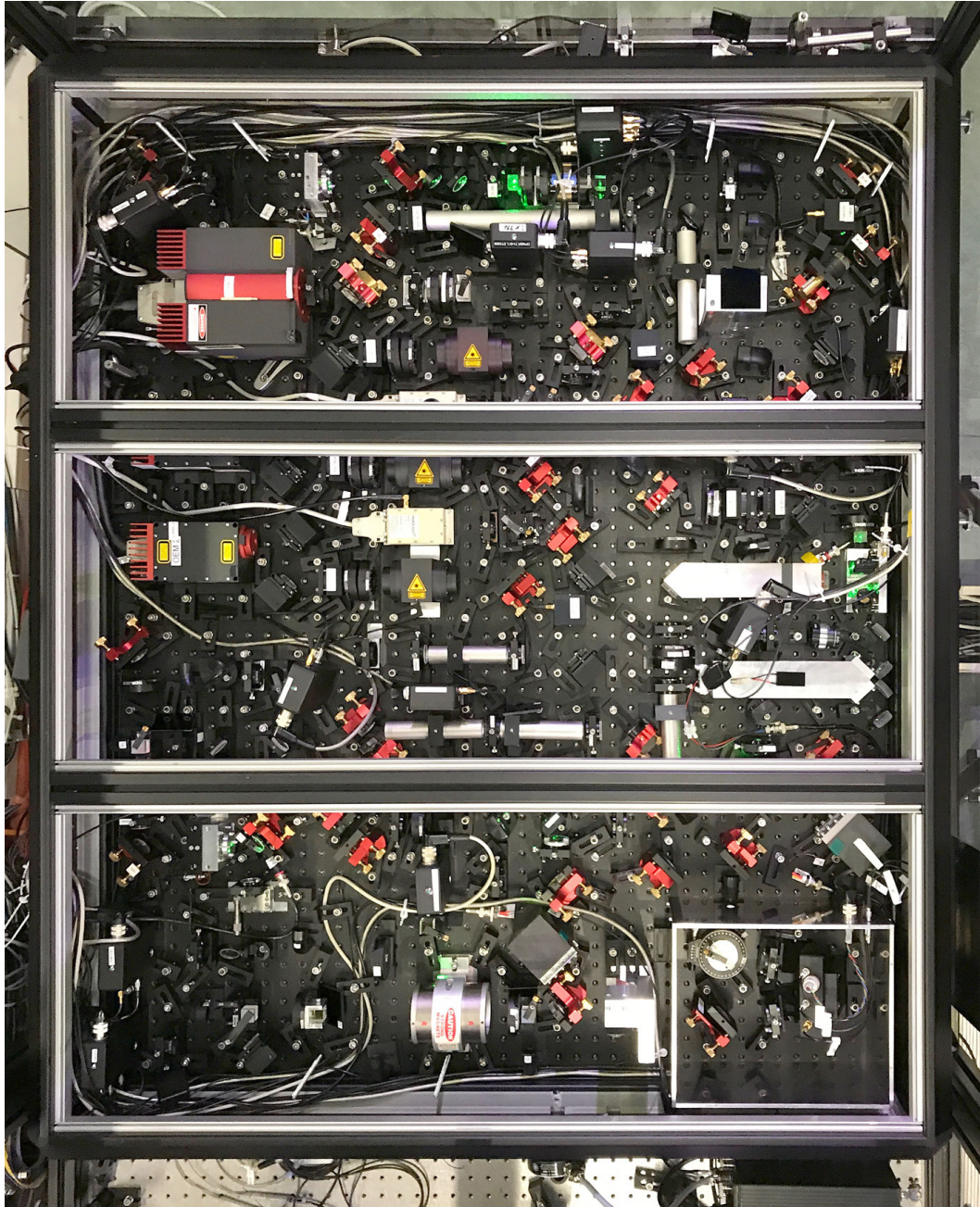


Figure 3.2: Photo of the squeezed-light source. In normal operation the squeezer is shielded from outside influences by opaque covers and an additional acrylic-glass housing over the complete optical bench.

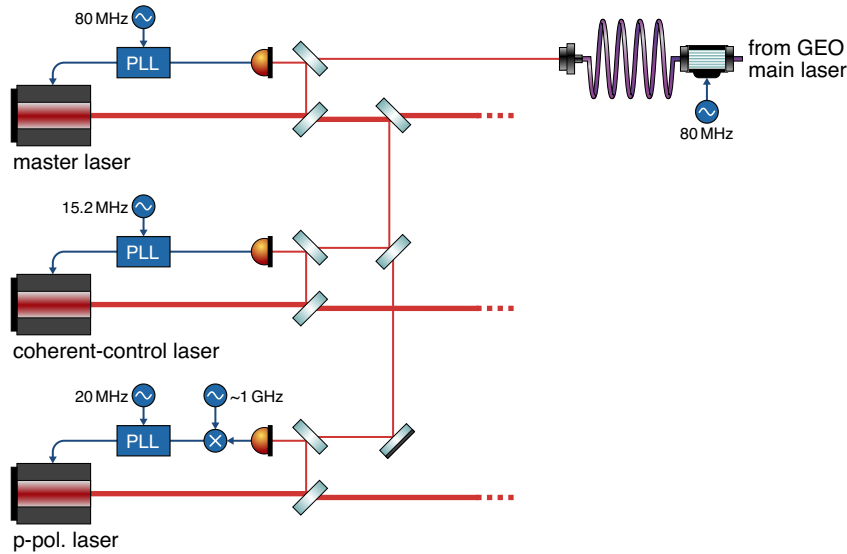


Figure 3.3: Squeezer auxiliary lasers and PLL setup. Three lasers are used in the squeezer setup. The 2 W master laser is phase locked to the GEO 600 laser using a pick-off beam that is sent to the squeezer table via an optical fibre. The other two auxiliary lasers are then phase locked to the master laser. There are additional out-of-loop photodiodes that are omitted here for simplicity.

The three squeezer lasers have been running for a total of over eight years and almost continuously since the installation at the GEO 600 site in 2010.² Over this time span the output power of all three lasers fell by about 30 %, which falls well within the expected degradation due to ageing pump diodes. The process is irreversible and will eventually make it necessary to replace the lasers' pump diodes. So far, however, the degradation could be compensated by a combination of pump-current adjustments and the change of neutral-density filters to keep power levels throughout the system approximately constant. In particular, for the power necessary to pump the second-harmonic generation of the green field, there is still a lot of headroom. A large fraction of the infrared light from the 2 W master laser is dumped in the current setup and can be made available if necessary.

As part of the laser maintenance, the amplitude-stabilization loops were retuned once after about seven years of operation. At this point, increasing the loop gains to compensate for the power degradation lead to a slight improvement of amplitude

² The only short exceptions where the lasers were not running occurred during a few large-scale commissioning activities, such as work inside GEO 600's vacuum system. During such times all laser sources are switched off for safety reasons.

noise at frequencies of about 400 kHz. This was however not critical for the squeezing performance.

The PLL systems include a built-in locking automation that serves to regain lock after an external disturbance without any manual intervention. Only occasionally (on a timescale of once per several months) the PLL slow feedbacks that act on the lasers' temperatures reach the end of their actuation range. In this case manual tuning of the laser temperatures becomes necessary to offload the feedbacks, enabling the PLL to lock again. This happens especially after significant changes of the environmental conditions (like outside temperature) or when maintenance work on GEO 600's main laser causes an overall shift of the carrier frequency.

The auxiliary laser used for creating the coherent-control sidebands sometimes showed instances of transient excess phase noise. This would show up as highly non-stationary noise in the in-loop PLL signal and all dependent control loops, significantly degrading the squeezing performance. We could trace back the root of the problem to the laser source itself. The behaviour was very sensitive to environmental conditions and would often stop temporarily after a change of the laser temperature, pump current, or even with slight mechanical pressure on the laser housing. However, we could not make out a clear pattern and the transient nature of the effect made it hard to study. Multimode operation of the laser was briefly suspected as the underlying mechanism, but could be excluded by changing the operating temperature to intentionally drive the laser into a multimode regime and observing that the problematic behaviour was not reproduced.

Ultimately, since the excess phase noise could not easily be fixed but occurred only sporadically, it was remedied by automatically closing the squeezer shutter at times when it would otherwise negatively influence the detector. For this automation, the in-loop error signals of all three PLLs are monitored and the RMS noise is calculated within the digital control system. The shutter is triggered when the RMS noise level of any PLL crosses twice the nominal level for more than one second. All instances of the anomalous laser behaviour are easily recognized by this automation. Since its implementation in 2016, only 3.5 hours or 0.04 % of squeezed light application were lost due to this effect. Should the problem persist and reach a level where it has a significant impact on the total squeezing time, the best option would be a replacement of the faulty laser.

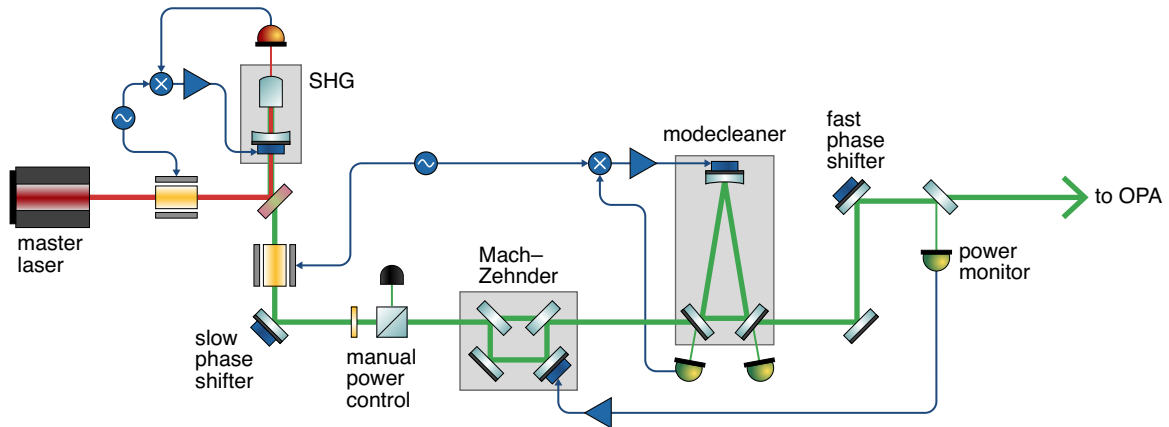


Figure 3.4: Green pump generation and intensity stabilization. The pump field at 532 nm is generated in the SHG. A modecleaner cavity serves to suppress unwanted higher-order spatial modes and reduce high-frequency amplitude and phase fluctuations. The resulting power level sent to the OPA is actively controlled with a Mach-Zehnder interferometer.

3.3 Green pump light

The OPA requires pump light at twice the carrier frequency (corresponding to a wavelength of 532 nm). This is produced from the 2 W master laser in a second-harmonic generator (SHG). For optimal squeezing performance it needs to be amplitude stabilized [Kha⁺12a] and cleaned of any contributions from higher-order spatial modes and sideband fields. Figure 3.4 illustrates the path of the pump light and the relevant control loops.

One of the major challenges in the long-term operation of the GEO 600 squeezed-light source proved to be maintaining a high level of available pump power. Several degradation processes led to a generally declining power level and needed to be addressed regularly.

3.3.1 SHG

The second-harmonic generator consists of a nonlinear crystal made from 7% magnesium-oxide-doped lithium niobate (MgO:LiNbO₃) placed inside an optical cavity. The cavity has a finesse of nominally $\mathcal{F} \approx 60$ for the infrared light and negligible finesse for the green light due to a dichroic coupling mirror. The cavity length is stabilized to maintain resonance using the Pound–Drever–Hall control scheme [Dre⁺83]

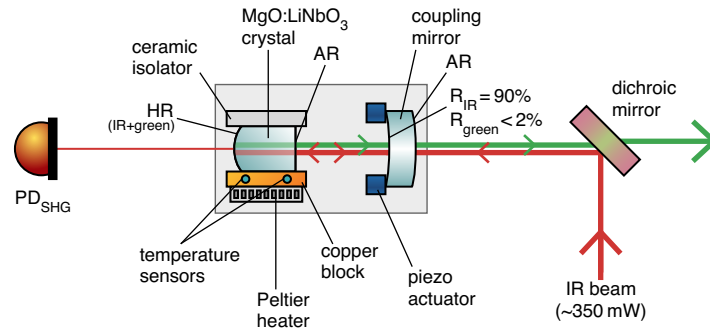


Figure 3.5: Schematic cross section of the SHG cavity.

with the error signal taken from a photodiode in transmission of the SHG. Also, the crystal temperature is actively controlled to ensure matching propagation phases of the infrared and green fields for high conversion efficiency [McK08]. The SHG is constructed as a very compact, almost fully enclosed structure, providing high mechanical stability and shielding against environmental influences like air currents. Figure 3.5 shows a schematic cross section of the cavity assembly. The nominal output power of the SHG is slightly above 100 mW of green light.

One standard maintenance task for the SHG is the occasional manual tuning of the temperature setpoint. The temperature control already serves to counteract the major part of all environmental changes. However, temperature gradients lead to a small variable offset between the temperature at the sensor and in the middle of the crystal. Undisturbed, this offset drifts slowly over the timespan of a few months, at which point a manual retuning helps to restore the conversion efficiency. More importantly, the temperature also needs to be newly set after changes of the laser frequency of GEO 600's main laser. The tuning can either be done by minimizing the amount of unconverted infrared light in transmission of the SHG, or, more directly, by maximizing the green output power on one of the downstream photodiodes. The latter proved to be the more reliable method. The tuning process needs to be done slowly because the time until the complete system reaches thermal equilibrium is significantly higher than the settling time of the temperature-stabilization loop itself.

Another infrequent maintenance task is to correct for slow alignment drifts. The experience was that over a timespan of several months, such drifts would reduce the overlap of the infrared beam with the SHG eigenmode by a few percent. The alignment can be checked by scanning the cavity length and observing the transmitted power. Higher-order transverse modes due to misalignment show up as additional

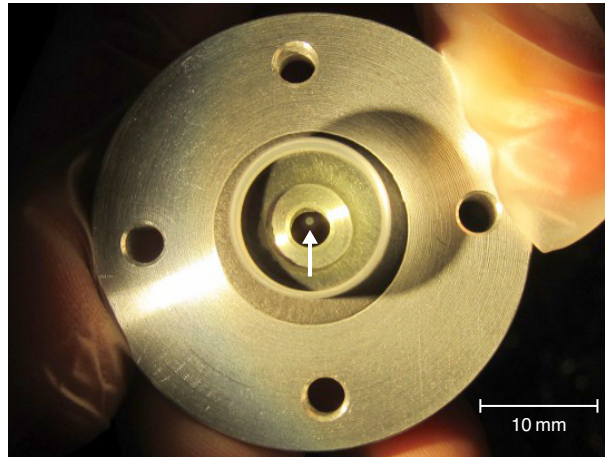


Figure 3.6: Photo of the degraded SHG coupling mirror. A small white spot is visible right at the centre (marked with an arrow) where the beam hits the optical surface. The discolouration had a slightly annular shape, which is consistent with other reports of laser-induced contamination [Wag14].

resonance peaks in such a mode scan and the alignment can be tuned by minimizing the misalignment peaks. For coarse alignment (for example after work on the SHG) it can be helpful to ensure a correct phase-matching temperature during the scan. In this way visible green light is generated and can be used to judge the alignment by eye. For fine alignment it is better to offset the temperature so that the second-harmonic generation is suppressed and does not influence the infrared mode scan.

Apart from temperature and alignment drifts, there was another more severe degradation process of the SHG: In 2013, over three years into its operation, we noticed that the SHG's conversion efficiency was slowly declining from 53% during the initial characterization to only 24% at that point. The reduced efficiency was linked to a lowered cavity finesse, indicating excess losses inside the cavity. We replaced the coupling mirror with a new one and found that this restored the old performance completely, suggesting that the extra loss was completely localized to the coupling mirror itself. Optical inspection of the mirror surface showed a white surface discolouration at the location where the light hits the cavity-facing side of the mirror. Figure 3.6 shows a photograph of the degraded mirror after removal.

After the first replacement of the coupling mirror the SHG efficiency stayed constant for a while and then started to degrade again, this time at a much faster rate. At this point, regular replacements became necessary, on average every three months. Figures 3.7 and 3.8 illustrate the SHG power trend over several years.

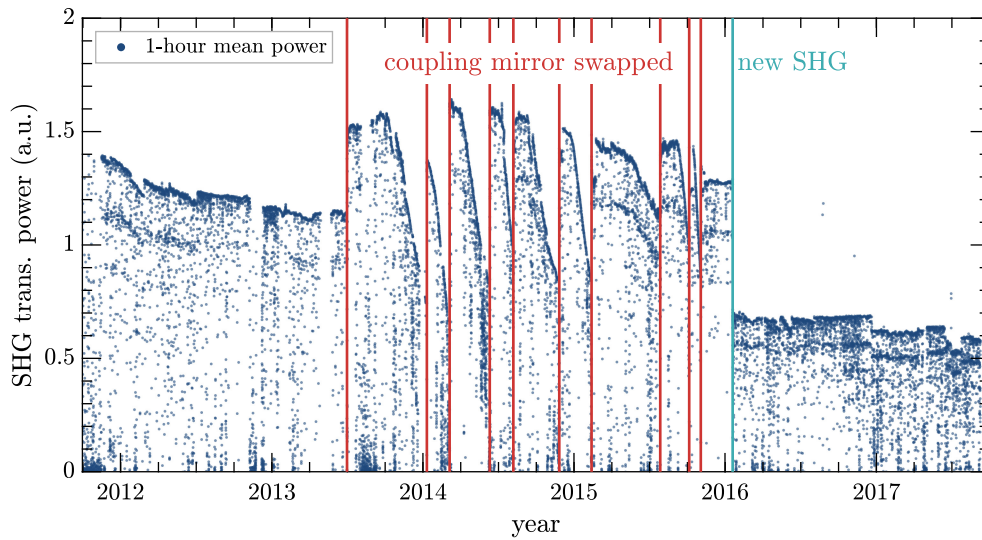


Figure 3.7: SHG power over the years. Shown here is the amount of DC infrared power measured by the photodiode in transmission of the SHG. This is a direct measure for the circulating infrared power and thus the cavity finesse. After a slow decline over the first years of operation, a replacement of the coupling mirror restored old performance. Afterwards a more rapid degradation was observed, requiring the installation of a new cleaned mirror a further nine times. Finally at the beginning of 2016 a completely new SHG was installed, which stopped the strong degradation. The lower power level for the new SHG is due to a changed transmissivity of the crystal's highly reflective coating and does not indicate lower circulating power.

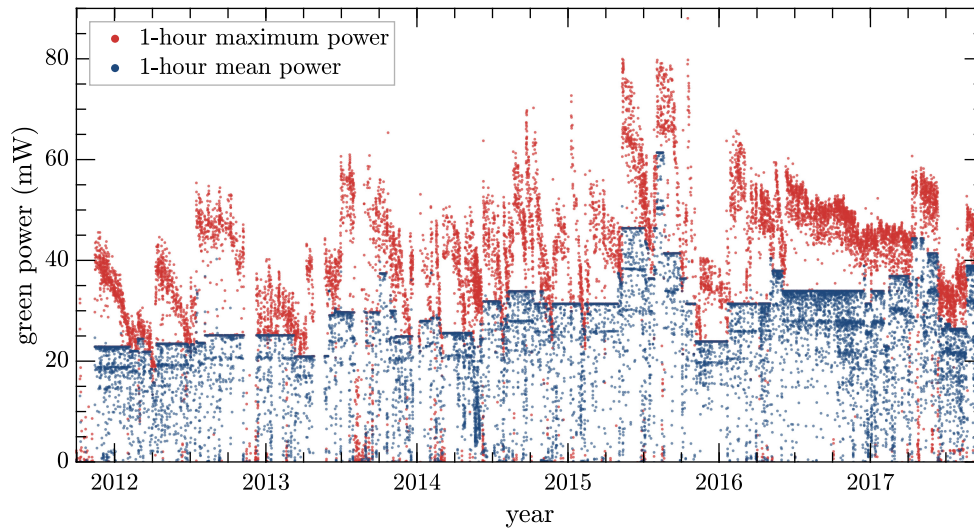


Figure 3.8: Green pump power over the years. This graph shows the level of the green pump power at the pick-off right before the OPA. The y-axis is calibrated to the corresponding power impinging on the OPA. The pump power level is mostly controlled to a fixed level, but during each relock the Mach-Zehnder interferometer is shortly driven to maximum transmission. The recorded maximum levels can therefore be used as an indication of the total available green power (but note that this does not include the power dumped at the manual power control). There is a general downwards trend visible, interspersed by frequent sharp increases whenever adjustments were made. The setpoint for the green power was adjusted throughout the years to accommodate for a changing efficiency of the OPA (see section 3.4) and changing levels of phase noise or backscattering (see chapter 4). The pump power level was also sometimes temporarily lowered below the optimum setting when low available power meant that stable locking would otherwise not be possible.

3.3 Green pump light

It was found that the discoloured spot on the optic could be wiped off with acetone, bringing the mirror back to its old performance. This means that some material was deposited superficially and no damage was caused in the coating or bulk of the mirror itself. The fact that only the coupling mirror, but not the cavity-facing facet of the nonlinear crystal was affected³ strongly suggests that the impinging green light was responsible for the deposition process. If there are contaminants inside the SHG enclosure the radiation pressure of the green light can push them away from the crystal facet and towards the coupling mirror. It was tested whether reducing the amount of green power by intentionally offsetting the phase-matching temperature would slow down the degradation process, but this led to no clear change of the rate of decline.

Contamination effects very similar to our own observations are described in the literature from the field of space-based laser optics [Can04; Wag14; Kok⁺17]. The phenomenon is described as *laser-induced contamination*: Molecules in the laser beam are both ionized and pushed towards the optic by the interaction with the high-energy light field and thereby deposited on the surface. The exact mechanisms are multi-faceted and still a subject of active research. Laser-induced contamination is reported mostly for short laser wavelength (green to ultraviolet) and high-intensity beams. It is seen especially in the presence of organic material in enclosed spaces, where outgassing can lead to high partial pressures of the contaminants. Open assemblies that are well ventilated or exposed to vacuum are assumed to be less affected.

Most materials used in the construction of our SHG are not expected to outgas significantly. The most likely candidates for the observed contamination are either thermal paste or a vacuum grease (used in the assembly because it increased the convenience during alignment of the part that holds the coupling mirror). The most plausible scenario is that over time outgassing molecules from the vacuum grease were deposited on the coupling mirror by the green-light-induced contamination process. During the mirror replacements the greased parts were moved, possibly exposing the inside of the SHG enclosure to more vacuum grease, which would explain the much faster degradation after the first replacement.

Eventually, at the beginning of 2016 we replaced the complete SHG with a new one

³ If there was a damage of the crystal surface it is possible that replacing the coupling mirror slightly changed the alignment of the cavity mode, thus avoiding the previously damaged spot. However, the many replacements of the mirror always restored most of the old performance and it is unlikely that old damages would have been avoided each time.

constructed specifically without any vacuum grease and thermal paste. Since then the obvious degradation of the SHG is halted. In 2017, after the new SHG had been in operation for 19 months, an unexpectedly low output power triggered another check of the coupling mirror. This time, no signs of new contamination were found.

Other experiments often use potassium titanyl phosphate (KTiOPO_4) instead of lithium niobate for second-harmonic generation, achieving significantly higher conversion efficiencies. These experiments also often report degrading SHG performance [e.g. Lia⁺04; Mei11; Kha11]. In those cases, however, the degradation was mostly attributed to bulk defects of the nonlinear crystal itself, such as *grey tracking* [Bou⁺99]. In comparison, the surface degradation we observed is much easier to fix. Green-light-induced contamination might become a serious consideration again in doubly resonant nonlinear cavities [e.g. Vah⁺16], where significant amounts of green light are also impinging on the crystal surface which might be harder to clean or replace. There especially, care must be taken to avoid possible contaminants.

3.3.2 Modecleaner for the green pump light

A triangular high-finesse ring cavity serves to clean the green beam by mainly transmitting the fundamental mode. Apart from suppressing the unwanted higher-order transverse modes of the beam, the modecleaner also reduces high-frequency amplitude and phase fluctuations and removes the control sidebands that could otherwise degrade the squeezing performance. Like the SHG, the modecleaner is controlled with the Pound–Drever–Hall locking scheme, this time with the error signal generated in reflection of the cavity.

The modecleaner has a finesse of nominally $\mathcal{F} = 562$. This means that, when locked on resonance, several watts of green light are circulating inside the cavity. Therefore one might expect to see similar or even stronger degradation effects than with the SHG. And indeed, this was the case: The initially installed modecleaner deteriorated over the timespan of two years, at which point its power transmissivity had fallen from 97% to only 47%. This corresponded to an internal loss of roughly 0.5% or 5000 ppm compared to the nominal value of 150 ppm. It is interesting to note that a similar degradation of an almost identical modecleaner for green light was also observed by Meier [Mei11]. There, a much higher circulating power of 400 W was used and the cavity performance fell sharply after only 250 hours.

In both cases the degraded modecleaners had used vacuum compatible glue to fix the mirrors to the spacer. This appears to be the most likely source of contamination.

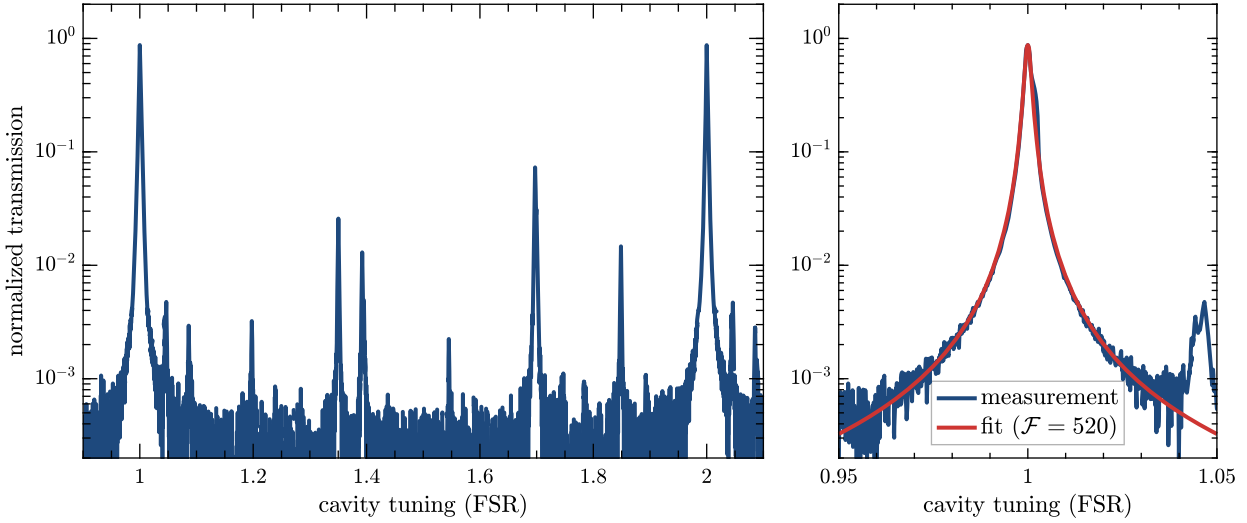


Figure 3.9: Mode scan of the green modecleaner cavity. The left panel shows a scan over one free spectral range. Nonlinearities of the piezo actuator have been corrected. The right panel shows a magnified view of the fundamental peak, together with the fitted model used for determining the cavity finesse.

For the GEO 600 squeezer a new modecleaner was built with identical specifications, but this time avoiding the glue by clamping the mirrors in place. With this, the degradation was significantly slowed, but not completely eliminated.

The new modecleaner was characterized about four years into its operation, when the transmissivity had slightly fallen to about 83%. For this, I performed detailed mode scans of the cavity (see figure 3.9). These scans showed a cavity finesse for the fundamental mode of $\mathcal{F} = 520 \pm 10$. A numerical model (using the interferometer-modelling software FINESSE [Fre⁺04; Fre14]) showed that this indicated internal losses of (1050 ± 230) ppm, which is also compatible with the observed reduction of transmissivity (see figure 3.10). I additionally determined the finesse for the first- and second-order transverse modes. It was expected that a localized loss due to dirt accumulation at the centre of the beam might lead to a mode-dependent effect on the finesse. However, this could not be confirmed within the limits of the measurement uncertainty.

Two of the three modecleaner mirrors are hit off-centre by the beam. By turning those mirrors in their fixture, we could expose a new spot of the mirror to the beam. (The spot size is small enough that there is no overlap.) Doing so improved the finesse to $\mathcal{F} = 550 \pm 10$, indicating a reduction of the internal losses to (390 ± 200) ppm, or very roughly one third of what they had been before. This confirms that the excess

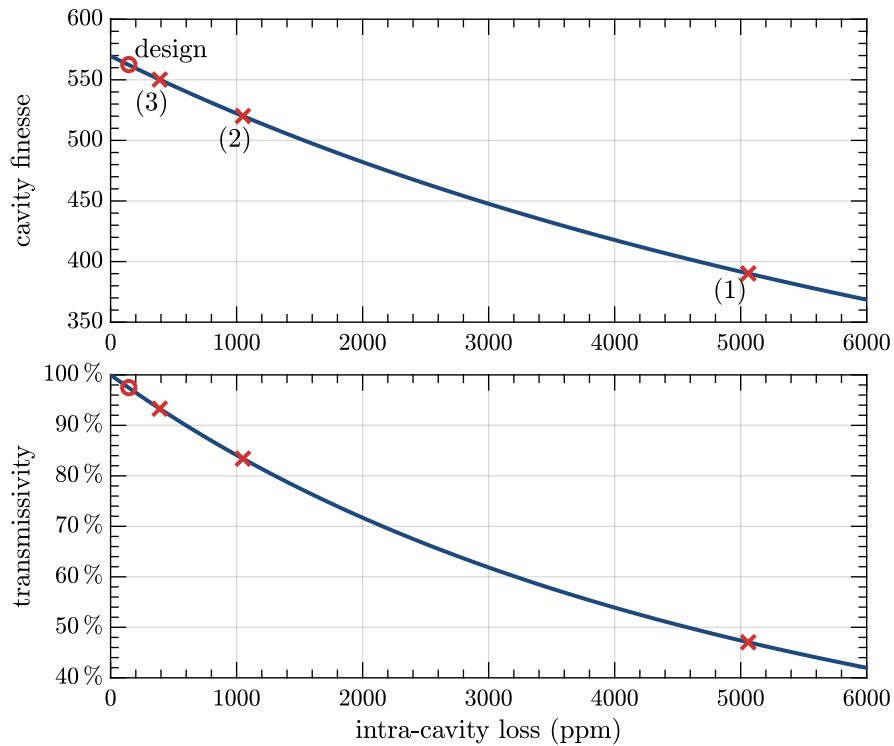


Figure 3.10: Finesse and transmissivity of the green modecleaner as a function of internal losses. The red crosses mark the values determined at different points over the last years: **(1)** is the severely degraded first modecleaner after two years of operation. **(2)** is the new modecleaner after four years of operation. **(3)** shows the improved performance of the second modecleaner after turning the coupling mirrors. This plot is based on a numerical simulation of the cavity in FINESSE.

losses were again localized to only the exposed part of the mirror surfaces.

The fact that we still observed a slight degradation for the cavity without any obvious organic contaminants (though at a much slower rate than when using glue), indicates that laser-induced contamination effects might not be avoidable completely in future long-term applications. However, as long as maintenance interventions are only required every few years, this does not pose a significant issue.

3.3.3 Power control with a Mach–Zehnder interferometer

In the presence of the described degradation processes it is essential to actively control the level of green pump power sent to the OPA. A compact Mach–Zehnder interferometer is used as the actuator, which can vary its transmitted power depending on the selected operating point. It is placed before the modecleaner, so that any beam imperfections it could introduce are filtered out. The power monitor used for the control is placed after the modecleaner at a pick-off close to the OPA, so as to sample the power going towards the OPA as closely as possible (see figure 3.4).

For effective and stable control the Mach–Zehnder interferometer needs some headroom and cannot be operated too close to its transmission maximum or minimum. Operation at roughly the middle of the fringe is ideal. There is a manual power control unit consisting of a half-wave plate and a polarizing beamsplitter where excess green power can be dumped (also to protect the photodiodes). At times when the total available power level is low, the Mach–Zehnder interferometer can be controlled up to about 85% transmissivity. Beyond that, stable locking is no longer ensured and fluctuations lead to frequent lock losses.

The compact design of the Mach–Zehnder interferometer [Kha11] makes it inherently quite stable. Only a few realignments were necessary over the years, mostly when work on the modecleaner changed the overall beam path. The alignment can be tuned very precisely by consecutively blocking the two interferometer paths and aligning the remaining beam to the modecleaner cavity.

3.4 Optical parametric amplifier

The actual squeezed-light source itself is formed by the OPA. This nonlinear cavity is similar to the SHG, but uses periodically poled potassium titanyl phosphate (PPKTP) as the nonlinear medium. Figure 3.11 shows the OPA cavity together with

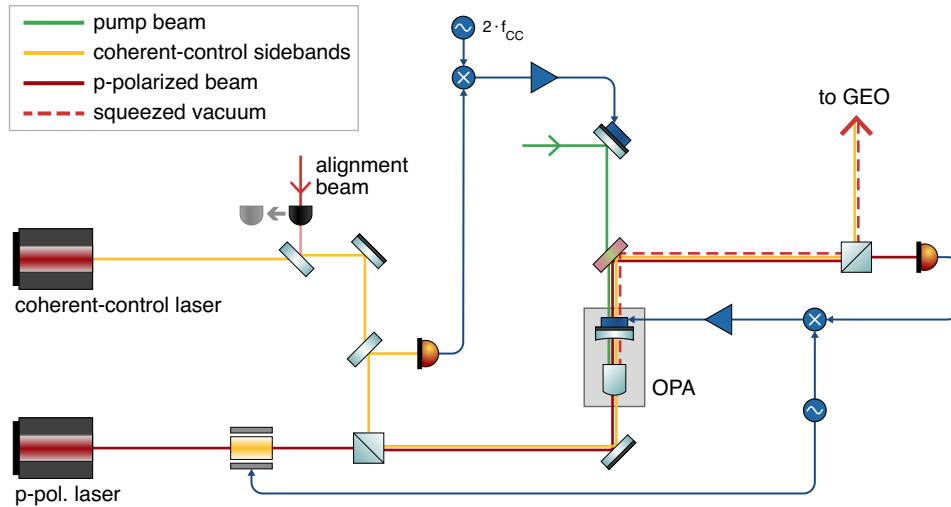


Figure 3.11: Diagram of the OPA and surrounding beam paths. The OPA cavity is pumped with the green pump field through the coupling mirror. The cavity length is stabilized with a p-polarized beam injected from the backside. The coherent-control field is phase-locked to the pump and serves as a phase reference for the squeezed vacuum field. For diagnostic purposes an additional bright alignment beam can be injected into the OPA.

all impinging light fields.

Similar to the SHG, the OPA has a nominal finesse of $\mathcal{F} = 75$ for infrared light and very low finesse for the green pump light. The cavity length is stabilized using a beam in the p-polarization, orthogonal to the polarization of the generated squeezed-vacuum field.

3.4.1 Bright alignment beam

The squeezed vacuum field generated in the OPA contains only a tiny amount of photons which can generally not be detected on a photodiode and therefore cannot be used for aligning the OPA. In order to mark the OPA's fundamental mode, we need to inject a bright light field at the carrier frequency. For this purpose there is a dedicated alignment beam that is a pick-off from the master laser and that is injected into the OPA through the highly reflective back-surface of the crystal. This beam is normally blocked but can be unblocked during commissioning and maintenance work. The bright alignment beam is crucial for several different alignment tasks:

3.4 Optical parametric amplifier

The light can be used to drive the OPA as a second-harmonic generator. The green light emitted from the OPA then travels backwards along the pump light path and can be used to align the modecleaner and OPA relative to each other with a mode scan of the modecleaner cavity.

The bright alignment beam that is transmitted through the OPA shares the same mode as the squeezed vacuum field and thus travels along the same path and will experience the same losses. As such, it is important for alignment when using the on-board balanced homodyne detector (see section 3.5) or when aligning and mode-matching the squeezed light source to GEO 600, and it is instrumental in characterizing the injection path, as is described in chapter 4.

If the OPA is pumped with second-harmonic light, the bright alignment field will experience classical amplification or deamplification by the parametric gain [McK08]

$$g(P_{\text{pump}}) = \frac{P_{\text{trans}}(P_{\text{pump}})}{P_{\text{trans}}(P_{\text{pump}} = 0)} = \frac{1 + \frac{P_{\text{pump}}}{P_{\text{thres}}} + 2 \cos(\phi) \sqrt{\frac{P_{\text{pump}}}{P_{\text{thres}}}}}{\left(1 - \frac{P_{\text{pump}}}{P_{\text{thres}}}\right)^2} \quad (3.1)$$

where P_{pump} is the pump power and ϕ is the relative phase of the pump field. For $\phi = 0$ the seed field is amplified and for $\phi = \pi$ it is deamplified. The threshold power P_{thres} is a characteristic property of the OPA cavity that depends on (among other things) the nonlinear coupling and the cavity-internal losses. The threshold power determines how much pump power is needed to reach specific levels of squeezing and antisqueezing. Measuring the parametric amplification of the bright alignment beam with different pump-power settings can be used to determine the threshold power (see section 3.4.4).

Seen from the backside where the bright alignment beam is injected, the OPA cavity is highly under-coupled and only a small fraction of the light field is transmitted. In our setup, the power of the bright alignment beam after the OPA was a few hundred microwatts. In some cases higher beam powers were desirable to make the detection of the beam easier. For this, pumping with green light was a relatively easy way to temporarily boost the usable power by about one order of magnitude. We developed a technique where we locked the pump phase to hold the infrared output power at a constant level, thus additionally stabilizing the bright alignment beam for improved loss measurements.

3.4.2 Coherent-control field

One major development that allows for the detection and control of true squeezed vacuum fields is the *coherent-control scheme* [Vah⁺06; Che⁺07; Che07]. High-frequency squeezing experiments often use bright squeezed states, but at low frequencies a bright field would generally spoil the squeezing performance by introducing technical noise. So, in order to detect low-frequency squeezing, no bright field at the carrier frequency should be present. Instead, sideband fields can be sent along with the squeezed vacuum to generate phase- and alignment-control signals.

The coherent-control auxiliary laser provides a single sideband, offset against the carrier by the angular sideband frequency $+\Omega = 2\pi f_{\text{CC}}$. This light field is injected into the OPA from the backside (see figure 3.11) where it interacts with the green pump light. The input electric field can be written as

$$E_{\text{in}}^{\text{CC}}(t) \propto \alpha_{\text{CC}} e^{i(\omega_0 + \Omega)t + i\phi_{\text{CC}}}, \quad (3.2)$$

with amplitude α_{CC} and phase ϕ_{CC} . The nonlinear squeezing interaction in the OPA converts this to a field [Che07]

$$E_{\text{out}}^{\text{CC}}(t) \propto \sqrt{2} \cosh(r) \alpha_{\text{CC}} e^{i(\omega_0 + \Omega)t + i\phi_{\text{CC}}} + \sqrt{2} \sinh(r) \alpha_{\text{CC}} e^{i(\omega_0 - \Omega)t - i\phi_{\text{CC}} - 2i\theta}, \quad (3.3)$$

where r and θ are the squeezing parameter and phase as defined in section 2.1.6. This means that a second sideband at frequency offset $-\Omega$ is created. The process is called *difference-frequency generation*. Intuitively it can be understood as green photons at frequency $2\omega_0$ splitting into two photons at $\omega_0 + \Omega$ and $\omega_0 - \Omega$. Both sidebands increase in amplitude with increasing parametric gain and the relative amplitude imbalance

$$\frac{\cosh(r) - \sinh(r)}{\frac{1}{2}(\cosh(r) + \sinh(r))} = 2e^{-2r} \quad (3.4)$$

decreases. At typical parametric gains, some imbalance remains (e.g. 6% for 15 dB of parametric gain).

In order to use the coherent-control sidebands as a phase reference for the squeezed vacuum field, the phase between the sidebands and the pump field needs to be constant. For this we detect the beat of the two sidebands leaking out through the backside of the OPA on a single photodiode. Demodulating at the beat frequency $2f_{\text{CC}}$ with an appropriate demodulation phase gives a signal [Che07]

$$i_{\text{CC}} \propto \sinh(2r) \alpha_{\text{CC}} \sin(2\theta - 2\phi_{\text{CC}}). \quad (3.5)$$

Driving this signal to zero by acting on the pump phase thus fixes the phase relation between pump and coherent-control sidebands. For the GEO 600 squeezer, the achieved control bandwidth is 7 kHz. The green pump phase is controlled by a combination of two piezo actuators: A slow actuator with large range is located in front of the green modecleaner so that misalignments caused by the large deflection are suppressed. A faster low-range actuator is placed between the green modecleaner and the OPA. In principle it would also be possible to instead shift the phase ϕ_{CC} of the single coherent-control sideband. Phase actuation with arbitrarily large range could be achieved here by actuating on the laser frequency via the local oscillator of the respective PLL.

The use of the coherent-control sidebands for phase and alignment control of the squeezed field to the interferometer is then described in detail in sections 4.2 and 4.3 of the next chapter.

3.4.3 Phase matching

For efficient parametric amplification in the OPA two different phase-matching conditions must be met: Firstly, the cavity is locked on resonance using the p-polarized beam but also needs to be resonant for the main s-polarized carrier field. The PPKTP crystal is birefringent and so, in general, a frequency offset needs to be applied to the p-polarized laser in order to achieve co-resonance. Secondly, the propagation phases of the second-harmonic pump and the fundamental carrier field need to be matched [McK08]. This is achieved by changing the crystal temperature. However, the crystal temperature also affects the birefringence, making the two phase-matching conditions inherently coupled. The matter is further complicated by the fact that through residual absorption the pump beam locally heats up the crystal, which can only be partially compensated by the active temperature control. Therefore, the phase matching is different for different pump-power levels and will change over time if the absorption is increased through degradation effects. Finally, common changes of the laser frequencies involved will also affect the phase matchings.

Between the OPA temperature and the p-pol. frequency offset, the temperature is the more critical parameter when it comes to compensating for typical environmental fluctuations. To maintain a high parametric gain, the temperature setpoint was tuned in a semi-automatic procedure about once a week. Benefits from retuning the p-pol. frequency offset were only observed after months of operation, or after significant changes of the pump power.

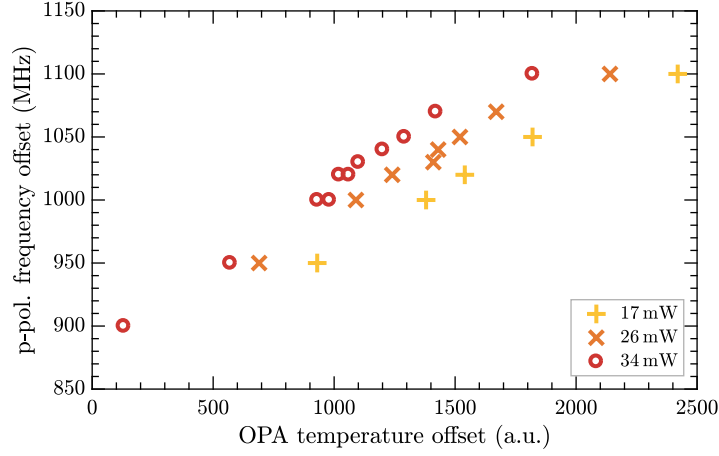


Figure 3.12: Optimal frequency offset of the p-pol. laser as a function of OPA temperature. For each data point the frequency offset and crystal temperature were tuned to achieve co-resonance of the p- and s-polarized fields inside the OPA. The measurement was repeated for three different pump power levels. Higher pump powers require lower temperature offsets to compensate for the local heating due to pump absorption.

Imperfect phase matching only decreases the efficiency of the nonlinear process and thus can in principle be compensated by higher pump powers to still achieve the same squeezing performance. Ideally, a squeezing application should always have the ability to generate more parametric amplification than is actually needed. Realistically, however, we often did operate close to the maximum achievable parametric gain and were sometimes limited by it, so that good tuning of the phase matching was essential.

3.4.4 Measuring the parametric gain

There are several different figures of merit for optimizing the OPA’s parametric gain: The classical amplification and deamplification can be measured by injecting the bright alignment beam and observing the output power as a function of pump power and phase (see equation 3.1). Another method is to measure the amplitude of the beat of the two coherent-control sidebands (equation 3.5). This can lead to slightly different results because it samples the gain not at the carrier frequency, but (asymmetrically) at the two coherent-control sideband frequencies. The difference is small, however, since the coherent-control frequency (15.2 MHz) is within the OPA’s bandwidth (about 60 MHz). If desirable, both measurement methods can be made independent of the p-pol. co-resonance condition by not locking the OPA length, but

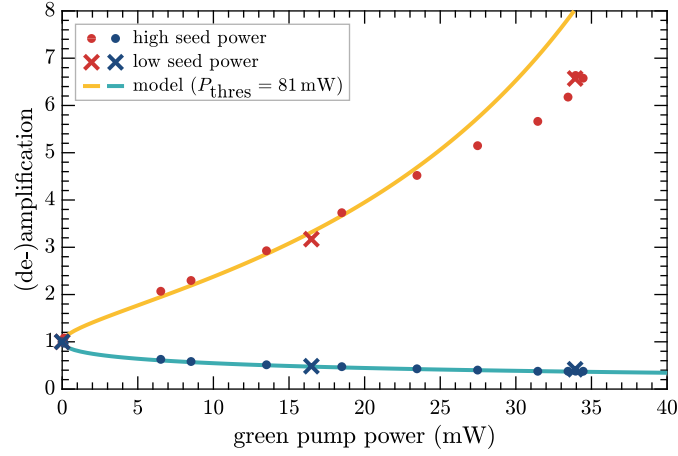


Figure 3.13: Parametric amplification and deamplification of the bright alignment beam as a function of green pump power. For each data point the OPA temperature was optimized to achieve good phase matching. A best-fit model is shown for pump powers below 20 mW. At higher pump powers the measured values start to deviate increasingly from the model. Two different seed powers of the bright alignment beam were used in order to test whether the amplification is affected by pump depletion, which does not appear to be the case.

scanning it slowly and observing the maximum amplification.

In several measurements of the parametric gain with varying pump powers it was observed that the amplification and deamplification deviated from the model predictions. For high pump powers the gain was lower than expected (see figure 3.13). Depletion of the pump field was excluded as the underlying reason by significantly reducing the seed power. A possible explanation is that the heating of the nonlinear medium by the pump beam degrades the phase matching. The overall temperature change was already compensated in these measurements, but high pump powers will create an increasingly strong temperature gradient across the beam width. This will lead to a situation where the phase matching condition can only be met for some part of the beam profile, reducing the overall efficiency. Similar thermal dephasing effects are reported by Meier for the case of high-power SHGs [Mei11]. The observed deviations from the model appeared more pronounced in later measurements, possibly indicating an increase of absorption.

The most direct way to judge the parametric gain is to measure the resulting squeezing and antisqueezing. For frequencies far below the OPA bandwidth and initially neglecting imperfections, the squeezing ratio as a function of pump power is

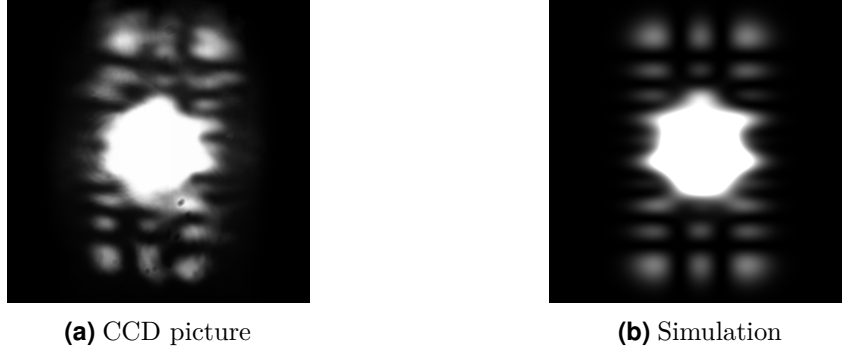


Figure 3.14: Output mode of the damaged OPA. After about four years of operation, the OPA showed a deformed mode shape with a clear TEM_{29} contribution. The left panel is a CCD picture of the beam exiting the OPA. The right panel is a qualitative simulation showing how scattering into higher-order modes inside the cavity can lead to a comparable beam shape if eleventh-order modes are co-resonant with the fundamental. The picture used an uncalibrated CCD and is intentionally overexposed in the centre in order to better resolve the outer mode shape. In a separate measurement it was determined that the higher-order modes made up about 8% of the total beam power.

given by [McK08]

$$R_{\pm}(P_{\text{pump}}) = \left(\frac{1 \pm \sqrt{P_{\text{pump}}/P_{\text{thresh}}}}{1 \mp \sqrt{P_{\text{pump}}/P_{\text{thresh}}}} \right)^2. \quad (3.6)$$

The effects of losses and phase noise can be added to the model as described in section 2.2 of the previous chapter. Like for the amplification of the bright beam, deviations from the model are to be expected for high pump powers.

3.4.5 OPA cavity degradation

Over the years, the performance of the OPA cavity degraded. The initial characterization indicated a threshold power of 61 mW, but it was found to have increased to over 100 mW after about four years of operation. At the same time the cavity finesse was lowered from 75 to roughly 60. Like for the SHG, we replaced the coupling mirror of the OPA, but achieved no improvement and found no sign of contamination on the old mirror's surface. In contrast to the case of the SHG, in the OPA green light is also travelling towards the cavity-facing surface of the crystal. If there were laser-induced contamination, it would also have been on the crystal surface, which we did not check.

3.5 On-board balanced homodyne detector

However, more importantly, further investigations of the degraded OPA revealed that its output mode (visible by letting the bright alignment beam resonate inside the OPA) was distorted. In addition to the fundamental TEM_{00} beam there was a significant contribution from a very high-order transverse mode that was very similar to TEM_{29} (see figure 3.14). We attribute this beam distortion to scattering into higher-order modes inside the cavity due to a damaged crystal. The particular mode visible at the output was most likely dominant because it happened to be co-resonant with the fundamental.⁴ The distortion observed for the bright beam acted as a loss mechanism for the squeezed vacuum field and degraded the squeezing significantly. As a consequence, the complete OPA cavity was replaced with a new one at the end of 2013, restoring old performance.

3.5 On-board balanced homodyne detector

Part of the GEO 600 squeezer assembly is a balanced homodyne detector on the same optical breadboard. It takes its local oscillator signal from a pick-off of the master laser which is additionally filtered with a modecleaner (very similar to the green-pump modecleaner). The homodyne detector was important for the construction and initial characterization of the squeezer before and during its installation at GEO 600. In the later operation, it also served as a diagnostic tool. Figure 3.15 shows an example measurement that was done to confirm the improved performance after the replacement of the damaged OPA.

Switching between sending the squeezed field towards the interferometer or towards the homodyne detector requires careful realignment each time and re-establishing a high homodyne visibility was not always easy. As such, homodyne detection was used sparingly. For most maintenance and characterization tasks, measuring the squeezing level directly as it is applied to the interferometer is preferable to using the on-board homodyne detector. However, by eliminating the influence of most of the injection path, use of the homodyne detector can help when characterizing the performance of the OPA specifically.

⁴ A FINESSE simulation based on the known properties of the cavity confirmed this, but the parameter uncertainties are relatively high.

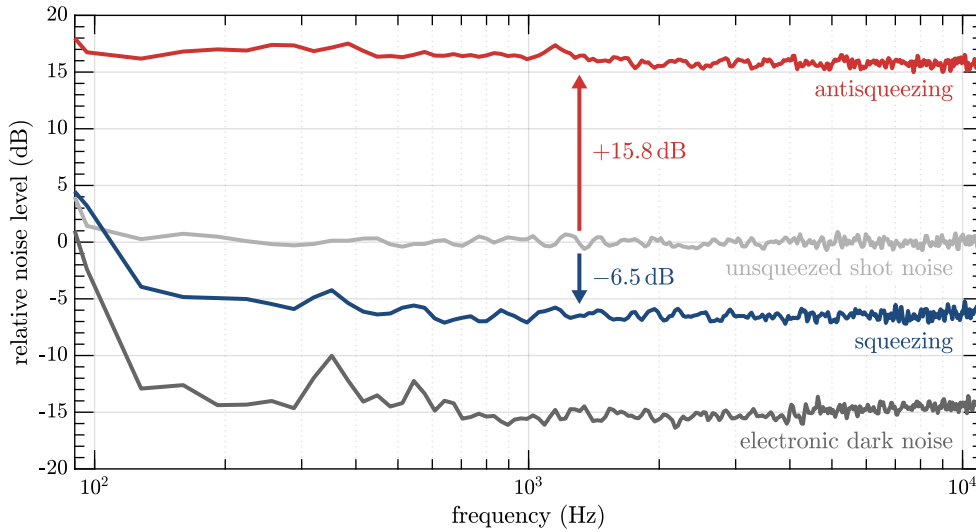


Figure 3.15: Balanced homodyne measurement of the GEO 600 squeezed-light source shortly after installing the replacement OPA in 2013. In this measurement, the mode overlap between the squeezed field and the local-oscillator beam was only 92% (visibility 96%). Accounting for this and for further known detection losses, we derive that about 10 dB of squeezing was present at the output of the OPA.

3.6 Automated operation

The goal is to operate the GEO 600 squeezed-light application around the clock with as few technical interruptions as possible. The need for interventions by a human operator should be limited to a minimum. For this purpose, a digital automation system was designed and implemented [Las10; Grä13] and has been improved over the years. It proves to be very reliable and is successful in providing a high duty cycle of the squeezer.

3.6.1 Locking of the squeezer subsystems

The length and phase control of the different squeezer subsystems (as described in the previous sections) are all implemented as analogue control loops. For the automation they are connected to GEO 600's digital Control and Data System (CDS) [Bor10]. For each subsystem, the in-loop error-point signal, the applied feedback, and the DC light-power level on the relevant photodiodes are recorded digitally. These values are compared to set thresholds in the real-time CDS model to derive the lock status. CDS can act on the control loops by requesting them to lock or unlock, switching

3.6 Automated operation

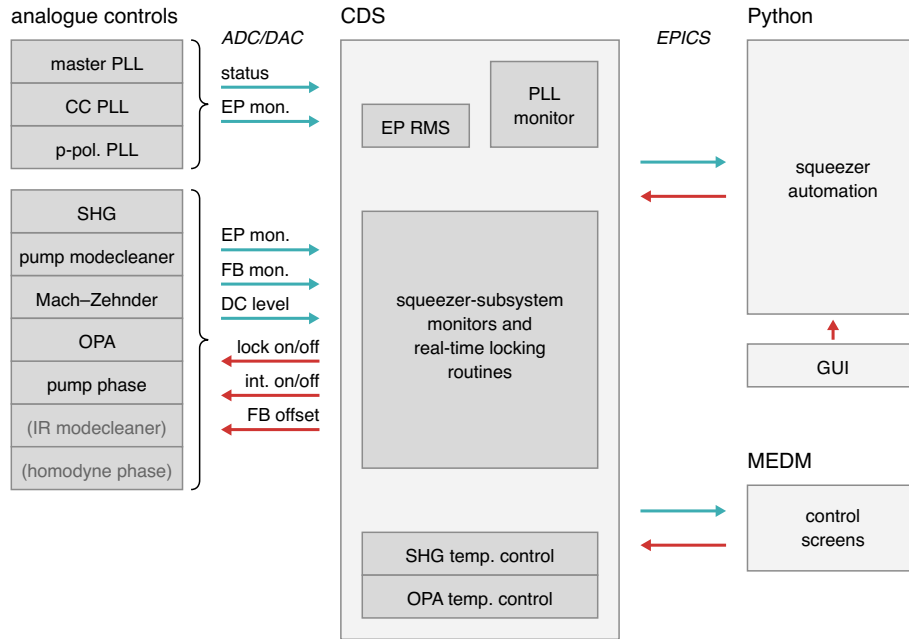


Figure 3.16: Overview of the squeezer’s digital control and automation. Most control loops are implemented in analogue electronics but are monitored and switched by the real-time digital control system. A PYTHON program handles the high-level automation.

analogue integrator stages, and adding feedback offsets. The PLL controllers have a built-in locking automation and are passively monitored by CDS. Temperature control of the SHG and OPA are handled completely digitally in CDS.

Complementing the fast real-time CDS code (model rate 32 kHz) is a slower PYTHON program to handle the high-level automation. The automation program constantly monitors the locking status and sequentially relocks all affected subsystems when a problem occurs. In undisturbed operation, the most common cause of relocks is when a control loop approaches the end of its actuation range and needs to be relocked on a new operating point. Such relocks occur a few times a day and usually interrupt the squeezing operation for just a few seconds. If locking does not succeed repeatedly or if a subsystem stays in lock only for short stretches of time, further automatic locking attempts are paused for ten minutes. Such instances are often indicative of an issue that will eventually require manual intervention, such as degrading power levels. Over the last years some more data channels were added to be monitored by the automation in order to better recognize known error states. Specifically, monitoring the in-loop PLL error signals allowed for the proper handling of occasional excess laser noise (as was described in section 3.2). The timing of the relocking procedure

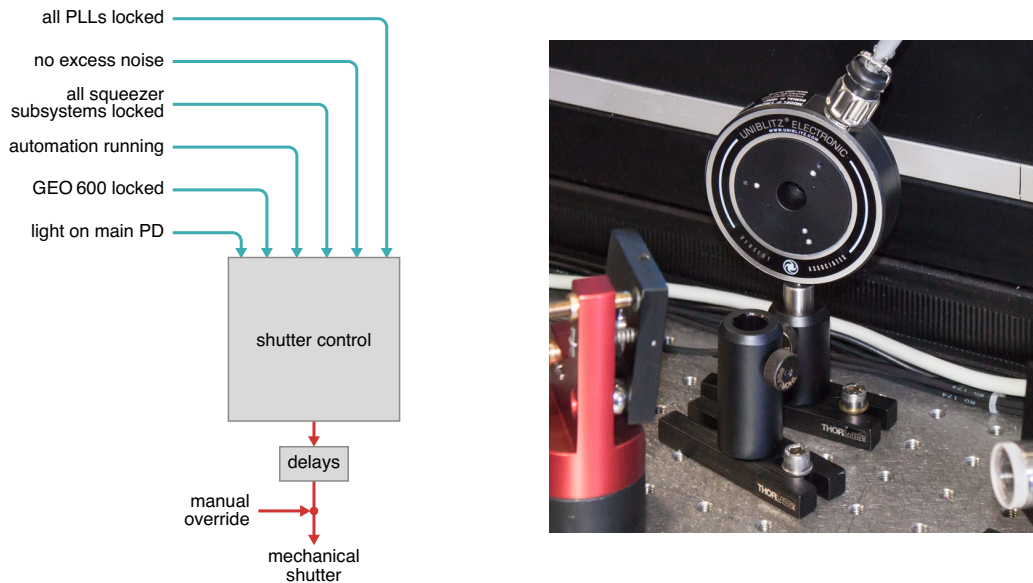


Figure 3.17: Overview of the shutter control. The beam path between the squeezer and the interferometer is blocked by a mechanical shutter within fractions of a second when a disturbance is registered.

was initially designed with wait times of several seconds between steps. We found that we could optimize this without impairing the reliability of the lock acquisition such that the complete procedure now takes less than three seconds. The impact on the overall duty cycle is small, but instant locking is very convenient during maintenance work. The PYTHON program has a graphical user interface that allows for manual toggling of the individual loops and also provides direct controls to scan the feedbacks. Further digital monitoring and control is done through the CDS user interface MEDM (Motif Editor and Display Manager). Descriptions of the most important control screens are collected in appendix B.

3.6.2 Shutter control

A nice feature of squeezed-light injection is that it is very easy to decouple the squeezer completely from the interferometer in case of any problems: Blocking the beam path between the squeezed-light source and the injection point immediately stops any influence the squeezer could have on the interferometer. If the squeezer experiences a disturbance, the interferometer can continue operating, just without the quantum-noise improvement. Therefore, temporary dropouts of the squeezer do not significantly impact the overall duty cycle of the gravitational-wave detector.

Blocking the injection path is also an important tool for characterizing the squeezing performance by comparing the detector noise with and without application of the squeezed-vacuum state (see chapter 5).

At GEO 600 we use a fast mechanical shutter located just outside the box that houses the squeezed-light source. The shutter is from the *Uniblitz* product line by Vincent Associates Inc. [Vin15] (both models ‘CS25’ and ‘LS6’ have been used). The nominal closing time is below 10 ms. Backscattering at the shutter blades in the closed state is not a major concern because the shutter is separated from the interferometer by two Faraday isolators. Experimental observations show that only in the moment of closing can the fast movement cause a minor glitch in the interferometer signal.

During earlier operation of the squeezer at GEO 600 the shutter was controlled by the high-level automation script. In this mode we found that in some instances closing could take up to about 1 s after a squeezer subsystem lost lock, during which time technical noise from the uncontrolled squeezer could degrade the interferometer performance. In extreme cases this can cause the interferometer itself to lose lock. In order to minimize this effect, the control is now handled directly in the fast real-time model. For this, a number of relevant status channels are aggregated and closing of the shutter is triggered as soon as any of those is signalling a problem. Figure 3.17 shows an overview of this shutter control scheme.

The shutter is designed for a maximum toggling rate of 5 Hz. We observed a failure mode where a fluctuating status signal led to very fast toggling, eventually overheating the shutter’s magnetic coil. To prevent this in the future, small delays were introduced in the real-time code, so that the shutter only changes its state when the new state is consistently requested over a certain amount of time. The delays can be set asymmetrically for opening and closing to still allow for very fast closing. Currently the closing delay is 50 ms while the opening delay is 1 s. For maintenance and commissioning the shutter status can always be manually overridden.

3.6.3 Duty cycle

Overall, with the combination of fast automated relocking and regular manual maintenance a very high duty cycle of the squeezed-light source was achieved. From the beginning of 2012⁵ up to the end of 2017 the detector was operational with squeezing for 70 % of the time (see figure 3.18). The squeezed-light source itself was

⁵ From this point onwards the squeezer status information was continuously recorded. Only a few days are missing from the analysis where no data is available.

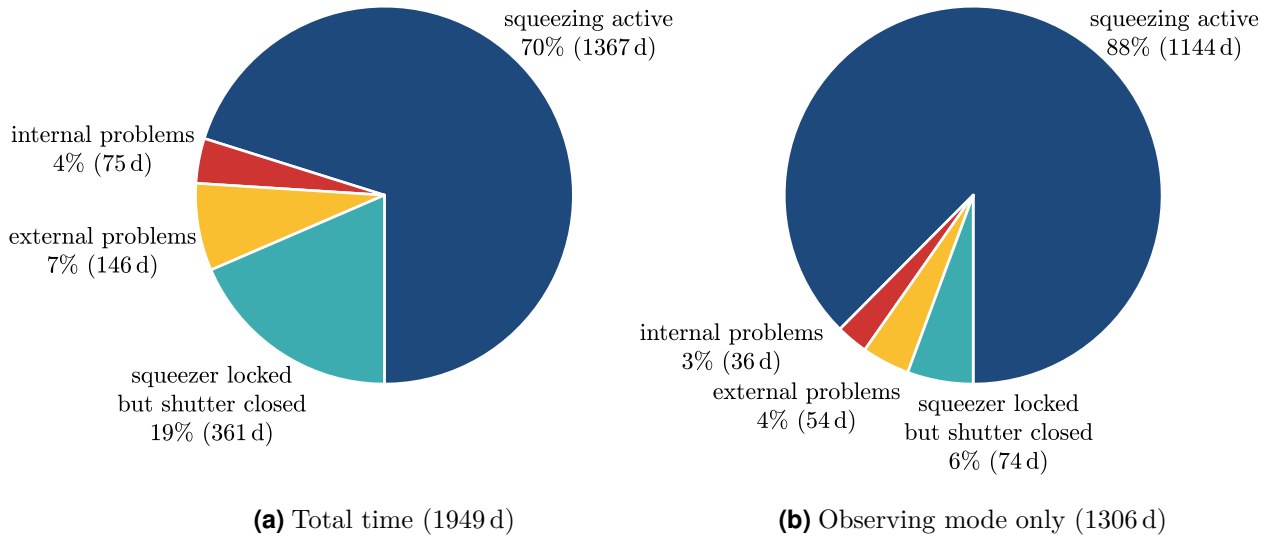


Figure 3.18: Duty cycle of the GEO 600 squeezed-light source from beginning of 2012 to the end of 2017.

fully locked for an additional 19 % where the shutter was closed (mostly because the interferometer was unlocked), resulting in a total duty cycle of 89 %. About two thirds of the unlocked time can be attributed to external circumstances. Power outages, computer crashes and times where the squeezer lasers or PLLs were switched off fall into this category. The remaining third is directly related to unlocked subsystems of the squeezer. If we limit the analysis to only those times where GEO 600 was in observing mode (fully locked with no experiments or maintenance work going on) the total squeezer duty cycle was 93 %.

Squeezed light injection

The essential challenge of the integration of squeezed light to gravitational-wave detectors is the interfacing of the squeezed-light source with the interferometer. The fragile squeezed vacuum state needs to be injected and reach the main photodetector with the highest possible optical efficiency and with a stable phase relation to the interferometer carrier field.

This chapter includes the main results of my thesis and will describe the many aspects of squeezing integration at GEO 600: the active control systems for squeezing phase and alignment, the mitigation of different forms of optical losses, the effects of stray light backscattered from the squeezing source, and ways to lower the limiting contribution of electronic noise.

The investigations into different phase control systems were led by Katherine Dooley. The implementation of the automatic alignment system was my responsibility. Hartmut Grote developed the new low-noise detection electronics together with Michael Weinert. Matteo Leonardi assembled and tuned the new Faraday isolator setup which I had designed.

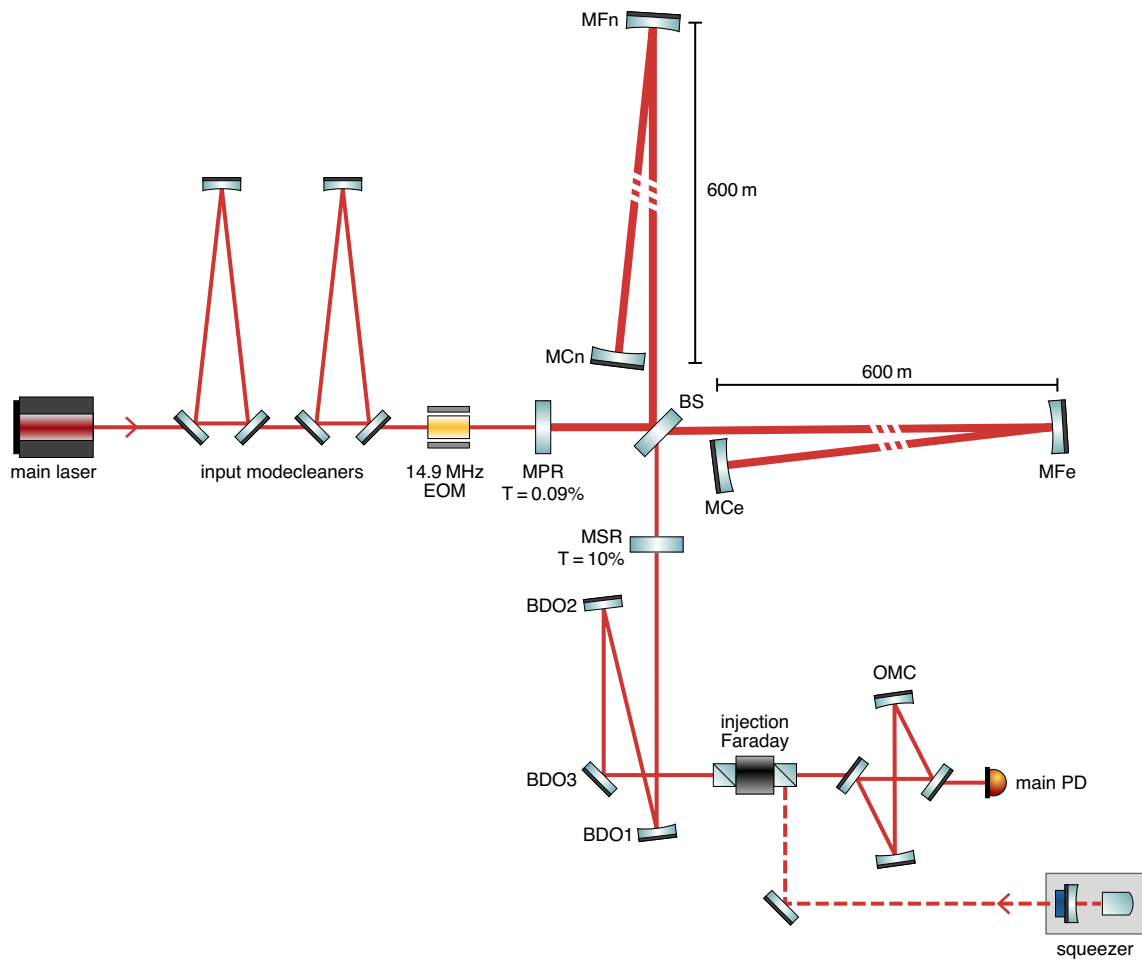


Figure 4.1: Schematic overview of the GEO 600 gravitational-wave detector.

4.1 The GEO 600 gravitational wave detector

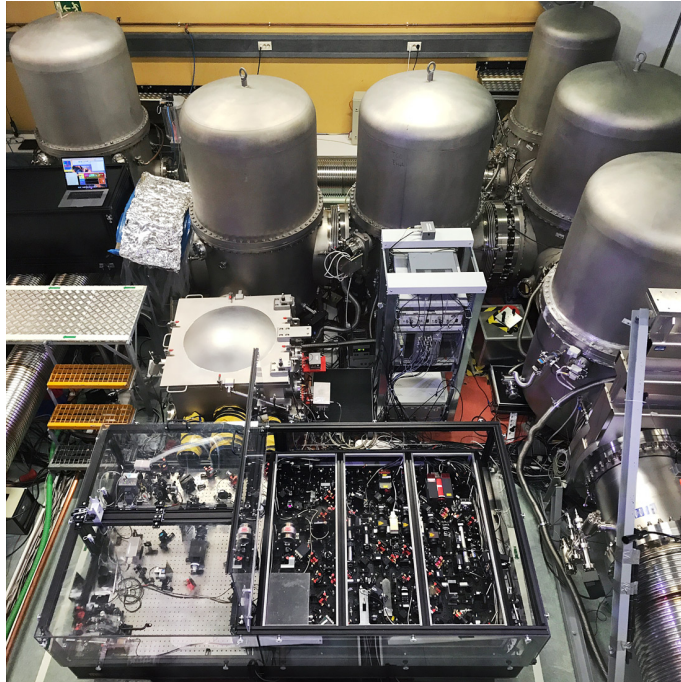


Figure 4.2: The inside of the detector’s main building. The squeezed-light source is visible in the foreground. The injection Faraday, OMC and main PD are housed in the small square vacuum chamber in the middle of the picture.

4.1 The GEO 600 gravitational wave detector

GEO 600 is a British–German gravitational-wave detector located in Ruthe near Hannover, Germany. It is a dual-recycled Michelson interferometer with 600 m long arms. In contrast to the other large-scale detectors it does not have resonant arm cavities, but the arms are folded once, increasing the effective length by a factor of two.

Figure 4.1 shows a simplified optical layout of the interferometer. All core optics are housed in a common vacuum envelope and are suspended for seismic isolation. Various active control loops serve to stabilize the optics’ longitudinal and angular relations.

The squeezed-light source is located near the output optics of the interferometer on a separate optical bench in air (see figure 4.2). From there the squeezed vacuum is injected into the vacuum system and towards the interferometer via a Faraday rotator. The squeezed vacuum field is reflected by the locked interferometer and travels alongside the interferometer output field through the output modecleaner (OMC) to be detected on the main photodetector.

4.2 Phase control

The most critical control for the squeezed-light injection is making sure that the squeezing ellipse is oriented optimally with respect to the readout quadrature. This squeezing-angle control uses the coherent-control sidebands (CCSBs, introduced in section 3.4.2) travelling alongside the squeezed vacuum field as the phase reference. Different ways of generating an error signal for the relative phase between the squeezer's CCSBs and the interferometer light fields have been tested at GEO 600.

As described in section 2.2.3, the achievable squeezing level depends on the overall RMS phase fluctuations of the squeezed light field. Contributions to the RMS can come from constant or slowly changing offsets, residual noise within the control bandwidth (about 2 kHz), and high-frequency fluctuations in the audio and radio band. All three aspects have been improved over time.

This section summarizes the results that we published in [Doo⁺15] and adds further experimental results.

4.2.1 Three ways to generate the coherent-control signal

The coherent-control error signal is derived from the optical beat of the CCSBs with either the interferometer's carrier light field, or existing control sidebands of the interferometer called Michelson sidebands (MISBs). The CCSBs are frequency offset against the carrier by $f_{CC} = 15.2$ MHz and the MISB frequency is $f_{MI} = 14.9$ MHz. The beat signals can be detected at several different ports where the respective light fields are available. Three different ports with different combinations of light fields have been tested at GEO 600 (see figure 4.3 for an overview):

1. CCSBs versus carrier at a pick-off port (beat frequency 15.2 MHz)
2. CCSBs versus MISBs in reflection of the OMC (beat frequency 300 kHz)
3. CCSBs versus carrier in transmission of the OMC (beat frequency 15.2 MHz)

The first option is the simplest one which was used initially at GEO 600 and also for the LIGO Hanford squeezing experiment [LSC13]: The beat of the CCSBs with the interferometer carrier itself is detected at a 1% pick-off directly at the interferometer output. This pick-off is nominally used for generating alignment signals for the differential alignment of the interferometer's end mirrors [Gro03]. The

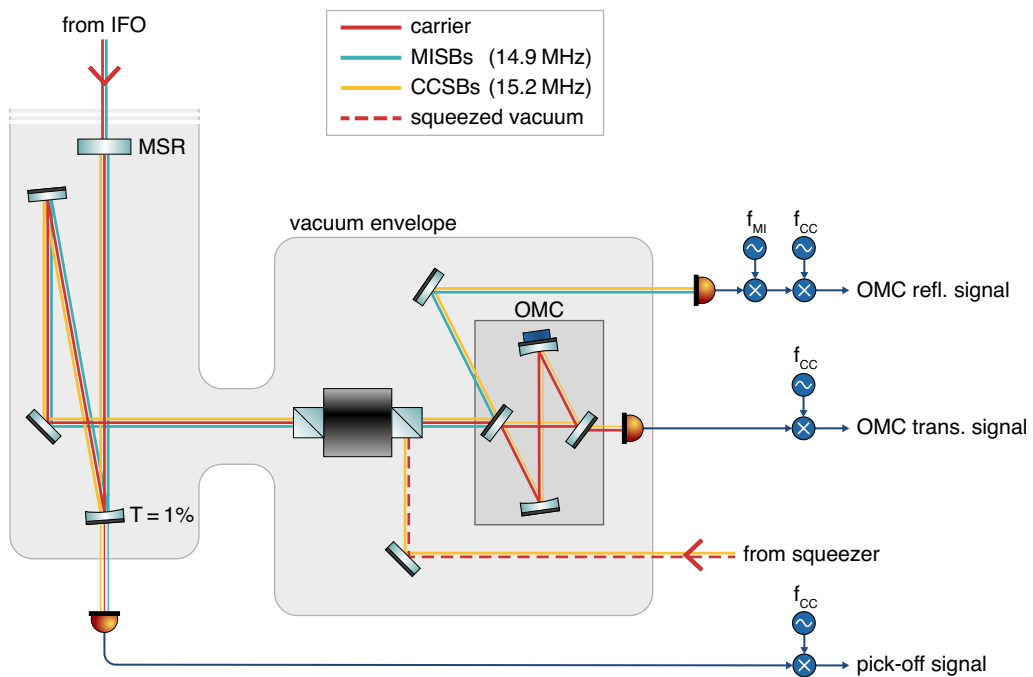


Figure 4.3: The GEO 600 output path with the three possible locations to generate the squeezer phase-control signal. Coherent-control sidebands are injected with the squeezed vacuum field and serve as the phase reference for the squeezing angle. The error signal is derived either from the beat with the Michelson control sidebands or the carrier light field itself.

coherent-control signal can be generated from the existing quadrant photodetector by demodulating its sum output at the beat frequency of 15.2 MHz. The main limitation of this error signal stems from the fact that the carrier field at the interferometer output before the OMC is strongly contaminated by higher-order modes (HOMs) caused by imperfections of the interferometer optics [Pri12; Wit15]. During typical operation, only about one fifth of the total power at the interferometer output is TEM₀₀ carrier light [Wit⁺14]. The presence of HOMs negatively impacts the signal-to-noise ratio (SNR) of the resulting error signal. In combination with small misalignments or mode-mismatches of the coherent-control field, the carrier HOMs will also lead to non-stationary lock-point errors [Dwy13; Oel⁺14; Oel16]. Such lock-point errors constitute false phase information which the control loop will follow, thus contributing to the overall fluctuations of the squeezing angle.

Compared to the carrier light field the MISBs are spatially much cleaner. Due to their shifted frequency and the interferometer's Schnupp asymmetry [Gro03] the MISBs are further away from the destructive-interference condition. Therefore, a higher fraction of the fundamental TEM₀₀ mode leaves the output port, making it the dominant mode contribution. The lower HOM content means that a coherent-control signal derived from the MISBs avoids most of the lock-point errors of the carrier pick-off signal. The beat of the CCSBs against the MISBs at their difference frequency of 300 kHz could be detected at the 1 % pick-off port as well. However, since both fields are almost completely reflected by the OMC, it is preferable to measure them at the OMC-reflection port where their amplitude is not reduced, allowing for a better SNR. The carrier HOMs also present at the OMC-reflection port increase the overall shot noise but do not otherwise contribute to the beat signal at 300 kHz.

The third option to generate the coherent-control signal is to detect the beat of the CCSBs with the carrier light field, but this time in transmission of the OMC on the main PD that also provides the gravitational-wave signal. For the carrier this has the great advantage of strongly suppressing all HOMs. The CCSBs are also suppressed by the OMC, but their offset frequency is sufficiently small compared to the OMC bandwidth of 2.9 MHz that roughly 1 % of the sideband power is still transmitted. Together with the absence of additional light fields that would increase the shot noise, the shot-noise-limited SNR of the OMC transmitted signal is comparable to the one derived in OMC reflection (depending on the exact experimental parameters [Doo⁺15; Oel16]). The OMC transmission signal could potentially be improved in the future by choosing a lower coherent-control frequency, thus transmitting more of the sidebands. The development of squeezing control signals that do not rely on a pick-off port is particularly important in future squeezing applications where pick-offs in the output chain should be avoided as far as possible as they contribute to optical losses.

4.2.2 Performance of the different phase-control signals

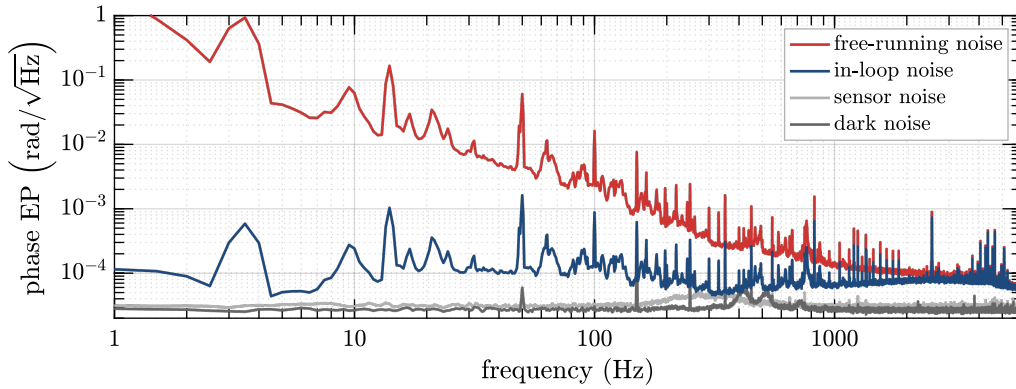
All three ways to generate the squeezer-phase signal have been commissioned at GEO 600. Demodulation of the photodiode signals at the respective beat frequencies happens in analogue electronics.¹ The demodulation phase is set with a voltage-controlled phase shifter. Choosing the demodulation phase determines the setpoint of the phase control. The control loop is implemented in analogue electronics with an additional digital path for tunable low-frequency control.

The phase of the squeezer is actuated by shifting the frequency of the squeezer master laser. For this, the frequency of the PLL's local oscillator can be modulated. Actuating on the frequency to control the phase means that the controller has an intrinsic integrating behaviour with infinite DC gain. The complete phase-control scheme that relies on several nested loops is illustrated in figure 4.8.

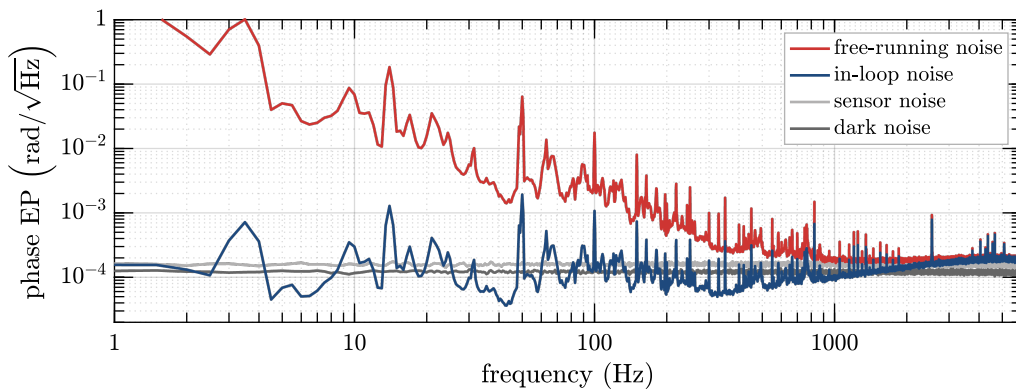
Figure 4.4 shows typical error-point spectra calibrated to $\text{rad}/\sqrt{\text{Hz}}$ for the three different signals. The sensing noise floor is determined by blocking the CCSBs. Ideally, the remaining signal should be dominated by shot noise. However, the major part of the noise remains even with no light on the photodetectors, indicating that the sensing noise in our experimental setup is dominated by technical noises. The OMC-reflected signal currently only uses a fraction of the available light. Increasing this fraction is one way to improve the signal-to-noise ratio. The loop gains are chosen such that the in-loop noise is suppressed to about the sensing-noise level. With higher gains the loop would impress technical noise on the system, degrading the out-of-loop performance again. Above several kilohertz the measured signal is dominated by technical noise so that the highest usable unity-gain frequency is about 2 kHz.

The in-loop performances for all three possible error signals is very similar. A difference becomes apparent when looking at the resulting squeezing: The squeezed shot-noise level is stationary when controlling the phase with the OMC-reflection signal or the OMC-transmission signal, but for the pick-off signal it becomes non-stationary. The shot-noise level shows strong low-frequency variations, at times even introducing antisqueezing (see figure 4.5). This shows that there are indeed

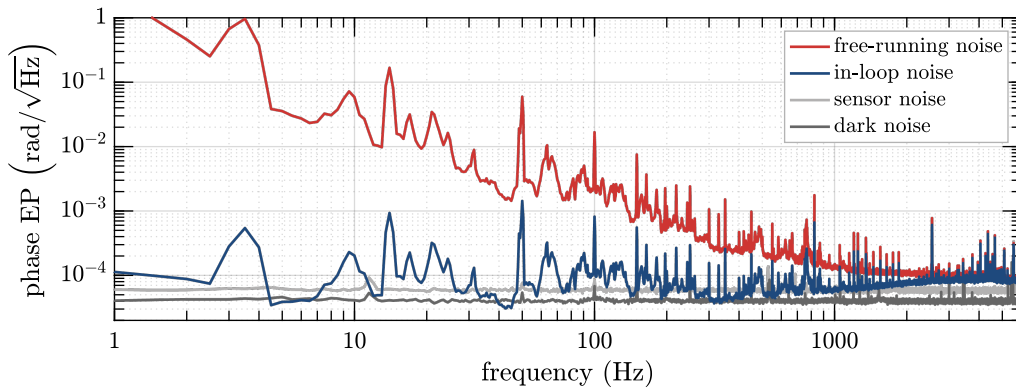
¹ The 300 kHz demodulation of the OMC-reflection signal is achieved by a double demodulation, first at 14.9 MHz, then at 15.2 MHz. This way all three possible signals can reuse the same electronics starting from the 15.2 MHz demodulator, which allows for easy switching between them.



(a) Pick-off (CCSBs vs. carrier)



(b) OMC reflection (CCSBs vs. MISBs)



(c) OMC transmission (CCSBs vs. carrier)

Figure 4.4: Spectra of squeezer phase error signals. For good comparability the in-loop noise spectra for the three signals were taken during a single lock stretch of the interferometer. The out-of-loop spectra are calculated from the in-loop measurement with the known transfer function of the controller. Sensor noise was measured by blocking the CCSBs and dark noise by blocking all light on the PDs.

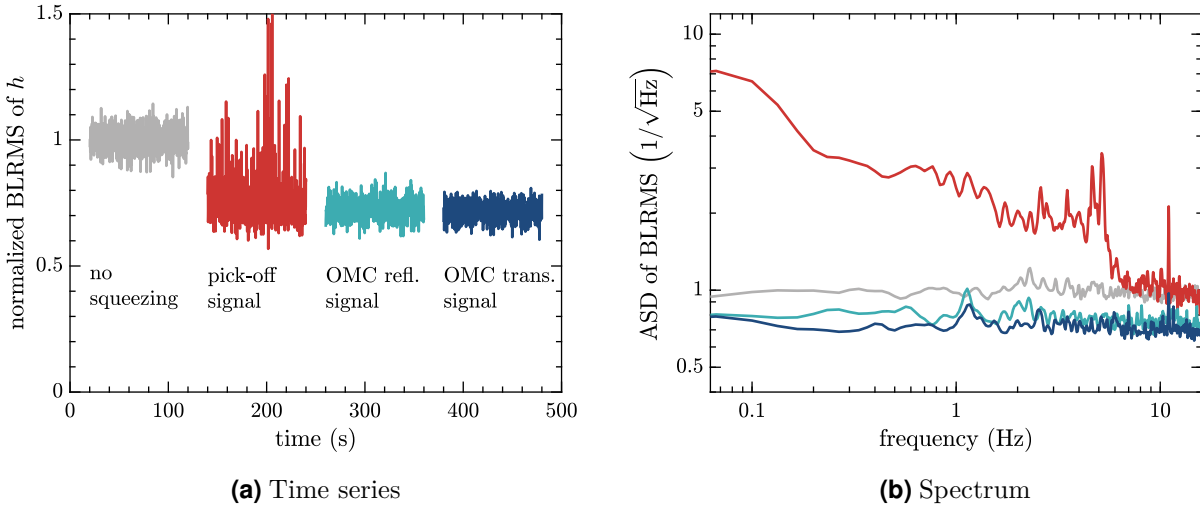


Figure 4.5: Squeezing-level fluctuations with different phase-control signals. Shown here is the shot-noise level calculated as the band-limited RMS of the detector’s output signal over a frequency band of 4 kHz to 5 kHz. The left panel depicts typical 100 s time series for operation with each of the three squeezer phase signals, and also for the unsqueezed case. The right panel shows the corresponding spectra, each averaged over a 20-minute period. A clearly nonstationary behaviour with excess low-frequency fluctuations is observed for the pick-off signal due to the influence of higher-order modes. Comparison with simulated data shows that for the other two control schemes as well as for the unsqueezed case the observed fluctuations are at the expected level of purely Gaussian noise.

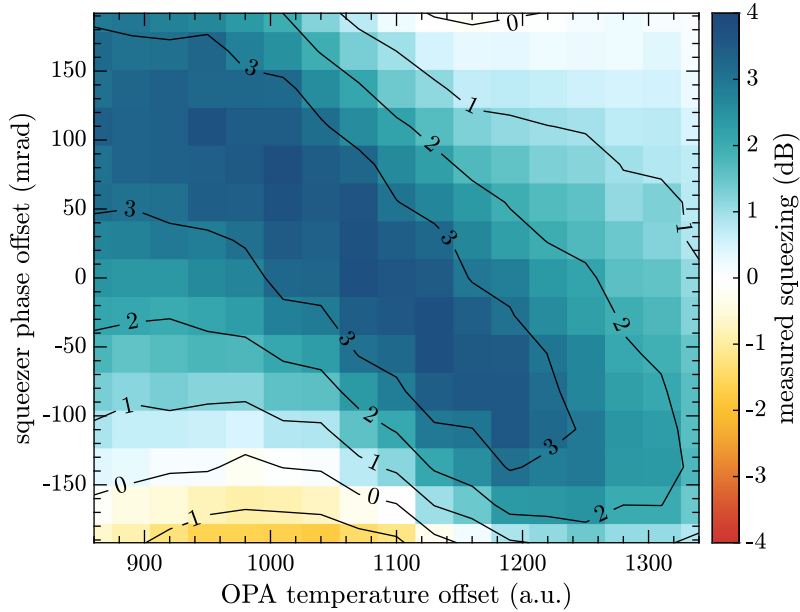


Figure 4.6: Influence of OPA temperature on the optimal squeezing phase. Changes of the OPA temperature reduce the parametric gain and additionally introduce a phase offset of the CCSBs which needs to be compensated in the phase control to reach good squeezing levels again. The plot shows experimental results of varying the temperature offset and phase offset while recording the resulting shot-noise level of the detector at 3.5 kHz. Each coloured square corresponds to a 10 s measurement.

significant lock-point errors for the pick-off signal caused by the varying HOMs.²

4.2.3 Noise locking

Several different effects can introduce DC shifts of the CCSB phase. If uncompensated, such shifts will introduce an error of the squeezing phase. The dominant effect is caused by residual temperature drifts of the OPA. These will affect the phase matching of the p-polarized locking field so that the OPA will no longer be perfectly

² For the first demonstration of squeezing at GEO 600 [LSC11] the pick-off signal was used for phase control and did not show major lock-point errors. This is because at that time a different signal-recycling mirror with lower transmission of $T = 1.9\%$ was installed, which leads to a significantly lower HOM content of the interferometer output beam [MS91; Pri12]. Only for the current signal-recycling mirror with $T = 10\%$ do we see the negative influence of the now increased HOM content.

resonant for the s-polarized carrier (see section 3.4). In this case, the two CCSBs will experience asymmetric phase shifts, causing an offset of the resulting coherent-control signal with respect to the actual squeezing angle [Kha⁺12a]. The active stabilization of the OPA temperature and pump power help greatly to reduce this effect, but environmental changes still introduce slow drifts on timescales of hours. Figure 4.6 illustrates the dependence of the optimal phase setpoint on the OPA temperature. Other contributing factors that can influence the relative phase of the coherent-control signal are a change of the sideband imbalance due to variations of the parametric gain [Oel16], and varying phase shifts introduced in the demodulation electronics.

In a short-term experiment such DC offsets of the coherent control can be compensated by manually tuning the phase setpoint for optimal squeezing. For long-term stable operation this process needs to be automated. To this end, a dither-locking scheme implemented in CDS is applied [Gro⁺13]: The squeezing angle is modulated with a small amplitude (by introducing an offset of the coherent-control setpoint via the voltage-regulated phase shifter) and the resulting variations of the squeezing level are monitored. By continuously calculating the band-limited RMS of the detector output signal in a shot-noise-limited frequency band and demodulating it at the dither frequency, an error signal is obtained that has a zero crossing where maximum squeezing is achieved. With this the phase setpoint can be driven to always maintain optimal squeezing. This technique is called *noise locking* [McK⁺05]. Other vacuum-squeezing experiments have used noise locking instead of the coherent-control technique, but in order to achieve high bandwidths, a strong phase modulation must be introduced, which in itself reduces the mean squeezing level. For the case of GEO 600 where the high-frequency phase lock is completely handled by the coherent control and the noise lock only takes the role of a very slow drift control, the modulation depth can be chosen much smaller, so as to not significantly impact the overall squeezing level.

Choosing the dither amplitude requires a compromise: On the one hand the shot-noise level needs to be measurably affected in order to derive a usable error signal, on the other hand we want to maintain the best possible average squeezing. With a low dither amplitude, long integration of the error signal is necessary in order to achieve an acceptable SNR, which means that only a very slow control is possible. Over the last years we have used a dither at 11.6 Hz with an RMS amplitude in the order of a few milliradians. The amplitude was reduced over time as improvements of other imperfections increased the susceptibility to phase fluctuations. It was verified that the phase dither has no significant negative impact by comparing the squeezing performance with and without dither.

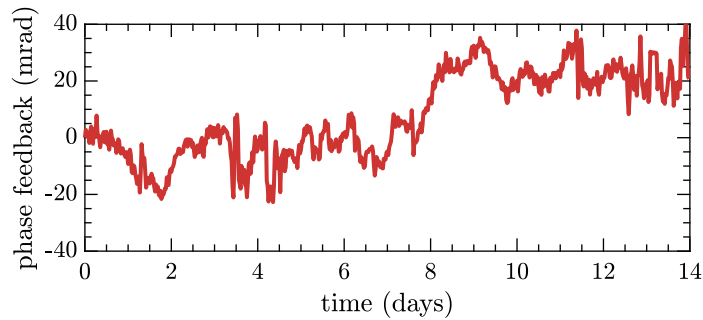


Figure 4.7: Two-week trend of the noise-lock feedback calibrated to units of mrad. The optimal squeezing angle drifts slowly by up to several tens of milliradians per day. Without the correction by the noise-lock loop this would lead to significant offsets of the observed squeezing angle. The calibration of this plot is only approximate because the phase actuator has a pronounced nonlinear response which is not considered here. The depicted data is taken from a relatively quiet period with few lock-losses and only minor experimental work on the detector.

The obtained unity-gain frequency is about 10 mHz. The low bandwidth means that the noise lock cannot compensate the lock-point errors observed for the pick-off signal, which are most pronounced at the suspension resonance frequencies of around 1 Hz, but it is well suited for compensating slowly changing environmental conditions. Since the noise-lock loop is so slow, it is important to hold the output during times when no error signal is available (when the interferometer or squeezer is unlocked), otherwise it can take a long time to recover an optimal operating point again after a disturbance. During experimental work on the squeezer, the noise-lock excitation can be increased temporarily in order to reach a higher unity-gain frequency. This reduces the settling time at the cost of higher RMS phase noise during the experiment.

The noise-locking technique has proven to be an important factor in keeping a constant squeezing level. Without it, manual tuning of the phase setpoint would be necessary every few days in order to prevent noticeable degradations (see figure 4.7).

4.2.4 Overview of the complete phase control scheme

The phase-control scheme relies on a number of interconnected control loops. Here I want to quickly reiterate the overall setup. Five different controllers are directly involved (see also sections 3.2 and 3.4.2 of the previous chapter):

1. The PLL that locks the squeezer master laser to GEO 600's main laser.

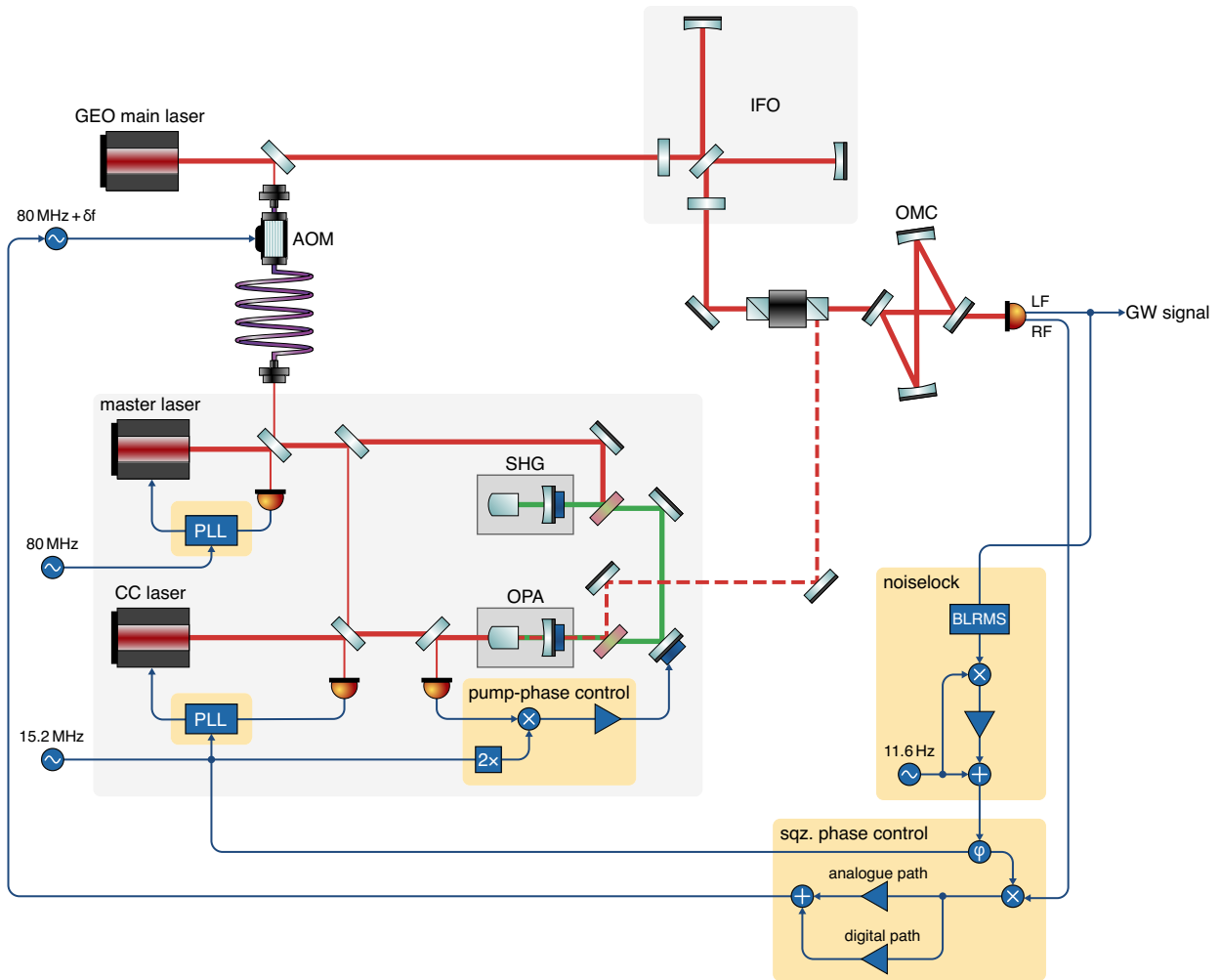


Figure 4.8: Overview of the complete squeezer-phase control scheme. Depicted is the case of using the coherent-control signal derived in transmission of the OMC. The schematic shows all relevant parts of the phase control, but is otherwise strongly simplified.

2. The PLL that locks the coherent-control laser to the master laser.
3. The pump-phase loop to fix the phase relation of pump and CCSBs.
4. The main squeezing-angle control using the coherent-control signal.
5. The slow noise-lock loop that corrects the phase setpoint.

Figure 4.8 is a representation of the complete phase-control setup as it is currently implemented.

4.2.5 Residual phase noise

In order to determine the expected effect of the remaining phase fluctuations on the squeezing performance we need to estimate the out-of-loop phase noise over all frequencies:³

At the very low-frequency end the noise lock effectively prevents any major offsets. However, as mentioned, the necessary phase dither for the noise lock introduces a small RMS phase error. From a rough calibration of the phase actuator and the known digital modulation depth we estimate this contribution to be 3 mrad.

Within the 2 kHz bandwidth of the coherent-control loop the intrinsic phase fluctuations are heavily suppressed, but due to the sensor noise the suppression cannot be arbitrarily large. From the observed in-loop error signal and the sensor-noise level we can calculate the estimated out-of-loop residual phase noise up to 2 kHz to be 4 mrad.

The free-running phase noise above the unity-gain frequency of the coherent control can be calculated from the difference of the observed error signal and the pure sensor noise. At these frequencies the error signal is very close to the sensor noise which allows only for a rough estimation. Above 45 kHz sensor noise dominates completely and no phase-noise measurement is possible. But since the free-running phase fluctuations fall off towards higher frequencies faster than $1/f$ those contributions are less significant. Between 2 kHz and 45 kHz about 13 mrad are measured.

³ I present here a phase-noise budget mostly derived from an extensive set of measurements performed at the end of 2014. Since then some minor improvements were achieved, but squeezing measurements indicate that the overall phase noise remains at a comparable level.

source	RMS phase fluctuation (mrad)
noise-lock dither	3
in-band acoustic (up to 2 kHz)	4
out-of-band acoustic (2 kHz to 45 kHz)	13
9 MHz signal-recycling sidebands	6
14.9 MHz Michelson sidebands	7
incoherent sum	17

Table 4.1: Known sources of residual phase noise when locking the squeezing angle with the coherent-control signal derived in transmission of the OMC.

Finally, there are contributions from the interferometer’s control sidebands that are partially transmitted through the OMC. To first order, these sidebands represent an amplitude modulation of the local-oscillator field at the interferometer output and thus should not constitute a phase fluctuation. However, in the presence of a sideband imbalance as well as due to the contrast defect of the interferometer, the sidebands can act as phase modulations of the readout-quadrature [Dwy⁺13; Doo⁺15]. The contributing parameters can be determined from scans of the OMC. We calculate that the Michelson sidebands contribute 7 mrad and the additionally present control sidebands for the signal-recycling cavity at 9 MHz add 6 mrad of phase fluctuations. During the early squeezing operation the MISBs had been stronger until they were identified as a limiting factor. Now they are lowered during normal operation of the interferometer and are only at their full amplitude during lock-acquisition to provide better error signals.

The different sources of phase-noise are summarized in table 4.1. Adding the contributions incoherently gives a total estimated phase noise of 17 mrad. Earlier independent estimations of the total RMS phase noise based on the observed squeezing and antisqueezing had suggested higher levels of more than 30 mrad. We assume now that the discrepancy is explained by the confounding effects of backscattering that were not previously considered (see section 2.2 and 4.6). Later measurements set a rough upper limit of 20 mrad for the RMS phase fluctuations (see section 5.3) and are thus compatible with the budget presented here. The precision of the latest measurements is limited by the available parametric gain.

Improving the phase-noise performance can be approached in two ways: raising the active suppression or increasing the intrinsic phase stability by reducing external

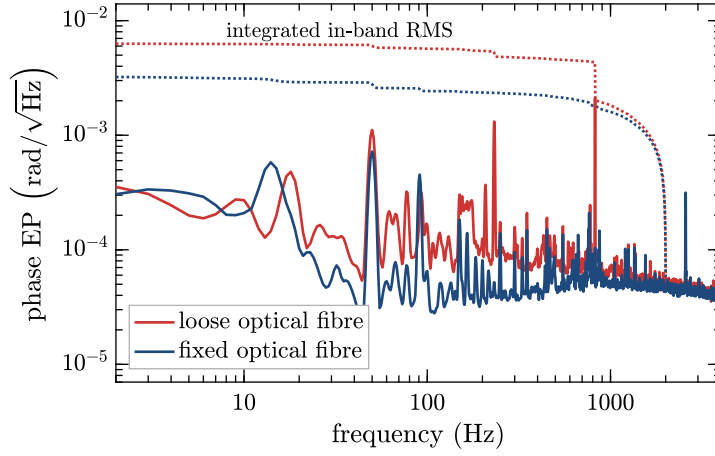


Figure 4.9: Phase noise caused by the optical fibre between GEO 600’s main laser and the squeezer. The red trace shows the in-loop error signal for a situation where the fibre was loosely hanging from the building’s steel frame. Fixing it to the concrete foundation reduced mechanical couplings, as shown by the blue trace. The particularly strong line at 820 Hz was caused by vibrations from one of the turbomolecular pumps that are part of GEO 600’s vacuum system.

noise couplings. In the current setup sensor noise is the limiting factor for the reachable noise suppression. Part of the technical noise for the OMC transmission signal was identified as RF pickup on the signal lines between the in-vacuum PD and the detection electronics. When we reduced this pickup by changing the shielding situation we significantly improved the sensor noise. The error signal is still not completely shot-noise limited, so further improvements of the electronics might be possible in the future.

The intrinsic phase stability of the squeezing injection at GEO 600 is to a large part determined by seismic or acoustic disturbances. These couple mechanically through optical path-length modulations of the OPA cavity [Dwy⁺13], the in-air injection path, and also the optical fibre that carries the phase reference from the main laser to the squeezer. We found that the fibre link was at times affected by mechanical vibrations strong enough to add significant phase noise. We were able to fix this by mounting the fibre more rigidly (see figure 4.9). Further improvements would be possible by additional acoustic shielding of the fibre should this become a limitation again in the future. Similarly, the in-air path could be further shielded. In a recent squeezing experiment Vahlbruch et al. observed free-running RMS phase fluctuations below 2 mrad with an in-air injection path [Vah⁺16] (although shorter than at GEO 600). This indicates that in-air operation itself should ultimately not be a showstopper for reaching very low phase-noise levels.

4.3 Alignment control

One of the most important aspects of maintaining good injection efficiency for the squeezed vacuum field is to properly align the beam path. In principle, three different alignments play a role for squeezing in interferometric gravitational-wave detectors such as GEO 600:⁴

1. The squeezed-vacuum field must be well aligned to the signal-recycling cavity so that it can be properly reflected from the interferometer (see section 4.5.3).
2. The squeezed-vacuum field must be well aligned to the fundamental mode of the interferometer output beam that forms the local oscillator field and carries the gravitational-wave signal.
3. The squeezed-vacuum field must be well aligned to the OMC's eigenmode in order to be transmitted for detection on the main photodetector.

These alignment requirements are of course not independent and coincide in the case where the interferometer is well aligned to the OMC. The OMC suppresses all relevant higher-order spatial modes by more than three orders of magnitude in power [Wit15]. This means that in terms of squeezing (and antisqueezing) we can safely neglect HOMs of the OMC and limit the analysis to the OMC's fundamental mode. The task of aligning the squeezed-vacuum field can then be described as matching the squeezer mode to the OMC. The effects of combined mismatches in squeezing injection for a slightly different interferometer configuration have been studied in detail by Töyrä et al. [Töy⁺17].

In tabletop experiments careful alignment by hand is necessary, but it is then typically stable enough to not change significantly during the course of a measurement. The same is no longer true in the context of large-scale gravitational-wave detectors where alignment between distant individually suspended optics needs to be maintained over long timescales. Such a system will show slow alignment drifts and also potentially significant alignment fluctuations at frequencies close to the resonances of the seismic isolation system. For this reason we have implemented an automatic system to continually sense and control the alignment of the squeezed beam. GEO 600 was the first squeezing experiment to use such a control and it is foreseen that this

⁴ Future frequency-dependent squeezing applications additionally need to consider the alignment of the filter cavity.

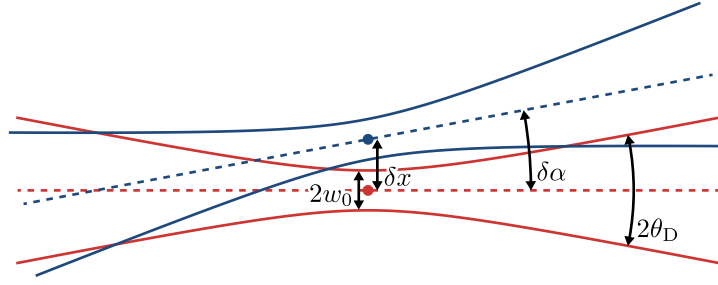


Figure 4.10: Relative alignment of two Gaussian beams. A general misalignment can be described as a combination of a lateral and angular offset at the position of the waist.

will be an essential requirement for maintaining high squeezing levels in all future gravitational-wave detectors [Oel⁺14]. The results described in this section have also been published in [Sch⁺16].

4.3.1 The effect of misalignment

Small misalignments of a Gaussian beam can be described as a partial shift of fundamental-mode power into the first-order Hermite–Gauss modes (TEM_{10} and TEM_{01}) [Rüd⁺81]. This causes an effective loss for the fundamental mode. A lateral shift of the beam axis results in coupling to the first-order modes in phase with the fundamental mode, while an angular tilt results in coupling 90° out of phase [And84]. A general mismatch in either the vertical or horizontal plane can then be described by the complex coupling coefficient⁵

$$\varepsilon = \frac{\delta x}{w_0} + i \frac{\delta \alpha}{\theta_D}, \quad (4.1)$$

where δx and $\delta \alpha$ are the lateral and angular offsets, w_0 is the beam’s waist size, and $\theta_D = \frac{\lambda}{\pi w_0}$ is its divergence angle (see figure 4.10). The absolute value of this misalignment parameter $|\varepsilon|$ is a conserved quantity under propagation through an ideal optical system [Kwe05]. We call $|\varepsilon|$ the *relative misalignment*. The effective

⁵ As far as I know, this handy formalism was first introduced by Patrick Kwee in his diploma thesis [Kwe05] in the German language. English-language descriptions are found in [Kwe⁺07] and [Kwe10].

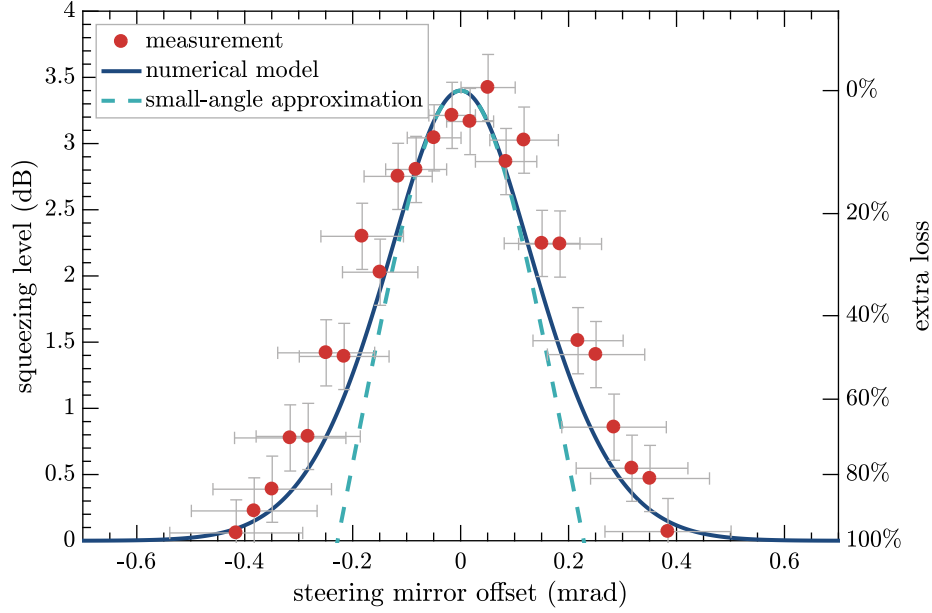


Figure 4.11: Degradation of squeezing due to misalignment. As an example, this plot shows the effect of misaligning a particular steering mirror in the squeezing injection path. Measured data is compared to an independently derived numerical model (done in FINESSE [Fre⁺04; Fre14]) that is based on the known parameters of the optical path. The good agreement between measurement and theory gives confidence in the actuator calibration and the optical model. The small remaining mismatch falls well within the calibration uncertainty.

power loss of the fundamental mode is given by the square of $|\varepsilon|$:

$$l = |\varepsilon|^2 = \frac{\delta x^2}{w_0^2} + \frac{\delta \alpha^2}{\theta_D^2}. \quad (4.2)$$

The effect this has on the squeezed light field is the same as any other loss (as was described in section 4.5). Figure 4.11 shows an example of reduced squeezing due to intentional static misalignment of an optic in the squeezing-injection path. For fluctuating misalignments the average loss is determined by the RMS of $|\varepsilon(t)|$.

The impact that a misaligned mirror has on the alignment of the beam depends on the mirror's longitudinal position z_m along the beam path relative to the waist. For a small beam deflection $\beta \ll 1$ (for which the mirror itself turns by $\beta/2$) we can calculate the resulting misalignment geometrically [Kwe05]: The angular offset of the beam axis is $\delta \alpha = \beta$ and the lateral shift at the waist is $\delta x \approx -z_m \beta$ resulting in

a total misalignment of⁶

$$\varepsilon(\beta, z_m) = \beta \left(-\frac{z_m}{w_0} + i \frac{1}{\theta_D} \right). \quad (4.3)$$

This expression tells us both how strongly the mirror influences the alignment and in which degree of freedom (lateral, angular, or a combination of the two). The argument of $\varepsilon(\beta, z_m)$ is

$$\begin{aligned} \arg [\varepsilon(\beta, z_m)] &= \frac{\pi}{2} + \arctan \left(\frac{z_m \theta_D}{w_0} \right) \\ &= \frac{\pi}{2} + \zeta(z_m), \end{aligned} \quad (4.4)$$

where $\zeta(z_m)$ is the Gouy phase [Sie86] of the beam at the location of the mirror. This means that two mirrors affect the alignment in the same degree of freedom if their Gouy-phase separation is 0° or 180° . The effects are orthogonal for a Gouy-phase separation of 90° .

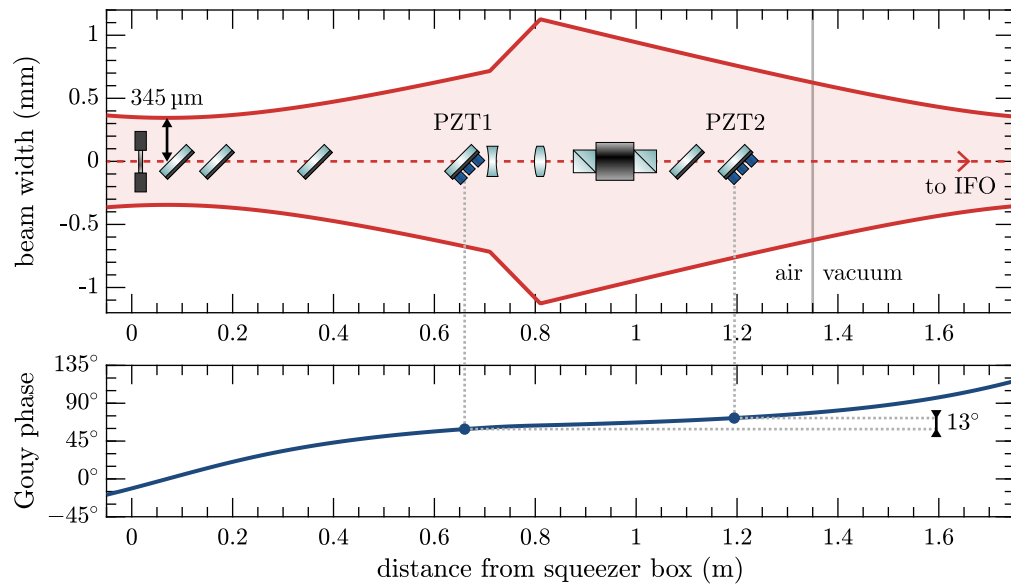
4.3.2 Alignment actuators

The squeezing injection path for GEO 600 includes two active steering mirrors mounted on three-axis piezo stages. These alignment actuators are digitally controlled by CDS and can locally rotate and tilt⁷ the beam axis by up to about 1 mrad (3 arc minutes). Much larger offsets are possible by manually adjusting the mounts of the steering mirrors.

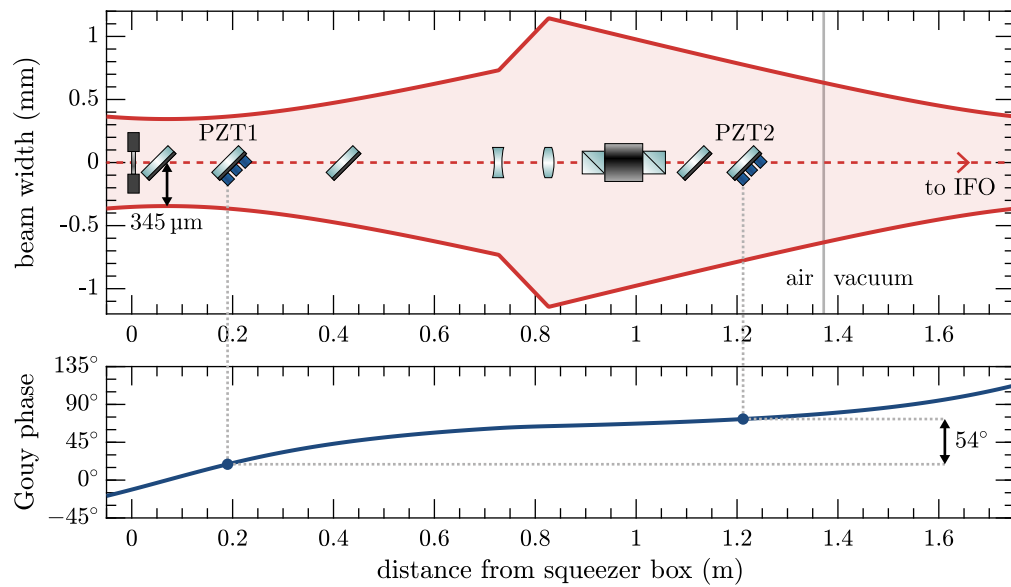
The two actuators need to be spaced apart along the beam path for good Gouy-phase separation to make sure that all four alignment degrees of freedom (angular and lateral in rotation and tilt) are accessible. In the initial setup of the path, the Gouy phase separation was only $(13 \pm 3)^\circ$. In the course of a redesign of the injection path in 2016 we improved the Gouy-phase separation to $(54 \pm 5)^\circ$. This change increases the dynamic range in one of the degrees of freedom by about a factor of four and helps to reduce cross couplings. Reaching perfect separation of 90° would require

⁶ We assume here that between the misaligned mirror and the waist there are no curved optics that would change the beam parameters. The same calculation can be done even with curved optics in the path, but care must be taken to use the parameters of the beam as they are at the location of the mirror in question.

⁷ The convention at GEO 600 is to call beam movements in the horizontal plane *rotation* and in the vertical plane *tilt*. In other contexts these are also often referred to as *yaw* and *pitch*, respectively.



(a) Old beam path



(b) New beam path

Figure 4.12: Model of the in-air injection beam path for two different configurations, showing the increase of actuator separation. The locations of the most important optics on the injection bench are marked schematically. The beam parameters that the model is based on were measured in situ with a CCD beam profiler.

a new lens setup to fit the available space but is in principle possible. Figure 4.12 shows a model of the in-air injection path for the old and new configuration.

All in-air optical components of the injection path and the squeezer itself sit on a common optical bench, which provides good intrinsic stability of their relative alignment. Most of the alignment drifts and fluctuations that need to be compensated originate inside the vacuum system. It would therefore be preferable to have the alignment actuators located towards the end of the in-air path, such that movements of the actuators do not affect the path through any other in-air components. This is currently not the case due to spatial limitations together with the requirement for good Gouy-phase separation, but it will be a design consideration for future iterations of the path design.

The effects of the steering mirrors were calibrated with two independent methods: For the first method, the beam deflection β was measured with the help of a long-baseline test beam. This yields a calibration in degrees per given digital feedback signal. Together with a model of the optical path and using equation 4.3 this can then be converted to the relative misalignment $|\varepsilon|$. Both the deflection measurement as well as the path model have relatively large uncertainties. Therefore, as a second calibration, we have directly measured the resulting reduction of fundamental-mode overlap. For this, the squeezer's bright alignment beam was sent along the injection path, reflected off the signal-recycling mirror (with unlocked interferometer), and detected in transmission of the OMC locked onto the fundamental mode. We can thus directly measure the loss of fundamental-mode power when misaligning the beam with one of the steering mirrors. Figure 4.13 shows the results of these measurements where I have fitted a quadratic model to get a calibration factor for the relative misalignment $|\varepsilon|$ per digital feedback signal, or alternatively loss $l = |\varepsilon|^2$ per feedback signal squared. The two calibration methods give compatible results within the uncertainty. In the following, the more direct calibration of measuring the OMC transmission is used as the basis for all calibrated alignment signals.

4.3.3 Generating alignment signals with differential wavefront sensing

To continuously sense the alignment of the squeezed light field an alignment error signal is derived using the coherent-control sidebands as a marker, similar to what is done for the phase control. The sensing scheme is based on the *differential wavefront sensing* (DWS) technique [Mor⁺94a; Mor⁺94b; Hei99], in which the beat of two light fields is sensed on a quadrant photodetector (QPD) and demodulated at the beat frequency to derive a signal proportional to the relative misalignment of the

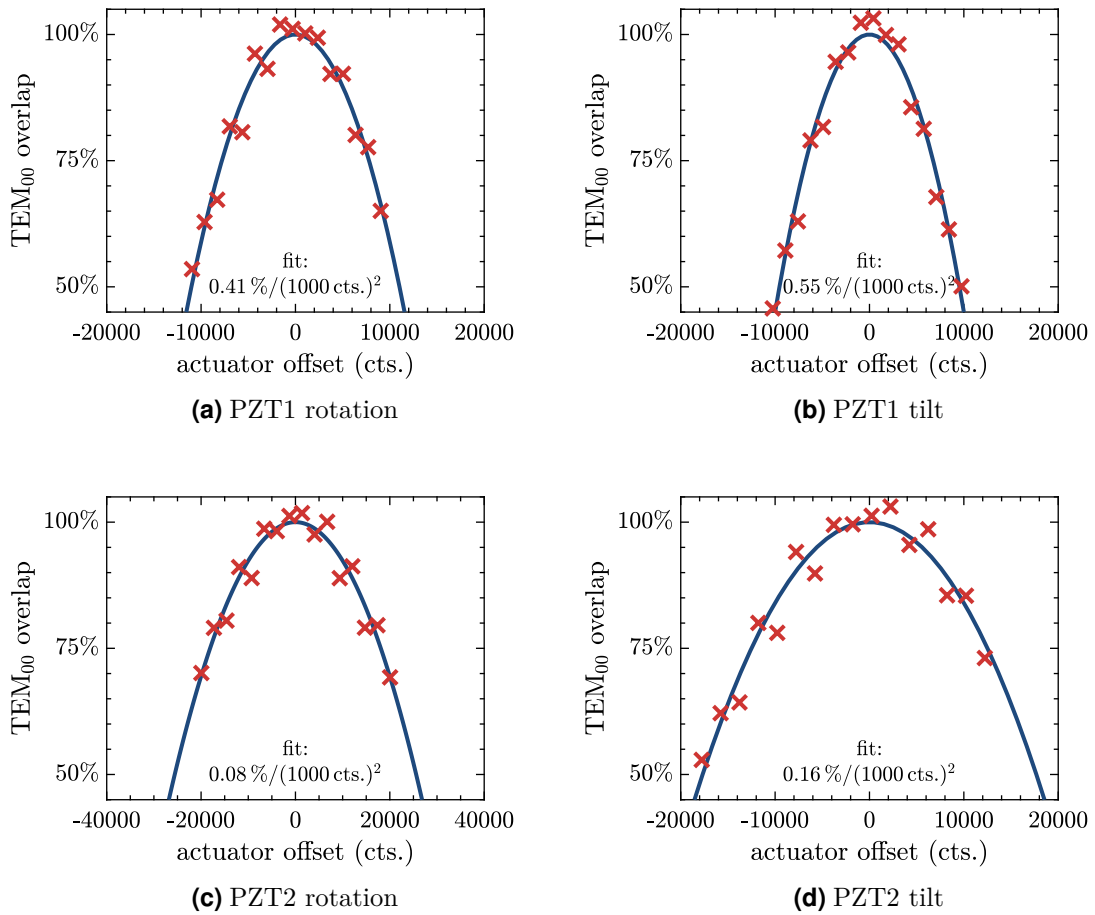


Figure 4.13: Measured calibration of the piezo alignment actuators for the squeezed light field.

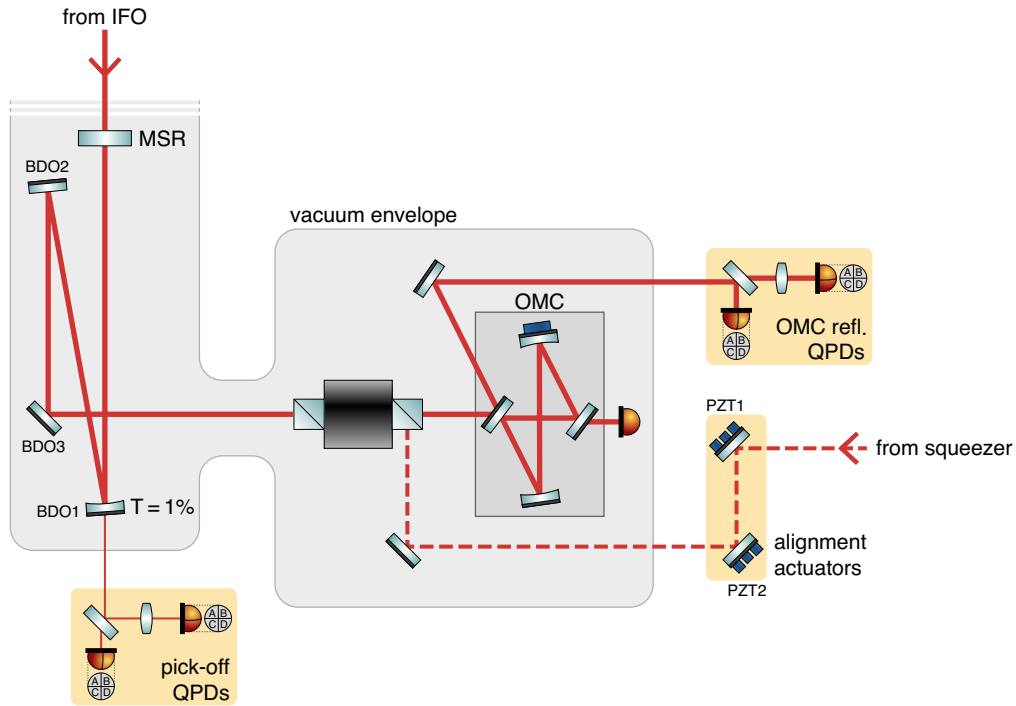


Figure 4.14: Alignment sensors and actuators in the squeezing injection path.

two beams. A single QPD senses the wavefront mismatch of the two beams in the horizontal and vertical directions at the location of the sensor. A set of two QPDs with good Gouy-phase separation can provide information about all four alignment degrees of freedom.

We use the general approach of aligning the squeezed beam to the beam that leaves the interferometer, which is in turn aligned to the OMC. Together, this ensures good alignment of the squeezed beam also to the OMC. The alignment of GEO 600's output beam onto the OMC is nominally done with a dither locking scheme that uses alignment modulations of the suspended beam-directing optics (BDOs) in the output path to maximize the transmission of the fundamental mode (marked with a so-called beacon signal) through the OMC [Pri⁺10; Smi⁺11; Pri12]. The dither frequencies lie between 3.5 Hz and 17 Hz and the system is limited to a control bandwidth of well below 100 mHz. A new alignment scheme for the OMC, using an adapted form of DWS, that promises faster control without the need for dithers is under development at GEO 600 and we could already demonstrate its effectiveness [Aff⁺14]. However, technical challenges mean that it is not yet in permanent use.

For aligning the squeezed field to the interferometer, the CCSBs can be referenced to either the interferometer carrier field or the Michelson sidebands. In the same way as for the phase control, directly using the interferometer carrier as the reference has the drawback of being affected by the pronounced HOM content. Using the spatially cleaner MISBs avoids this problem. Which combination of fields is used for generating the DWS signal is determined by the frequency at which the QPD signals are demodulated (15.2 MHz for CCSBs versus carrier, 300 kHz for CCSBs versus MISBs).

There are two possible locations in the GEO 600 output path where the alignment sensors can be placed (see figure 4.14): Initially, existing QPDs at the 1% pick-off were used (one of which also provides the signals for the differential alignment of the Michelson arms). Alternatively, the CCSBs and MISBs are also available in reflection of the OMC where the higher light power allows for better signal-to-noise ratios.

An option that has not yet been explored would be to use DWS to align the CCSBs (and with them the squeezed beam) not to the interferometer output fields but directly to the OMC eigenmode. Usually, DWS for aligning to a cavity uses the leakage of the resonating fundamental mode as the reference. For the OMC this leakage field is buried in the strong HOMs at the carrier frequency. Our newly developed OMC alignment scheme circumvents this by marking the leakage field with a 6 kHz modulation [Aff⁺14] (it is thus called *modulated* differential wavefront sensing, MDWS) and the same technique could be adapted for squeezing alignment in the future.

4.3.4 Beam centring

Under ideal conditions, a DWS signal is in first order independent of the overall beam position on the QPD and depends only on the relative alignment of the beating light fields that we are interested in [Mor⁺94a]. However, under realistic conditions, in the presence of second-order mode mismatches or with unbalanced modulation sidebands, there will be a small first-order coupling of the spot position into the derived alignment signals. This can lead to time-varying lock-point errors in addition to variations of the error-signal strength. To avoid any pointing effects, almost all QPDs at GEO 600 use active beam centring [Gro03].

For most QPDs it is sufficient to make sure that the DC power is symmetrically distributed over the four quadrants, but for the beams at the interferometer output the HOM content makes this method unreliable. Instead, once more we make use

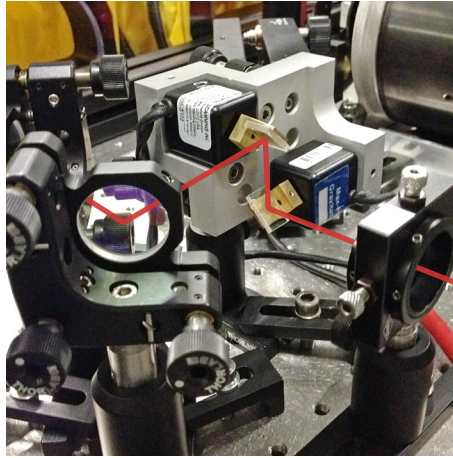


Figure 4.15: Galvanometer scanners for actively centring the beam on the QPDs.

of the spatially cleaner MISBs and centre them on the respective QPDs. This is achieved by detecting the power of the beat signal between the two sidebands at twice their modulation frequency $2f = 29.8$ MHz on the four quadrants. The centring is thus independent from the fluctuating HOM distribution at the carrier frequency. The $2f$ -centring technique was introduced to improve the signals for the differential arm alignment of the interferometer derived at the 1% pick-off port, where it proved to be very successful [Gro10]. We later also included $2f$ -centring for the newly introduced squeezing alignment sensors in reflection of the OMC. The centring control is implemented in analogue electronics with automatic gain normalization. It uses two galvanometer scanners per QPD for steering the beam (see figure 4.15) which provide a high actuation range of several degrees.

4.3.5 Gouy-phase telescope design

The set of two QPD alignment sensors in the OMC reflection path was specifically set up for the squeezing alignment and also to provide the signals for the newly developed fast interferometer-to-OMC alignment. The in-air optical setup includes lenses in order to achieve good Gouy phase separation of the sensors in a compact assembly. I designed the path layout using the software tool A LA MODE [Smi16] which allows for an automatic optimization of the parameters with user-defined criteria. The design goals were:

- Optimal Gouy-phase separation of 90° between the two QPDs.

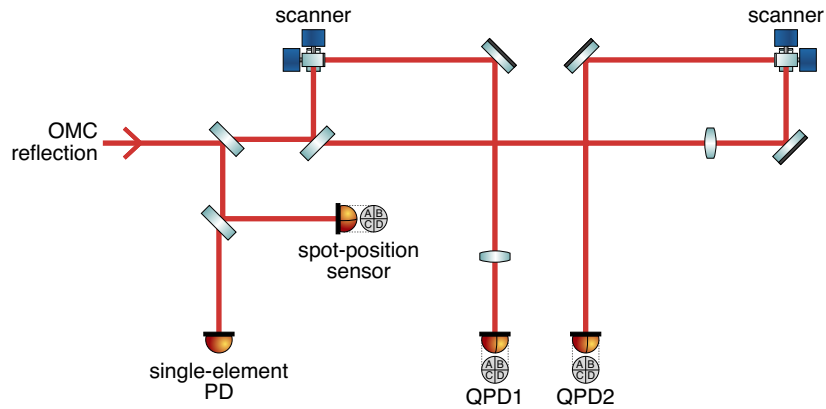


Figure 4.16: Optical layout of the OMC reflection path. The incident light is split into four parts: A single-element PD provides one of the possible squeezing-phase control signals (see section 4.2). A QPD without beam centring serves as a monitor for the overall beam pointing. The two further QPDs with beam centring can be used both for the squeezing alignment, as well as for alignment of the interferometer output field onto the OMC.

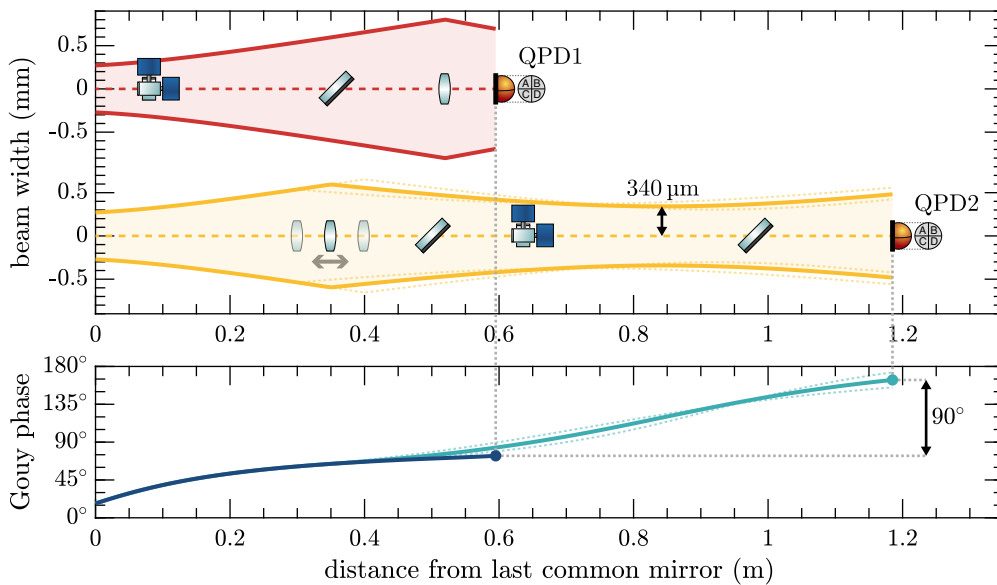


Figure 4.17: Model of the Gouy-phase telescope in reflection of the OMC, designed to provide optimal separation of the QPDs' sensing degrees of freedom. The separation can be tuned by at least $\pm 10^\circ$ by moving the lens in the QPD2 path.

Chapter 4 Squeezed light injection

- Spot size on the QPDs small enough to not clip, but large enough to not be affected by the gap between the quadrants [Wes16].
- Small spot size at the location of the scanners to fit the relatively small scanner mirrors.
- No beam waist on or close to an optic to avoid increased backscattering [Hil07].
- Compact overall design to fit the available space on the optical bench.
- Ability to fine-tune the Gouy-phase separation by moving a single lens.

The resulting optical assembly is depicted in figures 4.16 and 4.17.

The effectiveness of the simulation-aided Gouy-phase optimization was demonstrated when accidentally, due to a bug in the optimization objectives, the path was set up with 0° separation at first. Measurements in this state showed almost identical responses of both alignment sensors. Correcting the mistake and bringing the separation to the intended 90° immediately resulted in well-separated sensor responses.

4.3.6 Diagonalization of the alignment controls

The control loops for the automatic alignment of the squeezed beam are implemented digitally in CDS with only the fast demodulation at the beat frequency being done in analogue electronics. The digital control makes it easy to measure and set the correct actuation matrices that distribute the control signals to the actuator channels. We choose to implement the loops in the sensor basis: That is, each DWS signals from the QPDs is individually filtered and then fed back to a linear combination of the actuator channels. Ideally, the feedback derived from one error signal should not affect any of the other error signals.

The diagonalization was done in two steps: In a first step, we diagonalized the individual 3-axis piezo actuators. The actuators have three individual piezo elements arranged in a triangular pattern which need to be addressed in the right linear combination in order to get pure horizontal, vertical, or longitudinal actuation. We used a single QPD sensor (together with the squeezer-phase error signal for the longitudinal direction) to determine the right actuation matrix that minimizes the cross-talk between horizontal, vertical, and longitudinal degrees of freedom. The achieved separation between horizontal and vertical actuation is at least a factor

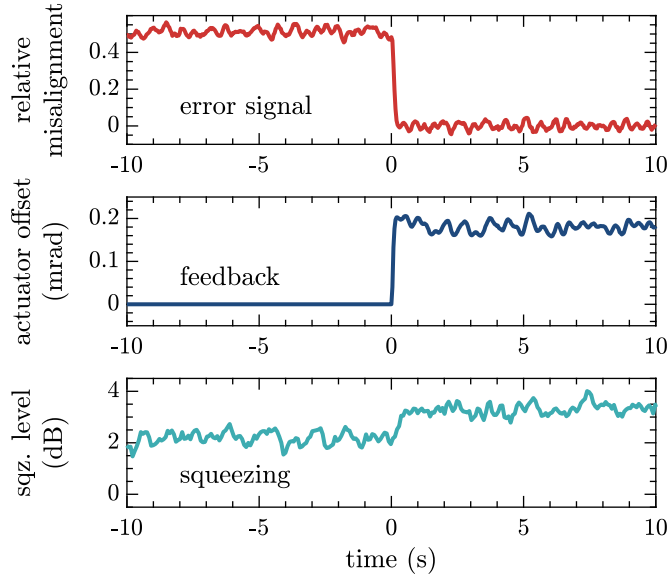


Figure 4.18: Switching the alignment control on. Starting from a state with one degree of freedom (here PZT2 rotation) severely misaligned, the alignment control is activated and drives the error point to zero, which improves the observed squeezing level.

of ten. Slight piezo nonlinearities that can lead to varying responses depending on the DC setpoint are one of the main limitations to reaching significantly higher separations. After the initial separation of the horizontal and vertical degrees of freedom, the second step was to determine the right combination of the two actuators to diagonalize the response with respect to the two QPDs.

The diagonalization is helped by the fact that the actuator responses have flat transfer functions within the bandwidth targeted for the squeezing alignment control.⁸ This means that the diagonalization can be frequency-independent. In one instance we observed excess angular-to-longitudinal cross-coupling at frequencies above 1 kHz. We were able to eliminate this by introducing analogue cut-off filters above the control bandwidth that prevent any unintended piezo actuation at high frequencies where the decoupling is no longer guaranteed.

4.3.7 Performance of the automatic squeezing alignment

The effectiveness of the alignment control is most obvious for correcting static offsets. Figure 4.18 illustrates the immediate improvement of the observed squeezing when activating the control from an intentionally misaligned state.

Throughout the last years we have been operating with different combinations of the available alignment signals that I described in section 4.3.3: As expected, the signals derived from the beat of the CCSBs with the carrier light are unreliable due to the influence of HOMs. So, we mostly used the signals referenced to the MISBs. Both sets of QPDs, at the pick-off port and in OMC reflection, can be used for this interchangeably. The higher available light power in OMC reflection does not yet play a significant role because in both cases technical noises currently limit the signal-to-noise ratio to similar levels. Figure 4.19 shows example spectra. Recently work is ongoing in the context of the new interferometer-to-OMC alignment scheme to improve the detection electronics of the OMC-reflection alignment sensors. This will also benefit the squeezing alignment control.

Figure 4.20 is a comparison of how stationary the squeezed shot-noise level is in different states of the alignment system: When aligning the squeezed light field to the carrier, lock-point errors lead to a varying shot-noise level. Aligning to the MISBs does not show this problem and the shot-noise level shows only the statistical fluctuations expected from pure Gaussian noise. However, the same is already true without any automatic alignment. This shows that (at the currently observed level of squeezing) free-running alignment fluctuations in the depicted frequency regime are small enough to not significantly impact the squeezing performance.

The effectiveness of the automatic alignment control can be demonstrated by intentionally introducing strong fluctuations. Figure 4.21 shows the very successful suppression of such an excitation that would otherwise completely spoil the squeezing level.

In regular operation, the alignment system shows its main worth as a reliable drift control. Without automatic alignment, drifts will accumulate noticeably over timescales of days, at which point manual realignment would become necessary. This can be even much more pronounced during times of experiments or maintenance work on the detector and the squeezed-light source. These can significantly affect the

⁸ In fact the piezo actuators include a passive low-pass filter at 8 Hz, but this is compensated in the digital filters.

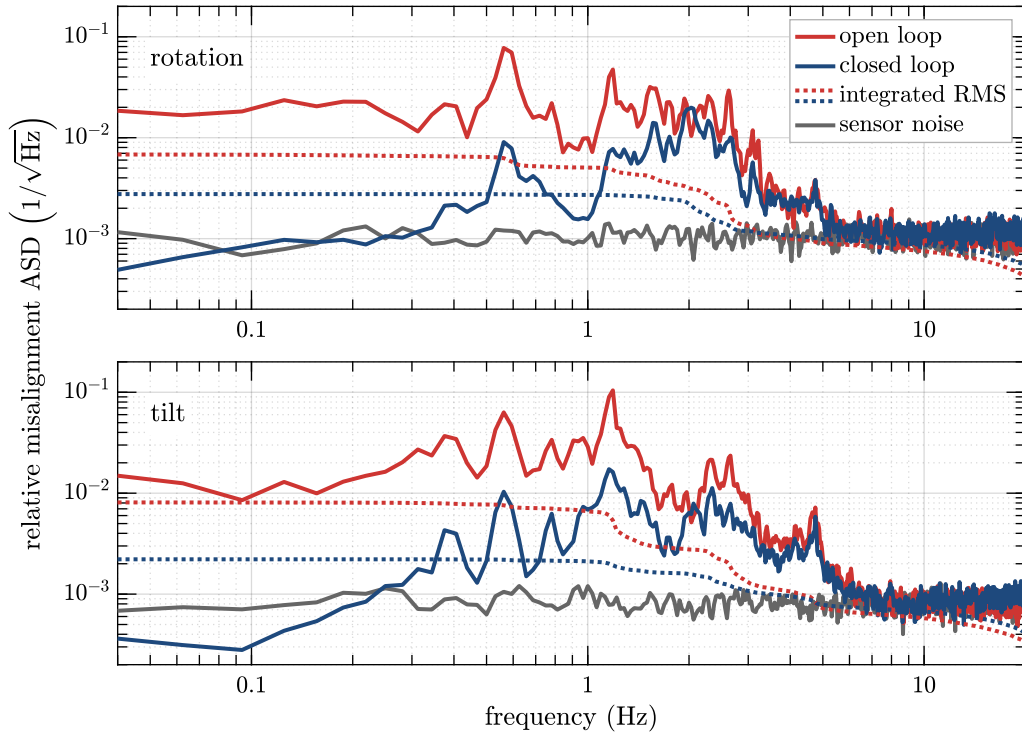


Figure 4.19: Spectra of horizontal and vertical alignment error signals from a QPD at the pick-off. In the depicted frequency band the RMS is dominated by alignment fluctuations caused by residual suspension movements and the alignment dithers used for the interferometer-to-OMC alignment. With the control loops closed, the fluctuations are partially suppressed up to the unity-gain frequency of about 3 Hz. The currently dominating alignment drifts happen at much lower frequencies and are very effectively cancelled by the control.

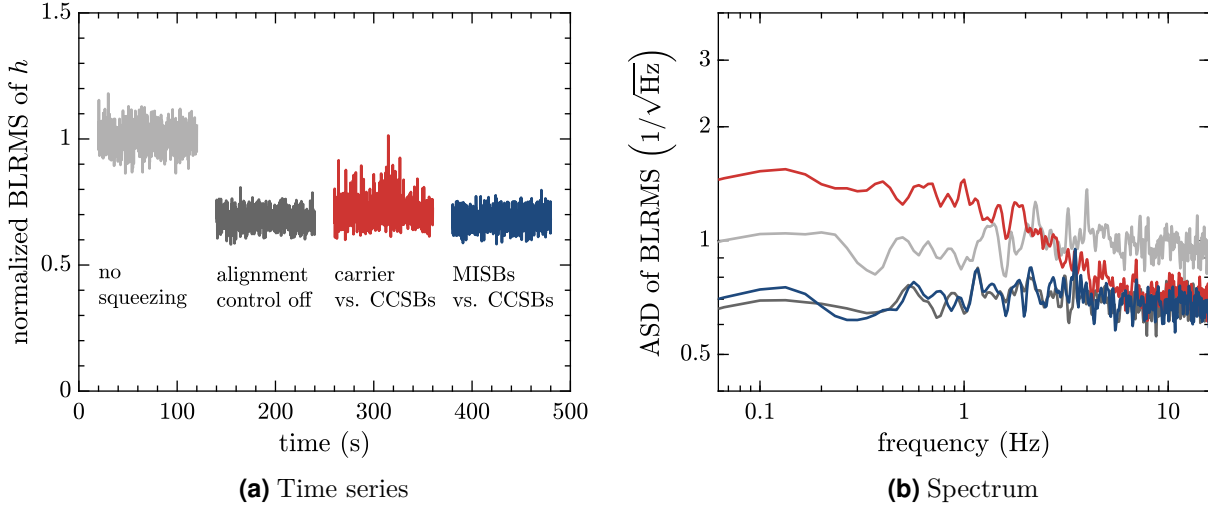
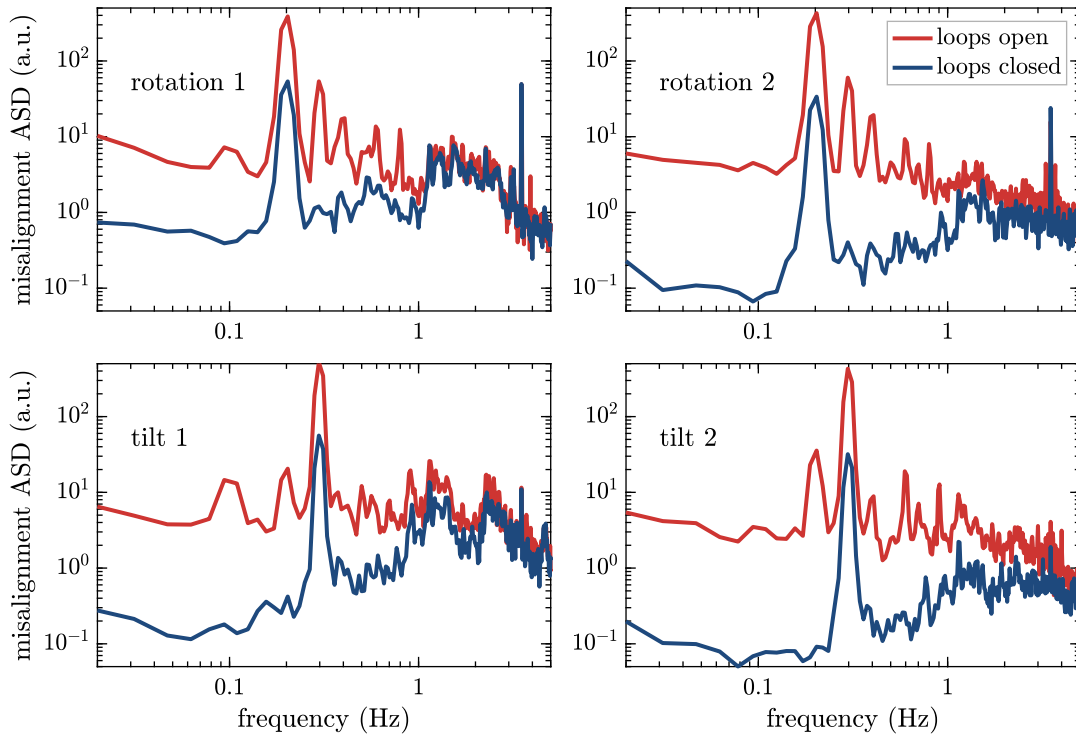


Figure 4.20: Squeezing-level fluctuations with different alignment-control signals. The alignment of the squeezed field was on average well centred for each of the states, but lock-point errors due to HOMs cause excess fluctuations when using the alignment signal derived from the interferometer carrier field. This plot uses the same parameters as in figure 4.5 that shows the similar result for the squeezer phase control.

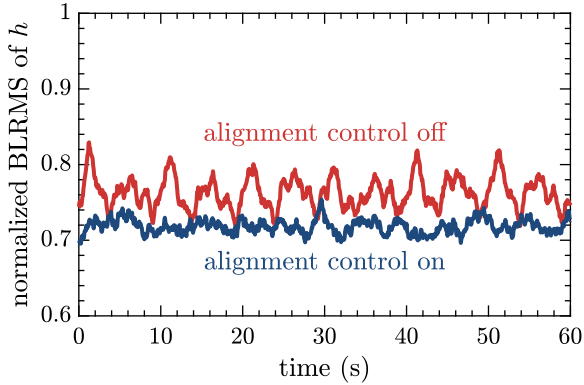
alignment. As an example, we have observed slight drifts of the light field leaving the squeezer when tuning the OPA temperature. Having an active alignment system helps greatly in such situations by reducing the number of parameters that need to be tracked and manually tuned.

It is currently sufficient to run the alignment control for only two of the four degrees of freedom, which already compensates almost all relevant misalignments over long periods of time. The remaining two uncontrolled degrees of freedom then have to be tuned by hand (or with the help of a semi-automatic script), but noticeable changes are only necessary every few months.

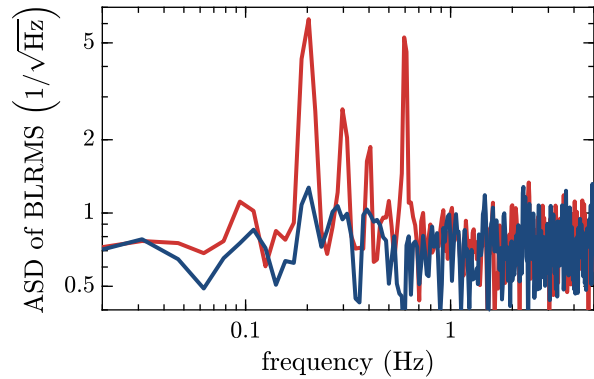
In the future with further improvements of the observed squeezing, especially by the reduction of other sources of loss, the requirements for good alignment will become more stringent. For this the current system is already well equipped and it can be further improved in the future.



(a) Alignment error signals



(b) Time series of shot-noise level



(c) Spectrum of shot-noise-level fluctuations

Figure 4.21: Suppressing an artificial alignment excitation. For this measurement strong alignment fluctuations were intentionally introduced in rotation (at 0.2 Hz) and tilt (at 0.3 Hz) which the automatic alignment system suppresses in all four sensing degrees of freedom. Without control, the alignment excitation degrades the squeezing and as a result the detector's shot-noise level fluctuates strongly at the excitation frequencies and their first harmonics. With activated control, the shot-noise level is stationary again, showing the effectiveness of the control.

4.4 Mode matching

In addition to the alignment of the beam axis, the waist size and longitudinal position also need to be matched between the squeezed beam, the interferometer beam, and the OMC eigenmode. Mismatches of the waist couple power from the fundamental mode to the second-order transverse modes. Two lenses in vacuum, together with one curved mirror in the output path form a mode-matching telescope to match the interferometer beam to the OMC (see figure 4.24 for an overview of all optics in the injection path). The matching is adjusted manually by moving the two lenses along the beam path. One of the lenses is mounted on a linear piezo-motor stage with a range of ± 5 mm for remote fine adjustment even with the vacuum tank closed [Wit15].

The direct matching of the interferometer carrier field to the OMC is once more hindered by the presence of the strong HOMs, in particular second-order modes. Instead, we again use the Michelson sidebands as the reference. The mode matching is adjusted to minimize the second-order transmission peaks of the MISBs in a mode scan of the OMC (see figure 4.22). We achieve a remaining mode mismatch of (1.0 ± 0.6) % for the MISBs. In a separate measurement we confirmed that the optimal mode matching for the interferometer carrier coincides with the optimal matching of the MISBs to within 1.5 %.

The mode matching of the squeezed light field can be adjusted separately with two dedicated in-air mode-matching lenses. We use the squeezer's bright alignment beam, bouncing it off the signal-recycling mirror with an unlocked interferometer, to judge the remaining mismatch in a mode scan of the OMC. A simulation shows that the mode matching is about ten times more sensitive to differential shifts of the lens positions than to their common position (see figure 4.23). Therefore, in order to simplify the adjustment in these two degrees of freedom separately, we have build a jig that moves both lenses together and allows for fine control of their distance with a micrometre screw.

We succeeded in reducing the second-order mode mismatch of the squeezed field to (1.5 ± 0.3) %. The remaining mismatch is dominated by astigmatism of the beam and thus cannot be corrected by longitudinal movements of the lenses alone. Simulations with the beam-propagation tool OPTOCAD [Sch14] show that the observed astigmatism is well explained by the fact that the curved mirror in the interferometer output path (BDO1) is hit under a small angle of about 3.5° , giving it slightly different effective radii of curvature in the horizontal and vertical plane. First tries to compensate this by additionally tilting one of the in-air mode-matching lenses

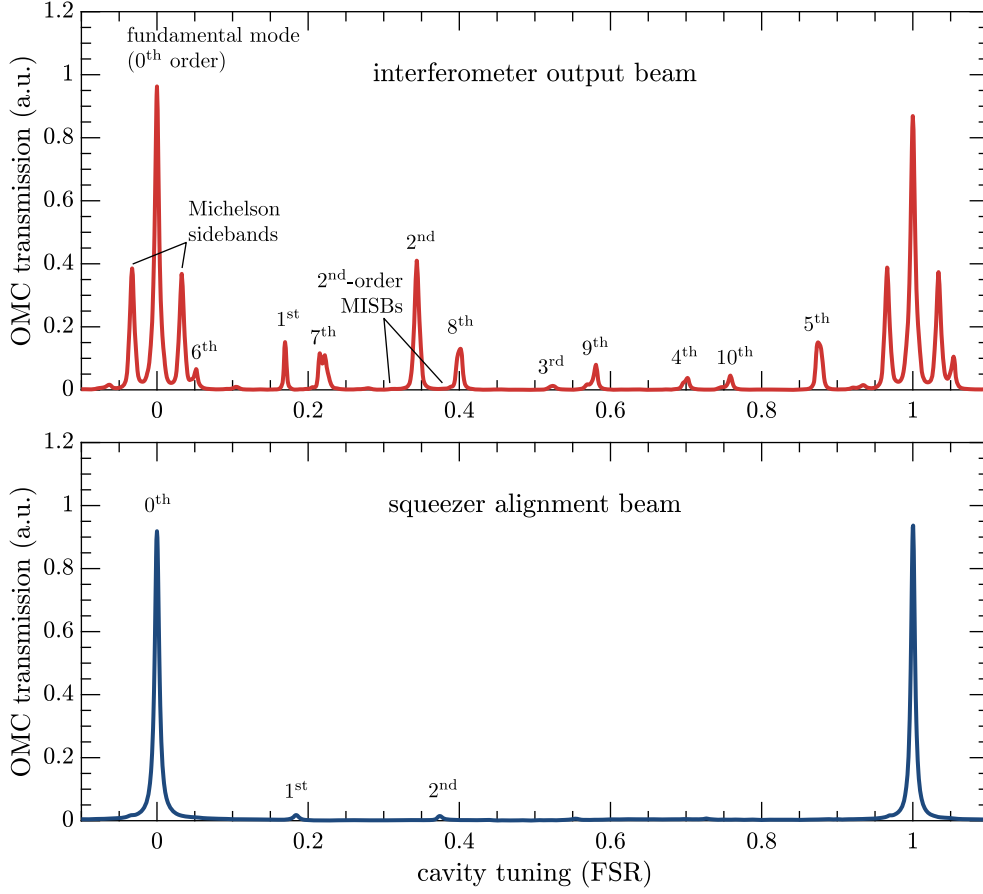


Figure 4.22: Mode scans of the OMC for the output of the locked interferometer (upper panel) and for the squeezer’s bright alignment beam (lower panel).⁹

were not successful because the required tilt limited the free aperture too much. For achieving near-perfect mode matching beyond 99 % in the future it might therefore be necessary to include an element in the injection path specifically designed to correct the astigmatism, like another curved mirror hit under an angle, or even thermally adaptive optics [Liu⁺13; Bro⁺16].

The mode matching is not expected to drift significantly: Longitudinal distances

⁹ At the time of the mode scan for the squeezer’s bright alignment beam a partly damaged suspension of the signal-recycling mirror introduced excess alignment fluctuations. This is why the mode scan shows a noticeable peak for the first-order mode. It is assumed that this is not a contributing factor during normal operation of the interferometer when the signal-recycling mirror is controlled by its active alignment system.

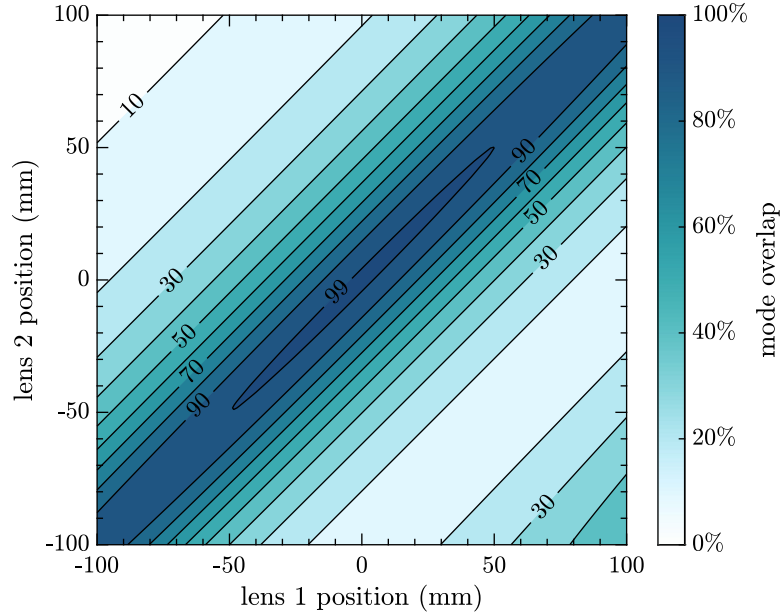


Figure 4.23: Influence of the two mode-matching lenses on the mode overlap between squeezed beam and OMC.

along the optical path have to change in the order of millimetres for an additional mismatch of 1%. Such shifts are only likely when the beam path is actively changed during commissioning work. We also checked whether thermal lensing inside the OPA¹⁰ might cause variations of the squeezer’s output mode, but we did not find a measurable influence. For these reasons, it is not foreseen that automatic mode-matching (analogues to the automatic alignment system) will soon become necessary. Good manual tunability of the mode-matching degrees of freedom is, however, key for achieving and maintaining very high mode overlap.

¹⁰ Thermal lensing is a well established effect, for example, in GEO 600’s input optics, though at much higher power levels [Aff14].

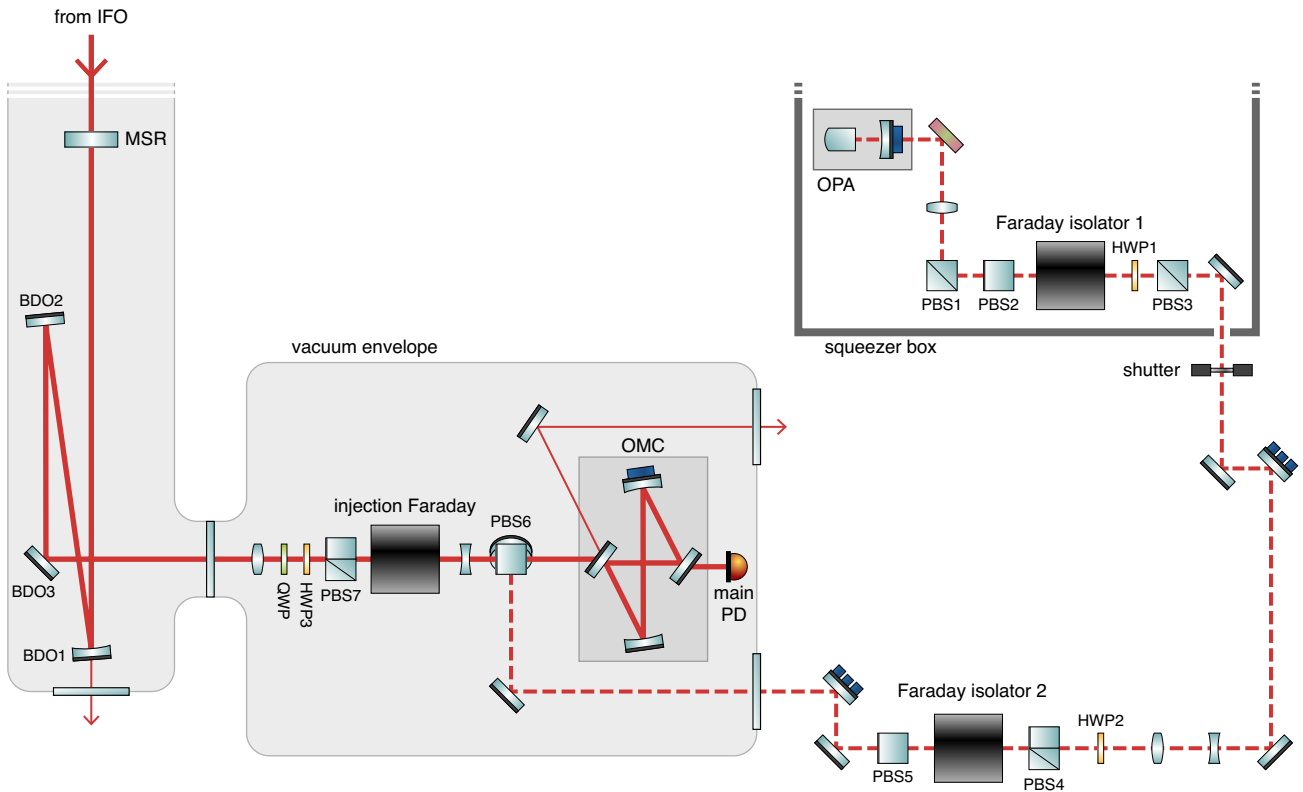


Figure 4.24: Overview of the complete squeezing injection path from the OPA to the OMC.

4.5 Optical losses

By far the most important limitation of the observable squeezing at GEO 600 is the combined effect of all optical losses that the squeezed vacuum field experiences on its way from the OPA, via the interferometer, to the detection PD. Figure 4.24 shows another schematic drawing of the injection path, this time with all optics included. Between the OPA and OMC the squeezed beam passes many highly-reflective mirrors, mode-matching lenses, AR-coated windows of the vacuum system, waveplates, polarizing beamsplitters, and Faraday rotators. Considering that many of these optics have multiple optical surfaces and that some of them are passed twice, there are more than 80 optical surfaces that the beam traverses. High-quality optics are used and individual losses are very small, but their combined contributions are significant.

4.5.1 Measuring optical losses

Most of the propagation losses along the path that the squeezed beam will experience can be measured with the help of the squeezer's bright alignment beam (see section 3.4.1). For this, we used either a calibrated photodiode powermeter or a simple large-area photodiode to measure the power of this beam at various positions. The power decrease along the path then is a direct measure of the optical losses that are present. There are, however, limitations to the accuracy of this technique:

- Fluctuations or drifts of the alignment beam's power level can influence the readings. Actively stabilizing the beam's power with the help of a pick-off PD in the squeezer box (as described in section 3.4.1) helped, but could not easily eliminate all fluctuations on the scale of fractions of a percent.
- Ambient light could introduce systematic errors and it was necessary to switch off all room lights for high-precision measurements.
- The photodiode response can vary by several percent depending on the exact spot where the beam hits and the angle of incidence. This makes it hard to reliably compare measurements done in different positions. We tried to mitigate this effect by always searching for the maximum response and by repeating measurements several times, but an uncertainty remains.
- Some positions along the beam path (especially within the vacuum system) were hard to access and close to the interferometer the beam size is too large to be captured completely by the PDs. So for certain sections of the path, only the overall losses could be determined.

With these limitations, the remaining uncertainty of the loss measurements is in the order of 1%. This means most low-loss components could not be confidently measured individually in situ. But we could measure combined losses along different sections of the path, getting very consistent results within the uncertainty (see section 4.5.6 for a summary of the results).

For a more fine-grained analysis, we additionally performed dedicated lab measurements of individual components. Two different methods were used to reduce the uncertainty of the measurements: In the first method, the differential power of two balanced beams paths was measured in a setup similar to a homodyne detector. The tested optic was then placed in one of the paths and the resulting power difference was recorded (see figure 4.25a). For the second method, we used an amplitude modulated

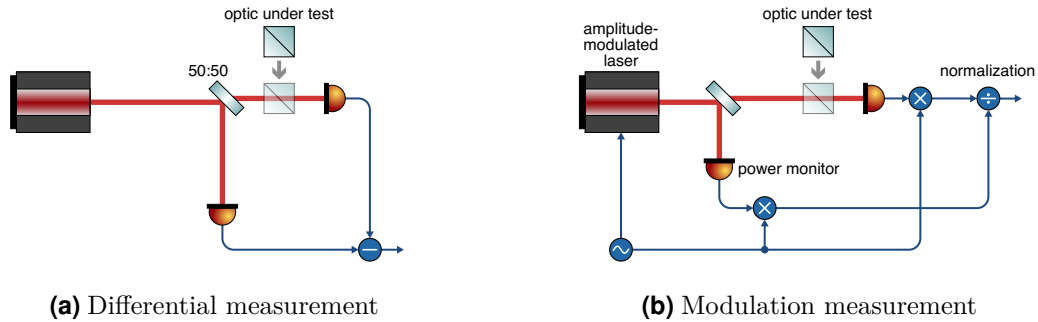


Figure 4.25: Two possible setups for accurately measuring losses of optical components in a dedicated lab measurement. Not shown are mode-matching lenses to get the beam to a comparable size as in the real injection path and additional polarizers for preparing the test beam in a very clean linearly polarized state.

laser beam and measured the modulated PD signal with a lock-in amplifier, thus avoiding disturbances at DC (such as ambient light). We additionally normalized all measurements with the laser output power, determined by a separate monitor PD (see figure 4.25b). Both methods yielded an uncertainty in the order of 0.05 %.

We characterized different polarizing beamsplitter (PBS) cubes from the same batch as the ones installed in the injection path at GEO 600 and got varying results for different specimens between $(0.23 \pm 0.05) \%$ and $(0.63 \pm 0.04) \%$ loss when properly tuned. State-of-the-art polarizers have demonstrated losses as low as 0.02 % [Ske⁺01] so this shows potential for improvements, especially when considering that the squeezed field currently passes nine polarizers on its way to the photodetector. Apart from the obvious dependence of the transmission on the polarizer’s rotation with respect to the polarization of the beam, we also found that the angle of incidence on the PBS played a measurable role: Optimal transmission as well as optimal extinction are reached not for normal incidence, but for slightly different offsets of a few degrees (see figure 4.26), indicating that explicit tuning of this degree of freedom is necessary for best performance.

4.5.2 Polarization effects

The many polarizing optics in the injection path that make up the injection Faraday rotator and two further Faraday isolators needed for backscatter isolation (see section 4.6) need to be well matched to each other for the beam to pass freely. A

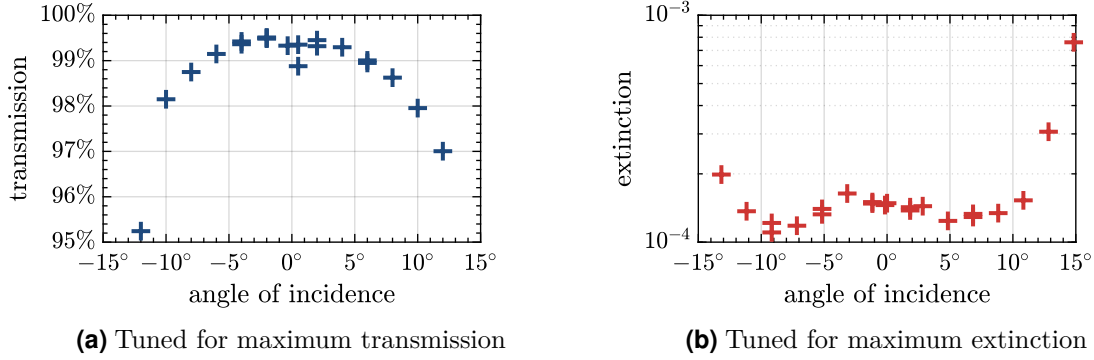


Figure 4.26: Measured angle-of-incidence dependence of a PBS tuned for maximum transmission (left panel) and maximum extinctions (right panel).

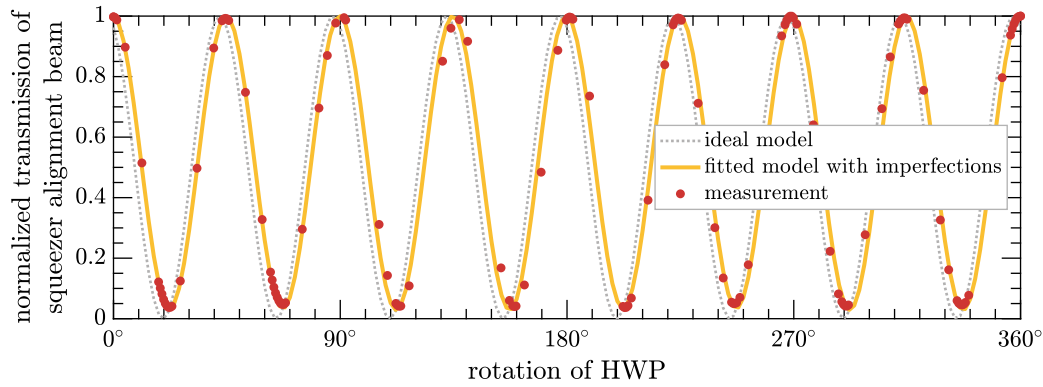
mismatch of the linear polarization by an angle α leads to a loss

$$l_{\text{pol}}(\alpha) = \sin^2 \alpha. \quad (4.5)$$

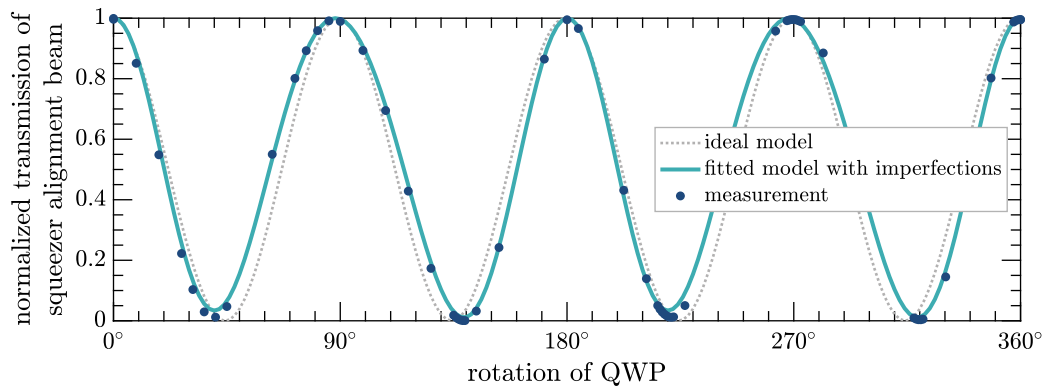
Spurious birefringence can additionally cause a slight ellipticity of the polarization which will also lead to optical losses on transmission through the linearly polarizing elements that follow.

For the in-air part of the injection path, all polarizers are held in fine-adjustable rotation mounts. Two half-wave plates (HWPs) serve to rotate the polarization (in order to assure that all optics are hit in either p- or s-polarization) and give additional freedom for adjustments. Optimizing the polarization for best transmission of the squeezed light field is relatively straightforward by using the bright alignment beam and minimizing its rejection at each of the polarizers it needs to pass.

The situation is slightly more complicated for the in-vacuum part of the beam path where the squeezed light field travels alongside the interferometer output beam: Initially, a single HWP on a remote-controlled rotation stage served to match the polarization of the interferometer to the injection Faraday. The Faraday's polarizers are not easily rotatable and thus cannot be tuned in situ. Ideally, the transmission of the squeezed beam should not depend on the setting of the HWP because it passes it twice, thus picking up a retardation of a full wavelength. Observationally, however, we found that the transmission of the squeezed beam significantly depended on the setting of the HWP and that optimal transmission for the squeezed field and optimal transmission for the interferometer field required waveplate settings several degrees



(a) Turning the half-wave plate



(b) Turning the quarter-wave plate

Figure 4.27: Measuring the transmission of the squeezer's alignment beam through the injection Faraday while individually turning the in-vacuum wave-plates. The measured values deviate from the assumed ideal situation, but they are well explained by including an additional parasitic birefringence in the model.

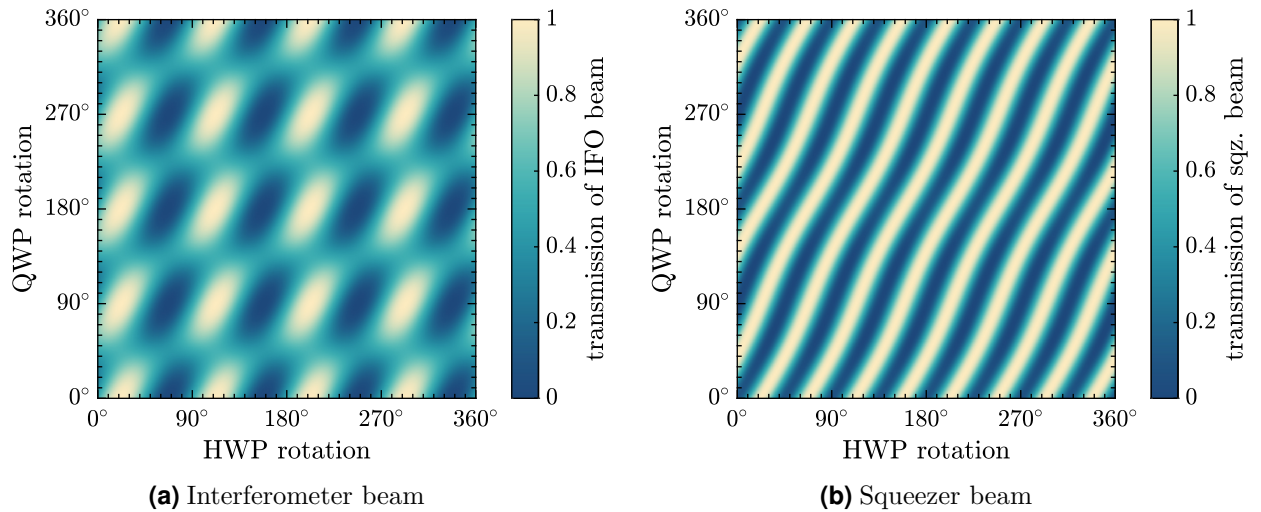


Figure 4.28: Simulated influence of waveplate settings on the transmission of the interferometer beam (left panel) and the squeezed beam (right panel). The squeezed beam is influenced in a different way because it passes the waveplates twice. The model includes the same estimated imperfections as in figure 4.27.

apart.¹¹

To investigate this further and to gain more control over the polarization we installed an additional remote-controlled quarter-wave plate (QWP) between interferometer and injection Faraday (see figure 4.24). By experimentally testing the influence of both waveplates on the two different light fields and comparing the results with a simulation (using a MATLAB toolbox that implements the Jones calculus [Vog14; Col05]) we could determine the observed deviations from the ideal behaviour are not consistent with imperfections of the waveplates. The observation can, however, be fully explained by assuming a slightly birefringent element in the optical path between interferometer and Faraday isolator (see figure 4.27). This parasitic birefringence adds an ellipticity to the polarization of the squeezed beam in the order of 4%, which would lead to a loss if not compensated with the help of the QWP. The most likely source of this imperfection is stress-induced birefringence in a window between the main vacuum system and the separate chamber that houses the Faraday, OMC and detection PD.

¹¹ The transmission of the squeezed beam through the in-vacuum path was measured once more with the bright alignment beam, bouncing it off the signal recycling mirror with an unlocked and misaligned interferometer, and measuring it in reflection of the OMC.

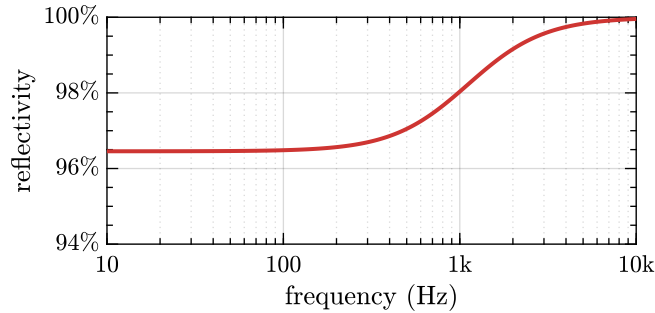


Figure 4.29: Simulated power reflectivity of the signal-recycling cavity for the squeezed field.

The simulations show that the combination of HWP and QWP is enough to theoretically achieve perfect transmission for both fields (see figure 4.28). In practice, the optimization in the two degrees of freedom is made difficult by the fact that the piezo motors for the remote rotation have inconsistent step sizes, in particular when driving them in both directions, making it hard to keep track of the exact position within the parameter space. We partly compensated for this limitation by mounting cameras to visually read off the waveplate rotation through viewports in the vacuum tank (which only yielded inaccurate results due to awkward viewing angles). In the future, the task of tuning the in-vacuum waveplates could be simplified by using mounts with rotary encoders.

4.5.3 Reflection off the interferometer

Once injected through the Faraday, the squeezed light field counterpropagates along the interferometer's output path. The locked Michelson interferometer effectively acts like a highly reflective mirror which together with the 90 % reflective signal-recycling mirror forms an over-coupled cavity. The effective reflectivity of the signal-recycling cavity for the squeezed field is then frequency dependent: Below the signal-recycling pole frequency of 1120 Hz the squeezed light field experiences the intra-cavity losses of the interferometer, which are in the order of 1000 ppm per round-trip, enhanced by the signal recycling factor. Above the pole frequency the squeezed field is reflected with high efficiency. Figure 4.29 shows the result of a FINESSE simulation for the reflectivity of signal-recycling cavity. The effective loss for low-frequency squeezing is estimated to be 3.5 %. In the frequency band from 1 kHz to 5 kHz, where squeezing is most important because shot-noise is dominating GEO 600's sensitivity, the reflection loss lies between 2 % and 0.2 %.

4.5.4 Transmission through the OMC

The output modecleaner contributes optical loss for the squeezed light field in the form of rejected light and through losses due to imperfections of the optical surfaces. With the squeezer's bright alignment beam we can directly measure the remaining light power that is reflected off the OMC when locked to the fundamental mode. Comparing this to total power reflected when the OMC is completely off-resonance gives the ratio of rejected light, which we measure to be $(5 \pm 1) \%$ (at its best tuning). Of this, about 0.5% are first-order modes caused by residual misalignment. 1.5% can be attributed to second-order modes due to the remaining astigmatism (as discussed in section 4.4). Mode scans of the OMC reveal that the remaining 3% are distributed among the many small transmission peaks of even higher-order modes. Since the OMC has a polarization degeneracy it will also reject light in the wrong polarization if there is a small mismatch between the OMC and the last polarizer. The resulting peak is, however, not resolvable in the mode scan, indicating that such a mismatch is below 0.2% .

The losses of the OMC that the fundamental mode experiences were measured in a dedicated lab experiment before its installation at GEO 600. For the currently installed OMC the losses were determined to be $(3.7 \pm 0.5) \%$. For an older but essentially identical model of the OMC [Wit15] more than 1% of loss was later attributed to the residual reflection of the input coupler's AR coating.

4.5.5 Quantum efficiency of the detection PD

The final effective loss for the squeezed light field comes from the non-perfect quantum efficiency of the main photodiode. GEO 600 uses a custom-made indium gallium arsenide (InGaAs) photodiode. The quantum efficiency of two identical photodiodes from the same manufacturing batch was determined by Vahlbruch et al. [Vah⁺16] to be $(99.5 \pm 0.5) \%$. In that experiment the efficiency was additionally increased by carefully optimizing the angle of incidence and by sending the residual AR reflection of about 0.3% back onto the photodiode. This technique is not used at GEO 600 where we thus expect an efficiency of about 99% .

4.5.6 Loss budget of the injection path

Combining the information from the various loss measurements throughout the injection path, we can derive an overall budget of all contributing losses that limit

loss mechanism	effective loss (%)
finite OPA escape efficiency	7
lenses, HR mirrors, etc.	3
in-air Faradays (two passes)	2×3
injection Faraday (two passes)	2×4.5
reflection off interferometer	1
pick off (two passes)	2×1
OMC mismatch (all mode orders combined)	5
OMC loss	4
finite PD quantum efficiency	1
total losses	32

Table 4.2: Loss budget of the squeezing injection at GEO 600. The listed losses describe the best estimates of the situation at the end of 2016.

the observed squeezing. In the following, I will describe the estimated loss budget as it was by the end of 2016 when, after a number of improvements of the input path, we had reached the highest squeezing levels so far of over 4 dB:

Starting at the squeezer, the OPA's escape efficiency is estimated to be 93% based on earlier homodyne measurements (see section 3.5). The losses of the two in-air Faraday isolators (including the polarizers and waveplates) were measured with the bright alignment beam to be about 3% each. The alignment-beam measurements also revealed additional propagation losses on the path between the OPA and the injection Faraday that were too small to attribute to specific locations but together contribute another 3% of power reduction. The combined losses of the in-vacuum path can be judged by comparing the power of the alignment beam power before entering the vacuum system and in reflection of the off-resonant OMC. With the interferometer unlocked, this loss is 19.5%. When taking into account the 10% transmissivity of the signal recycling mirror and the 1% pick-off (passed twice by the beam) this leaves an estimated 4.5% for each of the two passes through the injection Faraday. Finally, adding the losses of the reflection at the signal-recycling cavity, the OMC losses, and the PD's quantum efficiency results in an estimate for the total effective squeezing losses of 32%. This is consistent with the observed squeezing (see section 5.3). These results are summarized once more in table 4.2.

At the beginning of this thesis work at the end of 2012 the total losses had been roughly 55%. The improvement was achieved by the combined effect of a large number of

smaller steps. The most important of these were work on the mode matching between squeezer, interferometer and OMC, an extensive set of experiments to tune the in-air and in-vacuum polarization optics for best squeezing transmission, and a redesign of part of the injection path to reduce the number optical components.

4.5.7 A new design for the Faraday isolator assembly

Looking at the loss budget we can see that one of the most important contributions comes from the three Faraday isolators (one of them passed twice). Together they contribute an estimated 14% of optical loss. This is especially interesting since the total loss is higher than what the combination of all losses of the individual components would suggest, indicating that polarization mismatches between the components play a role which we might be able to improve by tuning alone.

There are two important requirements for achieving good tuning: On the one hand we need fine-grained control of all important tuning degrees of freedom (which include the polarizer rotations, angles of incidence, and the amount of polarization rotation of the Faraday rotator [Leo16]), on the other hand we need good figures of merit, ideally by measuring the light power not just in transmission of the complete assembly, but also at every external port of the polarizers.

To fulfil these requirements we have redesigned the Faraday isolator assembly. The plan is to first replace the in-vacuum Faraday and if successful, the same design will also be used for one or both in-air isolators. The main new feature of the assembly is the inclusion of photodiodes directly into the PBS mounts to monitor the light exiting at the rejection ports of the polarizers (see figure 4.30). This means that the rejected light power can be measured consistently while rotating or tilting the polarizers. We chose to use quadrant photodiodes and so additionally gain position information for the alignment of the beam through the centre of the assembly.

The whole setup is mounted on a breadboard. This allows us to do all initial tuning and characterization in the convenient environment of a cleanroom lab before moving the finished assembly into the vacuum chamber at GEO 600. It is expected that the final tuning needs to happen in situ.

For the in-vacuum Faraday there is a relatively large amount of light coming from the interferometer that is in the wrong polarization and is rejected by the first polarizer. This light needs to be effectively dumped so as to not cause stray light in the vacuum chamber that could reach the main photodetector and spoil the sensitivity. For this

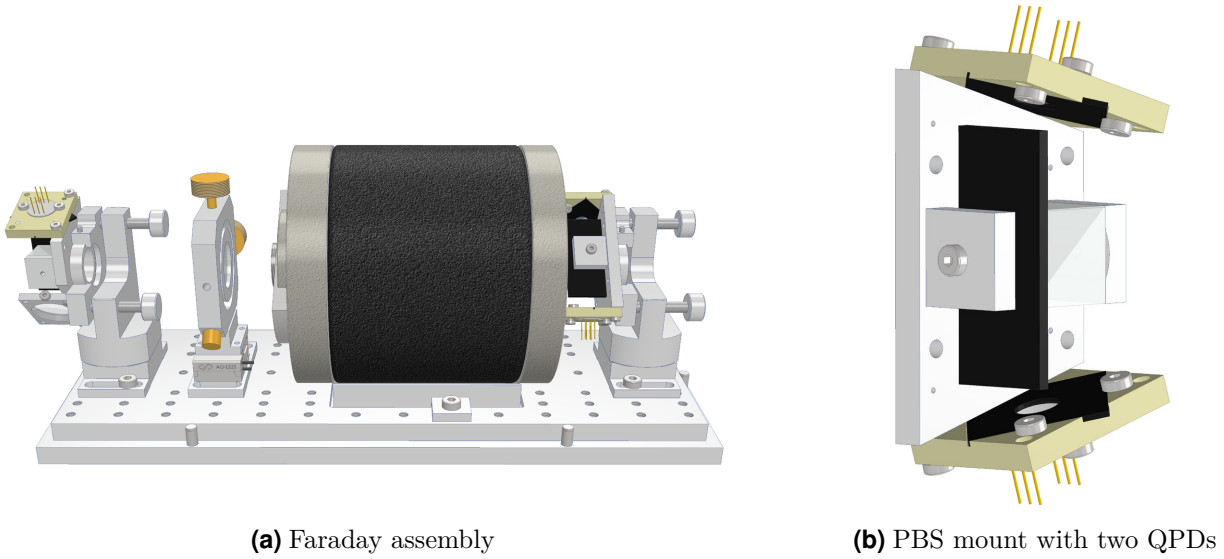


Figure 4.30: Drawing of the new Faraday assembly. The PBS mounts are equipped with quadrant photodiodes for the monitoring of all rejected light fields. The complete assembly is mounted on a common breadboard. For the in-vacuum Faraday a mode matching lens will be included within the Faraday assembly due to spatial constraints.

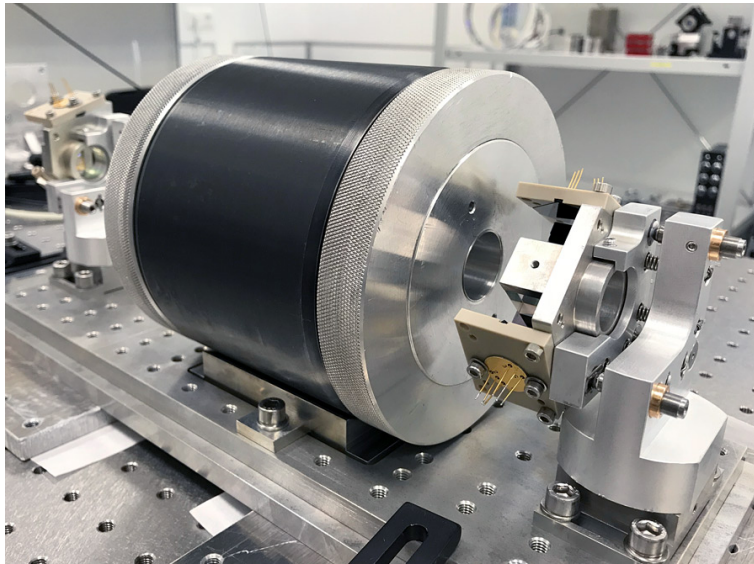


Figure 4.31: Photo of the completed Faraday assembly during characterization in the cleanroom lab.

Chapter 4 Squeezed light injection

reason, the design of the PBS mounts includes specifically cut black-glass absorbers that shield the edges of the quadrant photodiodes and contain the residual reflection of the photodiode's active area.

We successfully assembled the first new Faraday isolator off-site and were able to test its performance. Measurements were performed with an amplitude-modulated laser beam as described in section 4.5.1. After careful tuning, helped specifically by the new monitor ports, an isolation of (43.5 ± 0.1) dB was achieved and the double-pass loss of the complete assembly was measured to be (1.25 ± 0.78) %, corresponding to a single-pass loss of (0.62 ± 0.38) %. These are very good values that already achieve the typical targets laid out in designs for squeezing in third-generation detectors [Bar⁺12]. The installation of the Faraday in GEO 600 will follow as the next step.

4.6 Backscattering

Imperfections of the injection Faraday will couple some small fraction of the interferometer output beam into the squeezing injection path, travelling backwards towards the OPA. Stray light that reaches the OPA in the same spatial mode and polarization as the squeezed light field will be scattered back with high efficiency, eventually reaching the main photodetector where it will contribute unwanted noise. The in-air Faraday isolators are there to reduce the back-propagating stray light field with the goal to reduce its effect to an insignificant level.

As described in section 2.2.4, backscattering can cause linear and nonlinear coupling of the stray light field’s random phase fluctuations $\Phi + \delta\phi$ to the detector signal, as well as a linear coupling of the residual squeezing-angle fluctuations $\delta\theta$. To repeat the result, the analytically derived backscatter noise signal is

$$i_{\text{bsc}}(t) \approx \sqrt{\frac{\eta_{\text{inj}} P_{\text{stray}}}{P_{\text{out}}}} [e^{-r} \cos(\Phi) - e^{-r} \sin(\Phi) \delta\phi - 2 \sinh(r) \sin(\Phi) \delta\theta], \quad (4.6)$$

with squeezing parameter r .

4.6.1 Coupling of stray-light phase fluctuations

We studied the effects of backscattering by artificially introducing low-frequency path-length modulations of the squeezing injection path with the help of a longitudinal piezo actuator. For sufficiently large amplitudes, larger than one wavelength, the nonlinear coupling (described by the first term in equation 4.6) can up-convert the slow phase fluctuations into the detection band. This effect produces a characteristic ‘scattering shoulder’ in the spectrum of the detector output signal [Hil07].

Figure 4.32 shows the result of such an induced-backscattering experiment. The measurement was done both with and without pumping the OPA. As predicted by equation 4.6, the amount of backscattering depends on the OPA’s nonlinear gain. With the squeezing angle tuned for reducing the shot-noise, the backscatter noise is also attenuated by about the same factor.

Applying higher squeezing factors thus only improves backscattering due to stray-light phase fluctuations. We can therefore set an upper limit on the impact of this form of backscattering by looking at the detector’s output signal in the state where stray light reaches the OPA without any pump applied. This can then be compared to a

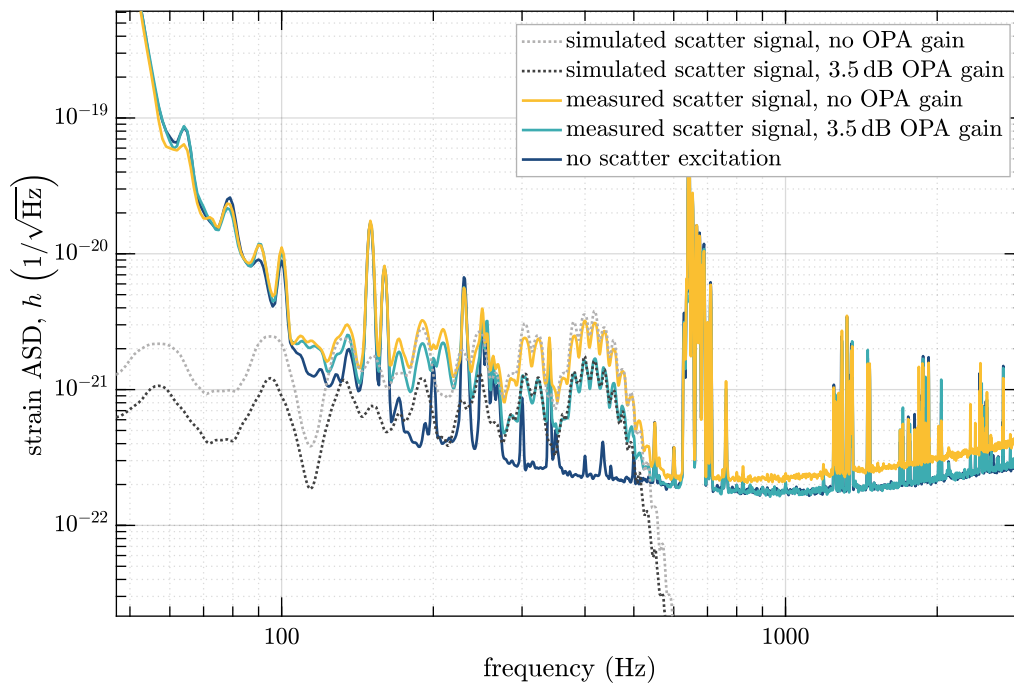


Figure 4.32: Backscatter noise in the interferometer output signal with an intentional large-amplitude excitation of the injection path length. The characteristic ‘scattering shoulder’ is visible. It is well modelled by a numerical simulation. When squeezing is applied, the backscattered noise is deamplified by the squeezing factor as predicted. The applied modulation had a peak-to-peak amplitude of 47 rad at a frequency of 19 Hz.

situation where the squeezer path is completely blocked with a high-quality beam dump. For GEO 600 no difference in the measured noise level was observed, showing that stray-light phase fluctuations are not a limiting source of noise at any frequency within the detection band. Experiments for the squeezing demonstration at LIGO Hanford had come to similar conclusions but could also show that for the more demanding requirements of future advanced detectors the backscatter immunity was not yet adequate at low frequencies [Chu⁺14]. This indicates that better optical isolation or more path-length stability will be needed at some point.

4.6.2 Linear coupling of squeezing-angle fluctuations

Another form of backscatter-induced detection noise is the linear coupling of squeezing angle-fluctuations as described by the third term of equation 4.6. We had first noticed experimental evidence for this effect when we observed an unexpected degradation of the squeezing level for high nonlinear-gain settings of the OPA. Initially this was attributed to excess RMS phase noise of the squeezer which would lead to similar observations. Backscattering was found as the underlying mechanism when it became clear the problem had started due to a lowered isolation of one of the Faraday isolators after a rerouting of the path through the respective optics. Subsequent experiments could confirm this by intentionally lowering the backscatter isolation and observing the effect on the squeezing level. Figure 4.33 shows the result of such an experiment, where a very small rotational offset of one of the Faraday’s polarizers introduced strong backscattering.

The additional noise on the photodetector caused by this form of backscattering is mostly white in GEO 600’s shot noise-limited frequency band (scaled to equivalent gravitational-wave strain h it will rise with f above the signal-recycling pole). This is because the residual squeezer phase noise $\widetilde{\delta\theta}(f)$ at these frequencies is also approximately white (see section 4.2). The coupling is additionally modulated with the sine of the randomly fluctuating mean phase of the stray light field ($\sin(\Phi)$ in equation 4.6). This was observed experimentally as a random variation of the noise level on second timescales. If we could control the mean phase of the stray light field to $\Phi \approx 0$ this would strongly mitigate the backscatter coupling. However, this phase depends on the uncontrolled path length of the in-air injection path and there is no readily available error signal.

The predicted scaling of this backscatter noise with the OPA’s nonlinear gain was confirmed: In contrast to the scattering due to fluctuations of the stray light field alone, the new effect rises for higher squeezing levels and is also independent of

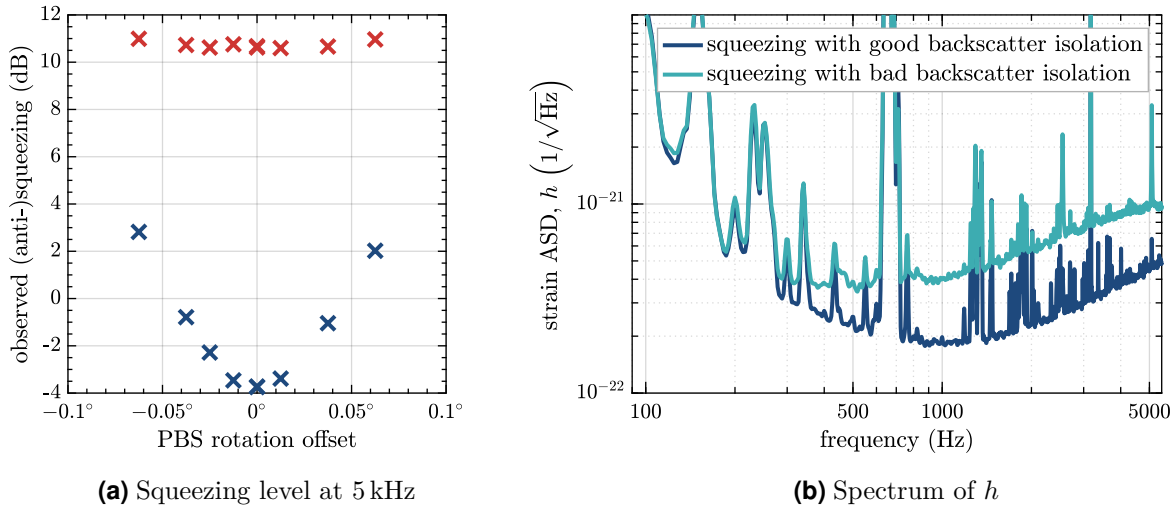


Figure 4.33: Observed detector noise when intentionally reducing backscatter isolation. Offsetting one of the polarizers by only 0.05° leads to excess noise that completely degrades the squeezing performance. The left panel shows the measured squeezing and antisqueezing levels for different isolations. The right panel shows a spectrum of the detector output signal h for good and bad backscatter isolation.

whether squeezing or antisqueezing is applied.

Now that the effect is identified, further quantitative analyses will need to follow in order to make confident statements about its magnitude that can also be applied to future squeezing at other detectors.

4.6.3 Optimizing the backscatter isolation

Over the past two years, limiting amounts of backscattering were a reoccurring problem, triggered either by excess squeezer phase noise (related to the laser malfunctions described in section 3.2) or by suboptimal optical isolation (mostly after work on the injection path). The isolation was tuned several times by fine adjusting the polarizer rotations and angles of incidence. As can be seen in figure 4.33, small polarizer rotations have a much larger impact on isolation of the Faradays than on the transmission.

In-situ measurements of the isolators showed that the injection Faraday couples interferometer light into the squeezing path with an isolation of (31 ± 2) dB and that

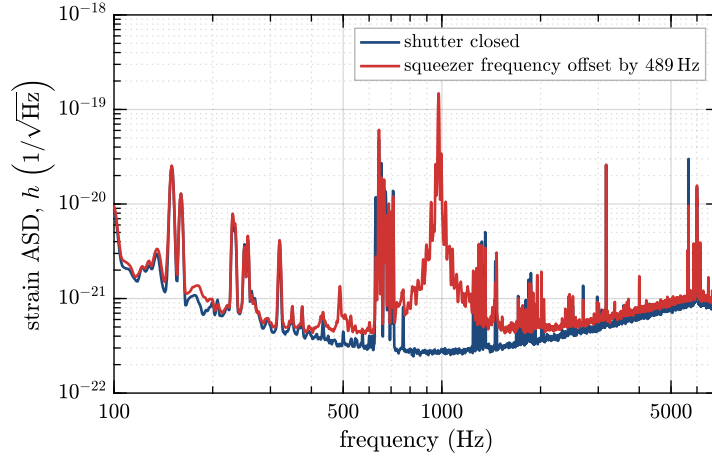


Figure 4.34: Backscattering with squeezer frequency offset.

the next in-air Faraday isolator adds another (32 ± 2) dB of isolation. At the second in-air isolator the power levels are too low to directly measure the isolation. It is however important to note that these values give the total power reduction measured over all impinging polarizations and modes. The isolation for the specific polarization and mode that matches the squeezed mode in the OPA might be different (better or worse).

In order to get a direct measure of the power of the stray light field reaching the OPA in the relevant mode we can offset the squeezer's master laser frequency with respect to the interferometer carrier: In this situation stray light photons from the interferometer at the carrier frequency will undergo difference-frequency generation in the OPA, creating light with a sideband frequency of twice the offset frequency. Interference with the interferometer carrier then leads to a strong beat signal in the interferometer output with an amplitude proportional to the square root of the stray-light power P_{stray} (see figure 4.34 for an example). This method proved to be a sensitive and very direct tool for in-situ optimization of the backscattering. Because it does require a locked interferometer the method could not be used for tuning the in-vacuum injection Faraday.

For the newly designed Faraday assembly described in section 4.5.7 it is likely that with the additional monitoring capabilities the same high isolation of over 40 dB that was demonstrated in the lab can also be reached once installed in the injection path. Thus improved, it is expected that backscatter noise will be at an insignificant level for GEO 600.

4.7 Electronic dark noise

In GEO 600's shot-noise limited frequency band above about 1 kHz the next highest technical noise source originates from electronic noise of the readout circuit. This circuit converts the PD's photocurrent into a voltage that is then digitally acquired. The presence of electronic noise will limit the amount of detectable squeezing (see section 2.2.2). Ideally, the noise should be significantly lower than the shot noise. This section will briefly summarize the results of a newly developed readout circuit for GEO 600 which are published in [Gro⁺16].

A basic photodiode detection circuit uses an ohmic resistance R to convert the photocurrent I into a voltage $U = IR$ (see figure 4.35a for an example circuit). The resistor experiences a fundamental thermal noise called *Johnson noise*. We can analyse this noise in relation to the shot-noise level in terms of their amplitude spectral densities: Without squeezing applied the ASD of the photocurrent's shot noise scales with the square root of the DC current \bar{I}

$$\tilde{I}^{\text{sn}}(f) = \sqrt{2e\bar{I}}. \quad (4.7)$$

Like the shot noise the Johnson noise is frequency independent. It scales with the square root of the temperature T [Joh28]:

$$\tilde{I}^T(f) = \sqrt{\frac{4k_{\text{B}}T}{R}}, \quad (4.8)$$

with Boltzmann constant k_{B} . We are interested in maximizing the ratio

$$\frac{\tilde{I}^{\text{sn}}}{\tilde{I}^T} = \sqrt{\frac{e\bar{I}R}{2k_{\text{B}}T}}. \quad (4.9)$$

The DC current \bar{I} will result in a voltage $\bar{U} = \bar{I}R$ so that we can rewrite the noise ratio as

$$\frac{\tilde{I}^{\text{sn}}}{\tilde{I}^T} = \sqrt{\frac{e\bar{U}}{2k_{\text{B}}T}}. \quad (4.10)$$

This shows us two obvious methods of decreasing the Johnson noise compared to the shot-noise level: We can increase the photocurrent and with it the detection voltage or we can lower the temperature of the resistor. Using high-voltage electronics or operating at cryogenic temperature both are technically challenging. A third option is to use a frequency dependent impedance that is small at DC, thus keeping \bar{U} low, but large in the detection frequency band to optimize the noise ratio.

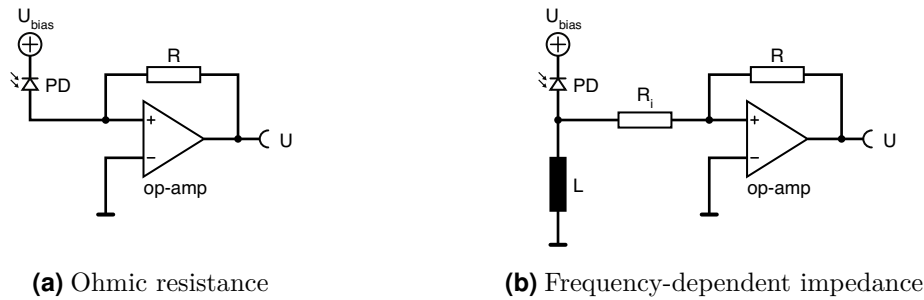


Figure 4.35: Detection schemes for photocurrent to voltage conversion.

A frequency-dependent readout impedance was implemented at GEO 600 in the form of a high-inductance coil. A simplified diagram of the circuit that was used is shown in figure 4.35b. At DC the photocurrent flows through the inductor L to ground and no high-voltage signal is generated. At audio frequencies most of the photocurrent flows towards the operational amplifier where it is converted to a voltage.

A large inductance of 2 H is used in order to achieve the desired frequency response. One challenge was to find a suitable core material for the coil. First tests revealed strong glitches in the readout signal triggered by low-frequency fluctuations of the photocurrent which were linked to Barkhausen noise [Wei09]. This problem was solved by the use of mu-metal as the core material which did not show any signs of Barkhausen noise.

The final circuit performed as predicted by simulations and successfully lowered the electronic noise of the detection electronics by more than a factor of 4 compared to the previous readout electronics that did not use a frequency-dependent impedance (see figure 4.36). In the old setup the electronic dark noise had been a factor of 7 below the unsqueezed shot noise level, which (following equation 2.85) has an equivalent effect of 2% optical losses. The new electronics reach a dark-noise clearance of 30, corresponding to an almost insignificant loss of 0.1%. At the time of the implementation an increase of the resulting squeezing level by 0.2 dB was observed which exactly matched the expectation.

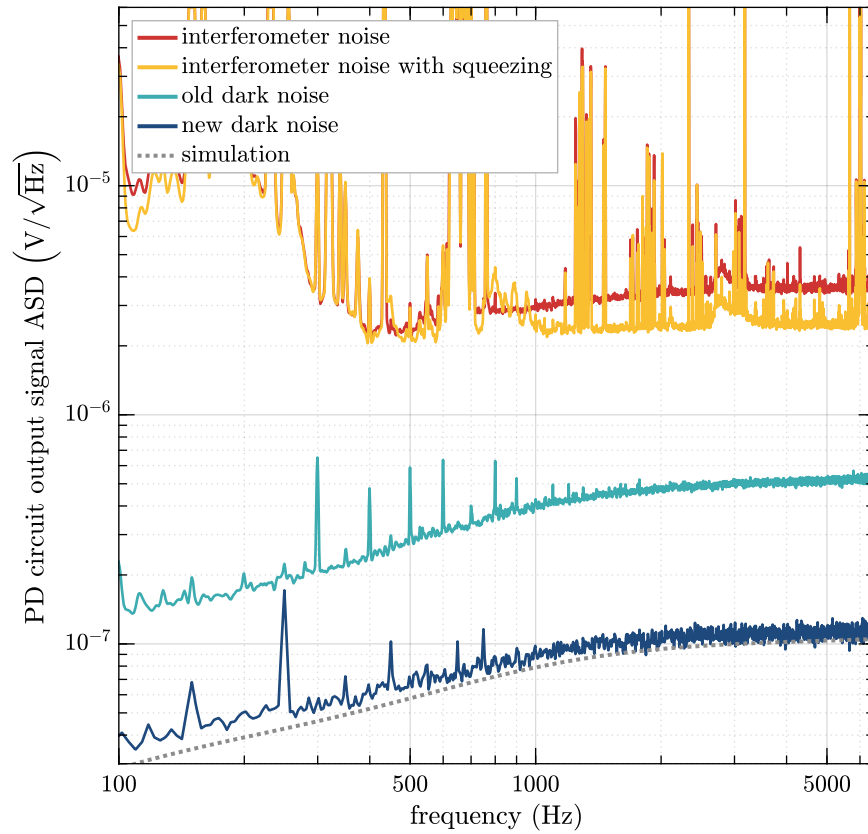


Figure 4.36: Improved dark noise with the new readout electronics. Shown here is a spectrum of the raw output signal from the main PD detection circuit. With the new readout electronics the circuit’s dark noise is reduced by about a factor of four, significantly increasing the dark-noise clearance of the detected signal.

Characterization and long-term performance

The success of the application of squeezing is ultimately determined by the impact it has on the detector noise. To characterize this we use a number of tools. Getting accurate and repeatable squeezing numbers for the achieved squeezing is important information during commissioning in order judge the effect of small changes.

This chapter presents the methods and conventions used for reliably measuring the squeezing performance, both after the fact by comparison to reference times without squeezing, as well as online. I will also describe how measurements of the observed squeezing and antisqueezing can be used to accurately estimate the parameters that characterize the imperfection of the squeezing injection, such as losses and phase noise.

The chapter will end with a description of the overall squeezing performance over the last years of operation.

The online squeezing monitor and the analysis of long-term trend data described here are based on earlier work by Jacob Slutsky and Hartmut Grote.

5.1 Detection-noise improvement by squeezing

The main result of squeezing at GEO 600 is immediately apparent when looking at the detector’s output signal for a time with and without squeezing. This is shown in figure 5.1. Above 300 Hz the noise floor is lowered by the squeezing and the detector’s peak sensitivity at around 1 kHz improves by a factor of 1.3. The highest improvement is reached above 4 kHz where the noise floor is almost completely dominated by shot noise.

The increased sensitivity is obtained without introducing additional noise at any other frequency and without negative side effects for the data quality. An analysis of noise transients (‘glitches’) in data stretches with and without squeezing applied confirmed that there is no increase of the glitch rate [Gro⁺13; Doo⁺16]. At the few times where the squeezed-light source experiences technical issues that would lead to excess noise in the interferometer the automatic shutter control (see section 3.6) reliably decouples the squeezer completely from the interferometer.

5.2 Measuring squeezing levels

It is easy to look at the plot of the output spectrum with and without squeezing and read off the approximate improvement of the high-frequency noise floor by eye. However, for making accurate and comparable statements we need to define exactly how we want to measure the squeezing level.

Due to the significant amount of technical noise features in a typical sensitivity spectrum of a gravitational-wave detector, the ratio between squeezed and unsqueezed noise will in general be different for different frequencies. The classical noise contributions will not be effected by the squeezing and so can partially mask the improvement of the quantum shot noise. To get a good figure of merit for commissioning of the squeezing injection at GEO 600 we choose to measure the squeezing ratio at the high-frequency end of the detection band (around 5 kHz) where most technical noises are significantly below the shot-noise level. Additionally we choose to only consider the improvement of the unresolved noise floor, disregarding the effect of the most prominent noise peaks that are known to be of a technical origin.¹

¹ At the same time we do not subtract the dark noise for calculating the squeezing level. Subtracting known contributions to the noise floor could be done to get the ‘pure’ quantum noise reduction, this would however only be indirectly related to the actually observed noise improvement.

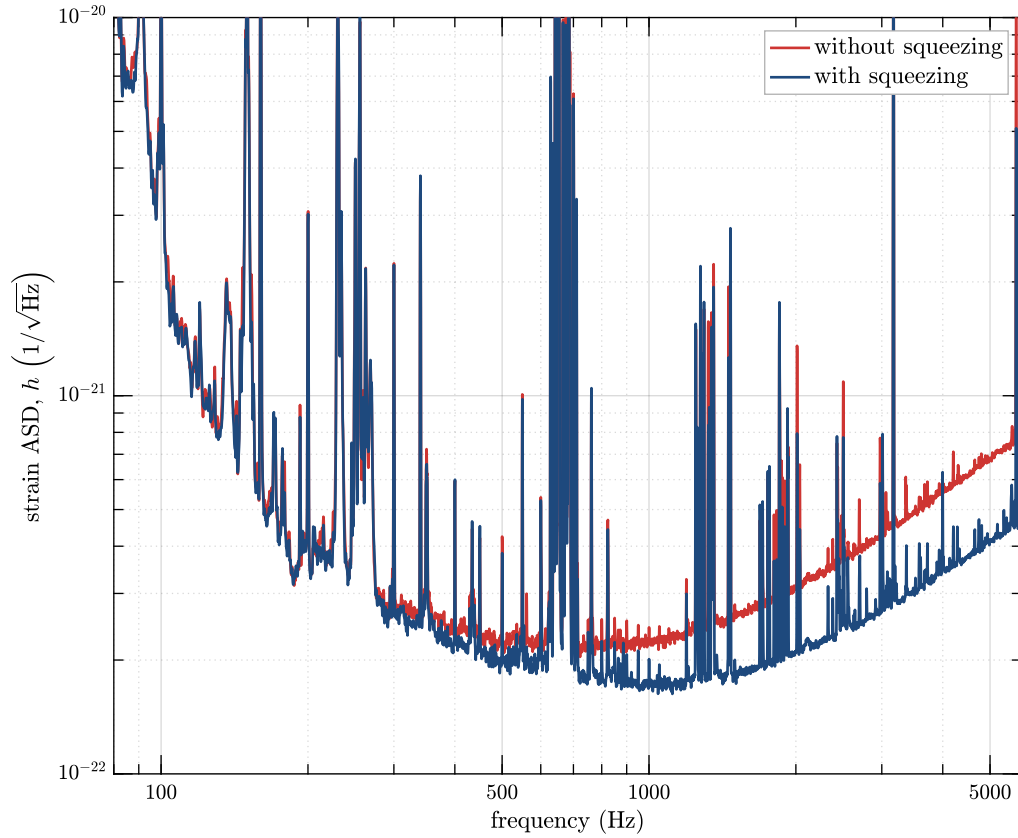


Figure 5.1: Spectrum of the detector output signal h with and without squeezing. At high frequencies where the noise is dominated by shot noise the squeezing improves the noise floor by a factor of 1.66 or 4.4 dB. This constitutes the highest observed squeezing level for GEO 600. The spectra are taken from two adjacent four-minute reference times and use a spectral estimation with logarithmic frequency resolution [TH06]. The prominent spectral lines around 650 Hz and its harmonics are caused by the violin modes of the interferometer suspensions.

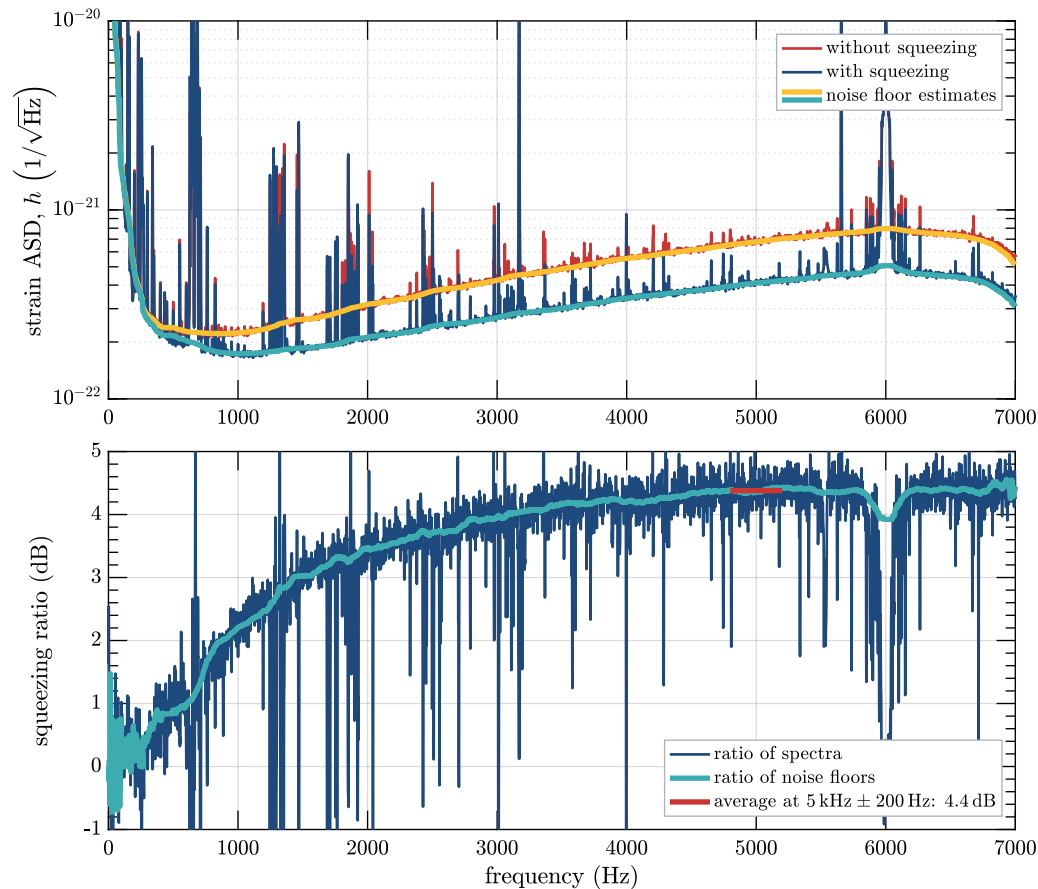


Figure 5.2: Calculating the squeezing level as the ratio of the squeezed and unsqueezed noise floors. The broad peak at 6 kHz is caused by a longitudinal modulation of the OMC. Above 6 kHz the calibration of the spectra is no longer correct and the falling noise floor is an artefact of the signal acquisition filters.

The reference level of unsqueezed shot-noise can vary over time, for example when the amount of circulating power inside the interferometer is changed. These changes need to be taken into account for calculating an accurate squeezing level. This is most easily achieved by taking a reference without squeezing at a time close to the squeezing reference, when the detector was known to be in the same state.

5.2.1 Calculating squeezing level from two reference times

I have written a simple MATLAB script for the automated calculation of the squeezing level using two reference times with the squeezer shutter open and closed. The script

performs the following steps:

1. Calculate the power spectral densities of $h(t)$ for the reference times with and without squeezing.
2. Estimate the noise floor of the spectra. This is done by running a windowed median filter over the spectral data after removing peaks by discarding outliers above the 80th percentile.
3. Calculate the spectral ratio of the two estimated noise floors.
4. Average the ratio over the frequency band of interest.
5. Convert to decibel.

The result of these calculations is illustrated in figure 5.2 (using the same reference times as in figure 5.1).

The result of this algorithm is repeatable to within about ± 0.1 dB. This makes it possible to assess even small changes of the squeezing injection.

5.2.2 Online estimation

During commissioning work such as tuning, but also to judge the long-term performance of the squeezing, it is desirable to additionally have a continuously updating online estimation of the currently observed squeezing level. We have implemented such a monitor signal in the digital real-time system CDS. Instead of relying on a reference time for the unsqueezed noise level it works with a fixed calibration, but automatically adjusts for changes of the light power level on the main photodetector.

The real-time code includes the following steps:

1. Generate a band-pass filtered version of the uncalibrated photodetector signal in the shot-noise limited band of interest.
2. Apply notch filters to remove known noise peaks and calibration lines.
3. Calculate the band-limited RMS value of the cleaned signal over a certain time

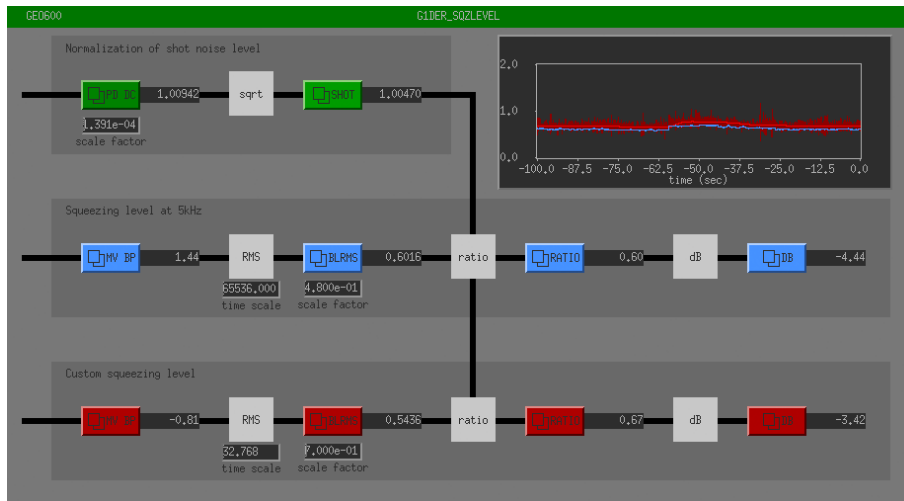


Figure 5.3: Interface of the online squeezing-level monitor.

window.

4. Normalize this with the square-root of the DC signal from the photodetector and a calibration factor.
5. Convert to decibel.

The absolute calibration can be adjusted by closing the squeezer shutter and making sure that the stated squeezing level without squeezing applied is 0 dB. This calibration step is performed by a simple script and could in the future be run regularly (for example whenever the shutter closes during science time) for a fully automated self calibration.

Figure 5.3 shows the MEDM interface of the online squeezing-level monitor. Two monitor channels are implemented in parallel. This allows it to adjust the monitored frequency band and the averaging time to the specific needs of different commissioning tasks.

5.3 Estimating parameters of the squeezing injection

Section 2.2 showed how to calculate the resulting squeezing levels for known imperfections, such as losses, phase noise, dark noise, and backscattering. Turning this around, we can also estimate the parameters of the imperfections from the observed

5.3 Estimating parameters of the squeezing injection

squeezing levels. This is an important tool as it can give a very reliable independent measure of the actual total imperfections.

The basic principle is to vary the amount of input squeezing by changing the pump power of the OPA and observe the resulting squeezing level at the detector output. Additionally, the squeezing phase can be offset by 90° to record the amount of antisqueezing. We can then fit the obtained data with a theoretical model that includes the different imperfections as variable parameters.

The fitted model can be expressed in the form of measured squeezing and antisqueezing as a function of the OPA pump power. In this case the nonlinear gain needs to be calculated for the applied pump power (following equation 3.1). This requires the threshold power as an additional model parameter which can either be measured in a separate measurement or be included as a free parameter in the fit. However, as was discussed in section 3.4.1, the actual nonlinear gain shows deviations from the theoretical model caused by thermal effects in the OPA crystal.

As an alternative method we can also fit a model of observed squeezing as a function of observed antisqueezing. This completely eliminates the need to estimate the nonlinear gain. We have applied both methods for the analysis of our gathered data and find that they give compatible results with similar uncertainty for the estimated parameters. However, the second method gives better confidence in the derived data as it eliminates an important source of systematic error.

An important limitation of the parameter estimation is that, as shown in section 2.2.5, the effects of backscattering and RMS phase noise, as well as dark noise and optical losses are mutually almost indistinguishable. We therefore fit a simplified model that includes only phase noise and losses, but then need to consider that this will misidentify backscattering as phase noise and dark noise as losses. Figure 5.4 shows the apparent phase noise for different levels of backscattering.

Over the course of the last years, we repeatedly performed characterization measurements with the described method of varying the pump power and recording and squeezing and antisqueezing levels. The results of three of these are shown as examples in figure 5.5. The resulting estimates of the total optical loss (including the effects of OPA escape efficiency and detection efficiency) range from 36 % to 44 % and are compatible with the independently estimated noise budgets at the respective times (see section 4.5.6). Estimates for the RMS phase noise vary significantly. For two of the shown cases the apparent phase noise was much higher than the expected value (see section 4.2.5). These measurements were taken at times when

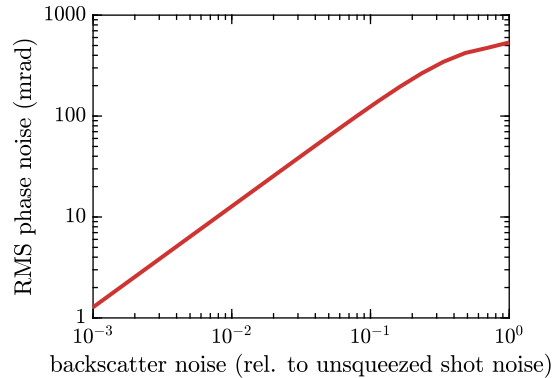


Figure 5.4: Apparent RMS phase noise as a function of backscattering. This plot shows the level of RMS phase noise that we get if we fit a model that considers only phase noise and losses to data that includes backscattering. So, for example, a backscatter level that is a factor 100 below the shot noise in the unsqueezed case would look like 13 mrad of phase noise. The plot assumes 40 % optical losses.

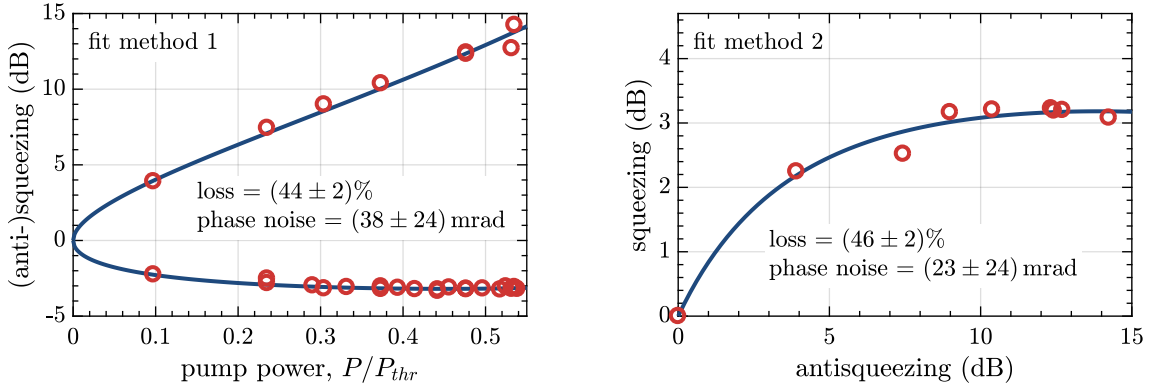
the Faraday isolators were tuned suboptimally and are thus explained by the effect of backscattering. For the third case, the best fitting model actually assumes 0 mrad of phase noise, but with a significant uncertainty. Comparison between the observation and the model gives an upper limit of 25 mrad of phase noise. If we assume that the actual phase noise level is 17 mrad as estimated in section 4.2.5 this gives an upper limit for backscattering at a level of 0.01 relative to shot noise.

5.4 Squeezing performance over the years at GEO 600

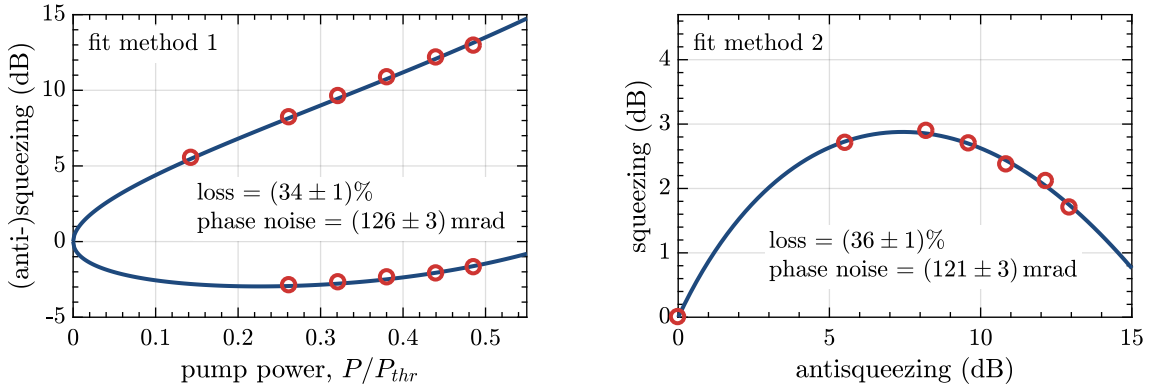
A reduction of the shot-noise level by squeezing was first observed at GEO 600 in 2010 reaching a squeezing level of up to 3.5 dB in a not yet continuous operation [LSC11]. During this first demonstration of squeezing GEO 600 was still using a different signal-recycling mirror (with a transmission of $T = 1.9\%$) which was exchanged at the end of 2010 as part of the GEO HF upgrade programme [Wil⁺06; Doo⁺16]. After this change squeezing was re-established and was put into quasi-continuous operation by the end of 2011. At this point the achieved squeezing improvement was about 2.0 dB.

Over the following years (which are covered by this thesis since the end of 2012) many small improvements of the injection efficiency resulted in a gradual increase of the observed squeezing level. Figure 5.6 shows a histogram of the effective squeezing

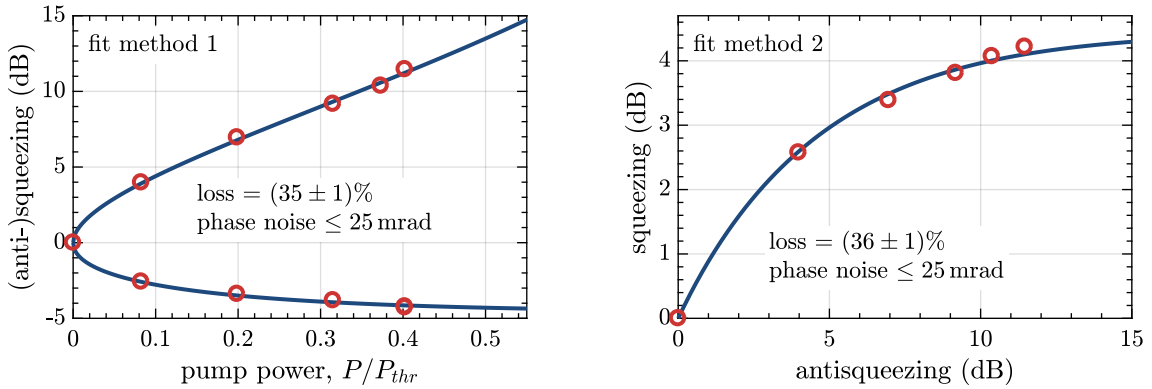
5.4 Squeezing performance over the years at GEO 600



(a) 2014-12-12



(b) 2016-03-17



(c) 2016-06-06

Figure 5.5: Estimating losses and phase noise. These plots show the results of two different methods for fitting a theoretical model to data measured while varying the OPA pump power. The estimated parameters are shown in the plot. The stated uncertainty reflects the statistical error only. The fitted model does not consider backscattering or dark noise.

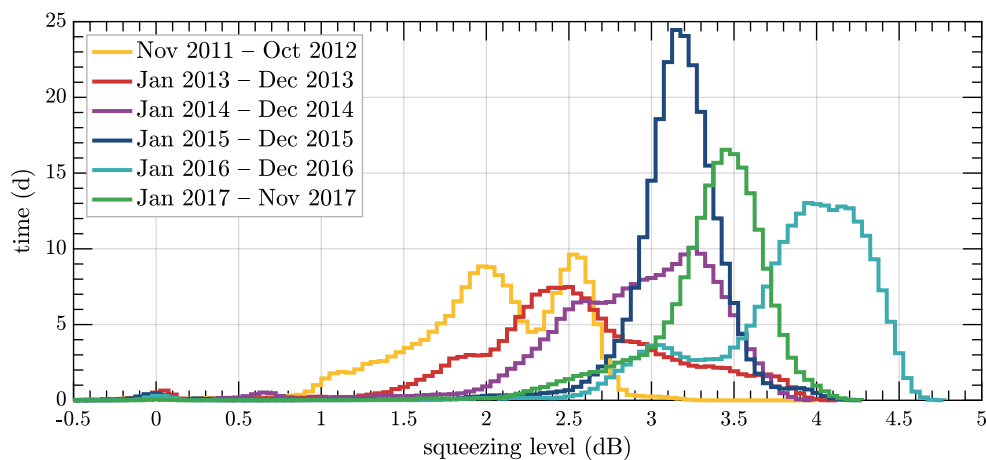


Figure 5.6: Histogram of the achieved squeezing level over the last six years of operation.

level for the years 2012 to 2017.²

After renewed efforts to optimally tune the mode matching and polarization of the squeezed beam, the best squeezing performance so far was reached in 2016 with several weeks at a level of 4.3 dB to 4.4 dB and a median squeezing level of 3.9 dB over the complete year.

In 2017 limitations of the available pump power due to degrading squeezer optics (see section 3.3) in combination with temporary backscattering problems led to lower squeezing levels. The backscattering problems were solved but at the same time we removed one of the high-quality Faraday isolators in order to develop the new Faraday assembly described in section 4.5.7. In order to maintain squeezing operation during this work we installed a replacement Faraday isolator which has a higher transmission loss of about 5%. In the near future, the reinstallation of the now significantly improved Faraday isolator promises to restore and surpass the previous best performance.

² The histogram shows the estimated squeezing level at 5 kHz derived from one of the online squeezing monitor channels. The monitor channel was slightly recalibrated after the fact by using known times of clean data without squeezing and making sure that for these the level is always 0 dB.

Summary and outlook

The focus of this thesis was the long-term stable injection of squeezed light in the gravitational-wave detector GEO 600, the operation of the squeezed-light source itself, and the ongoing optimization of the integration into the rest of the interferometer. During the last years, squeezed light was applied to GEO 600 almost continuously with a duty cycle of 88 % while the detector was in observing mode. Over the course of the thesis work, with the help of novel control techniques and improvements of the optical injection path, the effective squeezing level could be significantly increased. The highest observed non-classical enhancement of the detector's shot-noise limited sensitivity was 4.4 dB, which corresponds to a 40 % lower noise level and is equivalent to an increase in laser power by a factor of more than 2.7.

The operation of the squeezed-light source over many years showed its stability and good automatic control, but also revealed the need for maintenance and eventual signs of age. We identified laser-induced contamination as an important degradation mechanism and could improve it significantly by avoiding possible contaminants in all newly installed replacement parts. These findings already informed the design of a next generation of squeezed-light sources [Vah⁺16].

For the injection of the squeezed vacuum into the interferometer I have studied in detail the many real-world imperfections that limit the amount of effective quantum-noise reduction. Namely, these are optical losses, phase fluctuations, classical noise contributions, and backscattering. As an interesting result I was able to identify an observed, but so far unexplained, degradation of the squeezing performance as the combined effect of squeezing-angle fluctuations in the presence of backscattered light. Previous analyses had not considered this effect, but it turned out to be a considerable factor in our case. Follow-up investigations will need to study this form of backscattering in more detail in order to determine its impact on other planned

Chapter 6 Summary and outlook

squeezing experiments.

We tested several different approaches to the active control of squeezing phase and alignment and identified reliable error signals. Experimental work on the automatic alignment system for the squeezed beam will continue in the context of other ongoing investigations at GEO 600 focusing on modulated differential-wavefront sensing for the fast alignment control of the output optics.

Over the last years we put a lot of work into the reduction of optical losses. Careful in-situ fine-tuning of mode-matching and polarization optics was one of the key factors in this. We learned that we needed to adapt the infrastructure of the injection path to allow good access to all relevant tuning degrees of freedom. Different software tools for the reliable online and offline characterization of the squeezing performance were developed, making it possible to confidently track even small-scale changes.

Table 6.1 shows the estimated budget of imperfections from chapter 4 and compares it to a near-term and a long-term goal: Planned improvements of the optical path, in particular the installation of the already tested new Faraday assembly, promise significant reductions of the injection losses, as well as the reduction of backscattering down to insignificant levels. Together with further small-scale optimizations of the squeezer phase noise, we expect to be able to surpass 6 dB observed squeezing.

In the long term, the benchmark goal will be to achieve 10 dB non-classical noise reduction. This is the often assumed target for third-generation detector designs like the planned European Einstein Telescope [Pun⁺10]. Many of the individual steps necessary for reaching this level have already been demonstrated and there are no fundamental roadblocks in sight. Nevertheless, combining them in the setting of a large-scale detector will be a demanding technical challenge with not much room for unforeseen imperfections. A demonstration of 10 dB of squeezing in GEO 600 would, aside from the direct improvement of sensitivity, lend confidence to the third-generation plans.

Triggered also by the success of the GEO 600 squeezed-light application, both Advanced LIGO and Advanced Virgo opted for an early adoption of the technique and aim to include frequency-independent squeezing already in their currently ongoing upgrades. The lessons learned at GEO 600 directly influenced the design of the upcoming integrations and have thereby helped to pave the way towards making squeezing a standard feature of all gravitational-wave detectors.

Over the next years GEO 600 will continue to serve as a testbed for new interferometric

techniques. Among the suggestions is the implementation of balanced homodyne readout for the interferometer [FEF14; Ste+15] and a demonstration of a novel scheme for frequency-dependent squeezing using Einstein–Podolsky–Rosen entangled squeezed sidebands [Ma+17; Bro+17]. Both of these techniques would be intricately connected to the existing squeezing application and will benefit from the experience gathered so far.

	best so far	in reach	long-term goal
<i>loss mechanisms:</i>			
finite OPA escape efficiency	7 %	7 %	1 %
lenses, HR mirrors, etc.	3 %	2 %	0.5 %
in-air Faradays	$2 \times 3 \%$	$2 \times 1 \%$	$2 \times 0.6 \%$
injection Faraday	$2 \times 4.5 \%$	$2 \times 1 \%$	$2 \times 0.6 \%$
reflection off interferometer	1 %	1 %	1 %
pick off	$2 \times 1 \%$	$2 \times 1 \%$	$2 \times 0.1 \%$
OMC mismatch (all mode orders combined)	5 %	3 %	1 %
OMC loss	4 %	4 %	1 %
finite PD quantum efficiency	1 %	1 %	0.5 %
total losses	32 %	22 %	7.8 %
<i>other imperfections:</i>			
RMS phase noise	20 mrad	15 mrad	10 mrad
dark noise (rel. to unsqz. shot-noise)	0.03	0.03	≤ 0.03
backscattering (rel. to unsqz. shot-noise)	0.01	0.005	≤ 0.003
resulting observed squeezing	4.4 dB	6.2 dB	10.1 dB

Table 6.1: Comparison of imperfections and reachable squeezing levels now and in the future. All stated values are rough estimates and assume a shot-noise limited frequency regime of around 5 kHz.

Appendices

Detailed optical layout of GEO 600

Shown here is a detailed scale drawing of GEO 600's optical layout based on work by Roland Schilling using his beam-tracing software OPTOCAD [Sch14].

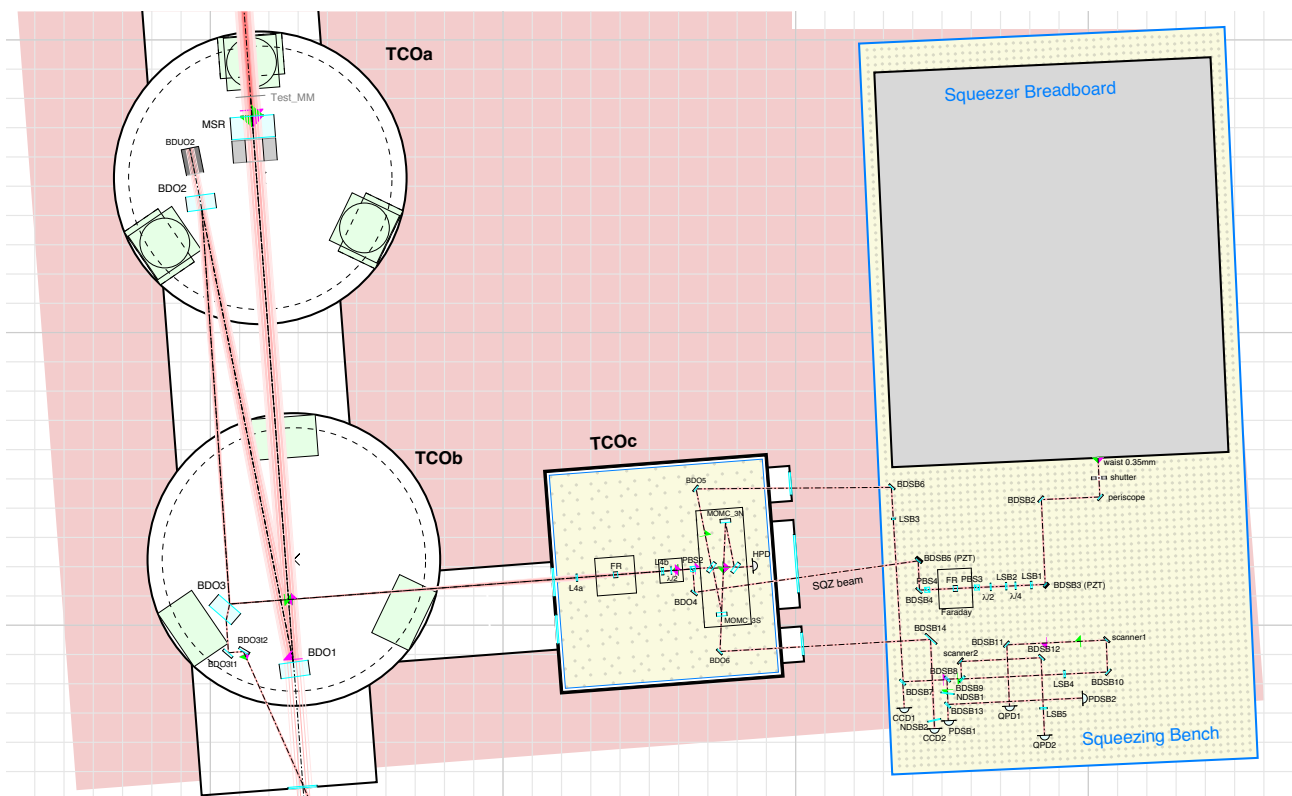
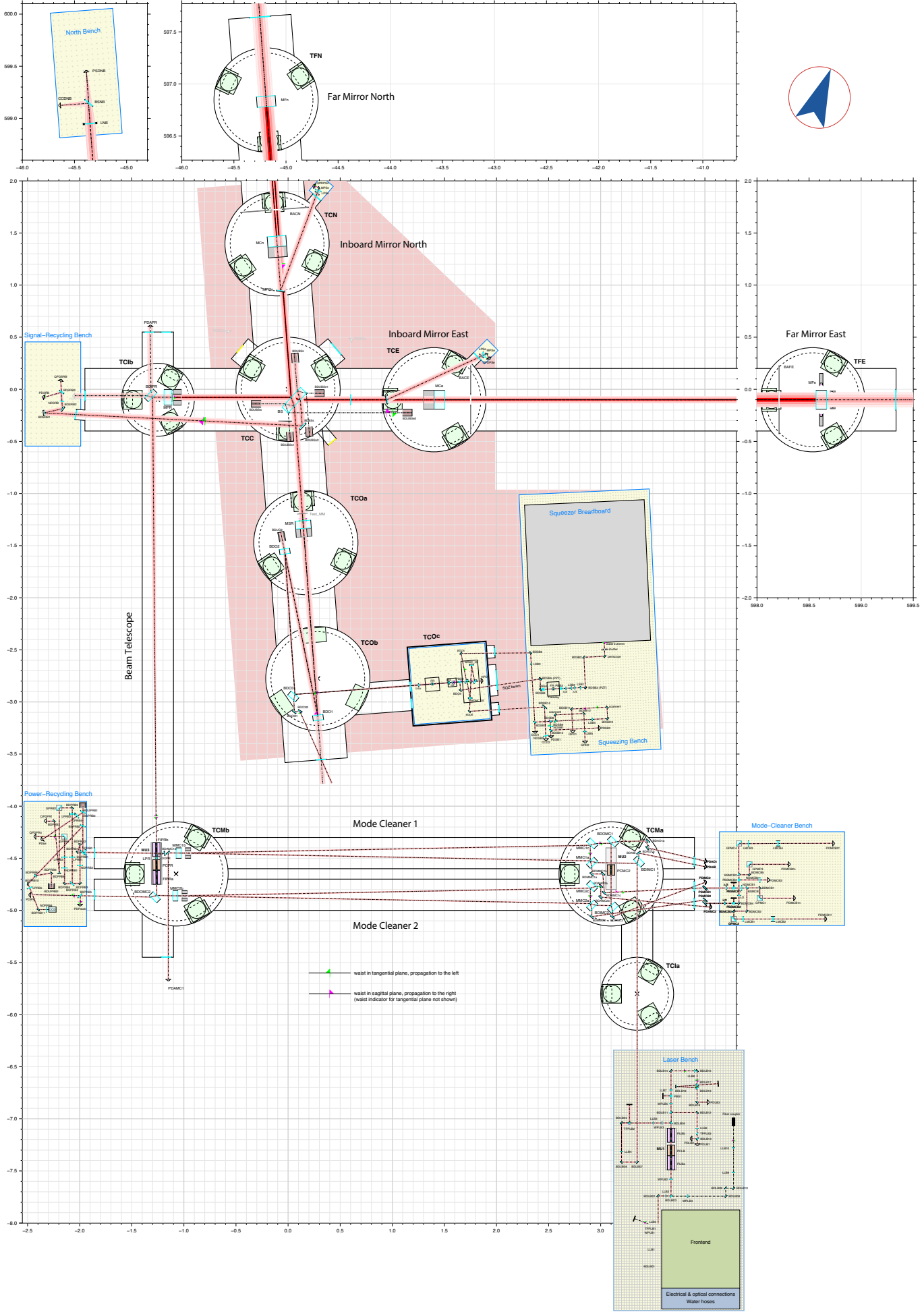


Figure A.1: Optical layout of the output path with squeezing injection.

Figure A.2 (next page): Complete optical layout of GEO 600.

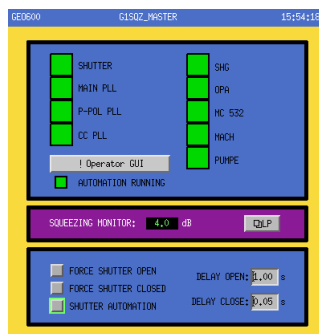


Manuals

The following are extracts from the GEO 600 online logbook that explain aspects of operating the squeezer and its control systems. The descriptions are fairly specific to the situation at GEO 600 and are included here as examples for typical squeezer operation work.

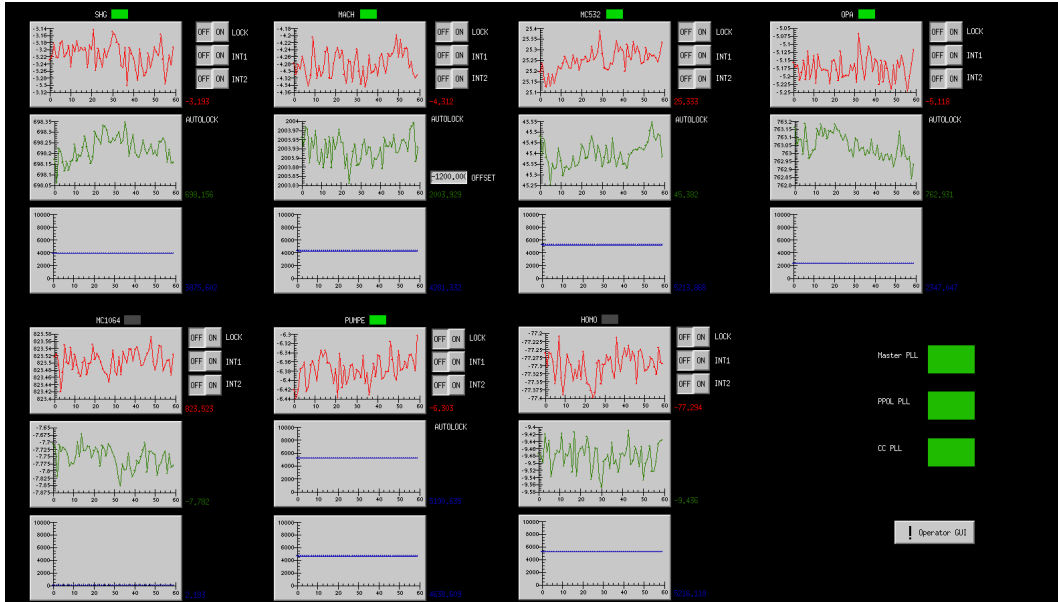
B.1 Overview of MEDM screens and monitors

SQZ_MASTER MEDM screen



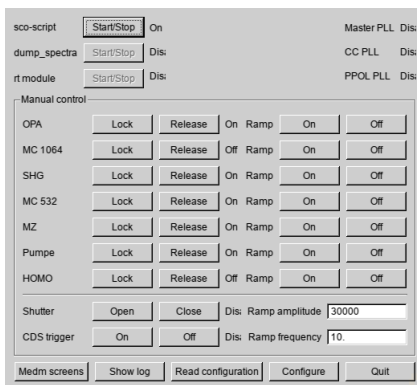
Shows the status of the individual squeezer control loops, the PLLs and the shutter. The current squeezing level that is displayed can be used as rough estimator but should not be trusted too much. The shutter can be manually set to be open or closed, but always make sure to set it back to 'automation' when going back to normal operation.

SQZ_DIAG MEDM screen



Detailed overview of all squeezer control loops. The red traces show error signals, the green traces DC levels and the blue traces feedback signals. The PUMPE loop (green pump phase) has two blue traces because it has a fast (top) and a slow (bottom) feedback. For the MACH loop (Mach Zehnder power control) an offset can be set to adjust the green pump power.

Operator GUI and automation script



The operator GUI of the squeezer automation script can be opened with the button on the SQZ_MASTER screen (takes a few seconds). Normally the automation (`sco-script`) should always be running. If the automation fails to relock the squeezer loops several

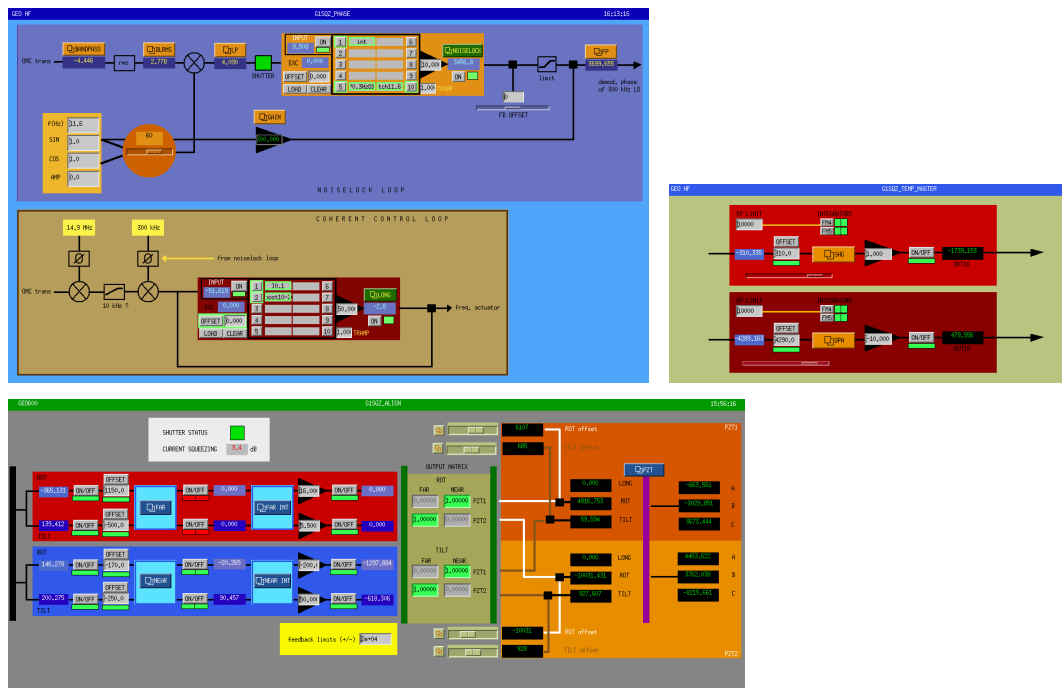
B.1 Overview of MEDM screens and monitors

times in a row it will wait for 10 minutes until starting another attempt. If you don't want to wait so long you can stop and start the automation.

With the automation stopped loops can be locked and unlocked manually with the 'lock' and 'release' buttons and the feedbacks can be ramped for unlocked loops. Because some loops depend on others, best lock the loops starting from the top. The MC1064 and HOMO loops are not used in normal operation.

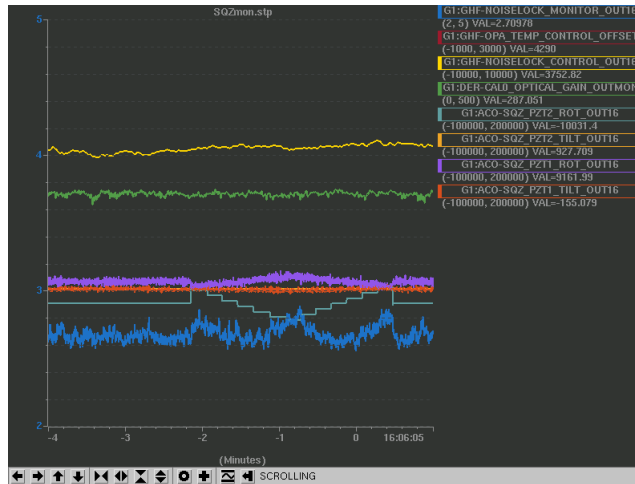
The automation script logs all actions it takes and all problems encountered in a text file located at `~/sco-working/log/sco.log` (accessible from all workstations).

SQZ_TEMP_MASTER, SQZ_PHASE and SQZ_ALIGN MEDM screens



These screens show the controls of SHG and OPA temperature, squeezing phase, and alignment. See the manual below for situations when things might need adjusting.

SQZmon Strip Tool graph



This live plot is mainly used for squeezer tuning. It can be opened by starting Strip Tool (via link button on sitemap) and loading `~/Templates/sqz/SQZmon.stp`. The blue trace shows the noiselock monitor, a BLRMS of h at around 5 kHz. The lower this value is, the better the squeezing. The green trace shows the interferometer's optical gain. Fluctuations here indicate problems that are probably not squeezer related. The other traces show feedbacks for alignment and OPA temperature.

B.2 List of possible problems

Too low green pump power

Symptoms: Squeezer is often loosing lock with the Mach Zehnder loop failing first, or it is not locking at all.

Fix: First to make sure that low green pump power is causing the problems, turn off the locking automation and manually lock first SHG then MC532 (green mode cleaner). When the mode cleaner is locking the automation will drive the Mach Zehnder to maximum transmission. In this state the Mach Zehnder DC level (green curve on DIAG screen) should be at least 100 cts. higher then in the locked state. Otherwise decrease the value in the offset field by some 200 cts. or as much as is necessary. The offset can also be negative. If the green pump power was lowered the OPA temperature has to be retuned.

OPA temperature not optimal

Symptoms: Low squeezing level, especially after special events like a room temperature change or after a slow drift over many days.

Fix: Tune the OPA temperature offset while looking at the noiselock monitor or some other squeezing monitor to get the best possible squeezing. You can also use the Matlab tuning script (`~/scripts/sqz_AA/tune.m`): Make sure that the `channel` variable is set to `G1:GHF-OPA_TEMP_CONTROL_OFFSET` and `tuningrange` is 120 and run the script. It will automatically try different temperature settings around the current setting and plot the resulting noiselock monitor signal and estimated squeezing level. When it is finished after about six minutes you can pick a good temperature setting and manually enter it on the MEDM screen. The script can safely be interrupted with `CTRL+C` which will set the temperature setting back to its old value.

Bad alignment of squeezed beam to the IFO

Symptoms: Low squeezing level, especially after alignment changes of the OMC or after a slow drift over many days.

Fix: Tune the alignment EP offsets of the 'NEAR' loops and do a beam walk by tuning the feedback offsets of PZT2. You can use the Matlab tuning script (`~/scripts/sqz_AA/tune.m`) for this: Set the `channel` variable to `G1:ACO-SQZ_NEAR_(ROT/TILT)_OFFSET` and `tuningrange` to 120, or `channel` to `G1:ACO-SQZ_PZT2_(ROT/TILT)_ADD_OFFSET` and `tuningrange` to 15000. Run the script. It will automatically try different settings around the current setting and plot the resulting noiselock monitor signal and estimated squeezing level. When it is finished after about six minutes you can pick a good setting and manually enter it on the MEDM screen. The script can safely be interrupted with `CTRL+C` which will set the setting back to its old value.

Noiselock phase loop out of range or otherwise stuck at bad setting

Symptoms: Bad squeezing level or even antisqueezing, especially after relocks. (This is sometimes a symptom of the shutter not being set to 'automation', but being forced open.)

Appendix B Manuals

Fix: Go to the SQZ_PHASE MEDM screen, turn off the noiselock loop, clear the filterbank's history and manually adjust the feedback offset to see whether the squeezing level can be improved. If the feedback ends up close to ± 30000 search for another optimum closer to zero feedback. You can also use the analogue phase knob (right squeezer rack, top crate, second module from the right) which has more range.

Phase noise caused by coherent-control PLL

Symptoms: Fluctuating and overall bad squeezing level, sometimes even antisqueezing. Or squeezer is often losing lock with the PUMPE loop (green pump phase) failing first. If the squeezer is still locked and shutter open the additional noise is visible in the error signal of the pump phase loop. If everything works as intended, the PLL RMS monitors should pick up this error state, causing the shutter to be forced closed.

Fix: Unfortunately we don't have a direct fix for this. The excess noise comes from the coherent-control laser and sometimes turning the PLL off and on again stops it temporarily. If it is negatively influencing GEO's sensitivity or stability you should just close the shutter for some time (maybe half an hour) and later try if the problem is gone. So far it never stayed for much longer than an hour at a time.

PLL not relocking

Symptoms: Squeezer is unlocked and PLL status indicators on SQZ_MASTER screen are red.

Fix: The master PLL sometimes does not stay locked when the IFO main laser is changing frequency during IFO relocking. In this case just wait until the IFO is stably locked. If a PLL is still not relocking you can try to adjust the scanning range by carefully tuning the temperature potentiometer on the respective laser controller (below the PLL boxes). Note down at which setting you start and very slowly move the knob until the status LED of the PLL blinks red or orange. Afterwards the PLL should automatically relock after some time (status LED stays orange).

Bibliography

- [Abb⁺17] B. P. Abbott et al. (LIGO Scientific Collaboration and J. Harms): ‘Exploring the sensitivity of next generation gravitational wave detectors’. *Classical and Quantum Gravity* 34.4 (2017), p. 44001. DOI: [10.1088/1361-6382/aa51f4](https://doi.org/10.1088/1361-6382/aa51f4) (see p. 8).
- [AD05] P. Aufmuth, K. Danzmann: ‘Gravitational wave detectors’. *New Journal of Physics* 7 (2005), p. 202. DOI: [10.1088/1367-2630/7/1/202](https://doi.org/10.1088/1367-2630/7/1/202) (see p. 3).
- [Aff14] C. Affeldt: ‘Laser power increase for GEO 600: Commissioning aspects towards an operation of GEO 600 at high laser power’. PhD thesis, Gottfried Wilhelm Leibniz Universität Hannover, 2014 (see pp. 12, 118).
- [Aff⁺14] C. Affeldt, K. Danzmann, K. L. Dooley, H. Grote, M. Hewitson, S. Hild, J. Hough, J. Leong, H. Lück, M. Prijatelj, S. Rowan, A. Rüdiger, R. Schilling, R. Schnabel, E. Schreiber, B. Sorazu, K. A. Strain, H. Vahlbruch, B. Willke, W. Winkler, H. Wittel: ‘Advanced techniques in GEO 600’. *Classical and Quantum Gravity* 31.22 (2014), p. 224002. DOI: [10.1088/0264-9381/31/22/224002](https://doi.org/10.1088/0264-9381/31/22/224002) (see pp. 7, 106, 107).
- [Ama⁺17] P. Amaro-Seoane, H. Audley, S. Babak, J. Baker, E. Barausse, P. Bender, E. Berti, P. Binetruy, M. Born, D. Bortoluzzi, J. Camp, C. Caprini, V. Cardoso, M. Colpi, J. Conklin, N. Cornish, C. Cutler, K. Danzmann, R. Dolesi, L. Ferraioli, V. Ferroni, E. Fitzsimons, J. Gair, L. G. Bote, D. Giardini, F. Gibert, C. Grmani, H. Halloin, G. Heinzl, T. Hertog, M. Hewitson, K. Holley-Bockelmann, D. Hollington, M. Hueller, H. Inchauspe, P. Jetzer, N. Karnesis, C. Killow, A. Klein, B. Klipstein, N. Korsakova, S. L. Larson, J. Livas, I. Lloro, N. Man, D. Mance, J. Martino, I. Mateos, K. McKenzie, S. T. McWilliams, C. Miller, G. Mueller, G. Nardini, G. Nelemans, M. Nofrarias, A. Petiteau, P. Pivato, E. Plagnol, E. Porter, J. Reiche, D. Robertson, N. Robertson, E. Rossi, G. Russano, B. Schutz, A. Sesana, D. Shoemaker, J. Slutsky, C. F. Sopuerta, T. Sumner, N. Tamanini, I. Thorpe, M. Troebs, M. Vallisneri, A. Vecchio, D. Vetrugno, S. Vitale, M. Volonteri, G. Wanner, H. Ward, P. Wass, W. Weber, J. Ziemer, P. Zweifel: *Laser Interferometer Space Antenna (LISA L3 mission proposal)*. 2017. arXiv: [1702.00786](https://arxiv.org/abs/1702.00786) (see p. 8).
- [And⁺16] U. L. Andersen, T. Gehring, C. Marquardt, G. Leuchs: ‘30 years of squeezed light generation’. *Physica Scripta* 91.5 (2016), p. 053001. DOI: [10.1088/0031-8949/91/5/053001](https://doi.org/10.1088/0031-8949/91/5/053001) (see p. 13).
- [And84] D. Z. Anderson: ‘Alignment of resonant optical cavities’. *Applied Optics* 23.17 (1984), p. 2944. DOI: [10.1364/AO.23.002944](https://doi.org/10.1364/AO.23.002944) (see p. 100).

Bibliography

- [App⁺07] J. Appel, D. Hoffman, E. Figueroa, A. I. Lvovsky: ‘Electronic noise in optical homodyne tomography’. *Physical Review A* 75.3 (2007), p. 035802. DOI: [10.1103/PhysRevA.75.035802](https://doi.org/10.1103/PhysRevA.75.035802) (see p. 41).
- [ATF06] T. Aoki, G. Takahashi, A. Furusawa: ‘Squeezing at 946 nm with periodically poled KTiOPO₄’. *Optics Express* 14.15 (2006), p. 6930. DOI: [10.1364/OE.14.006930](https://doi.org/10.1364/OE.14.006930) (see p. 42).
- [Bar⁺12] B. Barr, A. Bell, C. Bell, C. Bond, D. Brown, F. Brueckner, L. Carbone, K. Craig, A. Cumming, S. Danilishin, K. Dooley, A. Freise, T. Fricke, P. Fulda, S. Giampsis, N. Gordon, H. Grote, G. Hammond, J. Harms, S. Hild, J. Hough, S. Huttner, R. Kumar, H. Lück, N. Lockerbie, J. Macarthur, I. Martin, P. Murray, S. Reid, S. Rowan, D. Shoemaker, B. Sorazu, K. Strain, S. Tarabrin, K. Tokmakov, N. Voronchev: *LIGO 3 Strawman Design, Team Red* (LIGO-T1200046). 2012. URL: dcc.ligo.org/LIGO-T1200046/public (see p. 130).
- [BCM03] A. Buonanno, Y. Chen, N. Mavalvala: ‘Quantum noise in laser-interferometer gravitational-wave detectors with a heterodyne readout scheme’. *Physical Review D* 67.12 (2003), p. 122005. DOI: [10.1103/PhysRevD.67.122005](https://doi.org/10.1103/PhysRevD.67.122005) (see p. 36).
- [BHS18] L. Barsotti, J. Harms, R. Schnabel: ‘Squeezed vacuum states of light for gravitational wave detectors’. *Reports on Progress in Physics* (2018). DOI: [10.1088/1361-6633/aab906](https://doi.org/10.1088/1361-6633/aab906) (see p. 1).
- [Bla⁺12] D. G. Blair, E. J. Howell, L. Ju, C. Zhao (editors): *Advanced gravitational wave detectors*. Cambridge University Press, 2012 (see p. 12).
- [Bor10] R. Bork: *Advanced LIGO CDS design overview* (LIGO-T0900612). 2010. URL: dcc.ligo.org/LIGO-T0900612/public (see p. 78).
- [Bou⁺99] B. Boulanger, I. Rousseau, J. Feve, M. Maglione, B. Menaert, G. Marnier: ‘Optical studies of laser-induced gray-tracking in KTP’. *IEEE Journal of Quantum Electronics* 35.3 (1999), p. 281. DOI: [10.1109/3.748831](https://doi.org/10.1109/3.748831) (see p. 66).
- [BP10] J. S. Bendat, A. G. Piersol: *Random data: Analysis and measurement procedures*. J. Wiley & Sons, 2010 (see p. 34).
- [BR04] H.-A. Bachor, T. C. Ralph: *A guide to experiments in quantum optics*. Wiley-VCH, 2004 (see pp. 20, 22).
- [Bro⁺16] A. F. Brooks, B. Abbott, M. A. Arain, G. Ciani, A. Cole, G. Grabeel, E. Gustafson, C. Guido, M. Heintze, A. Heptonstall, M. Jacobson, W. Kim, E. King, A. Lynch, S. O’Connor, D. Ottaway, K. Mailand, G. Mueller, J. Munch, V. San-nibale, Z. Shao, M. Smith, P. Veitch, T. Vo, C. Vorvick, P. Willems: ‘Overview of Advanced LIGO adaptive optics’. *Applied Optics* 55.29 (2016), p. 8256. DOI: [10.1364/AO.55.008256](https://doi.org/10.1364/AO.55.008256) (see p. 117).
- [Bro⁺17] D. D. Brown, H. Miao, C. Collins, C. Mow-Lowry, D. Töyrä, A. Freise: ‘Broad-band sensitivity enhancement of detuned dual-recycled Michelson interferometers with EPR entanglement’. *Physical Review D* 96.6 (2017), p. 062003. DOI: [10.1103/PhysRevD.96.062003](https://doi.org/10.1103/PhysRevD.96.062003) (see p. 151).

- [BWS13] J. Bauchrowitz, T. Westphal, R. Schnabel: ‘A graphical description of optical parametric generation of squeezed states of light’. *American Journal of Physics* 81.10 (2013), p. 767. DOI: [10.1119/1.4819195](https://doi.org/10.1119/1.4819195) (see p. 26).
- [Can04] J. S. Canham: ‘Investigation of contamination effects on laser induced optical damage in space flight lasers’. *Earth Science Technology Conference*. 2004. DOI: [10.1.1.507.788](https://doi.org/10.1.1.507.788) (see p. 65).
- [Cav80] C. M. Caves: ‘Quantum-Mechanical Radiation-Pressure Fluctuations in an Interferometer’. *Physical Review Letters* 45.2 (1980), p. 75. DOI: [10.1103/PhysRevLett.45.75](https://doi.org/10.1103/PhysRevLett.45.75) (see p. 12).
- [Cav81] C. M. Caves: ‘Quantum-mechanical noise in an interferometer’. *Physical Review D* 23.8 (1981), p. 1693. DOI: [10.1103/PhysRevD.23.1693](https://doi.org/10.1103/PhysRevD.23.1693) (see pp. 12, 29, 34).
- [Che⁺05] S. Chelkowski, H. Vahlbruch, B. Hage, A. Franzen, N. Lastzka, K. Danzmann, R. Schnabel: ‘Experimental characterization of frequency-dependent squeezed light’. *Physical Review A* 71.1 (2005), p. 013806. DOI: [10.1103/PhysRevA.71.013806](https://doi.org/10.1103/PhysRevA.71.013806) (see pp. 12, 36).
- [Che07] S. Chelkowski: ‘Squeezed light and laser interferometric gravitational wave detectors’. PhD thesis, Gottfried Wilhelm Leibniz Universität Hannover, 2007 (see pp. 35, 72).
- [Che⁺07] S. Chelkowski, H. Vahlbruch, K. Danzmann, R. Schnabel: ‘Coherent control of broadband vacuum squeezing’. *Physical Review A* 75.4 (2007), p. 043814. DOI: [10.1103/PhysRevA.75.043814](https://doi.org/10.1103/PhysRevA.75.043814) (see p. 72).
- [Chu⁺11] S. S. Y. Chua, M. S. Stefszky, C. M. Mow-Lowry, B. C. Buchler, S. Dwyer, D. A. Shaddock, P. K. Lam, D. E. McClelland: ‘Backscatter tolerant squeezed light source for advanced gravitational-wave detectors’. *Optics Letters* 36.23 (2011), p. 4680. DOI: [10.1364/OL.36.004680](https://doi.org/10.1364/OL.36.004680) (see p. 47).
- [Chu⁺14] S. S. Y. Chua, S. Dwyer, L. Barsotti, D. Sigg, R. M. S. Schofield, V. V. Frolov, K. Kawabe, M. Evans, G. D. Meadors, M. Factourovich, R. Gustafson, N. Smith-Lefebvre, C. Vorvick, M. Landry, A. Khalaidovski, M. S. Stefszky, C. M. Mow-Lowry, B. C. Buchler, D. A. Shaddock, P. K. Lam, R. Schnabel, N. Mavalvala, D. E. McClelland: ‘Impact of backscattered light in a squeezing-enhanced interferometric gravitational-wave detector’. *Classical and Quantum Gravity* 31.3 (2014), p. 035017. DOI: [10.1088/0264-9381/31/3/035017](https://doi.org/10.1088/0264-9381/31/3/035017) (see pp. 43, 46, 133).
- [Col05] E. Collett: *Field guide to polarization*. SPIE, 2005 (see p. 124).
- [CS85] C. M. Caves, B. L. Schumaker: ‘New formalism for two-photon quantum optics. I. Quadrature phases and squeezed states’. *Physical Review A* 31.5 (1985), p. 3068. DOI: [10.1103/PhysRevA.31.3068](https://doi.org/10.1103/PhysRevA.31.3068) (see p. 17).
- [Dan⁺17] S. L. Danilishin, E. Knyazev, N. V. Voronchev, F. Y. Khalili, C. Gräf, S. Steinlechner, J.-S. Hennig, S. Hild: ‘A new type of quantum speed meter interferometer: measuring speed to search for intermediate mass black holes’ (2017). arXiv: [1702.01029](https://arxiv.org/abs/1702.01029) (see p. 7).

Bibliography

- [DBS13] R. Demkowicz-Dobrzański, K. Banaszek, R. Schnabel: ‘Fundamental quantum interferometry bound for the squeezed-light-enhanced gravitational wave detector GEO 600’. *Physical Review A* 88.4 (2013), p. 041802. DOI: [10.1103/PhysRevA.88.041802](https://doi.org/10.1103/PhysRevA.88.041802) (see p. 37).
- [DK12] S. L. Danilishin, F. Y. Khalili: ‘Quantum measurement theory in gravitational-wave detectors’. *Living Reviews in Relativity* 15.1 (2012), p. 5. DOI: [10.12942/lrr-2012-5](https://doi.org/10.12942/lrr-2012-5) (see pp. 1, 26).
- [Doo⁺15] K. L. Dooley, E. Schreiber, H. Vahlbruch, C. Affeldt, J. R. Leong, H. Wittel, H. Grote: ‘Phase control of squeezed vacuum states of light in gravitational wave detectors’. *Optics Express* 23.7 (2015), p. 8235. DOI: [10.1364/OE.23.008235](https://doi.org/10.1364/OE.23.008235) (see pp. 86, 88, 97).
- [Doo⁺16] K. L. Dooley, J. R. Leong, T. Adams, C. Affeldt, A. Bisht, C. Bogan, J. Degallaix, C. Gräf, S. Hild, J. Hough, A. Khalaidovski, N. Lastzka, J. Lough, H. Lück, D. Macleod, L. Nuttall, M. Prijatelj, R. Schnabel, E. Schreiber, J. Slutsky, B. Sorazu, K. A. Strain, H. Vahlbruch, M. Was, B. Willke, H. Wittel, K. Danzmann, H. Grote: ‘GEO 600 and the GEO-HF upgrade program: successes and challenges’. *Classical and Quantum Gravity* 33.7 (2016), p. 075009. DOI: [10.1088/0264-9381/33/7/075009](https://doi.org/10.1088/0264-9381/33/7/075009) (see pp. 54, 140, 146).
- [Dre⁺83] R. W. P. Drever, J. L. Hall, F. V. Kowalski, J. Hough, G. M. Ford, A. J. Munley, H. Ward: ‘Laser phase and frequency stabilization using an optical resonator’. *Applied Physics B Photophysics and Laser Chemistry* 31.2 (1983), p. 97. DOI: [10.1007/BF00702605](https://doi.org/10.1007/BF00702605) (see p. 60).
- [Dwy13] S. E. Dwyer: ‘Quantum noise reduction using squeezed states in LIGO’. PhD thesis, Massachusetts Institute of Technology, 2013 (see pp. 45, 46, 88).
- [Dwy⁺13] S. Dwyer, L. Barsotti, S. S. Y. Chua, M. Evans, M. Factourovich, D. Gustafson, T. Isogai, K. Kawabe, A. Khalaidovski, P. K. Lam, M. Landry, N. Mavalvala, D. E. McClelland, G. D. Meadors, C. M. Mow-Lowry, R. Schnabel, R. M. S. Schofield, N. Smith-Lefebvre, M. Stefszky, C. Vorvick, D. Sigg: ‘Squeezed quadrature fluctuations in a gravitational wave detector using squeezed light’. *Optics Express* 21.16 (2013), p. 19047. DOI: [10.1364/OE.21.019047](https://doi.org/10.1364/OE.21.019047) (see pp. 42, 97, 98).
- [Ein16] A. Einstein: ‘Näherungsweise Integration der Feldgleichungen der Gravitation’. *Sitzungsberichte der Königlich Preussischen Akademie der Wissenschaften (Berlin)* (1916), p. 688 (see p. 2).
- [Ein18] A. Einstein: ‘Über Gravitationswellen’. *Sitzungsberichte der Königlich Preussischen Akademie der Wissenschaften (Berlin)* (1918), p. 154 (see p. 2).
- [Eva⁺13] M. Evans, L. Barsotti, P. Kwee, J. Harms, H. Miao: ‘Realistic filter cavities for advanced gravitational wave detectors’. *Physical Review D* 88.2 (2013), p. 022002. DOI: [10.1103/PhysRevD.88.022002](https://doi.org/10.1103/PhysRevD.88.022002) (see p. 12).
- [FEF14] P. Fritschel, M. Evans, V. Frolov: ‘Balanced homodyne readout for quantum limited gravitational wave detectors’. *Optics Express* 22.4 (2014), p. 4224. DOI: [10.1364/OE.22.004224](https://doi.org/10.1364/OE.22.004224) (see p. 151).

- [Fra06] A. Franzen: *ComponentLibrary, vector graphics library for illustrations of optics experiments*. 2006. URL: www.gwoptics.org/ComponentLibrary (see p. xviii).
- [Fre⁺04] A. Freise, G. Heinzel, H. Lück, R. Schilling, B. Willke, K. Danzmann: ‘Frequency-domain interferometer simulation with higher-order spatial modes’. *Classical and Quantum Gravity* 21.5 (2004), S1067. DOI: [10.1088/0264-9381/21/5/102](https://doi.org/10.1088/0264-9381/21/5/102) (see pp. 67, 101).
- [Fre14] A. Freise: *FINESSE 2: Frequency domain INterferomEter Simulation SoftwarE, manual*. 2014. URL: www.gwoptics.org/finesse (see pp. 67, 101).
- [GK05] C. C. Gerry, P. L. Knight: *Introductory quantum optics*. Cambridge University Press, 2005 (see pp. 15, 17, 18, 26).
- [Gla63] R. J. Glauber: ‘Coherent and Incoherent States of the Radiation Field’. *Physical Review* 131.6 (1963), p. 2766. DOI: [10.1103/PhysRev.131.2766](https://doi.org/10.1103/PhysRev.131.2766) (see p. 17).
- [God⁺05] K. Goda, K. McKenzie, E. E. Mikhailov, P. K. Lam, D. E. McClelland, N. Mavalvala: ‘Photothermal fluctuations as a fundamental limit to low-frequency squeezing in a degenerate optical parametric oscillator’. *Physical Review A* 72.4 (2005), p. 043819. DOI: [10.1103/PhysRevA.72.043819](https://doi.org/10.1103/PhysRevA.72.043819) (see p. 46).
- [God⁺08] K. Goda, O. Miyakawa, E. E. Mikhailov, S. Saraf, R. Adhikari, K. McKenzie, R. Ward, S. Vass, A. J. Weinstein, N. Mavalvala: ‘A quantum-enhanced prototype gravitational-wave detector’. *Nature Physics* 4.6 (2008), p. 472. DOI: [10.1038/nphys920](https://doi.org/10.1038/nphys920) (see p. 54).
- [Grä13] C. Gräf: ‘Optical design and numerical modeling of the AEI 10m prototype sub-SQL interferometer’. PhD thesis, Gottfried Wilhelm Leibniz Universität Hannover, 2013 (see pp. 53, 78).
- [Gro03] H. Grote: ‘Making it work: Second generation interferometry in GEO 600!’ PhD thesis, Universität Hannover, 2003 (see pp. 86, 88, 107).
- [Gro10] H. Grote (for the LIGO Scientific Collaboration): ‘The GEO 600 status’. *Classical and Quantum Gravity* 27.8 (2010), p. 084003. DOI: [10.1088/0264-9381/27/8/084003](https://doi.org/10.1088/0264-9381/27/8/084003) (see p. 108).
- [Gro⁺13] H. Grote, K. Danzmann, K. L. Dooley, R. Schnabel, J. Slutsky, H. Vahlbruch: ‘First long-term application of squeezed states of light in a gravitational-wave observatory’. *Physical Review Letters* 110.18 (2013), p. 181101. DOI: [10.1103/PhysRevLett.110.181101](https://doi.org/10.1103/PhysRevLett.110.181101) (see pp. 13, 93, 140).
- [Gro⁺16] H. Grote, M. Weinert, R. X. Adhikari, C. Affeldt, V. Kringel, J. Leong, J. Lough, H. Lück, E. Schreiber, K. A. Strain, H. Vahlbruch, H. Wittel: ‘High power and ultra-low-noise photodetector for squeezed-light enhanced gravitational wave detectors’. *Optics Express* 24.18 (2016), p. 20107. DOI: [10.1364/OE.24.020107](https://doi.org/10.1364/OE.24.020107) (see p. 136).
- [Har⁺03] J. Harms, Y. Chen, S. Chelkowski, A. Franzen, H. Vahlbruch, K. Danzmann, R. Schnabel: ‘Squeezed-input, optical-spring, signal-recycled gravitational-wave detectors’. *Physical Review D* 68.4 (2003), p. 042001. DOI: [10.1103/PhysRevD.68.042001](https://doi.org/10.1103/PhysRevD.68.042001) (see p. 36).

Bibliography

- [Hei99] G. Heinzel: ‘Advanced optical techniques for laser-interferometric gravitational-wave detectors’. PhD thesis, Universität Hannover, 1999 (see p. 104).
- [Hil07] S. Hild: ‘Beyond the first generation: Extending the science range of the gravitational wave detector GEO 600’. PhD thesis, Gottfried Wilhelm Leibniz Universität Hannover, 2007 (see pp. 43, 110, 131).
- [Hil⁺09] S. Hild, H. Grote, J. Degallaix, S. Chelkowski, K. Danzmann, A. Freise, M. Hewitson, J. Hough, H. Lück, M. Prijatelj, K. A. Strain, J. R. Smith, B. Willke: ‘DC-readout of a signal-recycled gravitational wave detector’. *Classical and Quantum Gravity* 26.5 (2009), p. 055012. DOI: [10.1088/0264-9381/26/5/055012](https://doi.org/10.1088/0264-9381/26/5/055012) (see p. 32).
- [Hir⁺14] E. Hirose, T. Sekiguchi, R. Kumar, R. Takahashi: ‘Update on the development of cryogenic sapphire mirrors and their seismic attenuation system for KAGRA’. *Classical and Quantum Gravity* 31.22 (2014), p. 224004. DOI: [10.1088/0264-9381/31/22/224004](https://doi.org/10.1088/0264-9381/31/22/224004) (see p. 11).
- [Inn04] InnoLight GmbH: *Mephisto product line, user’s manual*. 2004 (see p. 55).
- [Inn08] InnoLight GmbH: *Phase-locked loop control electronic, user’s manual*. 2008 (see p. 55).
- [Joh28] J. B. Johnson: ‘Thermal agitation of electricity in conductors’. *Physical Review* 32.1 (1928), p. 97. DOI: [10.1103/PhysRev.32.97](https://doi.org/10.1103/PhysRev.32.97) (see p. 136).
- [Kha11] A. Khalaidovski: ‘Beyond the quantum limit: A squeezed-light laser in GEO 600’. PhD thesis, Gottfried Wilhelm Leibniz Universität Hannover, 2011 (see pp. 53, 66, 69).
- [Kha⁺12a] A. Khalaidovski, H. Vahlbruch, N. Lastzka, C. Gräf, K. Danzmann, H. Grote, R. Schnabel: ‘Long-term stable squeezed vacuum state of light for gravitational wave detectors’. *Classical and Quantum Gravity* 29.7 (2012), p. 075001. DOI: [10.1088/0264-9381/29/7/075001](https://doi.org/10.1088/0264-9381/29/7/075001) (see pp. 53, 60, 93).
- [Kha⁺12b] A. Khalaidovski, H. Vahlbruch, N. Lastzka, C. Gräf, H. Lück, K. Danzmann, H. Grote, R. Schnabel: ‘Status of the GEO 600 squeezed-light laser’. *Journal of Physics: Conference Series* 363 (2012), p. 012013. DOI: [10.1088/1742-6596/363/1/012013](https://doi.org/10.1088/1742-6596/363/1/012013) (see p. 53).
- [Kim⁺01] H. J. Kimble, Y. Levin, A. B. Matsko, K. S. Thorne, S. P. Vyatchanin: ‘Conversion of conventional gravitational-wave interferometers into quantum nondemolition interferometers by modifying their input and/or output optics’. *Physical Review D* 65.2 (2001), p. 022002. DOI: [10.1103/PhysRevD.65.022002](https://doi.org/10.1103/PhysRevD.65.022002) (see p. 12).
- [Kok⁺17] D. Kokkinos, H. Schroeder, K. Fleury-Frenette, M. P. Georges, W. Riede, G. Tzeremes, P. Rochus: ‘Laser optics in space failure risk due to laser induced contamination’. *CEAS Space Journal* 9.2 (2017), p. 153. DOI: [10.1007/s12567-016-0137-1](https://doi.org/10.1007/s12567-016-0137-1) (see p. 65).
- [Kwe05] P. Kwee: ‘Charakterisierung von Lasersystemen für Gravitationswellendetektoren’. Diploma thesis, Universität Hannover, 2005 (see pp. 100, 101).

- [Kwe⁺07] P. Kwee, F. Seifert, B. Willke, K. Danzmann: ‘Laser beam quality and pointing measurement with an optical resonator’. *Review of Scientific Instruments* 78.7 (2007), p. 073103. DOI: [10.1063/1.2754400](https://doi.org/10.1063/1.2754400) (see p. 100).
- [Kwe10] P. Kwee: ‘Laser characterization and stabilization for precision interferometry’. PhD thesis, Gottfried Wilhelm Leibniz Universität Hannover, 2010 (see p. 100).
- [Las10] N. Lastzka: ‘Numerical modelling of classical and quantum effects in non-linear optical systems’. PhD thesis, Gottfried Wilhelm Leibniz Universität Hannover, 2010 (see pp. 53, 78).
- [LC13] M. D. Lang, C. M. Caves: ‘Optimal quantum-enhanced interferometry using a laser power source’. *Physical Review Letters* 111.17 (2013), p. 173601. DOI: [10.1103/PhysRevLett.111.173601](https://doi.org/10.1103/PhysRevLett.111.173601) (see p. 37).
- [LC14] M. D. Lang, C. M. Caves: ‘Optimal quantum-enhanced interferometry’. *Physical Review A* 90.2 (2014), p. 025802. DOI: [10.1103/PhysRevA.90.025802](https://doi.org/10.1103/PhysRevA.90.025802) (see p. 37).
- [Leo16] M. Leonardi: ‘Development of a squeezed light source prototype for Advanced Virgo’. PhD thesis, University of Trento, 2016 (see p. 128).
- [Lia⁺04] Z. M. Liao, S. A. Payne, J. Dawson, A. Drobshoff, C. Ebberts, D. Pennington, L. Taylor: ‘Thermally induced dephasing in periodically poled KTP frequency-doubling crystals’. *Journal of the Optical Society of America B* 21.12 (2004), p. 2191. DOI: [10.1364/JOSAB.21.002191](https://doi.org/10.1364/JOSAB.21.002191) (see p. 66).
- [Liu⁺13] Z. Liu, P. Fulda, M. A. Arain, L. Williams, G. Mueller, D. B. Tanner, D. H. Reitze: ‘Feedback control of optical beam spatial profiles using thermal lensing’. *Applied Optics* 52.26 (2013), p. 6452. DOI: [10.1364/AO.52.006452](https://doi.org/10.1364/AO.52.006452) (see p. 117).
- [LRR00] T. T. Lyons, M. W. Regehr, F. J. Raab: ‘Shot noise in gravitational-wave detectors with Fabry–Perot arms’. *Applied Optics* 39.36 (2000), p. 6761. DOI: [10.1364/AO.39.006761](https://doi.org/10.1364/AO.39.006761) (see p. 36).
- [LSC11] J. Abadie et al. (LIGO Scientific Collaboration): ‘A gravitational wave observatory operating beyond the quantum shot-noise limit’. *Nature Physics* 7.12 (2011), p. 962. DOI: [10.1038/nphys2083](https://doi.org/10.1038/nphys2083) (see pp. 13, 92, 146).
- [LSC13] J. Aasi et al. (LIGO Scientific Collaboration): ‘Enhanced sensitivity of the LIGO gravitational wave detector by using squeezed states of light’. *Nature Photonics* 7.8 (2013), p. 613. DOI: [10.1038/nphoton.2013.177](https://doi.org/10.1038/nphoton.2013.177) (see pp. 13, 86).
- [LSC15] J. Aasi et al. (LIGO Scientific Collaboration): ‘Advanced LIGO’. *Classical and Quantum Gravity* 32.7 (2015), p. 74001. DOI: [10.1088/0264-9381/32/7/074001](https://doi.org/10.1088/0264-9381/32/7/074001) (see pp. 7, 9, 10, 38).
- [LSC16] LIGO Scientific Collaboration: *LIGO Open Science Center release of GW150914*. 2016. DOI: [10.7935/K5MW2F23](https://doi.org/10.7935/K5MW2F23) (see p. 2).
- [LVC16a] B. P. Abbott et al. (LIGO Scientific Collaboration and Virgo Collaboration): ‘Observation of gravitational waves from a binary black hole merger’. *Physical*

Bibliography

- Review Letters* 116.6 (2016), p. 061102. DOI: [10.1103/PhysRevLett.116.061102](https://doi.org/10.1103/PhysRevLett.116.061102) (see pp. 1, 2, 4).
- [LVC16b] B.P. Abbott et al. (LIGO Scientific Collaboration and Virgo Collaboration): ‘GW151226: Observation of gravitational waves from a 22-solar-mass binary black hole coalescence’. *Physical Review Letters* 116.24 (2016), p. 241103. DOI: [10.1103/PhysRevLett.116.241103](https://doi.org/10.1103/PhysRevLett.116.241103) (see p. 4).
- [LVC17a] B.P. Abbott et al. (LIGO Scientific Collaboration and Virgo Collaboration): ‘GW170104: Observation of a 50-solar-mass binary black hole coalescence at redshift 0.2’. *Physical Review Letters* 118.22 (2017), p. 221101. DOI: [10.1103/PhysRevLett.118.221101](https://doi.org/10.1103/PhysRevLett.118.221101) (see p. 4).
- [LVC17b] B.P. Abbott et al. (LIGO Scientific Collaboration and Virgo Collaboration): ‘GW170814: A three-detector observation of gravitational waves from a binary black hole coalescence’. *Physical Review Letters* 119.14 (2017), p. 141101. DOI: [10.1103/PhysRevLett.119.141101](https://doi.org/10.1103/PhysRevLett.119.141101) (see pp. 4, 8).
- [LVC17c] B.P. Abbott et al. (LIGO Scientific Collaboration and Virgo Collaboration): ‘GW170817: Observation of gravitational waves from a binary neutron star inspiral’. *Physical Review Letters* 119.16 (2017), p. 161101. DOI: [10.1103/PhysRevLett.119.161101](https://doi.org/10.1103/PhysRevLett.119.161101) (see pp. 5, 8).
- [LVC17d] B.P. Abbott et al. (LIGO Scientific Collaboration, Virgo Collaboration and EM partners): ‘Multi-messenger observations of a binary neutron star merger’. *The Astrophysical Journal Letters* 848.2 (2017), p. L12. DOI: [10.3847/2041-8213/AA91C9](https://doi.org/10.3847/2041-8213/AA91C9) (see p. 5).
- [Ma⁺17] Y. Ma, H. Miao, B.H. Pang, M. Evans, C. Zhao, J. Harms, R. Schnabel, Y. Chen: ‘Proposal for gravitational-wave detection beyond the standard quantum limit through EPR entanglement’. *Nature Physics* 13.8 (2017), p. 776. DOI: [10.1038/nphys4118](https://doi.org/10.1038/nphys4118) (see pp. 36, 151).
- [Mar⁺16] D.V. Martynov et al.: ‘Sensitivity of the Advanced LIGO detectors at the beginning of gravitational wave astronomy’. *Physical Review D* 93.11 (2016), p. 112004. DOI: [10.1103/PhysRevD.93.112004](https://doi.org/10.1103/PhysRevD.93.112004) (see p. 38).
- [McK⁺04] K. McKenzie, N. Grosse, W.P. Bowen, S.E. Whitcomb, M.B. Gray, D.E. McClelland, P.K. Lam: ‘Squeezing in the audio gravitational-wave detection band’. *Physical Review Letters* 93.16 (2004), p. 161105. DOI: [10.1103/PhysRevLett.93.161105](https://doi.org/10.1103/PhysRevLett.93.161105) (see p. 54).
- [McK⁺05] K. McKenzie, E.E. Mikhailov, K. Goda, P.K. Lam, N. Grosse, M.B. Gray, N. Mavalvala, D.E. McClelland: ‘Quantum noise locking’. *Journal of Optics B: Quantum and Semiclassical Optics* 7.10 (2005), S421. DOI: [10.1088/1464-4266/7/10/032](https://doi.org/10.1088/1464-4266/7/10/032) (see p. 93).
- [McK08] K. McKenzie: ‘Squeezing in the audio gravitational wave detection band’. PhD thesis, The Australian National University, 2008 (see pp. 26, 46, 61, 71, 73, 76).

- [Mei11] T. Meier: ‘High-power CW green lasers for optical metrology and their joint benefit in particle physics experiments’. PhD thesis, Gottfried Wilhelm Leibniz Universität, 2011 (see pp. 66, 75).
- [Mia⁺14] H. Miao, H. Yang, R. X. Adhikari, Y. Chen: ‘Quantum limits of interferometer topologies for gravitational radiation detection’. *Classical and Quantum Gravity* 31.16 (2014), p. 165010. DOI: [10.1088/0264-9381/31/16/165010](https://doi.org/10.1088/0264-9381/31/16/165010) (see pp. 7, 36).
- [Mik⁺06] E. E. Mikhailov, K. Goda, T. Corbitt, N. Mavalvala: ‘Frequency-dependent squeeze-amplitude attenuation and squeeze-angle rotation by electromagnetically induced transparency for gravitational-wave interferometers’. *Physical Review A* 73.5 (2006), p. 053810. DOI: [10.1103/PhysRevA.73.053810](https://doi.org/10.1103/PhysRevA.73.053810) (see p. 36).
- [MM87] A. A. Michelson, E. W. Morley: ‘On the relative motion of the Earth and the luminiferous ether’. *American Journal of Science* s3-34.203 (1887), p. 333. DOI: [10.2475/ajs.s3-34.203.333](https://doi.org/10.2475/ajs.s3-34.203.333) (see p. 5).
- [Mor⁺94a] E. Morrison, B. J. Meers, D. I. Robertson, H. Ward: ‘Automatic alignment of optical interferometers’. *Applied Optics* 33.22 (1994), p. 5041. DOI: [10.1364/AO.33.005041](https://doi.org/10.1364/AO.33.005041) (see pp. 104, 107).
- [Mor⁺94b] E. Morrison, B. J. Meers, D. I. Robertson, H. Ward: ‘Experimental demonstration of an automatic alignment system for optical interferometers’. *Applied Optics* 33.22 (1994), p. 5037. DOI: [10.1364/AO.33.005037](https://doi.org/10.1364/AO.33.005037) (see p. 104).
- [MS91] B. J. Meers, K. A. Strain: ‘Wave-front distortion in laser-interferometric gravitational-wave detectors’. *Physical Review D* 43.10 (1991), p. 3117. DOI: [10.1103/PhysRevD.43.3117](https://doi.org/10.1103/PhysRevD.43.3117) (see p. 92).
- [Oel⁺14] E. Oelker, L. Barsotti, S. Dwyer, D. Sigg, N. Mavalvala: ‘Squeezed light for advanced gravitational wave detectors and beyond’. *Optics Express* 22.17 (2014), p. 21106. DOI: [10.1364/OE.22.021106](https://doi.org/10.1364/OE.22.021106) (see pp. 46, 88, 100).
- [Oel16] E. Oelker: ‘Squeezed states for advanced gravitational wave detectors’. PhD thesis, Massachusetts Institute of Technology, 2016 (see pp. 42, 88, 93).
- [Oel⁺16] E. Oelker, T. Isogai, J. Miller, M. Tse, L. Barsotti, N. Mavalvala, M. Evans: ‘Audio-band frequency-dependent squeezing for gravitational-wave detectors’. *Physical Review Letters* 116.4 (2016), p. 041102. DOI: [10.1103/PhysRevLett.116.041102](https://doi.org/10.1103/PhysRevLett.116.041102) (see p. 36).
- [OFW12] D. J. Ottaway, P. Fritschel, S. J. Waldman: ‘Impact of upconverted scattered light on advanced interferometric gravitational wave detectors’. *Optics Express* 20.8 (2012), p. 8329. DOI: [10.1364/OE.20.008329](https://doi.org/10.1364/OE.20.008329) (see p. 43).
- [Pri⁺10] M. Prijatelj, H. Grote, J. Degallaix, M. Hewitson, S. Hild, C. Affeldt, A. Freise, J. Leong, H. Lück, K. A. Strain, H. Wittel, B. Willke, K. Danzmann: ‘Control and automatic alignment of the output mode cleaner of GEO 600’. *Journal of Physics: Conference Series* 228 (2010), p. 012014. DOI: [10.1088/1742-6596/228/1/012014](https://doi.org/10.1088/1742-6596/228/1/012014) (see p. 106).

Bibliography

- [Pri12] M. Prijatelj: ‘Gravitational wave detection with pristine light: The implementation of an output mode cleaner at GEO 600’. PhD thesis, Gottfried Wilhelm Leibniz Universität Hannover, 2012 (see pp. 88, 92, 106).
- [Pun⁺10] M. Punturo et al.: ‘The Einstein Telescope: A third-generation gravitational wave observatory’. *Classical and Quantum Gravity* 27.19 (2010), p. 194002. DOI: [10.1088/0264-9381/27/19/194002](https://doi.org/10.1088/0264-9381/27/19/194002) (see pp. 8, 150).
- [Rüd⁺81] A. Rüdiger, R. Schilling, L. Schnupp, W. Winkler, H. Billing, K. Maischberger: ‘A mode selector to suppress fluctuations in laser beam geometry’. *Optica Acta: International Journal of Optics* 28.5 (1981), p. 641. DOI: [10.1080/713820609](https://doi.org/10.1080/713820609) (see p. 100).
- [Sau17] P. R. Saulson: *Fundamentals of interferometric gravitational wave detectors*. World Scientific, 2017 (see pp. 2, 5, 33, 35, 36).
- [SC85] B. L. Schumaker, C. M. Caves: ‘New formalism for two-photon quantum optics. II. Mathematical foundation and compact notation’. *Physical Review A* 31.5 (1985), p. 3093. DOI: [10.1103/PhysRevA.31.3093](https://doi.org/10.1103/PhysRevA.31.3093) (see p. 17).
- [Sch14] R. Schilling: *OPTOCAD: A Fortran 95 module for tracing Gaussian TEM₀₀ beams through an optical set-up, user’s guide, version 0.94a*. 2014. URL: www2.mpg.de/~ros (see pp. 116, 155).
- [Sch⁺16] E. Schreiber, K. L. Dooley, H. Vahlbruch, C. Affeldt, A. Bisht, J. R. Leong, J. Lough, M. Prijatelj, J. Slutsky, M. Was, H. Wittel, K. Danzmann, H. Grote: ‘Alignment sensing and control for squeezed vacuum states of light’. *Optics Express* 24.1 (2016), p. 146. DOI: [10.1364/OE.24.000146](https://doi.org/10.1364/OE.24.000146) (see p. 100).
- [Sch17] R. Schnabel: ‘Squeezed states of light and their applications in laser interferometers’. *Physics Reports* 684 (2017), p. 1. DOI: [10.1016/j.physrep.2017.04.001](https://doi.org/10.1016/j.physrep.2017.04.001) (see pp. 13, 17).
- [Sie86] A. E. Siegman: *Lasers*. University Science Books, 1986 (see p. 102).
- [Ske⁺01] K. D. Skeldon, D. A. Clublely, G. P. Newton, S. Thieux, M. von Gradowski, B. W. Barr: ‘Measurements of an ultra-low loss polarizer for $\lambda = 1064$ nm using a high finesse optical cavity’. *Journal of Modern Optics* 48.4 (2001), p. 695. DOI: [10.1080/09500340108230941](https://doi.org/10.1080/09500340108230941) (see p. 121).
- [Slu⁺85] R. E. Slusher, L. W. Hollberg, B. Yurke, J. C. Mertz, J. F. Valley: ‘Observation of squeezed states generated by four-wave mixing in an optical cavity’. *Physical Review Letters* 55.22 (1985), p. 2409. DOI: [10.1103/PhysRevLett.55.2409](https://doi.org/10.1103/PhysRevLett.55.2409) (see pp. 13, 54).
- [Smi⁺11] N. Smith-Lefebvre, S. Ballmer, M. Evans, S. Waldman, K. Kawabe, V. Frolov, N. Mavalvala: ‘Optimal alignment sensing of a readout mode cleaner cavity’. *Optics Letters* 36.22 (2011), p. 4365. DOI: [10.1364/OL.36.004365](https://doi.org/10.1364/OL.36.004365) (see p. 106).
- [Smi16] N. Smith: *A LA MODE: Modematching and beam propagation solutions for MATLAB*. 2016. URL: github.com/nicolassmith/alm (see p. 108).

- [Som12] K. Somiya (for the KAGRA Collaboration): ‘Detector configuration of KAGRA – the Japanese cryogenic gravitational-wave detector’. *Classical and Quantum Gravity* 29.12 (2012), p. 124007. DOI: [10.1088/0264-9381/29/12/124007](https://doi.org/10.1088/0264-9381/29/12/124007) (see p. 8).
- [SS09] B. S. Sathyaprakash, B. F. Schutz: ‘Physics, astrophysics and cosmology with gravitational waves’. *Living Reviews in Relativity* 12.2 (2009). DOI: [10.12942/lrr-2009-2](https://doi.org/10.12942/lrr-2009-2) (see pp. 1, 4, 5).
- [Ste⁺12] M. S. Stefszky, C. M. Mow-Lowry, S. S. Y. Chua, D. A. Shaddock, B. C. Buchler, H. Vahlbruch, A. Khalaidovski, R. Schnabel, P. K. Lam, D. E. McClelland: ‘Balanced homodyne detection of optical quantum states at audio-band frequencies and below’. *Classical and Quantum Gravity* 29.14 (2012), p. 145015. DOI: [10.1088/0264-9381/29/14/145015](https://doi.org/10.1088/0264-9381/29/14/145015) (see p. 43).
- [Ste⁺15] S. Steinlechner, B. W. Barr, A. S. Bell, S. L. Danilishin, A. Gläufke, C. Gräf, J.-S. Hennig, E. A. Houston, S. H. Huttner, S. S. Leavey, D. Pascucci, B. Sorazu, A. Spencer, K. A. Strain, J. Wright, S. Hild: ‘Local-oscillator noise coupling in balanced homodyne readout for advanced gravitational wave detectors’. *Physical Review D* 92.7 (2015), p. 072009. DOI: [10.1103/PhysRevD.92.072009](https://doi.org/10.1103/PhysRevD.92.072009) (see p. 151).
- [TH06] M. Tröbs, G. Heinzel: ‘Improved spectrum estimation from digitized time series on a logarithmic frequency axis’. *Measurement* 39.2 (2006), p. 120. DOI: [10.1016/j.measurement.2005.10.010](https://doi.org/10.1016/j.measurement.2005.10.010) (see p. 141).
- [Töy⁺17] D. Töyrä, D. D. Brown, M. Davis, S. Song, A. Wormald, J. Harms, H. Miao, A. Freise: ‘Multi-spatial-mode effects in squeezed-light-enhanced interferometric gravitational wave detectors’. *Physical Review D* 96.2 (2017), p. 022006. DOI: [10.1103/PhysRevD.96.022006](https://doi.org/10.1103/PhysRevD.96.022006) (see p. 99).
- [Vah⁺06] H. Vahlbruch, S. Chelkowski, B. Hage, A. Franzen, K. Danzmann, R. Schnabel: ‘Coherent control of vacuum squeezing in the gravitational-wave detection band’. *Physical Review Letters* 97.1 (2006), p. 011101. DOI: [10.1103/PhysRevLett.97.011101](https://doi.org/10.1103/PhysRevLett.97.011101) (see pp. 54, 72).
- [Vah⁺07] H. Vahlbruch, S. Chelkowski, K. Danzmann, R. Schnabel: ‘Quantum engineering of squeezed states for quantum communication and metrology’. *New Journal of Physics* 9.10 (2007), p. 371. DOI: [10.1088/1367-2630/9/10/371](https://doi.org/10.1088/1367-2630/9/10/371) (see p. 54).
- [Vah08] H. Vahlbruch: ‘Squeezed light for gravitational wave astronomy’. PhD thesis, Gottfried Wilhelm Leibniz Universität Hannover, 2008 (see pp. 53, 54).
- [Vah⁺08] H. Vahlbruch, M. Mehmet, S. Chelkowski, B. Hage, A. Franzen, N. Lastzka, S. Goßler, K. Danzmann, R. Schnabel: ‘Observation of squeezed light with 10-dB quantum-noise reduction’. *Physical Review Letters* 100.3 (2008), p. 033602. DOI: [10.1103/PhysRevLett.100.033602](https://doi.org/10.1103/PhysRevLett.100.033602) (see p. 54).
- [Vah⁺10] H. Vahlbruch, A. Khalaidovski, N. Lastzka, C. Gräf, K. Danzmann, R. Schnabel: ‘The GEO 600 squeezed light source’. *Classical and Quantum Gravity* 27.8 (2010), p. 084027. DOI: [10.1088/0264-9381/27/8/084027](https://doi.org/10.1088/0264-9381/27/8/084027) (see pp. 13, 53, 54).

Bibliography

- [Vah⁺16] H. Vahlbruch, M. Mehmet, K. Danzmann, R. Schnabel: ‘Detection of 15 dB squeezed states of light and their application for the absolute calibration of photoelectric quantum efficiency’. *Physical Review Letters* 117.11 (2016), p. 110801. DOI: [10.1103/PhysRevLett.117.110801](https://doi.org/10.1103/PhysRevLett.117.110801) (see pp. 13, 66, 98, 126, 149).
- [Vin15] Vincent Associates Inc.: *Uniblitiz datasheet*. 2015. URL: www.uniblitiz.com/technical-documents (see p. 81).
- [Virgo15] F. Acernese et al. (Virgo Collaboration): ‘Advanced Virgo: A second-generation interferometric gravitational wave detector’. *Classical and Quantum Gravity* 32.2 (2015), p. 024001. DOI: [10.1088/0264-9381/32/2/024001](https://doi.org/10.1088/0264-9381/32/2/024001) (see pp. 7, 38).
- [Vog14] M. Vogel: *Mueller–Stokes–Jones calculus, toolbox for MATLAB*. 2014. URL: www.mathworks.com/matlabcentral/fileexchange/45087-mueller-stokes-jones-calculus (see p. 124).
- [Wad⁺13] A. R. Wade, S. S. Y. Chua, M. S. Stefszky, D. A. Shaddock, D. E. McClelland: ‘Path length modulation technique for scatter noise immunity in squeezing measurements’. *Optics Letters* 38.13 (2013), p. 2265. DOI: [10.1364/OL.38.002265](https://doi.org/10.1364/OL.38.002265) (see p. 47).
- [Wag14] P. Wagner: ‘Laser-induced contamination on high-reflective optics’. Master’s thesis, Hochschule Darmstadt, 2014 (see pp. 62, 65).
- [Wei09] R. Weiss: *Collection of reports on Barkhausen noise* (LIGO-T0900061). 2009. URL: dcc.ligo.org/LIGO-T0900061/public (see p. 137).
- [Wes16] T. Westphal: ‘A coating thermal noise interferometer for the AEI 10 m prototype facility’. PhD thesis, Gottfried Wilhelm Leibniz Universität Hannover, 2016 (see p. 110).
- [Wil⁺04] B. Willke, P. Aufmuth, C. Aulbert, S. Babak, R. Balasubramanian, B. W. Barr, S. Berukoff, G. Cagnoli, C. A. Cantley, M. M. Casey, S. Chelkowski, D. Churches, C. N. Colacino, D. R. M. Crooks, C. Cutler, K. Danzmann, R. Davies, R. J. Dupuis, E. Elliffe, C. Fallnich, A. Freise, S. Goßler, A. Grant, H. Grote, S. Grunewald, J. Harms, G. Heinzl, I. S. Heng, A. Hepstonstall, M. Heurs, M. Hewitson, S. Hild, J. Hough, R. Ingley, Y. Itoh, O. Jennrich, R. Jones, S. H. Hutter, K. Kawabe, C. Killow, K. Kötter, B. Krishnan, V. Leonhardt, H. Lück, B. Machenschalk, M. Malec, R. A. Mercer, C. Messenger, S. Mohanty, K. Mossavi, S. Mukherjee, S. Nagano, G. P. Newton, M. A. Papa, M. Perreurlloyd, M. Pitkin, M. V. Plissi, V. Quetschke, V. Re, S. Reid, L. Ribichini, D. I. Robertson, N. A. Robertson, S. Rowan, A. Rüdiger, B. S. Sathyaprakash, R. Schilling, R. Schnabel, B. F. Schutz, F. Seifert, A. M. Sintes, J. R. Smith, P. H. Sneddon, K. A. Strain, I. Taylor, C. I. Torrie, C. Ungarelli, A. Vecchio, H. Ward, U. Weiland, H. Welling, P. Williams, W. Winkler, G. Woan, I. Zawischa: ‘Status of GEO 600’. *Classical and Quantum Gravity* 21.5 (2004), S417. DOI: [10.1088/0264-9381/21/5/006](https://doi.org/10.1088/0264-9381/21/5/006) (see p. 7).
- [Wil⁺06] B. Willke, P. Ajith, B. Allen, P. Aufmuth, C. Aulbert, S. Babak, R. Balasubramanian, B. W. Barr, S. Berukoff, A. Bunkowski, G. Cagnoli, C. A. Cantley, M. M. Casey, S. Chelkowski, Y. Chen, D. Churches, T. Cokelaer, C. N. Colacino, D. R. M. Crooks, C. Cutler, K. Danzmann, R. J. Dupuis, E. Elliffe, C. Fallnich,

- A. Franzen, A. Freise, I. Gholami, S. Goßler, A. Grant, H. Grote, S. Grunewald, J. Harms, B. Hage, G. Heinzl, I. S. Heng, A. Hepstonstall, M. Heurs, M. Hewitson, S. Hild, J. Hough, Y. Itoh, G. Jones, R. Jones, S. H. Huttner, K. Kötter, B. Krishnan, P. Kwee, H. Lück, M. Luna, B. Machenschalk, M. Malec, R. A. Mercer, T. Meier, C. Messenger, S. Mohanty, K. Mossavi, S. Mukherjee, P. Murray, G. P. Newton, M. A. Papa, M. Perreur-Lloyd, M. Pitkin, M. V. Plissi, R. Prix, V. Quetschke, V. Re, T. Regimbau, H. Rehbein, S. Reid, L. Ribichini, D. I. Robertson, N. A. Robertson, C. Robinson, J. D. Romano, S. Rowan, A. Rüdiger, B. S. Sathyaprakash, R. Schilling, R. Schnabel, B. F. Schutz, F. Seifert, A. M. Sintes, J. R. Smith, P. H. Sneddon, K. A. Strain, I. Taylor, R. Taylor, A. Thüring, C. Ungarelli, H. Vahlbruch, A. Vecchio, J. Veitch, H. Ward, U. Weiland, H. Welling, L. Wen, P. Williams, W. Winkler, G. Woan, R. Zhu: ‘The GEO-HF project’. *Classical and Quantum Gravity* 23.8 (2006), S207. DOI: [10.1088/0264-9381/23/8/S26](https://doi.org/10.1088/0264-9381/23/8/S26) (see pp. 54, 146).
- [Wit+14] H. Wittel, H. Lück, C. Affeldt, K. L. Dooley, H. Grote, J. R. Leong, M. Prijatelj, E. Schreiber, J. Slutsky, K. A. Strain, M. Was, B. Willke, K. Danzmann: ‘Thermal correction of astigmatism in the gravitational wave observatory GEO 600’. *Classical and Quantum Gravity* 31.6 (2014), p. 65008. DOI: [10.1088/0264-9381/31/6/065008](https://doi.org/10.1088/0264-9381/31/6/065008) (see pp. 12, 88).
- [Wit15] H. Wittel: ‘Active and passive reduction of high order modes in the gravitational wave detector GEO 600’. PhD thesis, Gottfried Wilhelm Leibniz Universität Hannover, 2015 (see pp. 12, 88, 99, 116, 126).
- [WM08] D. F. Walls, G. J. Milburn: *Quantum Optics*. Springer-Verlag, 2008. DOI: [10.1007/978-3-540-28574-8](https://doi.org/10.1007/978-3-540-28574-8) (see pp. 15, 16, 20, 22, 25).

Publications

- H. Grote, M. Weinert, R. X. Adhikari, C. Affeldt, V. Kringel, J. Leong, J. Lough, H. Lück, **E. Schreiber**, K. A. Strain, H. Vahlbruch, H. Wittel: ‘High power and ultra-low-noise photodetector for squeezed-light enhanced gravitational wave detectors’. *Optics Express* 24.18 (2016), p. 20107. DOI: [10.1364/OE.24.020107](https://doi.org/10.1364/OE.24.020107).
- K. L. Dooley, J. R. Leong, T. Adams, C. Affeldt, A. Bisht, C. Bogan, J. Degallaix, C. Gräf, S. Hild, J. Hough, A. Khalaidovski, N. Lastzka, J. Lough, H. Lück, D. Macleod, L. Nuttall, M. Prijatelj, R. Schnabel, **E. Schreiber**, J. Slutsky, B. Sorazu, K. A. Strain, H. Vahlbruch, M. Was, B. Willke, H. Wittel, K. Danzmann, H. Grote: ‘GEO 600 and the GEO-HF upgrade program: successes and challenges’. *Classical and Quantum Gravity* 33.7 (2016), p. 075009. DOI: [10.1088/0264-9381/33/7/075009](https://doi.org/10.1088/0264-9381/33/7/075009).
- **E. Schreiber**, K. L. Dooley, H. Vahlbruch, C. Affeldt, A. Bisht, J. R. Leong, J. Lough, M. Prijatelj, J. Slutsky, M. Was, H. Wittel, K. Danzmann, H. Grote: ‘Alignment sensing and control for squeezed vacuum states of light’. *Optics Express* 24.1 (2016), p. 146. DOI: [10.1364/OE.24.000146](https://doi.org/10.1364/OE.24.000146).
- T. Adams, J. R. Leong, J. Slutsky, M. Was, C. Affeldt, J. Degallaix, K. L. Dooley, H. Grote, S. Hild, H. Lück, D. M. Macleod, L. K. Nuttall, M. Prijatelj, **E. Schreiber**, B. Sorazu, K. A. Strain, P. J. Sutton, H. Vahlbruch, H. Wittel, K. Danzmann: ‘Cost-benefit analysis for commissioning decisions in GEO 600’. *Classical and Quantum Gravity* 32.13 (2015), p. 135014. DOI: [10.1088/0264-9381/32/13/135014](https://doi.org/10.1088/0264-9381/32/13/135014).
- K. L. Dooley, **E. Schreiber**, H. Vahlbruch, C. Affeldt, J. R. Leong, H. Wittel, H. Grote: ‘Phase control of squeezed vacuum states of light in gravitational wave detectors’. *Optics Express* 23.7 (2015), p. 8235. DOI: [10.1364/OE.23.008235](https://doi.org/10.1364/OE.23.008235).
- C. Affeldt, K. Danzmann, K. L. Dooley, H. Grote, M. Hewitson, S. Hild, J. Hough, J. Leong, H. Lück, M. Prijatelj, S. Rowan, A. Rüdiger, R. Schilling, R. Schnabel, **E. Schreiber**, B. Sorazu, K. A. Strain, H. Vahlbruch, B. Willke, W. Winkler, H. Wittel: ‘Advanced techniques in GEO 600’. *Classical and Quantum Gravity* 31.22 (2014), p. 224002. DOI: [10.1088/0264-9381/31/22/224002](https://doi.org/10.1088/0264-9381/31/22/224002).
- M. Adier, ... **E. Schreiber**, ... J.-P. Zendri: ‘Progress and challenges in advanced ground-based gravitational-wave detectors’. *General Relativity and Gravitation* 46.8 (2014), p. 1749. DOI: [10.1007/s10714-014-1749-4](https://doi.org/10.1007/s10714-014-1749-4).

Publications

- H. Wittel, H. Lück, C. Affeldt, K.L. Dooley, H. Grote, J.R. Leong, M. Prijatelj, **E. Schreiber**, J. Slutsky, K.A. Strain, M. Was, B. Willke, K. Danzmann: ‘Thermal correction of astigmatism in the gravitational wave observatory GEO 600’. *Classical and Quantum Gravity* 31.6 (2014), p. 65008. DOI: [10.1088/0264-9381/31/6/065008](https://doi.org/10.1088/0264-9381/31/6/065008).
- M. Steinke, **E. Schreiber**, D. Kracht, J. Neumann, P. Weßels: ‘Development of a cascaded Raman fiber laser with 6.5 W output power at 1480 nm supported by detailed numerical simulations’. *CLEO EUROPE/IQEC*. IEEE, 2013. DOI: [10.1109/CLEOE-IQEC.2013.6801366](https://doi.org/10.1109/CLEOE-IQEC.2013.6801366).
- **E. Schreiber**: ‘Korrelierte Michelson-Interferometer im Megahertzbereich’. Diploma thesis, Gottfried Wilhelm Leibniz Universität Hannover, 2010.

Further publications co-authored as a member of the LSC

- B.P. Abbott, ... **E. Schreiber**, ... J. Zweizig: ‘GW170608: Observation of a 19-solar-mass Binary Black Hole Coalescence’ (2017). arXiv: [1711.05578](https://arxiv.org/abs/1711.05578).
- B.P. Abbott, ... **E. Schreiber**, ... M. Serra-Ricart: ‘A gravitational-wave standard siren measurement of the Hubble constant’. *Nature* 551.7678 (2017), p. 85. DOI: [10.1038/nature24471](https://doi.org/10.1038/nature24471).
- B.P. Abbott, ... **E. Schreiber**, ... P. Ubertini: ‘Gravitational waves and gamma-rays from a binary neutron star merger: GW170817 and GRB 170817A’. *The Astrophysical Journal* 848.2 (2017), p. L13. DOI: [10.3847/2041-8213/aa920c](https://doi.org/10.3847/2041-8213/aa920c).
- B.P. Abbott, ... **E. Schreiber**, ... P.A. Woudt: ‘Multi-messenger observations of a binary neutron star merger’. *The Astrophysical Journal Letters* 848.2 (2017), p. L12. DOI: [10.3847/2041-8213/AA91C9](https://doi.org/10.3847/2041-8213/AA91C9).
- B.P. Abbott, ... **E. Schreiber**, ... J. Zweizig: ‘Estimating the contribution of dynamical ejecta in the kilonova associated with GW170817’. *The Astrophysical Journal Letters (in press)* (2017). arXiv: [1710.05836](https://arxiv.org/abs/1710.05836).
- B.P. Abbott, ... **E. Schreiber**, ... J. Zweizig: ‘First narrow-band search for continuous gravitational waves from known pulsars in advanced detector data’ (2017). arXiv: [1710.02327](https://arxiv.org/abs/1710.02327).

Further publications co-authored as a member of the LSC

- B.P. Abbott, ... **E. Schreiber**, ... J. Zweizig: ‘GW170814: A three-detector observation of gravitational waves from a binary black hole coalescence’. *Physical Review Letters* 119.14 (2017), p. 141101. DOI: [10.1103/PhysRevLett.119.141101](https://doi.org/10.1103/PhysRevLett.119.141101).
- B.P. Abbott, ... **E. Schreiber**, ... J. Zweizig: ‘GW170817: Implications for the stochastic gravitational-wave background from compact binary coalescences’. *Submitted to Physical Review Letters* (2017). arXiv: [1710.05837](https://arxiv.org/abs/1710.05837).
- B.P. Abbott, ... **E. Schreiber**, ... J. Zweizig: ‘GW170817: Observation of gravitational waves from a binary neutron star inspiral’. *Physical Review Letters* 119.16 (2017), p. 161101. DOI: [10.1103/PhysRevLett.119.161101](https://doi.org/10.1103/PhysRevLett.119.161101).
- B.P. Abbott, ... **E. Schreiber**, ... J. Zweizig: ‘On the progenitor of binary neutron star merger GW170817’. *The Astrophysical Journal Letters (in press)* (2017). arXiv: [1710.05838](https://arxiv.org/abs/1710.05838).
- B.P. Abbott, ... **E. Schreiber**, ... J. Zweizig: ‘Search for post-merger gravitational waves from the remnant of the binary neutron star merger GW170817’. *Submitted to Astrophysical Journal Letters* (2017). arXiv: [1710.09320](https://arxiv.org/abs/1710.09320).
- A. Albert, ... **E. Schreiber**, ... J. Zweizig: ‘Search for high-energy neutrinos from binary neutron star merger GW170817 with ANTARES, IceCube, and the Pierre Auger Observatory’. *Submitted to Astrophysical Journal Letters* (2017). arXiv: [1710.05839](https://arxiv.org/abs/1710.05839).
- B.P. Abbott, ... **E. Schreiber**, ... L. Wang: ‘Upper limits on gravitational waves from Scorpius X-1 from a model-based cross-correlation search in Advanced LIGO data’. *The Astrophysical Journal* 847.1 (2017), p. 47. DOI: [10.3847/1538-4357/aa86f0](https://doi.org/10.3847/1538-4357/aa86f0).
- B.P. Abbott, ... **E. Schreiber**, ... P. Weltevrede: ‘First search for nontensorial gravitational waves from known pulsars’ (2017). arXiv: [1709.09203](https://arxiv.org/abs/1709.09203).
- B.P. Abbott, ... **E. Schreiber**, ... J. Zweizig: ‘All-sky search for periodic gravitational waves in the O1 LIGO data’. *Physical Review D* 96.6 (2017), p. 062002. DOI: [10.1103/PhysRevD.96.062002](https://doi.org/10.1103/PhysRevD.96.062002).
- B.P. Abbott, ... **E. Schreiber**, ... D.P. Anderson: ‘First low-frequency Einstein@Home all-sky search for continuous gravitational waves in Advanced LIGO data’ (2017). arXiv: [1707.02669](https://arxiv.org/abs/1707.02669).
- B.P. Abbott, ... **E. Schreiber**, ... J. Zweizig: ‘Search for intermediate mass black hole binaries in the first observing run of Advanced LIGO’. *Physical Review D* 96.2 (2017), p. 022001. DOI: [10.1103/PhysRevD.96.022001](https://doi.org/10.1103/PhysRevD.96.022001).
- A. Albert, ... **E. Schreiber**, ... J. Zweizig: ‘Search for high-energy neutrinos from gravitational wave event GW151226 and candidate LVT151012 with ANTARES and

Publications

- IceCube'. *Physical Review D* 96.2 (2017), p. 022005. DOI: [10.1103/PhysRevD.96.022005](https://doi.org/10.1103/PhysRevD.96.022005).
- B.P. Abbott, ... **E. Schreiber**, ... R.J. Evans: 'Search for gravitational waves from Scorpius X-1 in the first Advanced LIGO observing run with a hidden Markov model'. *Physical Review D* 95.12 (2017), p. 122003. DOI: [10.1103/PhysRevD.95.122003](https://doi.org/10.1103/PhysRevD.95.122003).
 - B.P. Abbott, ... **E. Schreiber**, ... J. Zweizig: 'GW170104: Observation of a 50-solar-mass binary black hole coalescence at redshift 0.2'. *Physical Review Letters* 118.22 (2017), p. 221101. DOI: [10.1103/PhysRevLett.118.221101](https://doi.org/10.1103/PhysRevLett.118.221101).
 - B.P. Abbott, ... **E. Schreiber**, ... A. Vano Vinuales: 'Effects of waveform model systematics on the interpretation of GW150914'. *Classical and Quantum Gravity* 34.10 (2017), p. 104002. DOI: [10.1088/1361-6382/aa6854](https://doi.org/10.1088/1361-6382/aa6854).
 - B.P. Abbott, ... **E. Schreiber**, ... X. Zhang: 'Search for gravitational waves associated with gamma-ray bursts during the first Advanced LIGO observing run and implications for the origin of GRB 150906B'. *The Astrophysical Journal* 841.2 (2017), p. 89. DOI: [10.3847/1538-4357/aa6c47](https://doi.org/10.3847/1538-4357/aa6c47).
 - B.P. Abbott, ... **E. Schreiber**, ... S. Sigurdsson: 'Search for continuous gravitational waves from neutron stars in globular cluster NGC 6544'. *Physical Review D* 95.8 (2017), p. 082005. DOI: [10.1103/PhysRevD.95.082005](https://doi.org/10.1103/PhysRevD.95.082005).
 - B.P. Abbott, ... **E. Schreiber**, ... P. Weltevrede: 'First search for gravitational waves from known pulsars with Advanced LIGO'. *The Astrophysical Journal* 839.1 (2017), p. 12. DOI: [10.3847/1538-4357/aa677f](https://doi.org/10.3847/1538-4357/aa677f).
 - B.P. Abbott, ... **E. Schreiber**, ... J. Zweizig: 'Calibration of the Advanced LIGO detectors for the discovery of the binary black-hole merger GW150914'. *Physical Review D* 95.6 (2017), p. 062003. DOI: [10.1103/PhysRevD.95.062003](https://doi.org/10.1103/PhysRevD.95.062003).
 - B.P. Abbott, ... **E. Schreiber**, ... J. Zweizig: 'Directional limits on persistent gravitational waves from Advanced LIGO's first observing run'. *Physical Review Letters* 118.12 (2017), p. 121102. DOI: [10.1103/PhysRevLett.118.121102](https://doi.org/10.1103/PhysRevLett.118.121102).
 - B.P. Abbott, ... **E. Schreiber**, ... J. Zweizig: 'Upper limits on the stochastic gravitational-wave background from Advanced LIGO's first observing run'. *Physical Review Letters* 118.12 (2017), p. 121101. DOI: [10.1103/PhysRevLett.118.121101](https://doi.org/10.1103/PhysRevLett.118.121101).
 - B.P. Abbott, ... **E. Schreiber**, ... J. Harms: 'Exploring the sensitivity of next generation gravitational wave detectors'. *Classical and Quantum Gravity* 34.4 (2017), p. 44001. DOI: [10.1088/1361-6382/aa51f4](https://doi.org/10.1088/1361-6382/aa51f4).

Further publications co-authored as a member of the LSC

- B.P. Abbott, ... **E. Schreiber**, ... J. Zweizig: ‘All-sky search for short gravitational-wave bursts in the first Advanced LIGO run’. *Physical Review D* 95.4 (2017), p. 042003. DOI: [10.1103/PhysRevD.95.042003](https://doi.org/10.1103/PhysRevD.95.042003).
- B.P. Abbott, ... **E. Schreiber**, ... J. Zweizig: ‘The basic physics of the binary black hole merger GW150914’. *Annalen der Physik* 529.1-2 (2017), p. 1600209. DOI: [10.1002/andp.201600209](https://doi.org/10.1002/andp.201600209).
- B.P. Abbott, ... **E. Schreiber**, ... J. Zweizig: ‘The rate of binary black hole mergers inferred from Advanced LIGO observations surrounding GW150914’. *The Astrophysical Journal Letters* 833 (2016). DOI: [10.3847/2041-8205/833/1/L1](https://doi.org/10.3847/2041-8205/833/1/L1).
- B.P. Abbott, ... **E. Schreiber**, ... J. Zweizig: ‘Prospects for observing and localizing gravitational-wave transients with Advanced LIGO and Advanced Virgo’. *Living Reviews in Relativity* 19.1 (2016), p. 1. DOI: [10.1007/lrr-2016-1](https://doi.org/10.1007/lrr-2016-1).
- B.P. Abbott, ... **E. Schreiber**, ... J. Zweizig: ‘First targeted search for gravitational-wave bursts from core-collapse supernovae in data of first-generation laser interferometer detectors’. *Physical Review D* 94.10 (2016), p. 102001. DOI: [10.1103/PhysRevD.94.102001](https://doi.org/10.1103/PhysRevD.94.102001).
- B.P. Abbott, ... **E. Schreiber**, ... J. Zweizig: ‘Results of the deepest all-sky survey for continuous gravitational waves on LIGO S6 data running on the Einstein@Home volunteer distributed computing project’. *Physical Review D* 94.10 (2016), p. 102002. DOI: [10.1103/PhysRevD.94.102002](https://doi.org/10.1103/PhysRevD.94.102002).
- B.P. Abbott, ... **E. Schreiber**, ... J. Zweizig: ‘Upper limits on the rates of binary neutron star and neutron star–black hole mergers from Advanced LIGO’s first observation run’. *The Astrophysical Journal* 832.2 (2016), p. L21. DOI: [10.3847/2041-8205/832/2/L21](https://doi.org/10.3847/2041-8205/832/2/L21).
- B.P. Abbott, ... **E. Schreiber**, ... Y. Zlochower: ‘Improved analysis of GW150914 using a fully spin-precessing waveform model’. *Physical Review X* 6.4 (2016), p. 041014. DOI: [10.1103/PhysRevX.6.041014](https://doi.org/10.1103/PhysRevX.6.041014).
- B.P. Abbott, ... **E. Schreiber**, ... J. Zweizig: ‘Binary black hole mergers in the first Advanced LIGO observing run’. *Physical Review X* 6.4 (2016), p. 041015. DOI: [10.1103/PhysRevX.6.041015](https://doi.org/10.1103/PhysRevX.6.041015).
- B.P. Abbott, ... **E. Schreiber**, ... Y. Zlochower: ‘Directly comparing GW150914 with numerical solutions of Einstein’s equations for binary black hole coalescence’. *Physical Review D* 94.6 (2016), p. 064035. DOI: [10.1103/PhysRevD.94.064035](https://doi.org/10.1103/PhysRevD.94.064035).
- B.P. Abbott, ... **E. Schreiber**, ... J. Zweizig: ‘Comprehensive all-sky search for periodic gravitational waves in the sixth science run LIGO data’. *Physical Review D* 94.4 (2016), p. 042002. DOI: [10.1103/PhysRevD.94.042002](https://doi.org/10.1103/PhysRevD.94.042002).

Publications

- B.P. Abbott, ... **E. Schreiber**, ... S. Rosswog: ‘Supplement: Localization and broadband follow-up of the gravitational-wave transient GW150914 (2016, ApJL, 826, L13)’. *The Astrophysical Journal Supplement Series* 225.1 (2016), p. 8. DOI: [10.3847/0067-0049/225/1/8](https://doi.org/10.3847/0067-0049/225/1/8).
- B.P. Abbott, ... **E. Schreiber**, ... J. Zweizig: ‘Characterization of transient noise in Advanced LIGO relevant to gravitational wave signal GW150914’. *Classical and Quantum Gravity* 33.13 (2016), p. 134001. DOI: [10.1088/0264-9381/33/13/134001](https://doi.org/10.1088/0264-9381/33/13/134001).
- B.P. Abbott, ... **E. Schreiber**, ... S. Teukolsky: ‘GW151226: Observation of gravitational waves from a 22-solar-mass binary black hole coalescence’. *Physical Review Letters* 116.24 (2016), p. 241103. DOI: [10.1103/PhysRevLett.116.241103](https://doi.org/10.1103/PhysRevLett.116.241103).
- B.P. Abbott, ... **E. Schreiber**, ... B. Wells: ‘Search for transient gravitational waves in coincidence with short-duration radio transients during 2007–2013’. *Physical Review D* 93.12 (2016), p. 122008. DOI: [10.1103/PhysRevD.93.122008](https://doi.org/10.1103/PhysRevD.93.122008).
- B.P. Abbott, ... **E. Schreiber**, ... Y. Zlochower: ‘Properties of the binary black hole merger GW150914’. *Physical Review Letters* 116.24 (2016), p. 241102. DOI: [10.1103/PhysRevLett.116.241102](https://doi.org/10.1103/PhysRevLett.116.241102).
- B.P. Abbott, ... **E. Schreiber**, ... J. Zweizig: ‘GW150914: First results from the search for binary black hole coalescence with Advanced LIGO’. *Physical Review D* 93.12 (2016), p. 122003. DOI: [10.1103/PhysRevD.93.122003](https://doi.org/10.1103/PhysRevD.93.122003).
- B.P. Abbott, ... **E. Schreiber**, ... J. Zweizig: ‘Observing gravitational-wave transient GW150914 with minimal assumptions’. *Physical Review D* 93.12 (2016), p. 122004. DOI: [10.1103/PhysRevD.93.122004](https://doi.org/10.1103/PhysRevD.93.122004).
- S. Adrián-Martínez, ... **E. Schreiber**, ... J. Zweizig: ‘High-energy neutrino follow-up search of gravitational wave event GW150914 with ANTARES and IceCube’. *Physical Review D* 93.12 (2016), p. 122010. DOI: [10.1103/PhysRevD.93.122010](https://doi.org/10.1103/PhysRevD.93.122010).
- B.P. Abbott, ... **E. Schreiber**, ... Y. Zlochower: ‘Tests of general relativity with GW150914’. *Physical Review Letters* 116.22 (2016), p. 221101. DOI: [10.1103/PhysRevLett.116.221101](https://doi.org/10.1103/PhysRevLett.116.221101).
- B.P. Abbott, ... **E. Schreiber**, ... J. Zweizig: ‘GW150914: Implications for the stochastic gravitational-wave background from binary black holes’. *Physical Review Letters* 116.13 (2016), p. 131102. DOI: [10.1103/PhysRevLett.116.131102](https://doi.org/10.1103/PhysRevLett.116.131102).
- B.P. Abbott, ... **E. Schreiber**, ... J. Zweizig: ‘GW150914: The advanced LIGO detectors in the era of first discoveries’. *Physical Review Letters* 116.13 (2016), p. 131103. DOI: [10.1103/PhysRevLett.116.131103](https://doi.org/10.1103/PhysRevLett.116.131103).

Further publications co-authored as a member of the LSC

- J. Aasi, ... **E. Schreiber**, ... J. Zweizig: ‘First low frequency all-sky search for continuous gravitational wave signals’. *Physical Review D* 93.4 (2016), p. 042007. DOI: [10.1103/PhysRevD.93.042007](https://doi.org/10.1103/PhysRevD.93.042007).
- J. Aasi, ... **E. Schreiber**, ... J. Zweizig: ‘Search of the Orion spur for continuous gravitational waves using a loosely coherent algorithm on data from LIGO interferometers’. *Physical Review D* 93.4 (2016), p. 042006. DOI: [10.1103/PhysRevD.93.042006](https://doi.org/10.1103/PhysRevD.93.042006).
- B.P. Abbott, ... **E. Schreiber**, ... S. Rosswog: ‘Localization and broadband follow-up of the gravitational-wave transient GW150914’. *The Astrophysical Journal Letters* 826.1 (2016), p. L13. DOI: [10.3847/2041-8205/826/1/L13](https://doi.org/10.3847/2041-8205/826/1/L13).
- B.P. Abbott, ... **E. Schreiber**, ... J. Zweizig: ‘All-sky search for long-duration gravitational wave transients with initial LIGO’. *Physical Review D* 93.4 (2016), p. 042005. DOI: [10.1103/PhysRevD.93.042005](https://doi.org/10.1103/PhysRevD.93.042005).
- B.P. Abbott, ... **E. Schreiber**, ... J. Zweizig: ‘Astrophysical implications of the binary black hole merger GW150914’. *The Astrophysical Journal* 818.2 (2016), p. L22. DOI: [10.3847/2041-8205/818/2/L22](https://doi.org/10.3847/2041-8205/818/2/L22).
- B.P. Abbott, ... **E. Schreiber**, ... J. Zweizig: ‘Observation of gravitational waves from a binary black hole merger’. *Physical Review Letters* 116.6 (2016), p. 061102. DOI: [10.1103/PhysRevLett.116.061102](https://doi.org/10.1103/PhysRevLett.116.061102).
- J. Aasi, ... **E. Schreiber**, ... J. Zweizig: ‘Searches for continuous gravitational waves from nine young supernova remnants’. *The Astrophysical Journal* 813.1 (2015), p. 39. DOI: [10.1088/0004-637X/813/1/39](https://doi.org/10.1088/0004-637X/813/1/39).
- J. Aasi, ... **E. Schreiber**, ... J. Zweizig: ‘Characterization of the LIGO detectors during their sixth science run’. *Classical and Quantum Gravity* 32.11 (2015), p. 115012. DOI: [10.1088/0264-9381/32/11/115012](https://doi.org/10.1088/0264-9381/32/11/115012).
- J. Aasi, ... **E. Schreiber**, ... J. Zweizig: ‘Advanced LIGO’. *Classical and Quantum Gravity* 32.7 (2015), p. 74001. DOI: [10.1088/0264-9381/32/7/074001](https://doi.org/10.1088/0264-9381/32/7/074001).
- J. Aasi, ... **E. Schreiber**, ... J. Zweizig: ‘Directed search for gravitational waves from Scorpius X-1 with initial LIGO data’. *Physical Review D* 91.6 (2015), p. 062008. DOI: [10.1103/PhysRevD.91.062008](https://doi.org/10.1103/PhysRevD.91.062008).
- J. Aasi, ... **E. Schreiber**, ... J. Zweizig: ‘Narrow-band search of continuous gravitational-wave signals from Crab and Vela pulsars in Virgo VSR4 data’. *Physical Review D* 91.2 (2015), p. 022004. DOI: [10.1103/PhysRevD.91.022004](https://doi.org/10.1103/PhysRevD.91.022004).
- J. Aasi, ... **E. Schreiber**, ... J. Zweizig: ‘Searching for stochastic gravitational waves using data from the two colocated LIGO Hanford detectors’. *Physical Review D* 91.2 (2015), p. 022003. DOI: [10.1103/PhysRevD.91.022003](https://doi.org/10.1103/PhysRevD.91.022003).

Publications

- J. Aasi, ... **E. Schreiber**, ... J. Zweizig: ‘Improved upper limits on the stochastic gravitational-wave background from 2009–2010 LIGO and Virgo data’. *Physical Review Letters* 113.23 (2014), p. 231101. DOI: [10.1103/PhysRevLett.113.231101](https://doi.org/10.1103/PhysRevLett.113.231101).
- M. G. Aartsen, ... **E. Schreiber**, ... J. Zweizig: ‘Multimessenger search for sources of gravitational waves and high-energy neutrinos: Initial results for LIGO–Virgo and IceCube’. *Physical Review D* 90.10 (2014), p. 102002. DOI: [10.1103/PhysRevD.90.102002](https://doi.org/10.1103/PhysRevD.90.102002).
- J. Aasi, ... **E. Schreiber**, ... J. Zweizig: ‘First all-sky search for continuous gravitational waves from unknown sources in binary systems’. *Physical Review D* 90.6 (2014), p. 062010. DOI: [10.1103/PhysRevD.90.062010](https://doi.org/10.1103/PhysRevD.90.062010).
- J. Aasi, ... **E. Schreiber**, ... J. Zweizig: ‘Implementation of an \mathcal{F} -statistic all-sky search for continuous gravitational waves in Virgo VSR1 data’. *Classical and Quantum Gravity* 31.16 (2014), p. 165014. DOI: [10.1088/0264-9381/31/16/165014](https://doi.org/10.1088/0264-9381/31/16/165014).
- J. Aasi, ... **E. Schreiber**, ... A. von Kienlin: ‘Search for gravitational waves associated with γ -ray bursts detected by the interplanetary network’. *Physical Review Letters* 113.1 (2014), p. 011102. DOI: [10.1103/PhysRevLett.113.011102](https://doi.org/10.1103/PhysRevLett.113.011102).
- J. Aasi, ... **E. Schreiber**, ... Y. Zlochower: ‘The NINJA-2 project: detecting and characterizing gravitational waveforms modelled using numerical binary black hole simulations’. *Classical and Quantum Gravity* 31.11 (2014), p. 115004. DOI: [10.1088/0264-9381/31/11/115004](https://doi.org/10.1088/0264-9381/31/11/115004).
- J. Aasi, ... **E. Schreiber**, ... J. Zweizig: ‘Methods and results of a search for gravitational waves associated with gamma-ray bursts using the GEO 600, LIGO, and Virgo detectors’. *Physical Review D* 89.12 (2014), p. 122004. DOI: [10.1103/PhysRevD.89.122004](https://doi.org/10.1103/PhysRevD.89.122004).
- J. Aasi, ... **E. Schreiber**, ... J. Zweizig: ‘Search for gravitational radiation from intermediate mass black hole binaries in data from the second LIGO–Virgo joint science run’. *Physical Review D* 89.12 (2014), p. 122003. DOI: [10.1103/PhysRevD.89.122003](https://doi.org/10.1103/PhysRevD.89.122003).
- J. Aasi, ... **E. Schreiber**, ... J. Zweizig: ‘Search for gravitational wave ringdowns from perturbed intermediate mass black holes in LIGO–Virgo data from 2005–2010’. *Physical Review D* 89.10 (2014), p. 102006. DOI: [10.1103/PhysRevD.89.102006](https://doi.org/10.1103/PhysRevD.89.102006).
- J. Aasi, ... **E. Schreiber**, ... B. W. Stappers: ‘Gravitational waves from known pulsars: Results from the initial detector era’. *The Astrophysical Journal* 785.2 (2014), p. 119. DOI: [10.1088/0004-637X/785/2/119](https://doi.org/10.1088/0004-637X/785/2/119).
- J. Aasi, ... **E. Schreiber**, ... J. Zweizig: ‘Application of a Hough search for continuous gravitational waves on data from the fifth LIGO science run’. *Classical and Quantum Gravity* 31.8 (2014), p. 085014. DOI: [10.1088/0264-9381/31/8/085014](https://doi.org/10.1088/0264-9381/31/8/085014).

Further publications co-authored as a member of the LSC

- J. Aasi, ... **E. Schreiber**, ... J. Zweizig: ‘Constraints on cosmic strings from the LIGO-Virgo gravitational-wave detectors’. *Physical Review Letters* 112.13 (2014), p. 131101. DOI: [10.1103/PhysRevLett.112.131101](https://doi.org/10.1103/PhysRevLett.112.131101).
- J. Aasi, ... **E. Schreiber**, ... W. Zheng: ‘First searches for optical counterparts to gravitational-wave candidate events’. *The Astrophysical Journal Supplement Series* 211.1 (2014), p. 7. DOI: [10.1088/0067-0049/211/1/7](https://doi.org/10.1088/0067-0049/211/1/7).
- J. Aasi, ... **E. Schreiber**, ... J. Zweizig: ‘Search for long-lived gravitational-wave transients coincident with long gamma-ray bursts’. *Physical Review D* 88.12 (2013), p. 122004. DOI: [10.1103/PhysRevD.88.122004](https://doi.org/10.1103/PhysRevD.88.122004).
- J. Aasi, ... **E. Schreiber**, ... J. Zweizig: ‘Directed search for continuous gravitational waves from the Galactic center’. *Physical Review D* 88.10 (2013), p. 102002. DOI: [10.1103/PhysRevD.88.102002](https://doi.org/10.1103/PhysRevD.88.102002).
- J. Abadie, ... **E. Schreiber**, ... X.-L. Zhang: ‘Search for gravitational waves associated with gamma-ray bursts during LIGO science run 6 and Virgo science runs 2 and 3’. *The Astrophysical Journal* 760.1 (2012), p. 12. DOI: [10.1088/0004-637X/760/1/12](https://doi.org/10.1088/0004-637X/760/1/12).
- J. Abadie, ... **E. Schreiber**, ... J. Zweizig: ‘All-sky search for gravitational-wave bursts in the second joint LIGO-Virgo run’. *Physical Review D* 85.12 (2012), p. 122007. DOI: [10.1103/PhysRevD.85.122007](https://doi.org/10.1103/PhysRevD.85.122007).
- J. Abadie, ... **E. Schreiber**, ... J. Zweizig: ‘Upper limits on a stochastic gravitational-wave background using LIGO and Virgo interferometers at 600–1000 Hz’. *Physical Review D* 85.12 (2012), p. 122001. DOI: [10.1103/PhysRevD.85.122001](https://doi.org/10.1103/PhysRevD.85.122001).
- J. Abadie, ... **E. Schreiber**, ... J. Zweizig: ‘First low-latency LIGO+Virgo search for binary inspirals and their electromagnetic counterparts’. *Astronomy & Astrophysics* 541 (2012), A155. DOI: [10.1051/0004-6361/201218860](https://doi.org/10.1051/0004-6361/201218860).
- J. Abadie, ... **E. Schreiber**, ... J. Zweizig: ‘Search for gravitational waves from intermediate mass binary black holes’. *Physical Review D* 85.10 (2012), p. 102004. DOI: [10.1103/PhysRevD.85.102004](https://doi.org/10.1103/PhysRevD.85.102004).

Acknowledgements

I would like to sincerely thank so many people who have contributed to making my PhD such an exiting and enjoyable time.

First I thank Karsten Danzmann for giving me the extraordinary opportunity of working in this field at a truly outstanding institute.

I would like to thank Roman Schnabel who with the work of his group laid the foundation of my PhD project and who kindly agreed to review this thesis. Many years ago it was you who first sparked my interest in squeezed light in a very exiting lecture on non-classical interferometry.

Thank you Kate Dooley for being such an important guidance at the beginning of my PhD time. I learned a lot from you.

I am incredibly grateful to Hartmut Grote who showed so much trust in me, opened many doors, and sent me half around the world. Not least, I have to thank you for bringing me to GEO in the first place.

Henning Vahlbruch, I thank you for everything. It is a pleasure working with you and I am time and again impressed by your expertise and by your kindness.

A great thank you to my fellow squeezers of the past years Jim Lough and Matteo Leonardi for so many enlightening discussions and shared hours in the cleanroom.

I owe Christoph Affeldt my deepest gratitude for all his support. You were instrumental in getting this thesis started.

And also to the rest of the GEO team – Aparna, Harald, Holger, Jake, Jon, Marc, Michael, Michał, Mirko, Suresh, Volker and Walter – I want to say thank you. It was great to share my time with you.

I say thank you to the prototype people and so many other nice people from our institute and across the collaboration.

For reading small or very large parts of this thesis and providing me with so many helpful comments I have to thank Christoph, David, Florian, Hartmut, Henning, Holger, Jim, Matteo and Moritz.

Finally I thank my friends and above all my family for all the unconditional support.

The first detections of gravitational waves have opened an exciting new field of astronomy. One of the most fundamental limitations for the sensitivity of current and future interferometric gravitational-wave detectors is imposed by the quantum nature of light: Quantum vacuum fluctuations entering the interferometer through the readout port will contribute to the detection noise, at high frequencies in the form of shot noise and at low frequencies by radiation pressure noise. A promising way to reduce this quantum noise is the injection of squeezed states of light that have a lower uncertainty in one quadrature than the vacuum state. The GEO 600 gravitational-wave detector demonstrated the use of squeezed light in 2010 and it is now the first detector to routinely apply squeezing to improve its sensitivity beyond the limits set by classical quantum shot noise.

This thesis details the practical aspects of long-term stable and efficient squeezed-light integration in a large-scale gravitational-wave detector. Imperfections that can limit the amount of observable non-classical noise improvement, such as optical losses and phase fluctuations, were studied in detail and methods for their mitigation were developed. Novel control schemes for the active stabilisation of the squeezed light field's phase and alignment were one main focus of the investigations. At the same time, important experience was gathered in the operation of the squeezed light source over long timescales.

Over the course of the thesis work, improvements were implemented that significantly increased the performance of the squeezed-light application. Squeezing was injected with an overall duty cycle of 88 %, reaching a noise reduction of up to 4.4 dB, corresponding to a 40 % lowered shot-noise level.

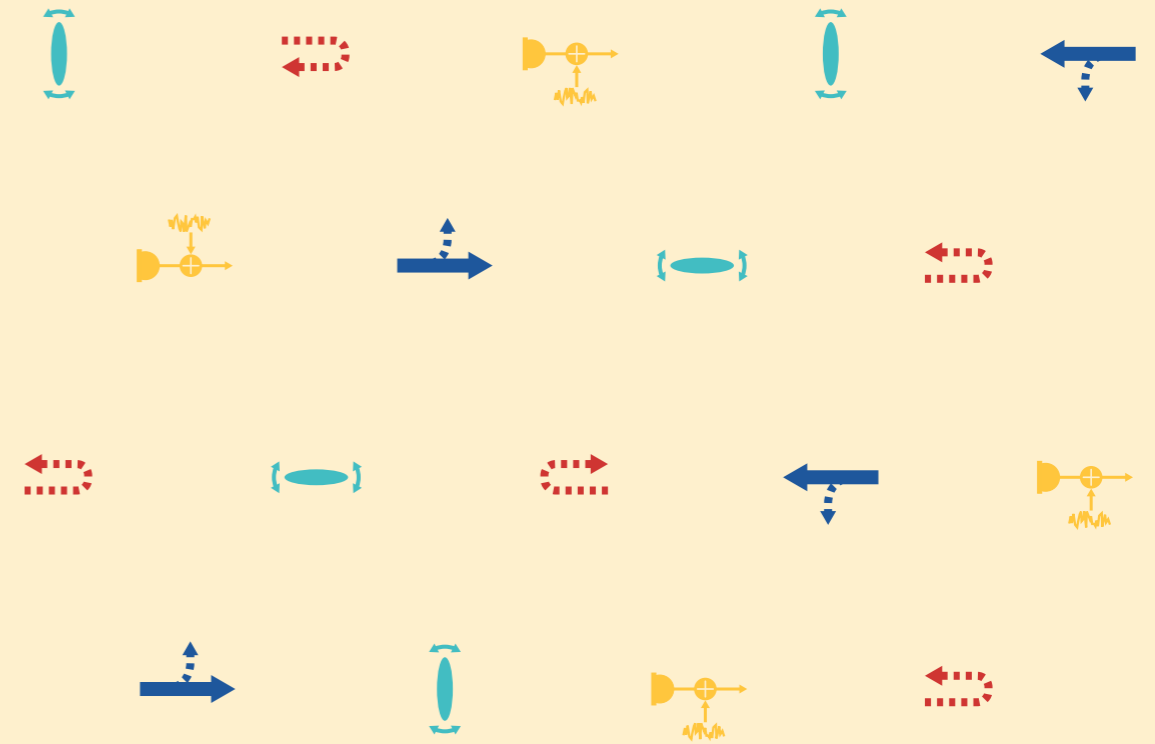
This work has firmly established the practical application of squeezing as a mature technology. The gained knowledge will directly inform the implementation of squeezed light for all future gravitational-wave detectors.



A digital version of this thesis is available at: dcc.ligo.org/LIGO-P1800001/public

Gravitational-wave detection beyond the quantum shot-noise limit
The integration of squeezed light in GEO 600

EMIL SCHREIBER



EMIL SCHREIBER

Gravitational-wave detection beyond the quantum shot-noise limit **The integration of squeezed light in GEO 600**

